The Dissertation Committee for Rachel Elizabeth Chisolm Certifies that this is the approved version of the following dissertation:

Climate Change Impacts and Water Security in the Cordillera Blanca, Peru

Committee:

Daene C. McKinney, Supervisor

Ginny Catania

Robert Gilbert

Ben R. Hodges

Paola Passalacqua

Climate Change Impacts and Water Security in the Cordillera Blanca, Peru

by

Rachel Elizabeth Chisolm, B.S., M.S.E.

Dissertation

Presented to the Faculty of the Graduate School of

The University of Texas at Austin

in Partial Fulfillment

of the Requirements

for the Degree of

Doctor of Philosophy

The University of Texas at Austin

August, 2016

Acknowledgements

As with any work of this magnitude, this dissertation would not have been possible without the involvement of many people. First, I would like to thank my advisor, Dr. Daene McKinney for his mentorship and guidance throughout my PhD; you have been the best advisor that anyone could ask for. I would like to thank Dr. Jorge Recharte at The Mountain Institute (TMI) for giving me the opportunity to investigate the links between research and climate-resilient development. The TMI staff have given invaluable support on the ground and ensured that the impact of this work extends beyond the scientific community by helping to communicate these results to the local population and decision-makers in Peru. I would like to thank Alejo Cochachin at the Unidad de Glaciología y Recursos Hídricos (UGRH) and Karla Rodriguez Vergara for providing data. I am grateful to the Instituto Nacional de Investigación en Glaciares y Ecosistemas de Montaña (INAIGEM), UGRH, and the regional authorities at the Instituto Nacional de Defensa Civil (INDECI) for their collaboration, and I am indebted to volunteers at TMI for their assistance with field work. I am especially grateful to the support staff at the Center for Research in Water Resources (CRWR) for their patience and assistance in navigating the complicated logistics that are always present with institutional grants that involve travel and living abroad.

I would like to thank my committee members for reading this dissertation and giving valuable feedback to make it better, and I want to thank my mother, Dr. Marsha Chisolm, for proofreading this dissertation. Current and former members of the McKinney research group have been excellent partners in this work, and the students at CRWR have always provided a great sounding board for new ideas. Of course, this work would not have been possible without the financial support of the United States Agency

for International Development (USAID) through the Climate Change Resilient Development project and the Securing Mountain Watershed and Livelihoods project with The Mountain Institute.

Finally, I would like to thank my friends and family for their moral support and prayers throughout the long and arduous process of completing this PhD. I could not have done this without the help of God who has been my source of strength and endurance, allowing me to do the work that I love in spite of illness throughout.

With men this is impossible, but with God all things are possible. (Matthew 19:26)

You answered me when I called to you;
with your strength you strengthened me. (Psalm 138:3)

The Lord has done this,
and it is marvelous in our eyes. (Psalm 118:23)

Climate Change Impacts and Water Security in the Cordillera Blanca, Peru

Rachel Elizabeth Chisolm, PhD

The University of Texas at Austin, 2016

Supervisor: Daene C. McKinney

Abstract: This dissertation addresses two aspects of climate change impacts on water resources in the Cordillera Blanca mountain range in Ancash, Peru: glacial lake outburst floods (GLOFs) and water availability. Peru is one of the countries most impacted by climate change, largely due to the abundance of glaciers that play an integral role in the water resources systems of the Peruvian Andes and the coastal region. A warming climate has resulted in the accelerated retreat of many of these glaciers in recent decades. The two greatest impacts of climate change on water security in the Cordillera Blanca are GLOFs and water scarcity during the dry season. This dissertation studies both of these facets of water security in the Cordillera Blanca, Peru.

As new glacial lakes emerge and existing lakes continue to grow, they pose an increasing risk of GLOFs that can be catastrophic to the communities living downstream. In this work, particular emphasis is placed on the upper watershed processes that typically comprise a GLOF event. Dynamics of avalanche-generated impulse waves are investigated through three-dimensional hydrodynamic lake simulations of potential GLOF scenarios at Lake Palcacocha, Peru. At Artesonraju Glacier, an emerging lake has recently formed and continues to grow as the glacier retreats. Future lake volumes are projected from ground penetrating radar measurements of ice thickness. With these projections of future lake conditions, possible future hazard conditions are studied at

Artesonraju, and a new analytical method is presented for calculating approximate overtopping volumes from avalanche-generated waves.

Climate change impacts on water availability have been studied through the analysis of approximately 50 years of precipitation data from a weather station in the Cordillera Blanca. These data have been analyzed for trends and changes in variability in precipitation patterns. As a foundation for climate-resilient development, precipitation trends and changes in variability have been linked to possible impacts on agricultural projects. The results of the precipitation data analysis were compared to studies of local perceptions of climate change, and it was concluded that people's perceptions of change in precipitation patterns often do not reflect the trends observed in the gauged data.

Table of Contents

List of Tables

List of Figures

Chapter 1: Introduction

Peru is one of the countries most impacted by climate change, largely due to the abundance of glaciers that play an integral role in the water resources systems of the Peruvian Andes and the coastal region. Peru is home to over 70% of the world's tropical glaciers, many of which are located in the Cordillera Blanca mountain range in the Ancash Department[1] (Kaser and Osmaston 2002). Tropical glaciers are an essential component of the water resources systems in the mountainous regions where they are located, and the contiguous lowland coastal areas have large agricultural economies and populations dependent on glacial melt to meet their water resources needs. A warming climate has resulted in the accelerated retreat of many of these glaciers in recent decades (Rabatel et al., 2013). The glaciers in the Cordillera Blanca play a particularly dominant role since they act as a buffer to store water and release it consistently throughout the dry season, and since most of the electricity in the region comes from hydropower produced from glacial runoff (Bradley et al., 2006). A more immediate and hazardous effect of glacial retreat is the flood risk from glacial lakes that are forming at the termini of glaciers in the Cordillera Blanca. As new lakes emerge and existing lakes continue to grow in area and volume, they pose an increasing risk of glacial lake outburst floods (GLOFs) that can be catastrophic to the communities living downstream. A number of GLOFs have occurred in the Cordillera Blanca that have resulted in great loss of life and property, including a catastrophic GLOF in 1941 from Lake Palcacocha that destroyed much of the city of Huaraz and killed ~1,800 people (Wegner, 2014). *This dissertation aims to study the impact of climate change in glacial watersheds of the Cordillera Blanca*

[1] Departments are Peruvian administrative regions.

and the effects that these changes are having on nearby populations, thus providing the foundation for climate-resilient development.

Peru is no stranger to the impacts of climate change, and the government has been implementing lake safety systems in the lakes of the Cordillera Blanca since the threat of GLOFs began to emerge in the mid 1900's (Carey, 2010). However, the Peruvian government still lacks the necessary tools to incorporate climate change and its impacts into policy and planning measures. Although some of the impacts of climate change in the Peruvian Andes are very well known, the current understanding of the exact nature of climate change and its impacts is still very limited. One major difficulty is that climate change is by definition a non-stationary process, making future projections difficult and uncertain. Nonetheless, an attempt must be made to provide the people of Ancash with the information and tools to plan for resilient development in the face of climate change, moving away from a reactive mode where changes are addressed as they come.

Although this dissertation is in large part forward looking, the basis of this work is deeply rooted in the past. Knowledge of past GLOF events and climate records can inform our understanding of the interconnected nature of high mountain glacial watershed systems, the impacts of climate change on these systems and the risks for downstream communities. The current state of knowledge must govern our analysis of climate change impacts, and an assessment of the present condition of water resources systems provides a suitable baseline. But, the purpose of scientific research is to advance the state of knowledge and improve our understanding of how the world works. We must take advantage of this forward-thinking perspective to assist the people of Ancash in adapting to climate change so that they do not remain fixed in the past. This can be done by using advancements in our knowledge of climate change impacts to improve planning practices and proactively prepare for the future. A planning mentality that is rooted in the

past without also looking towards the future can have negative consequences. For example, the lake safety system that was implemented at Lake Palcacocha in the 1970's was designed for the size of the lake at the time and did not account for potential lake growth. If the present knowledge of climate change existed at the time, perhaps this could have been foreseen; this was not the case, and now the lake is approximately 17 times larger than it was in 1974, rendering the existing lake safety system inadequate for the current lake dimensions. Now that we know something of the impact of climate change and the important role of climate change impacts on the natural systems of the Cordillera Blanca, action must be taken to study these impacts and use this knowledge to develop a plan of action for adaptive and resilient development.

The objective of this dissertation is to assess the impact of climate change on high mountain glacial watershed systems in the Cordillera Blanca with a focus on water security issues. This analysis considers two specific issues: GLOF hazard assessment and water resources availability. Chapters 2 and 3 address the need for new methods to assess GLOF hazard, and Chapter 4 looks at methods for climate data analysis that may be relevant to public investment projects. Although each has a slightly different focus, all three of these chapters are oriented towards improving local understanding of climate change impacts on high mountain glacial watershed systems with an emphasis on producing data and tools that could be useful within the development context to promote the resilience of the local populations to climate change.

1.1 BACKGROUND

1.1.1 MOTIVATION

This dissertation is motivated primarily by two factors: 1) the impacts of climate change that have been observed in the Cordillera Blanca, and 2) the movement to promote climate-resilient development and build "green infrastructure." The first point is one that is a frequent topic of discussion in Peru, as the impacts of climate change have already begun to affect the security and livelihoods of the local population. Depending on where they live, different sectors of the population in the Sierra of Ancash are concerned about distinct climate change impacts. People who live in the cities tend to be more concerned about GLOFs, as the cities are built along the edge of rivers, and they are more likely to be in the path of destruction if a GLOF were to occur. People who live in rural areas more often live on higher ground where the threat of a GLOF is less prevalent; however, their livelihoods frequently depend on agriculture, so they are typically more concerned about water availability for their crops.

The second point motivating this work is related to the local climate change impacts that have been observed, but it is also part of a greater movement in society that seeks to make development more sustainable by incorporating climate change analysis into evaluations of development activities. This work has been primarily funded by development projects of the United States Agency for International Development (USAID), so the importance of linking scientific research with development goals has been ever present. USAID has developed protocols for climate-resilient development that are summarized in Section 1.1.2, and the Peruvian government has recently begun to require the incorporation of climate change vulnerability analysis in all public investment project (PIP) proposals, part of their initiative to promote "green infrastructure". However, to be able to counteract or mitigate the effects of climate change for more

sustainable development, more knowledge is needed about local climate change processes and impacts. At present, there is very little quantitative knowledge about the local impacts of climate change; to be able to manage these impacts, we must first improve our understanding of the physical nature of climate change in the region. *This dissertation aims to begin to fill this knowledge gap so that decision makers may be better equipped to combat the effects of climate change and achieve their goals of sustainable development*. The following sub-sections introduce the study area and some basic concepts that are integral to this dissertation.

1.1.1 Study Area

The geographic study area for this dissertation is the Sierra of the Ancash Department of Peru. The Sierra of Ancash includes three glaciated mountain ranges: the Cordillera Blanca, the Cordillera Huayhuash, and the Cordillera Huallanca (Figure 1.1). The largest of these is the Cordillera Blanca that contains many of the highest peaks in the Americas. Glacial runoff from the peaks of the Cordillera Blanca contributes a crucial portion of the dry season flow in the Santa River and its tributaries. The Santa River, the primary river in the Ancash Department, flows north through the valley called the Callejón de Huaylas from its source at Lake Conococha until it reaches the Cañon del Pato where it leaves the mountains and turns west towards the Pacific coast. As the Santa River flows through the Callejón de Huaylas, it is bordered by the Cordillera Blanca to the east and the Cordillera Negra mountain range to the west. The major cities in this area are Huaraz (the most populous), Carhuaz and Caraz. The eastern side of the Cordillera Blanca, called the Conchucos zone, is typically wetter than the western side, and this zone drains towards the Marañon River, a tributary to the Amazon. The individual study

sites are marked in Figure 1.1 and include Lake Palcacocha (Chapter 2), Artesonraju Glacier (Chapter 3) and the weather station at Cachicadan (Chapter 4).

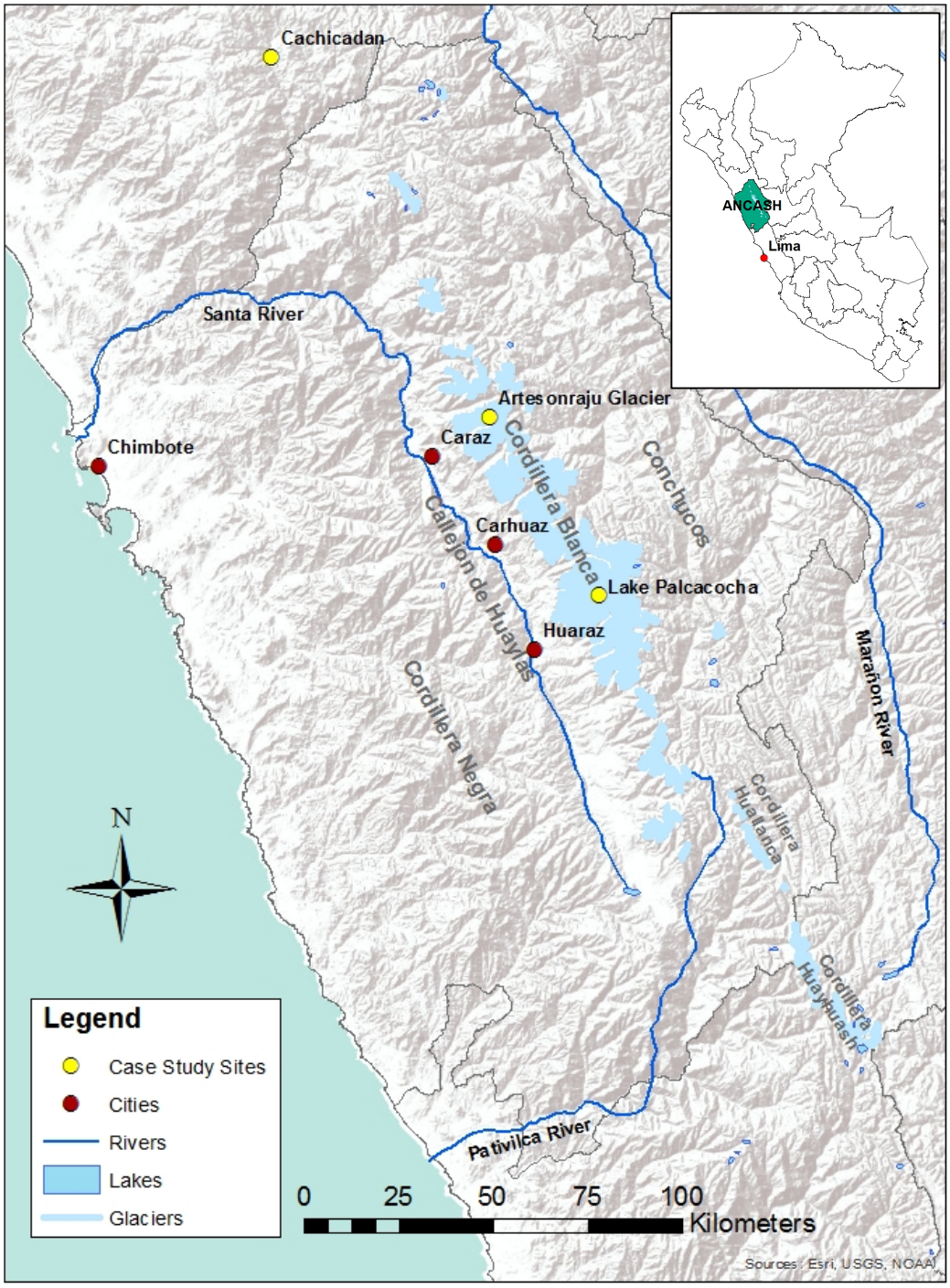

Figure 1.1- The Sierra of Ancash, study area for this dissertation

1.1.2 Climate-Resilient Development

The methodology for climate change vulnerability analysis developed by USAID (2014) is considered as part of the context for this work. USAID's methodology is very general and provides almost no technical guidance, so one contribution of this work is to provide tools for technical analysis of climate change and vulnerability that can be applied in decision-making processes within the political framework of the region. The process of the USAID (2014) framework is outlined below with the following suggested steps for undertaking climate-resilient development projects:

1) Scope
    1.1. Frame the planning process
        1.1.1. Identify development goals
        1.1.2. Identify inputs and enabling conditions
    1.2. Identify climate and non-climate stressors
        1.2.1. Climate stressors: variability and climate change
2) Assess: What contributes to the vulnerability of inputs?
3) Design
    3.1. Identify adaptation options
    3.2. Select evaluation criteria
    3.3. Evaluate options
    3.4. Select a course of action
4) Implement and manage
5) Evaluate and adjust

Within this framework, the analysis of this dissertation focuses on:

a) Identification of climate stressors and

b) Identification of the impacts of climate stressors on inputs to development goals (or public investment projects)

The ways in which the steps of the USAID method outlined above have been incorporated into this dissertation and enhanced with more detailed technical analyses are described below.

- *Preliminary analysis: climate change trends and projections*

  This is an additional step that is proposed as part of this dissertation. The focus of climate-resilient development is necessarily climate change, so an indispensable precursor to any vulnerability analysis is a stock-taking of available data and local knowledge about climate change. This should include analysis of historical data for trends and use of the best available projections from regional or global climate models.

- *1.1.2 Identify inputs*

  This step involves identifying the key resources and how they are used. The case study in this work focuses on water as a key resource.

- *1.2.1 Identify climate stressors*

  The most obvious variables affected by climate change are temperature and precipitation, but there can be secondary consequences that must also be considered. Chapter 4 of this dissertation focuses on identifying changes in precipitation patterns that may be stressors for agricultural projects. Chapters 2

and 3 address one specific secondary consequence of climate change (glacier retreat) and the impacts of this on downstream communities.

- *2. Assess*

  This is the step that is least defined in the USAID framework but is crucial to climate change vulnerability assessment. This step is addressed in Chapter 4 through discussions about what changes in precipitation patterns might mean in terms of their impacts on agricultural projects. The examples of practical application presented in Chapter 4 are meant to illustrate how this step might be carried out within this framework for climate-resilient development. Because very few guidelines are given on how to undertake this assessment, a major contribution of this dissertation is the application of scientific analysis to this process.

- *3.1 Identify adaptation options*

  Within this step, USAID identifies one adaptation option as "improving access to science analysis for decision-making" that includes data availability, predictions and analysis tools as well as the ability to access and use this information (USAID, 2014). However, one could argue that improving access to science and analysis should be an overall objective rather than one particular adaptation option. The work presented in this dissertation is an effort to do just this.

The USAID framework emphasizes that development goals should be the drivers of change. Within this framework, climate change should be considered primarily through ways to make the activities proposed to meet development goals more sustainable. Projects can have adaptation as their primary objective. However, many projects that have development as their primary objective can also be adaptation projects if they are robust to many potential scenarios of climate change. The climate change data analysis presented in Chapter 4 is meant to assist this second type of project. With improved understanding of the changes that are happening, projects can be adapted to be more sustainable under a range of potential climate outcomes.

1.1.3 High Mountain Glacial Watershed Systems

The evolution of glacial lakes and the resulting increase in flood risk is a very complicated process with many varying components. The different components of the glacial watershed system and their interconnected relationships make it difficult to gain a comprehensive understanding of the system as a whole. The glacial watershed system is influenced by many factors, including a changing climate, glacier hydrology and thermodynamics, glacier lake mass balance, lake dynamics, and slope stability (see Figure 1.2 for a schematic of all of the system components and their linkages). All of these factors contribute to the risk faced by downstream communities from GLOFs.

The most common GLOF triggers are landslides, avalanches, or ice calving into a lake (Emmer and Vilímek, 2013; Emmer and Cochachin, 2013; Awal et al., 2010; Bajracharya et al., 2007b; Richardson and Reynolds, 2000; Costa and Schuster, 1988). These avalanche events can cause large waves that propagate across the lake and may overtop the terminal moraine. The steps of a typical chain of processes for a GLOF event

are the following: (1) large avalanche masses reaching nearby lakes, (2) wave generation, propagation, and runup across lakes, (3) terminal moraine overtopping and/or moraine breaching, (4) flood propagation along downstream valleys; and (5) inundation of riverine populated areas (Worni et al., 2014; Westoby et al., 2014b). Most studies simulating the GLOF process chain have modeled each of these individual processes separately with the results from one step in the process chain being used as inputs to subsequent steps (e.g. Schneider et al., 2014; Westoby et al., 2014b, Worni et al., 2014).

This dissertation focuses on individual processes of the upper portions of the glacial watershed system rather than analyzing the entire system in detail. This research uses a process-based approach to incorporate knowledge gained by studying individual components of the system (in this work, primarily the lake dynamics) to obtain a more complete understanding of the glacial watershed system as a whole.

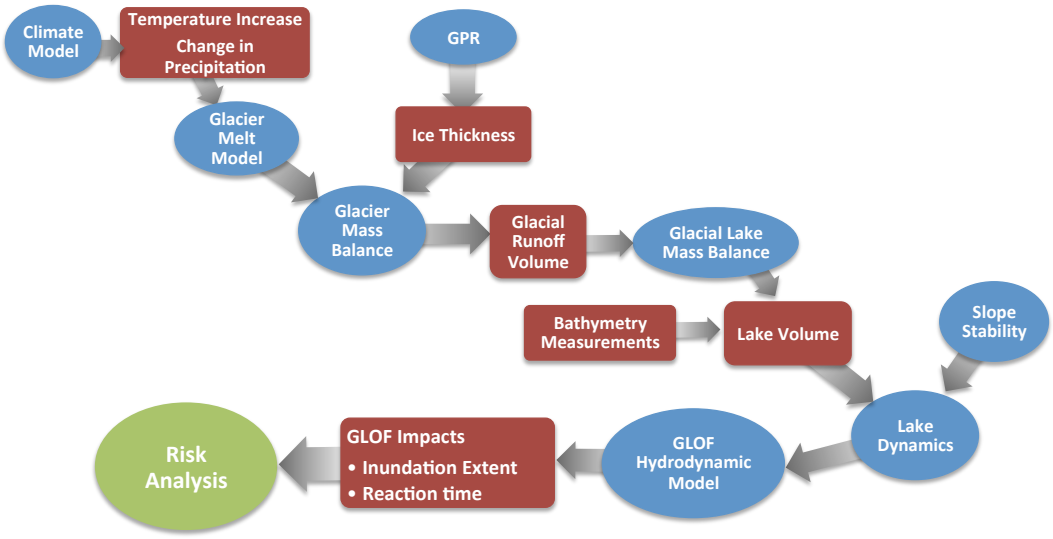

Figure 1.2- Process schematic of the components of glacial watershed systems that contribute to GLOF risk. Key data needed to assess GLOF risk are depicted as red squares, and the blue circles represent key processes.

1.2 RESEARCH OBJECTIVES

This dissertation addresses two aspects of water security, GLOF hazard and water availability, and is founded on two principles:

1) The impacts of climate change on water resources in the Cordillera Blanca can be better understood by studying individual components and processes that comprise the high mountain glacial watershed systems of the region.
2) The research findings from studying these components can be applied broadly to influence methodologies for the analysis of vulnerability of water resources and infrastructure to climate change.

Chapter 2 and Chapter 3 focus on hazards by looking at the impact of climate change on glacier retreat and GLOF hazard. For this purpose, two case study sites were selected because they are representative of the characteristics that make lakes susceptible to outburst flooding. The focus of this part of the dissertation is on the upper portion of the glacial watershed system, from the glaciers to the lake-damming terminal moraines. These two case study sites (shown in Figure 1.1) are introduced below.

- *Lake Palcacocha* was used to study the lake hydrodynamics of avalanche-induced waves that are often part of GLOF events.
- *Artesonraju Glacier* was used to study the emergence and growth of glacial lakes that may become dangerous in the future.

The objectives of this part of the dissertation include:

a) Gaining a better understanding of the dynamics of avalanche-generated waves in glacial lakes and how these waves influence GLOF hazard (Chapter 2)

b) Understanding the role of emerging glacial lakes with future hazard conditions in these variable systems under climate change (Chapter 3)

Chapter 4 focuses on water availability and the links between scientific research and development. This is done through analysis of precipitation data with an emphasis on relating historic trends and variability to their implications for agricultural projects. There has been very little analysis of historic climate data in the Sierra of Ancash, and the objective of Chapter 4 is to develop standard protocols for climate data analysis that can be applied in the assessment of vulnerability to climate change for new development projects. Peru's Ministry of Economy and Finance (MEF) is now requiring that all public investment project proposals include climate change in the risk and vulnerability assessment of projects (MEF, 2015). However, quantitative information on climate change and its impacts is almost non-existent, and access to historical climate data is very limited. If climate change is to be an integral part of policy and decision-making in Peru, there is an evident need to improve our understanding of climate change impacts from a scientific perspective in a way that this knowledge can be transferred to decision-makers. This work emphasizes the linkage between scientific research and its application for long-term planning and adaptation measures. With this part of the dissertation, we hope to move towards bridging the gap between scientific research and development by

adapting research to fit the needs of the people, thus promoting climate-resilient development. The methods used to reach this objective are based on the following ideas:

- The need for high-level science to understand physical processes and improve technical understanding
- Use of advancements in scientific understanding to develop simple analysis tools *These must be simple enough that non-experts can use them and apply them broadly*.
- Promotion of decision-making practices that compensate for limited information by allowing for high levels of uncertainty (making use of the best available data)
- Presentation of information in a way that is useful to decision-makers

The ultimate goal of this work is to help local entities understand their changing water resources landscape and equip them with the tools to adapt and protect the lives, property and livelihoods of the people who may be affected. While this work focuses on the technical aspects of climate change vulnerability analysis, it has been done in close cooperation with stakeholders and other collaborators who are working on the accompanying social and political processes in adaptation initiatives. It has been important to understand the sociopolitical context of the case study region to ensure that the work meets the needs of the people and is adapted to the local modus operandi.

In summary, the objective of this dissertation is to *advance understanding of climate change impacts on water security in the Sierra of Ancash, including flood risk and water supply*.

1.3 RESEARCH QUESTIONS

This research is motivated by a desire to understand the impact of climate change on water resources systems in glacierized catchments of the Sierra of Ancash and the effects of these changes on populations that are a part of the high mountain glacier ecosystem. The broader goal of the research is to study the individual components of high mountain glacial watershed systems and link these components to gain an improved understanding of how the system behaves as a whole; this includes analyses of the short-term processes that occur during a GLOF event as well as the long-term processes and changes that occur as the glacial watershed systems evolve with a warming climate. The research questions for this dissertation are divided into two categories: *GLOF hazard assessment* (Chapters 2 and 3) and *Linking Scientific Research and Climate-Resilient Development* (Chapter 4).

1.3.1 GLOF Hazard Assessment

Chapters 2 and 3 deal with the assessment of GLOF hazard and aim to answer research questions that focus on individual aspects of selected glacial watershed systems. The first two questions are related to the development of methods to assess current hazard levels and evaluate potential mitigation solutions in the context of the Lake Palcacocha case study (Chapter 2). The third question relates to forecasting future lake conditions and determining hazard levels based on those forecasts in the context of Artesonraju Glacier and the evolving glacial lake there (Chapter 3). This presents a unique opportunity to identify a potential problem and identify possible solutions before the lake becomes dangerous.

Research Question #1: What would the lake dynamics be during a GLOF event, and how would they influence the outflow hydrograph and GLOF hazard?

This research question has been addressed through hydrodynamic modeling of the impact of an avalanche into Lake Palcacocha, wave generation and propagation, and the subsequent moraine overtopping. Three scenarios of varying size avalanches have been analyzed. Outflow hydrographs from each scenario were used as inputs to a downstream inundation model (not part of this dissertation) (Somos-Valenzuela et al., 2016). The results of the downstream inundation modeling (using the results of the lake modeling as inputs) were used to determine if Lake Palcacocha is potentially dangerous under the current conditions.

Research Question #2: What impact would lowering the lake level have on the magnitude of a GLOF event, and how can a "safe" lake level be determined?

To answer this question, several lake lowering scenarios were simulated with the lake model. The results from these simulations were input into the downstream inundation model (in Somos-Valenzuela et al., 2016) to determine the effect of lake level reduction on hazard levels in Huaraz due to an outburst flood at Lake Palcacocha.

Research Question #3: What will emerging glacial lakes look like in the future, and how can we determine the level of hazard that they may pose?

This question has been evaluated through the use of geophysical surveys of the Artesonraju Glacier to project the future volume of the emerging lake when it reaches its fullest extent. This future lake projection was then used for a simplified analysis of a potential GLOF process chain, resulting in estimates of potential overtopping volumes from the fully formed lake at Artesonraju. A new analytical method for calculating overtopping volumes has been presented as a possible proxy for 3D simulations of the lake dynamics.

1.3.2 Linking Scientific Research and Climate-Resilient Development

Chapter 4 focuses on climate data analysis within the context of climate change vulnerability assessment for public investment projects, seeking to link scientific research with society to promote climate change adaptation. Most of the existing work on climate change vulnerability analysis seems to focus on general concepts rather than specific technical analyses. The major contribution of this work is to provide a concrete framework for the technical analysis of climate change impacts though specific methods for analyzing climate data in the context of policy and management decisions. Therefore, Research Question #4 relates to the need to breach the gap between science and society:

Research Question #4: How can the gap between science and policy in the context of climate change and adaptation in Ancash be breached by simplifying methodologies for vulnerability analysis without losing validity of results?

This was addressed through comparisons of local perceptions of climate change with analysis of historic data. It was hypothesized that local perceptions accurately reflect the trends in gauged climate data. To assess the validity of people's perceptions of change and evaluate the potential for climate change perceptions to be used in lieu of gauged data, precipitation data from the Cachicadan weather station (shown in Figure 1.1) were compared to results from a study of perceptions of climate change (Vergara Rodriguez, 2011). To facilitate this analysis, a specific research question (Research Question #5) and five specific hypotheses have been formulated for Chapter 4 to characterize precipitation patterns and trends. The hypotheses in Chapter 4 are based on the results from the study of local people's perceptions of climate change in Vergara Rodriguez (2011).

Research Question #5: Have the character and reliability of the rainy season changed in recent decades?

The research questions related to each chapter of this dissertation have influenced the methodological approach, and the hope is that the inferences drawn from the results will help inform our understanding of high mountain glacial watershed systems in the Sierra of Ancash. There is a great need to produce new information about these systems as well as to develop innovative methodologies that help us to evaluate the impacts of climate change on water security. The research presented in this dissertation is intended

not only to advance the state of knowledge about climate change and water security in the Sierra of Ancash, but also to promote climate-resilient development. It is conceivable that the conclusions drawn from this research can be used to produce practical tools for climate change vulnerability analysis in the context of development in Peru.

Chapter 2: Lake Hydrodynamics of Avalanche-Generated Waves at Lake Palcacocha

Glacial Lake Outburst Floods (GLOFs) are typically comprised of a chain of processes, including an initial trigger event and a sequence of events influenced by the trigger event. The case study of a potential GLOF at Lake Palcacocha, Peru, looks at a specific chain of events that could possibly be triggered by an avalanche. The processes involved in the GLOF simulation at Lake Palcacocha (illustrated in Figure 2.1) include: (1) avalanches above the lake; (2) lake dynamics resulting from the avalanche impact, including wave generation, propagation, and run-up; (3) terminal moraine overtopping and dynamic moraine erosion possibly leading to breaching; (4) flood propagation along downstream valleys; and (5) inundation of populated areas. Each of the steps in this process chain has been simulated individually with the results of each process feeding into simulations of subsequent steps in the process chain, finally leading to inundation intensities and hazard maps in the city of Huaraz (Somos-Valenzuela et al., 2016)[2].

This chapter focuses on simulations of avalanche-induced impulse wave generation, propagation, run-up and overtopping of the terminal (lake-damming) moraine with the objective of answering the first two research questions for Part I. These research questions are addressed through hydrodynamic lake modeling of Lake Palcacocha. Lake Palcacocha is important because of its location above the city of Huaraz with over 100,000 inhabitants and its potentially dangerous nature due to overhanging ice, a glacier above with steep slopes, and a full lake with relatively little freeboard.

---

[2] The results of the simulation of each process in the GLOF chain of events can be found in:

Somos-Valenzuela, M. A., Chisolm, R. E., Rivas, D. S., Portocarrero, C., & McKinney, D. C. (2016). Modeling a glacial lake outburst flood process chain: the case of Lake Palcacocha and Huaraz, Peru. *Hydrol. Earth Syst. Sci., 20*, 2519-2543. DOI:10.5194/hess-20-2519-2016, 2016.

My contribution to this paper was simulation of the lake dynamics, writing, and editing.

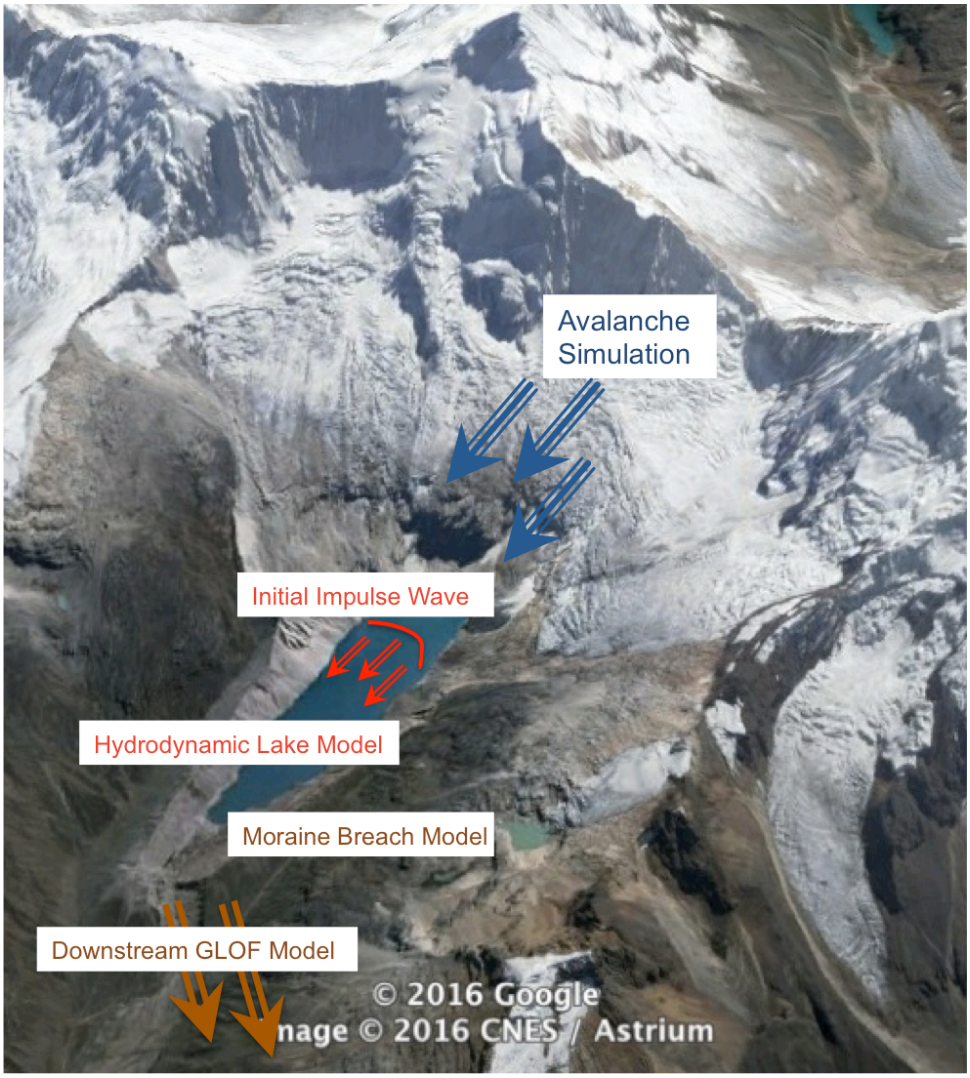

Figure 2.1- Schematic diagram of the processes to be modeled that are components of a potential GLOF event at Lake Palcacocha (background image from Google, 2013)

<u>Research Question #1:</u> What would the lake dynamics be during a GLOF event, and how would they influence the outflow hydrograph and GLOF hazard?

The first research question pertains to the hazard of Lake Palcacocha under current conditions. The results of the modeling provide projections of what would happen in the lake during a GLOF event, and the primary output from the simulations are

overtopping hydrographs that can be used as inputs to simulate the downstream impacts of a GLOF. Analysis of lake hydrodynamics from three-dimensional simulations can help gain a better understanding of the characteristics of avalanche-generated waves. This allows us to draw conclusions about what factors are most important and should be considered in future GLOF simulations. From this analysis, questions may be answered such as whether or not 3D simulations are necessary and how well empirical methods of calculating wave characteristics compare with the results of 3D simulations. The hypothesis motivating this comparison is that the empirical equations may be acceptable for the wave characteristics in the middle of the lake but not for run-up or overtopping calculations. Three-dimensional lake models are not always feasible for GLOF hazard assessment, so analysis of the wave dynamics in the lake can help identify what simplified methods are appropriate and when more complex modeling methods are necessary.

Research Question #2: What impact would lowering the lake level have on the magnitude of a GLOF event, and how can a "safe" lake level be determined?

Analysis of mitigation scenarios helps to understand the effect of lowering the lake level on the outflow hydrographs and downstream inundation. The overtopping hydrographs from the current lake level and lake-lowering scenarios have been used to predict the inundation extent in the city of Huaraz and the available response time (Somos-Valenzuela et al., 2016). The evaluation of different scenarios of lowering the lake level is key to developing a long-term mitigation strategy that would protect both life and property. Although this work does not include a risk assessment, the analyses of the physical processes that are the central focus of this research are a necessary foundation to any analysis of risk and vulnerability.

2.1 BACKGROUND

2.1.1 Lake Palcacocha

GLOFs have been a problem in the Cordillera Blanca for many years (Carey, 2010; Reynolds, 2003). The most significant event was when Lake Palcacocha burst in 1941, destroying much of the city of Huaraz and killing approximately 1800 people (Carey, 2010; Wegner, 2014). This event received much notice from national and international media and put the issue of GLOFs at the forefront of national attention. After the 1941 Huaraz flood, the Peruvian government instituted initiatives to reduce the GLOF risk in the Cordillera Blanca through monitoring glaciers and glacial lakes and implementing lake safety systems. These safety systems typically consist of tunnels to control lake levels, reinforced dams or a combination of the two. Scientists and engineers in Peru have several decades of experience managing glacial lakes in the Cordillera Blanca and mitigating GLOF risk (Carey, 2010; Portocarrero, 2014), but current lake management practices are based on studies that were performed decades ago and have not been updated to account for changes that have occurred since then, primarily increased water storage in glacial lakes. In this work, Lake Palcacocha (Figure 2.2) is used as a case study to investigate the impact of an avalanche event on the lake dynamics and the ensuing flood hydrograph.

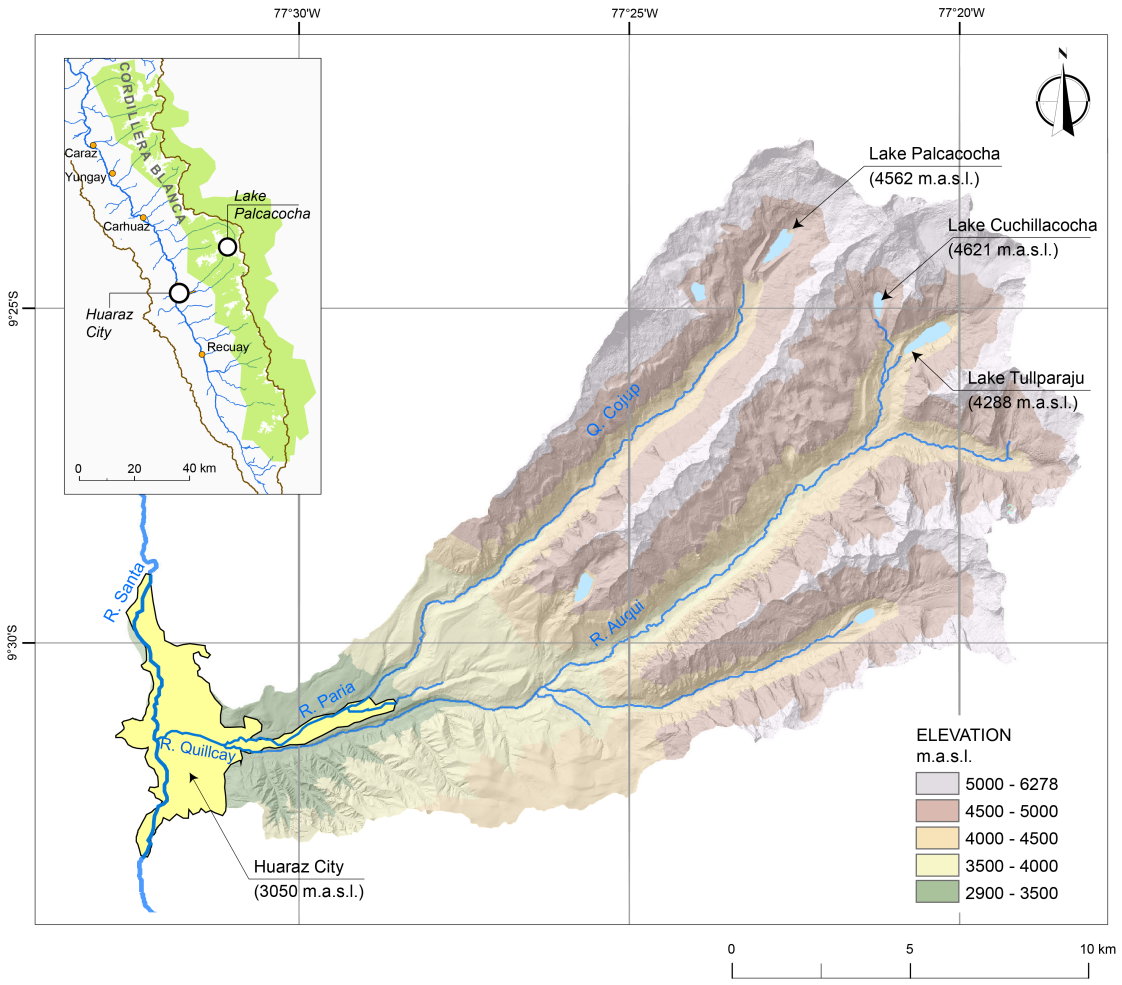

Figure 2.2- Location of Lake Palcacocha within the Cordillera Blanca, Peru (from Somos-Valenzuela et al., 2016)

Lake Palcacocha is situated in the Quilcay watershed above the city of Huaraz. It is approximately 20 km from Huaraz at an elevation of approximately 4562 masl. Above the lake are the Palcaraju and Pucaranra glaciers. The steep overhanging ice of the glacier terminus that is in contact with the lake makes it extremely prone to avalanche-generated waves. Additionally, the large volume of water contained in the lake provides a serious threat to downstream areas. The lake is surrounded on three sides by glacial moraines.

The lateral moraines are very tall with steep slopes; the southern lateral moraine is prone to landslides into the lake, and a slide from this moraine in 2003 caused minor damage from a wave that barely overtopped a portion of the terminal moraine (Vilimek et al., 2005). The original lake-damming terminal moraine was mostly eroded during the 1941 GLOF, and the lake is currently dammed by a smaller moraine that lies about 300 m back from the 1941 breach. A tunnel to maintain a constant lake level of 4562 m (8 m of freeboard) was constructed in 1974 (Reynolds, 2003), and two sections of the terminal moraine have been reinforced with concrete to protect them from erosion (see Figure 2.3 for photos of the terminal moraine complex).

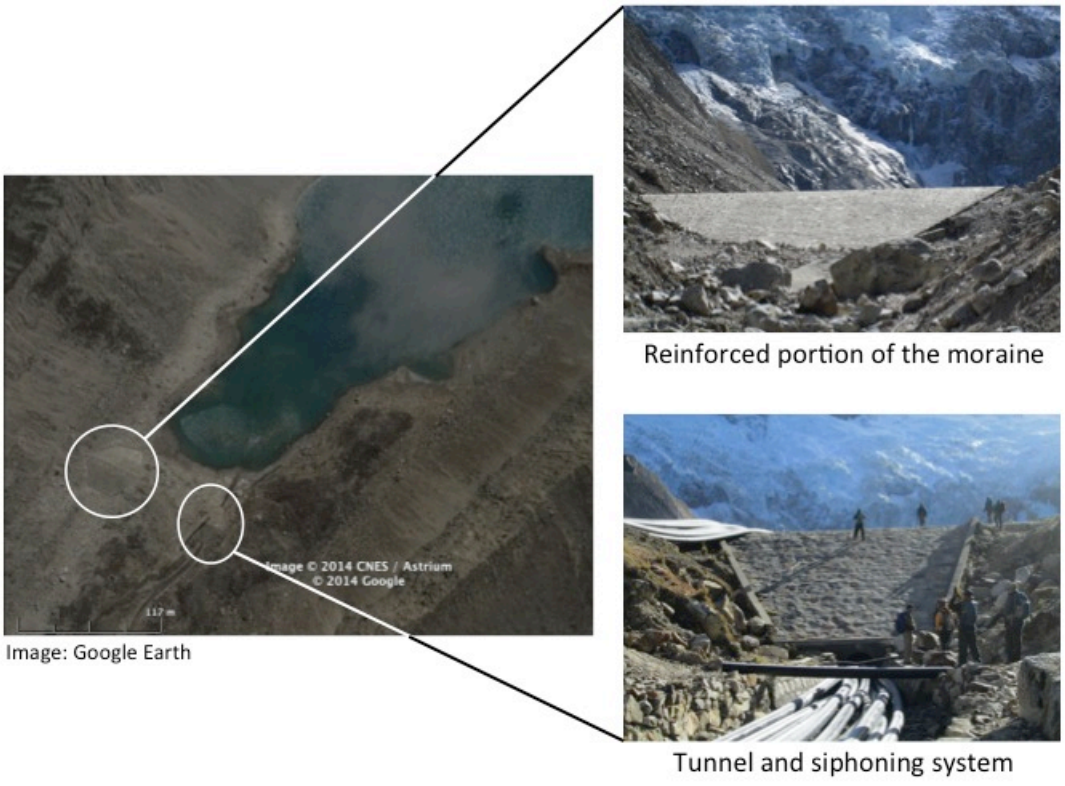

Figure 2.3- Terminal moraine complex at Lake Palcacocha

Before the 1941 GLOF that drained most of lake, Palcacocha contained an approximate volume of 10-12 million m^3 (INDECI, 2011). After the 1941 event, the lake was left with only 0.5 million m^3 of water. In recent years, the lake has grown very rapidly as the glacial tongue has retreated. Rivas et al. (2015) illustrate the growth of the lake through time with satellite imagery. Based on a bathymetric survey performed in 2009, the storage volume of the lake was approximately 17 million m^3 (UGRH, 2009). The lake has since retreated approximately 200 m more, and siphons are currently being used to lower the lake an additional 3-5 m; therefore, the current lake volume is not known precisely.

A few studies have investigated the potential GLOF hazard at Lake Palcacocha. Vilimek et al. (2005) discussed influence of glacial retreat on hazards at Palcacocha and studied the moraine composition and the potential for landslides from the lateral moraines; they also found seepage at the moraine dam. Emmer and Vilimek (2013) used a generalized methodology for GLOF hazard assessment at Lake Palcacocha and 5 other lakes in the Cordillera Blanca; of the 6 lakes evaluated, Palcacocha had the highest hazard level. Emmer and Vilimek (2014) examined mechanisms of the 1941 and 2003 GLOFs at Lake Palcacocha and compared them to other historic GLOFs in the Cordillera Blanca. Emmer et al. (2016) evaluated the effectiveness of lake safety systems in the Cordillera Blanca and found that the system at Lake Palcacocha resulted in a minimal decrease in GLOF susceptibility. The University of Texas at Austin has studied each step of a potential GLOF process chain in detail. Rivas et al. (2015) modeled a full moraine collapse using empirical equations and DAMBRK hydraulic simulations, and Somos-Valenzuela et al. (2016) give the results of simulations of each process in the potential GLOF chain of events. The lake model in this chapter is part of the work presented in Somos-Valenzuela et al. (2016).

The potential threat that Lake Palcacocha poses to the residents of Huaraz has been known for several years. Peruvian government institutions have produced several official reports about the situation (INDECI, 2011; ANA, 2013; INDECI, 2015; Valderrama et al., 2013; Espinoza, 2013), and a state of emergency was declared in 2010 (Diario la Republica, 2010; INDECI, 2011). The results of the lake modeling in this chapter and the other results in Somos-Valenzuela et al. (2016) have been presented to local authorities and decision-makers in Huaraz. Ongoing discussions about the GLOF modeling at Lake Palcacocha and hazard mapping in Huaraz have helped local authorities to understand the potential threat to Huaraz. As a result, a technical working group, comprised of local technical experts and international specialists, has been formed to address the situation. This group has developed a project proposal for an early warning system, terms of reference for additional studies needed to assess the conditions at Lake Palcococha, and a preliminary map of hazard due to a GLOF for the city of Huaraz. This technical working group has also begun to discuss potential actions to permanently decrease the GLOF hazard, including lowering the level of Lake Palcacocha.

2.1.2 Literature Review

Glacial Lake Outburst Floods

Glacier lake outburst floods (GLOFs) are common in many parts of the world, and moraine-dammed lakes such as those present in the Cordillera Blanca are particularly susceptible to outburst flooding. Climate change and accelerated glacial retreat have been increasing the GLOF hazard posed by glacial lakes in the Cordillera Blanca since the end of the Little Ice Age in the late 1800's (Carey, 2010). GLOFs can be highly destructive because the peak discharges can be several orders of magnitude larger than typical

outflows from glacial lakes (Benn and Evans, 2010). Some basic methods for evaluating the potential for glacial hazards have been established (e.g., Haeberli et al., 1989; Huggel et al., 2004; Clague and Evans, 2000), and the primary characteristics that signify a potentially hazardous glacial lake are the presence of overhanging ice and the likelihood of slope failure in the lake-damming terminal moraine. Understanding of the physical processes that can trigger a GLOF event is still limited. Therefore, it is difficult to determine a precise probability that an event may happen, and current probability estimates are only qualitative (e.g., high, medium or low probability of occurrence).

A number of GLOFs have occurred in the Cordillera Blanca in recent history, and several studies have looked at the events after they happened and attempted to reconstruct the GLOF characteristics. Worni et al. (2014) and Westoby et al. (2014a) give overviews of typical modeling approaches for the type of GLOF process chain considered here. Some researchers have simulated GLOFs with models of the individual processes that comprise a GLOF (e.g., Klimes et al., 2013; Schneider et al., 2014; Westoby et al., 2014b; Worni et al., 2014; Wang et al., 2015), but most have used two-dimensional or empirical simulations of the wave generation and progagation that likely are not effectively representing the physical processes. One difficulty for most sites where GLOFs are a concern is the lack of data about real events, so the potential hazard and impacts of a GLOF must be estimated from an analysis of the physical conditions and modeling the basic physical processes without relying on empirical calibrations. Predicting the impacts of an event that has not yet happened and that inherently carries much uncertainty about many of the event parameters is a significant challenge, but it is one that must be undertaken if we hope to make any progress in glacial hazard assessment in the Cordillera Blanca.

The final piece of the puzzle for adaptation to the changing landscape of GLOF hazards is the undertaking of mitigation measures to reduce risk. Lake safety systems intended to reduce GLOF risk include the construction of tunnels to control lake levels and reinforced dikes (Portocarrero, 2014; Reynolds, 1992; Reynolds et al., 1998; Reynolds, 2003). Although the methods for controlling glacial lakes to mitigate GLOF risk have been well-established, there has been very little discussion about accounting for the increased hazard brought about by climate change in the design of lake safety systems.

Impulse Waves Generated from Avalanches and Landslides

One of the most common trigger mechanisms for GLOF events in the Cordillera Blanca is an avalanche falling into the glacial lake (Emmer and Vilimek, 2013; Emmer and Cochachin, 2013), generating waves that are similar to waves generated from landslides into bodies of water. The dynamics of landslide-generated waves are very complex. To complicate matters further, it is very difficult to obtain field measurements of landslide-generated waves, and most of the data from real-life events are estimates based on residual evidence in the field. Many of the physical principles governing the mechanics of wave generation and propagation can be found in Dean and Dalrymple (1991).

Much of the work in this area has been focused on empirical models that replicate the wave characteristics (eg. Kamphuis and Bowering, 1970; Slingerland and Voight, 1979 and 1982; Fritz et al., 2004; Heller and Hager, 2010). Many of these empirical models are based on laboratory simulations using simplified setups (Heller et al., 2016). There have been a few studies that perform numerical simulations of wave generation and propagation of landslide generated waves, but most are still limited to simplified

cases and two-dimensional simulations (eg. Rzadkierwicz et al., 1997; Biscarini, 2010; Cremonesi et al., 2011; Ghozlani et al., 2013; Zweifel et al., 2007; Ataie-Ashtiani et al., 2011). The 2D shallow water equations do a poor job of representing the reality of wave generation and propagation because vertical accelerations cannot be neglected for slide-generated waves (Heinrich, 1992; Zweifel, et al. 2006). Recent developments in numerical simulations of landslide-generated waves include simulation of multi-phase flows, including a three-dimensional Navier-Stokes Volume of Fluid model (Abadie et al., 2010), a two-phase debris flow model (Kafle et al., 2016), and the application of Smoothed Particle Hydrodynamics (SPH) models (Heller et al., 2016; Wang et al., 2016) to simulate wave generation and propagation from slide impacts, but these studies still focus on simplified setups and geometries rather than real-world scenarios. Few scientists have looked at the issue of wave runup (eg. Synolakis, 1987 and 1991; Muller, 1995; Liu, et al. 2005; Etemad-Shahidi et al., 2016; Capel, 2015; Romano et al., 2015), and most use empirical formulas or simplified approaches for wave runup calculations, making assumptions about the lake geometry that may not be realistic (e.g., constant water depth and a regularly sloped dam).

Although models of real events are limited by the lack of validation data, there is clearly a need to move away from simplified cases such as sliding blocks or wedges and progress towards modeling cases that more closely resemble geometries and circumstances in the field. In addition, as technology progress, the computational expense of three-dimensional simulations becomes less problematic, and use of 3D numerical modeling can help overcome some of the limitations of 2D simulations.

Some of the problems associated with using a numerical fluid model to represent avalanche-generated impulse waves include: uncertainty in the make-up of avalanche material (eg. ratio of snow, ice and rock, density, viscosity) and representation of the

mixing and transfer of momentum when the avalanche material falls into the lake. The approach used in this dissertation was to model the mixing by representing both the lake and the avalanche as water (justified by the similar densities of water and the rock-ice mixture of avalanches) and accounting for the transfer of energy from the avalanche to the wave generation in the lake by matching the momentum of the avalanche with the momentum of the fluid entering the lake in the FLOW-3D simulations.

2.2 METHODS

Impulse waves resulting from the impact of an avalanche with the lake were simulated with a three-dimensional (3D) hydrodynamic model, FLOW-3D (Flow Science, 2012), with the objective of studying the wave generation and lake dynamics for avalanche-generated waves. A fully three-dimensional non-hydrostatic model was chosen to give as realistic a simulation environment as possible. Although two-dimensional shallow water models have been applied to simulations of avalanche-generated impulse waves (e.g., Heinrich, 1992; Zweifel et al. 2006), the size and characteristics of the waves indicate that a 3D model may be more appropriate because of highly variable water depths (i.e., wave heights) and significant vertical accelerations. Additional motivation for employing a 3D hydrodynamic model is the variable lakebed geometry of Palcacocha with a sharp discontinuity near the terminal moraine that significantly affects wave propagation and run-up in the lake. Lake Palcacocha is very deep near the glacier with depths up to 72 m, but the last several hundred meters adjacent to the terminal moraine are very shallow with depths mostly less than 10 m (Figure 2.4). Analytical calculations of wave run-up and overtopping typically consider regular or simplified lake geometries (e.g., uniform water depth and constant slope of the terminal moraine) that do not necessarily hold true in natural reservoirs (Synolakis, 1987, 1991; Muller, 1995; Liu et

al., 2005), making a hydrodynamic simulation necessary to represent the potential overtopping of the terminal moraine.

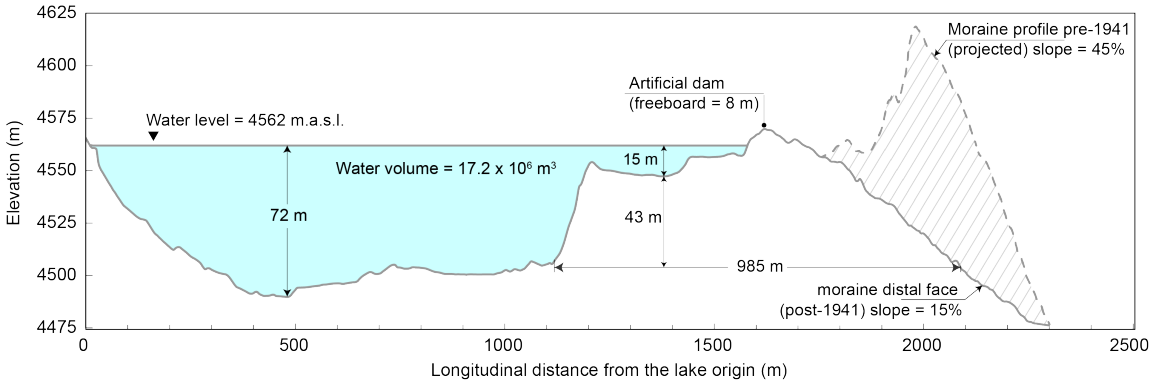

Figure 2.4- Longitudinal profile of Lake Palcacocha and its terminal moraine (factor of vertical exaggeration of 5) (from Somos-Valenzuela et al., 2016).

The 3D hydrodynamic model simulated the formation, propagation, run-up and moraine overtopping of an avalanche-generated impulse wave in Lake Palcacocha. Although the ultimate interest of the lake modeling is the downstream impact due to the outflow from the overtopping wave, the wave generation and propagation were studied to gain insights about how this type of wave behaves and what model elements are needed to accurately reproduce avalanche-generated waves of the magnitude typically seen in GLOFs. The primary output from the model is a discharge hydrograph of the overtopping wave, if there is any; these hydrographs were used as inputs to a downstream inundation model (Somos-Valenzuela et al., 2016).

The following sub-sections present the methodology for the Lake Palcacocha hydrodynamic simulations, including the model parameters and sensitivity analysis of those parameters (Section 2.2.1), the methods for representing the impact of the

avalanche with the lake (Section 2.2.2), the methods for studying wave characteristics in the lake (Section 2.2.3), and the avalanche and lake-lowering scenarios that were simulated (Section 2.2.4). In the analysis of the results, the sensitivity analysis is presented first (Section 2.3.1), followed by an analysis of the inflow for two different boundary condition methods (Section 2.3.2) and examination of the wave characteristics in the lake (Section 2.3.3) and the outflow hydrographs (Section 2.3.4). Finally, the mitigation scenarios are investigated, both for the impact of lake-lowering on the outflow hydrograph and the effects on downstream inundation (Section 2.3.5).

2.2.1 Model Grid, Simulation Parameters and Sensitivity Analysis

A fully three-dimensional, non-hydrostatic numerical scheme was employed in the FLOW-3D simulations using a re-normalization group (RNG) turbulence model with a dynamically computed mixing length. The grid size was chosen to be a balance between accuracy and computational efficiency.

Sensitivity to Turbulence Model

The sensitivity of the simulations to the turbulence model was tested by running repeat simulations of one scenario (large avalanche source, current lake level) for different turbulence model options in FLOW-3D. Each of these simulations was compared to the baseline model run with the RNG-dynamically computed mixing length. This turbulence model was chosen for all model runs because the appropriate value for the mixing length was unknown due to the highly variable nature of the flow, both spatially and temporally. Because there was no obvious length scale to use for a mixing

length, the RNG-dynamically computed mixing length model seemed like an appropriate choice.

The repeat simulations for the additional turbulence models were compared to the baseline model (RNG with constant mixing length) by calculating the percent difference in maximum wave height, peak overtopping flow rate, and total overtopping volume. Additionally, the root-mean-square deviation (RMSD) between the results of the baseline turbulence model and each additional turbulence model was calculated for the outflow hydrographs and the flow depth at each time step. The turbulence models include:

(1) RNG Model with a Dynamically Computed Mixing Length (baseline model)
(2) *k-epsilon* Model
(3) Laminar Flow
(4) Large Eddy Simulation (LES)
(5) Prandtl Mixing Length Model
(6) RNG Model with a Constant Mixing Length
(7) 1-equation Model with a Constant Mixing Length

The RNG (1), *k-epsilon* (2), Prandtl mixing length (5) and one-equation (7) turbulence models are Reynolds-averaged Navier-Stokes (RANS) eddy viscosity models that operate similarly (Moser, 2009). The Prandtl mixing length (5) and one-equation (7) models are the simplest of the eddy viscosity models employed in this study. The *k-epsilon* model (2) is a two-equation model that has a number of constants that use standardly defined values in the model. The RNG model (1) is a variant of the *k-epsilon* model where instead of using standard values for the undetermined constants, they are "derived" using renormalized group theory (Yakhot and Orszag, 1986). In FLOW-3D,

the constant mixing length defined in these two-equation models is a maximum length scale that limits the dissipation of energy, ensuring that dissipation in the models is not underrepresented (Isfahani and Brethour, 2009). The difference between this approach and the RNG dynamically computed mixing length model is that the RNG-dynamically computed mixing length model (1) does not use a constant mixing length that the other models use but computes a mixing length dynamically based on the actual flow conditions. This is particularly useful for the current application at Lake Palcacocha because there is no obvious choice of a length scale that should be used to define the mixing length.

The laminar (3) and LES (4) models function differently from the RANS eddy viscosity models discussed above. The laminar model (3) ignores turbulence and simulates the flow as entirely laminar. As turbulence tends to dissipate energy, it is expected that the laminar model will under-represent dissipation, although some numerical dissipation may occur in the laminar model. The LES model (4) simulates only the largest scales of turbulence by using a filter to remove the smaller scales; the effects of the smaller turbulence scales are accounted for within the model. The assumption is that the smallest scales of turbulence will be nearly homogeneous and isotropic; however, whether or not this assumption holds true depends on the filter size (Moser, 2009). The filter size used to separate the large turbulence scales from the small ones is often linked to the model grid size, and additional numerical errors can be introduced due to the filter width. The accuracy of an LES model depends on enough knowledge of the flow conditions so that the filter scale can be defined to allow for most of the large-scale turbulence to be resolved within the model itself rather than in the sub-grid representation of the small-scale turbulence (Pope, 2000). This goes beyond the scope of this work, and the LES model is included only as an additional point of comparison. The results from

the LES model should be viewed in light of these limitations and considering that the grid size was not determined according to the scale of turbulence that should be resolved in the model.

Sensitivity to Grid Size

The regular mesh consists of grid cells 6 m x 5.33 m x 6.5 m in the x, y and z-directions respectively, spanning distances of 2400 m (x-direction), 800 m (y-direction), and 650 m (z-direction). This grid size was used for all simulation scenarios except simulations that were run with a coarser mesh to assess the sensitivity of the simulation results to grid cell size. For the grid size sensitivity analysis, a coarse grid simulation (doubling the original cell grid size) was run for the large avalanche source scenario at the current lake level. The grid cell sizes for each of these simulations are given in Table 2.1.

Table 2.1- Model grid parameters for the regular mesh (used for all simulation scenarios) and coarse grid simulation (used for sensitivity analysis).

	Cell Size: x-direction (m)	**Cell Size: y-direction (m)**	**Cell Size: z-direction (m)**
Regular Mesh	6	5.33	6.5
Coarse Grid Simulation	12	10.67	13

For the coarse grid simulation results, the water depth was extrapolated to the finer grid by dividing the coarse grid cells into the equivalent number of cells in the regular mesh, and the water depth from each x-y grid cell of the coarse grid was given to each of the corresponding fine grid cells. To compare the coarse grid results to regular

model mesh, the root-mean-square error (RMSE) was calculated for the fluid depths at each time step. Additionally, the percent difference in peak overtopping flow rate and total overtopping volume and the RMSE of the outflow hydrograph were calculated for each coarse grid simulation.

2.2.2 Boundary Conditions: Representing Avalanche Impact

The problem of reproducing an avalanche-generated impulse wave in a hydrodynamic model is not an easy one because of the complicated dynamics of mixing and dissipation of energy that occur at the point of impact. The results of avalanche simulations (Somos-Valenzuela et al., 2014) performed in the Rapid Mass Movements (RAMMS) model (Christen et al., 2010; Bartelt et al., 2013) were used as inputs to the lake model because the avalanche entering the lake is the trigger for wave generation. Two different methods of representing the transfer of mass and momentum to the lake from the avalanche were used to determine how sensitive the results of the lake model are to the boundary conditions. Although they cannot provide a comprehensive uncertainty analysis, the variability in the results between the two boundary condition methods can give an approximation of the uncertainty associated with the avalanche impact and wave generation. Each method uses a different means for simulating the transfer of mass and momentum from the avalanche to the lake upon impact, but both initiate the simulation of the wave generation and propagation.

The two methods for simulating the avalanche boundary conditions are:

Avalanche Source

This method consists of representing the impact of the avalanche with the lake as a volume of water equivalent to the avalanche volume that flows into the lake from the terrain above. Worni et al. (2014) and Fah (2005) approach the problem in a similar way, simulating water instead of avalanche material. The density of the mixture of snow, rock and ice present in an avalanche is very close to the density of water (Schneider et al., 2014).

Although the viscosities of the two fluids are different, this approximation of substituting water for the avalanche fluid is handled through adjustments in the model that compensate for any reduction in the dissipation of energy due to the lower viscosity of water. To accomplish this, the results of the RAMMS avalanche model (Somos-Valenzuela et al., 2014) were used as calibration parameters; in FLOW-3D, the depth of the avalanche fluid volume and height above the lake at which it is released were iteratively adjusted until the velocities and depths of the avalanche fluid entering the lake matched the characteristics of the avalanche modeled in RAMMS. As long as the mass and momentum of the material hitting the lake in FLOW-3D are similar to that of the RAMMS-simulated avalanche, the initial displacement wave should behave similarly as well; the water in the lake is pushed by the incoming avalanche, but the avalanche material does not reach the moraine, and the displaced wave is what propagates across the lake. Differences may arise for reflected waves since the avalanche material might settle in a different way over the lake's bed according to the avalanche properties (water representing avalanche material is more free to flow in the lake than actual rock-ice avalanche material), but these differences are probably minimal.

Mass-momentum Source

The second method for representing boundary conditions, a *mass-momentum source*, involves constructing hydrographs from the avalanche simulations that approximate the volumetric flow rate of the avalanche entering the lake. An approximate hydrograph was created from the results of the RAMMS model (Somos-Valenzuela et al., 2014) by taking the depth and velocity at various points (approximately 10-15) along the edge of the lake for each time step. The average depth and velocity was then calculated for each time step, and the flow rate was calculated by multiplying the average depth, velocity, and the approximate avalanche width for each time step. Because the RAMMS simulations were not run long enough for the entire avalanche to enter the lake, these approximate hydrographs were modified so that the total inflow volume equals the avalanche volume.

The resulting hydrographs were used as the inflow at the boundary of the lake model and represent the input of mass and momentum that generates an impulse wave. This was done using the mass-momentum source function in FLOW-3D with the boundary condition defined by the hydrograph and cross-sectional area where the flow enters the lake. The depth and width of the cross-sectional area for the mass-momentum source were set so that the depths and velocities of the flow from the source area matched those of the avalanche model.

The two types of boundary conditions were compared by looking at their inflow hydrographs at the point of impact with the lake. This is a way to visualize the differences between the two methods at the inflow boundary of the lake; however, the most significant implications of each boundary condition method arise in the differences

in the resulting overtopping waves and hydrographs. Therefore, results from both boundary condition methods are presented at each step of analysis.

2.2.3 Wave Characteristics

There are five main phases for an avalanche-generated impulse wave such as the ones simulated in Lake Palcacocha: 1) the wave generation from the impact of the avalanche with the lake, 2) the propagation of the wave along the length of the lake, 3) the run-up that begins when the wave reaches the shallow portion of the lake, 4) the overtopping of the terminal moraine, and 5) the reflected wave from the portion of the wave that does not overtop the moraine. This section focuses on analysis of the wave characteristics within the lake, including the propagation and run-up phases; the overtopping hydrograph characteristics are presented separately in Section 2.3.4. The characterization of the separate processes of wave generation (Section 2.3.2), wave propagation and run-up (this section), and overtopping (Section 2.3.4) is important because empirical methods have been developed to model the wave generation, but the wave propagation often cannot be easily described by simple empirical equations, especially for glacial lakes, such as Lake Palcacocha, that are of varying depth. The wave generation is dependent primarily on the characteristics of the avalanche and the lake depth at the point of impact whereas the wave propagation is dependent on the initial wave characteristics and the lake bathymetry and surrounding topography. A better understanding of the processes of wave propagation and generation may allow for a simplified modeling process using the empirical method developed by Heller and Hager (2010) to determine the initial wave characteristics and then using those conditions to initiate a hydrodynamic model of the wave propagation and moraine overtopping.

To study the wave characteristics, the maximum wave height in the lake and the height of the wave above the moraine crest were computed. The maximum wave height as a function of distance along the lake was calculated to assess how the wave changes as it propagates across the lake. The main purpose of calculating the maximum wave height is for comparison with the empirical method of Heller and Hager (2010). At this point, the difficulty of model validation and quantifying uncertainty must be mentioned. This work is an attempt to model an event that has not yet occurred, and very little data are available from similar events in the past that can be used to calibrate or validate model results. The 2010 GLOF event at Lake 513 in the Cordillera Blanca of Peru can be used to see if the model results seem reasonable; however, that event occurred at a lake with different characteristics and there is a lot of discrepancy among the estimates of the magnitude of the avalanche, wave height and overtopping volume (Carey et al., 2012; Valderrama and Vilca, 2012; Schneider et al., 2014). Therefore, the results of the empirical model (Heller and Hager, 2010) are used as a point of comparison with the hydrodynamic lake modeling at Palcacocha.

The Heller and Hager (2010) method for calculating maximum wave characteristics is an empirical method that is based on field measurements and laboratory experiments and can be used for comparison with hydrodynamic model results; if the characteristics of the impulse wave in both the hydrodynamic model and empirical model are of the same order, we can have more confidence in the model results. However, the Heller and Hager method is only an approximation based on simplified representations of lake dimensions and avalanche characteristics. There are acceptable ranges of values for certain variables such as relative slide density, relative slide volume, relative slide width, and Froude number for which the equations hold true. For the case of calculating the wave height in Lake Palcacocha, all of the variables fall within the acceptable ranges

except the relative slide width; therefore, the wave characteristics calculated according to this method can be reasonably relied upon for purposes of comparison with the 3D simulation results but only to get an idea of the approximate wave dimensions.

2.2.4 Scenarios

Two sets of scenarios were simulated in the lake model of Palcacocha: avalanche scenarios and lake-lowering scenarios. First, simulations were run with the current lake conditions to facilitate analysis of the current GLOF hazard level. Three avalanche scenarios were selected to represent the range of potential avalanche sizes that might impact the lake. The three scenarios representing a small, medium and large avalanche were simulated in the lake model using the results of the RAMMS avalanche model. The avalanche sizes range from 0.5-3 x 10^6 m^3, and the characteristics for each scenario are given in Table 2.2. Although smaller avalanches are much more likely than larger ones, analyses of probabilities and return periods for each avalanche scenario are beyond the scope of this work. The methods for incorporating the avalanche characteristics and RAMMS simulation results from each scenario into the lake model are described in Section 2.1.2.

Table 2.2- Avalanche characteristics in RAMMS (from Somos-Valenzuela et al., 2016)

	Avalanche Event		
	Large	**Medium**	**Small**
Avalanche size (10^6 m^3)	3	1	0.5
Maximum depth of avalanche material at lake entry (m)	20	15	6
Maximum velocity of avalanche material at lake entry (m/s)	50	32	20
Time to reach the lake (seconds)	33	36	39
% of mass released that reaches the lake in 60 seconds	84	72	60

The second set of scenarios addresses the question of how the mitigation strategy of lowering the lake level might affect hazard levels. To answer the second research question, hydrodynamic modeling for Lake Palcacocha was performed with varying lake levels to study how the lake level influences the overtopping volume and GLOF risk and to determine what may be considered a "safe lake level." The lake-lowering scenarios that were simulated include lowering the lake level by 15 m and 30 m from the current water surface elevation of 4562 msl. These scenarios were selected based on what has been proposed by local government technical specialists in Huaraz. Scenarios of lowering the lake greater than 30 m were not simulated because it is highly unlikely that the Peruvian government would attempt to lower the lake more than this amount.

Each lake-lowering scenario was simulated with all three avalanche scenarios for a total of 9 scenarios (including the current lake level scenarios), and the overtopping volume and outflow hydrograph were calculated for each scenario. Each of the lake lowering scenarios was analyzed for reduction in peak overtopping flow rate and total overtopping volume. Although the focus of this work is on the lake hydrodynamics, the purpose of this research is to assess the potential for GLOFs to impact downstream populations. Therefore, flood intensities and hazard levels resulting from downstream inundation simulations (Somos-Valenzuela et al., 2015) are shown to facilitate analysis of the potential for lake lowering to influence the GLOF hazard levels in Huaraz. The inundation intensities are defined based on a combination of the water depth and velocity for each grid cell in the downstream inundation model (Table 2.3). The flood intensities are then combined with the likelihood of each scenario to denote a hazard level for each grid cell (Table 2.4). To evaluate how lake-lowering may alter the GLOF impacts in the city of Huaraz, the flood intensities and hazard levels for each lake lowering scenario are compared with those for the current lake level.

The question of how to come up with a final hazard assessment for each lake-lowering scenario arises when considering the downstream impacts, and it is not a simple issue to address. A "safe lake level" may be defined as a lake-lowering scenario for which the hydrodynamic model results show no overtopping of the terminal moraine for all avalanche scenarios. However, reducing the absolute risk to zero is rarely feasible or even possible. The lake-lowering scenarios selected for this work are unlikely to reduce the hazard for all avalanche scenarios to zero; therefore, the mitigation strategies must be analyzed for their relative impact on hazard levels in Huaraz. The definition of a "safe lake level" may be applied to each scenario (avalanche size + lake level), considering that the lake is safe if there is no overtopping and unsafe if the terminal moraine is overtopped. In reality, overtopping volumes less than 25,000 m^3 may be contained within the river channel, so a scenario is defined as "safe" if the total overtopping volume is less than 25,000 m^3. This definition is employed for the 9 scenarios simulated with the avalanche source; however, this is a simplified approach that does not account for any reduction in hazard for the mitigation scenarios that are "not safe" according to this definition. For this reason, the flood intensities in the city of Huaraz for each scenario are presented, but further analysis of risk in the city is beyond the scope of this work.

The scenarios simulated at Lake Palcacocha are summarized below. All scenarios were simulated in the lake model with both the avalanche source and mass-momentum source boundary conditions. It was not feasible to simulate all of the scenarios for both boundary conditions in the downstream inundation model (Somos-Valenzuela et al., 2015), so only the avalanche source simulations were continued downstream to Huaraz. The avalanche source results were chosen to input into the downstream inundation model because they resulted in higher peak flows and overtopping volumes. A conservative approach to hazard estimation requires that worst-case scenarios be used; because the

avalanche source simulations resulted in higher overtopping flows, they would result in more cautious hazard delineations.

Avalanche scenarios:

- Small (500,000 m^3)
- Medium (1,000,000 m^3)
- Large (3,000,000 m^3)

Lake-lowering scenarios:

- 0 m
- 15 m
- 30 m

Table 2.3- Flood Intensity Classification (from Somos-Valenzuela et al., 2016).

Intensity		**Maximum Velocity (m/s) x Maximum Depth (m)**		
		> 1.0	0.2 - 1.0	< 0.2
Maximum Depth (m)	> 1.0	High	High	High
	0.2 - 1.0	High	Medium	Low
	< 0.2	High	Low	Low

Flood Intensity
High
Medium
Low

Table 2.4- Flood Hazard Classification (from Somos-Valenzuela et al., 2016).

Hazard		**Likelihood**		
		High	Medium	Low
		Avalanche Size		
		Small	Medium	Large
Intensity	High	High	High	High
	Medium	High	Medium	Low
	Low	Medium	Low	Low

Hazard Level
High
Medium
Low

2.3 RESULTS AND ANALYSIS

For each scenario, FLOW-3D was used to model the avalanche-generated impulse wave, its propagation and the overtopping of the terminal moraine. The primary output from the model results are flow hydrographs generated for each scenario that are used as input to the downstream GLOF model. Overtopping wave discharge hydrographs were calculated at the moraine crest mid-way between the artificial dam and the 1941 breach (Figure 2.2).

For the three avalanche events listed in Table 2.2, FLOW-3D simulations of the resulting wave generation, propagation and overtopping of the damming-moraine were first run with the lake at the current level of 4562 msl using the two boundary condition methods. Each simulation was then repeated for the two lake-lowering scenarios.

2.3.1 Sensitivity Analysis: Grid Size and Turbulence Model

The sensitivity analysis simulations for the turbulence model and grid size were all run for the large avalanche scenario with the avalanche source boundary condition.

Sensitivity to Turbulence Model

For the large avalanche source scenario, the results using each of the turbulence models discussed in Section 2.1.1 were compared to the baseline model (RNG model with a dynamically-computed mixing length). The root-mean-square deviation (RMSD), shown in Figure 2.5, is a way to represent the average difference in fluid depth between the baseline model and each of the turbulence models. For all models, the highest RMSD values are for the time steps between 0 and 50 s when the water surface is most actively changing as the impulse wave is being generated and propagated across the lake. The laminar model and the LES model show the most deviation from the baseline model with

maximum RMSD values around 2.5 m. It is not surprising that the laminar model shows high deviations from the baseline model because this model inherently does not account for turbulence; the laminar model should be the least dissipative of all the models, and this is reflected in the peak flow rate, overtopping volume and maximum wave height (Table 2.5), which are all higher than the corresponding values from the baseline model. The LES model appears to be overly dissipative, giving the lowest values for all parameters used for comparison between the models. It is difficult to say why this is the case, but it could be due to inhomogeneity in the flow or numerical errors due to the filter scale.

The *k-epsilon*, Prandtl mixing length and RNG constant mixing length models may be more appropriate for this type of simulation, and they could be considered to be more representative of the effect of the turbulence model on simulation results. These three models are all similar RANS eddy viscosity models, and the results from these models are more closely aligned with the results from the baseline model, indicating that they behave similarly; however, there are still differences in fluid depth between the models. All three of these turbulence models have maximum RMSD values around 1.8 m, and the RMSD plateaus around 0.5 m by 200 seconds; after 200 s, the model begins to approach a steady state subsequent to the overtopping of the initial wave although there are still some disturbances from the reflected wave. The steady-state depth of the lake ranges from less than 10 m for the shallow portion to 72 m at the deepest part; even considering the increase in depth due to the maximum wave heights (approximately an additional 60 m), these differences in depth are not insignificant.

The highly variable bathymetry and fluid depths present an additional challenge in defining an appropriate mixing length and therefore introduce another source of uncertainty; many of the turbulence models used in this analysis require the definition of

a mixing length that ensures that the dissipation of energy is not underrepresented in the model. However, due to the irregular lakebed and highly variable surface elevations, there is not an obvious choice for a length scale to use in estimating the mixing length. Even if they are closer to the baseline model results than other models, there is no way to say if the results from the constant mixing-length models are more or less accurate because of the uncertainty in the mixing length with these turbulence models that may contribute to error.

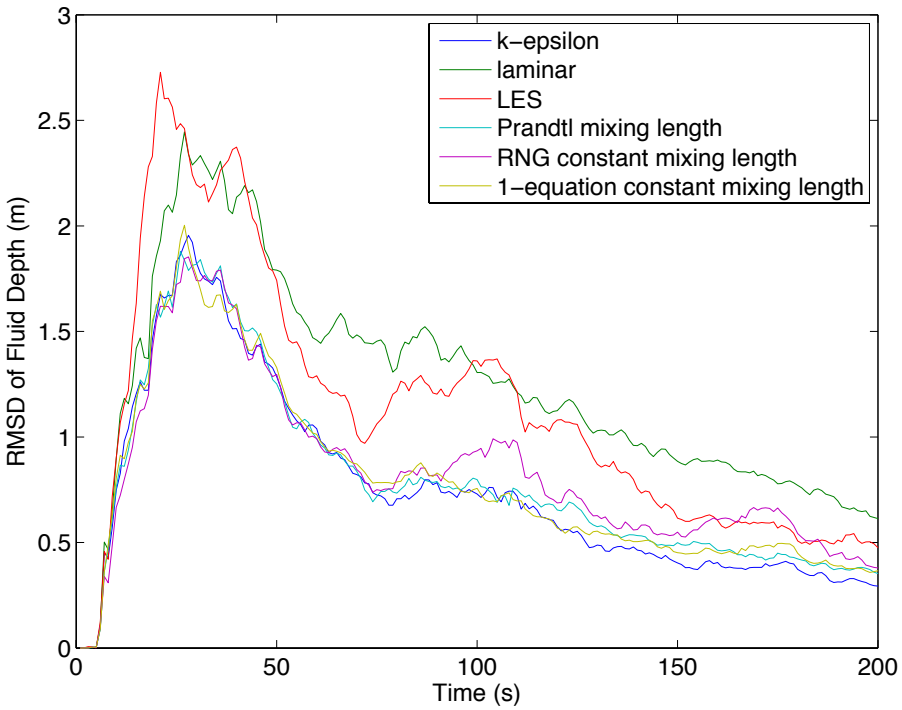

Figure 2.5- Root-mean-square deviation (RMSD) of fluid depth from the baseline model results (RNG-dynamically computed mixing length) for each turbulence model as a function of time

The overtopping hydrograph for each turbulence model is shown in Figure 2.6, and the RMSD of flow rate for each of the models are given in Table 2.5 along with

additional comparisons of the hydrographs, including the percent difference in flow rate and total overtopping volume. The largest differences in flow rate and overtopping volume come from the laminar and LES models with the laminar model producing higher flows and the LES model producing the lowest flow rates. The hydrographs from the other models closely match the overtopping hydrograph from the baseline model. The percent differences in peak flow rate from the eddy viscosity models range from around 0.25% for the Prandtl mixing length model to around 3% for the *k-epsilon* model. The differences in total overtopping volume are a little higher, although all are less than 5%, and the differences in maximum wave height are much less significant for all but the LES model, with most models giving differences in maximum wave height less than 2%.

The laminar model is the only model that gives higher flow rates and overtopping volumes than the baseline model, indicating that even if the turbulence model introduces uncertainty into the model results, the results of the baseline model are most likely conservative, giving possibly higher discharges. Considering all of the other sources of uncertainty in the models of the avalanche and wave generation, the turbulence model is one of the less-significant sources of uncertainty.

Table 2.5- Comparison of overtopping hydrograph characteristics between the baseline model (RNG-dynamically computed mixing length) and the other turbulence models tested

Turbulence Model	RMSD (m^3/s)	Peak Flow Rate (m^3/s)	% Difference: Peak Flow Rate	Total Overtopping Volume (x 10^6 m^3)	% Difference: Overtopping Volume	Maximum Wave Height (m)	% Difference: Maximum Wave Height
Baseline Model	---	78700	---	2.38	---	51.57	---
K-epsilon	726.0	76300	-3.05	2.27	-4.80	50.86	-1.38
Laminar Flow	3385.5	83900	6.61	2.47	3.60	52.38	1.57
LES	3046.7	72100	-8.39	2.13	-10.44	49.69	-3.64
Prandtl Mixing Length	815.9	78500	-0.25	2.29	-3.91	52.00	0.83
RNG Constant Mixing Length	1187.6	77600	-1.40	2.30	-3.60	51.48	-0.17
1 Equation Constant Mixing Length	1190.5	78000	-0.89	2.29	-4.02	51.99	0.80

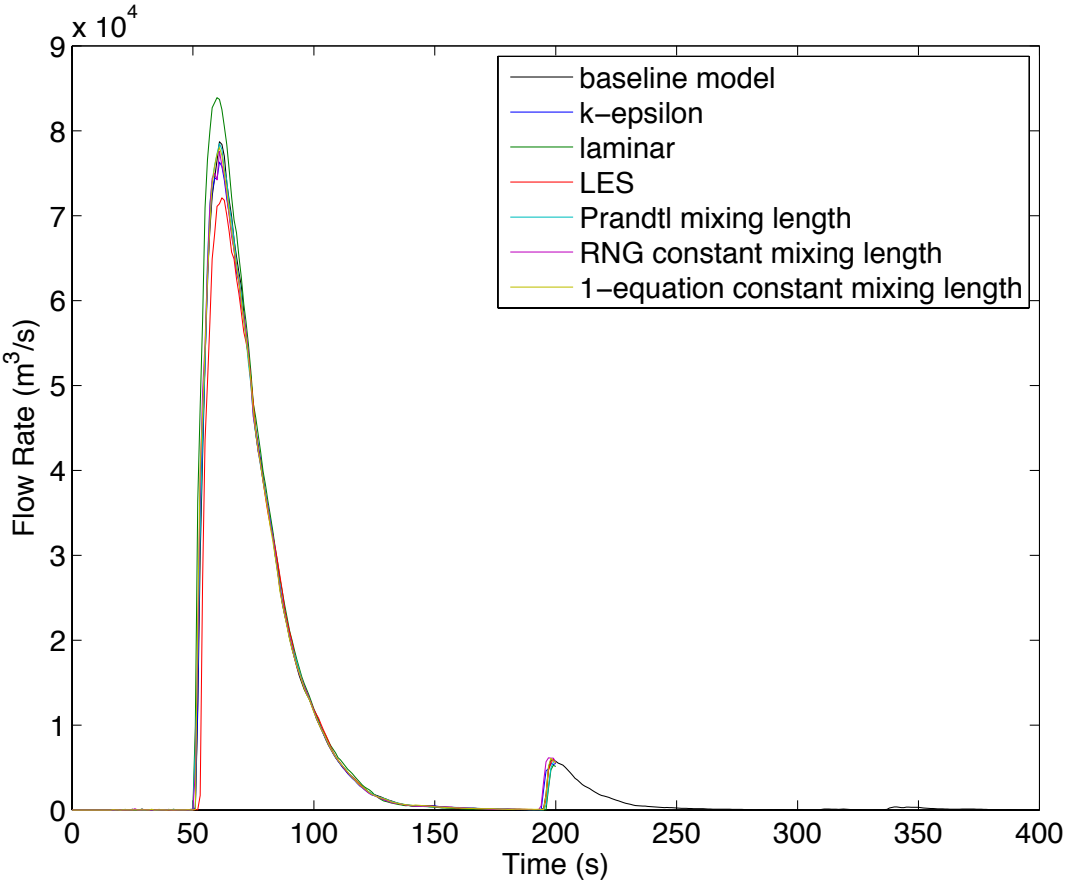

Figure 2.6- Overtopping hydrographs for each of the turbulence models run with the large avalanche source

Sensitivity to Grid Size

It can be expected that the model results will improve with refinement of the grid mesh. The grid cell size used for the simulations of Lake Palcacocha was selected to allow for sufficient resolution of the topographic and bathymetric features as well as the dynamic wave features during the wave generation and overtopping phases while also

balancing time and computational resources. The grid size chosen for the regular mesh was nearly the finest grid that could be used to run the model in a reasonable amount of time on a desktop PC. To assess the impact of grid size on model results, a simulation was run with a coarser grid (grid cell sizes are given in Table 2.1).

The root-mean-square error (RMSE) of fluid depth for the coarse grid simulation as compared to the results of the regular mesh is a good measure of the error introduced by changing the grid resolution (Figure 2.7). As with the turbulence models, the highest errors are in the first 50 seconds of the simulation time, during the wave generation, propagation and runup phases. However, there is a baseline level of error that comes simply from extrapolating the initial conditions to a coarser grid because the bathymetry and initial fluid depths cannot be represented as well in the coarse grid models. The RMSE at $t=0$ reflects this source of error. After about 50 seconds, the RMSE begins to level off at a relatively consistent level of approximately 1.5 m. This is about three times higher than the RMSD from the eddy viscosity turbulence models at the same point in time, indicating that increasing the grid size could introduce much more error than changing the turbulence model.

When comparing the hydrograph from the coarse grid simulation with the hydrograph from the regular mesh (Figure 2.8), it is clear that the coarse grid simulation gives overestimates of the discharge from overtopping. The RMSE of discharge for the coarse grid simulation is approximately 3300 m^3/s, not an insignificant amount, but less than the RMSD for the laminar flow model; the RMSE of discharge for the coarse grid model is still approximately three times the RMSD for the eddy viscosity turbulence models. The peak discharge from the coarse grid simulation is over 5% higher than the peak discharge from the regular grid size model (Table 2.6). The total overtopping volume is slightly higher for the coarse grid simulation, but the difference is less than

1%, so the coarse grid model may be better at estimating the total overtopping volume even if it does not get the wave dynamics and outflow hydrograph completely correct. Although the error resulting from using a coarser mesh is greater than the uncertainty from most of the turbulence models (apart from the laminar and LES models that are most likely not the best models to use for this problem), the uncertainty due to the grid size is still not a very large source of error. If computational time and resources are an issue, it may be possible to use a slightly larger grid size without compromising model results.

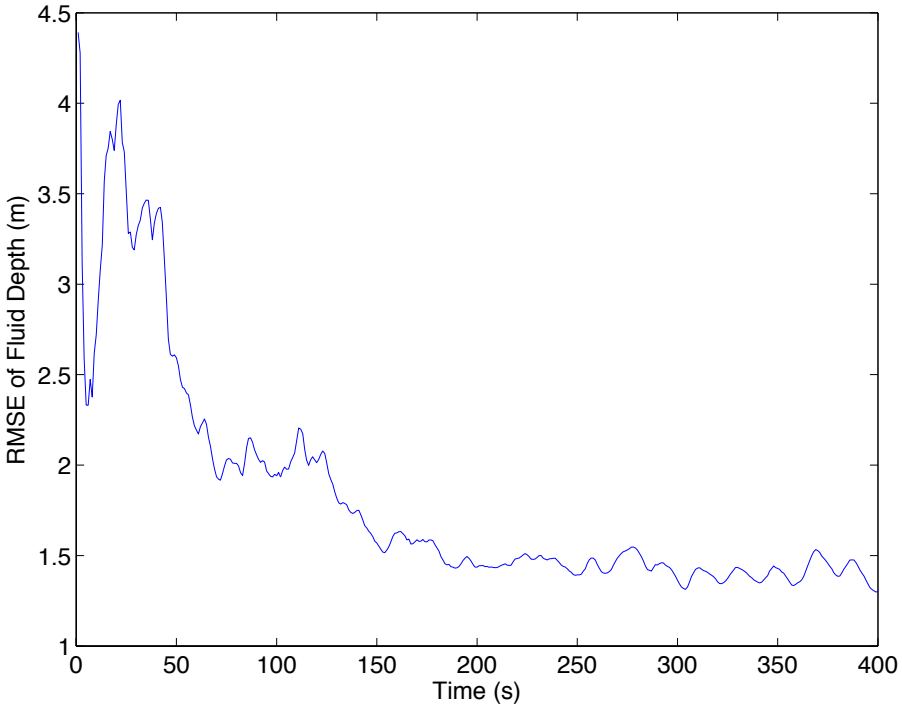

Figure 2.7- Root-mean-square error (RMSE) of fluid depth for the coarse grid simulation as compared to the regular grid mesh used for all other simulations

Table 2.6- Overtopping hydrograph characteristics for coarse grid simulation as compared to the regular mesh for the large avalanche source scenario

	RMSE (m^3/s)	Peak Overtopping Flow Rate (m^3/s)	% Difference: Peak Flow Rate	Total Overtopping Volume (10^6 m^3)	% Difference: Overtopping Volume
Regular Mesh	---	78700	---	2.38	---
Coarse Grid Simulation	3320.2	82900	5.34	2.41	0.98

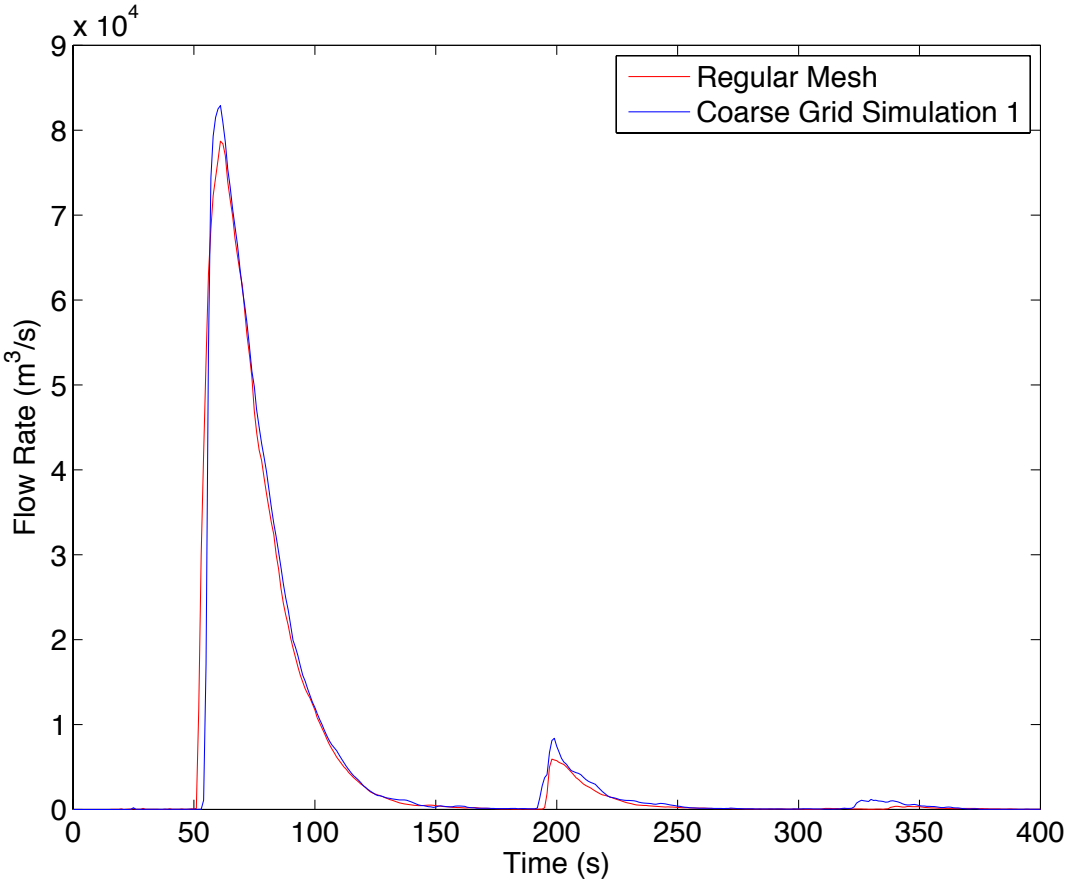

Figure 2.8- Overtopping hydrograph for the coarse grid simulation as compared with the hydrograph for the regular mesh for the large avalanche source scenario

2.3.2 Comparison of Boundary Conditions: Avalanche Source vs. Mass-momentum Source

The two boundary condition methods for representing the impact of the avalanche with the lake and the subsequent wave generation are the avalanche source, defined as a fluid region representing the avalanche from which water is released to flow downhill into the lake, and the mass-momentum source, characterized by an inflow hydrograph injected through a pre-defined cross-sectional area. The inflow hydrographs of the two boundary condition methods, as measured at the point of impact of the avalanche with the lake, for all three avalanche scenarios are shown in Figure 2.9 along with the hydrograph from the RAMMS avalanche model (Somos-Valenzuela et al., 2014).

For all three avalanche scenarios, the peak inflow for the avalanche source was significantly higher than the flow rates for the mass-momentum source. The mass-momentum source inflows are very close to those of the RAMMS model in each case because the boundary condition was defined to match the RAMMS avalanche hydrograph. The higher peak inflows for the avalanche source are probably because of the lower viscosity of water that allows the water to flow and spread out more quickly as compared to the mixture of materials in the avalanche; to compensate for this, the avalanche fluid release volume was more concentrated so that the fluid depths would not be too low, but the result is higher inflow rates over a shorter period of time. The peak inflow rates for the avalanche source range from nearly twice the peak flow rate of the RAMMS avalanche for the large scenario to over 5 times higher for the small scenario. Although the peak flow rates for the avalanche source are significantly higher than the peak flow from the RAMMS avalanche model, they are of much shorter duration. For the large scenario, peak discharge for the mass-momentum source at the point of overtopping of the terminal moraine (Table 2.9) is 14% less than the discharge for the avalanche source (compared to a difference of about 50% for the inflows). However, for the

medium and small scenarios, the difference in peak overtopping discharge between the two boundary condition models is more pronounced. The overtopping discharge for the medium mass-momentum source is 65% less than the discharge from the medium avalanche source; this difference is only slightly lower than the difference in peak inflow (~75%). The overtopping discharge for the small mass-momentum source is almost 91% less than the discharge for the small avalanche source; in comparison, the difference in peak inflow is around 80%. While the difference in overtopping volumes for the large avalanche and mass-momentum sources is only 9%, the total overtopping volume for the small mass-momentum source is over an order of magnitude less than the overtopping volume resulting from the small avalanche source (Table 2.9).

There are a few irregularities in the inflow hydrographs that should be mentioned. First, the large avalanche source inflow hydrograph has a forked peak. This is likely due to the way in which the initial avalanche fluid volume was defined; the volume of fluid that was released was probably not gradual enough so that as the fluid region was allowed to flow into a more natural state, the graduated levels in the water surface of the initial fluid region did not coalesce into one continuous surface but rather had two areas of peak flow depth. This is a problem that results from releasing blocks of water just above the lake; the initial fluid volume is not realistic, but the idea is that the water will even out into a natural flow before it reaches the lake. The fluid cannot be released at a point that is too high or the velocities will be excessive, but to get a high enough volume and with accurate depths, it is difficult to get an even flow by the time the water reaches the lake. A second irregularity that deserves mention is a smaller peak in the inflow hydrographs from the avalanche source in the medium and small scenarios. This second peak is likely the result of flow entering the lake from the sides. This, as such, is not unrealistic, as there is inflow from the sides of the lake in the avalanche model. However,

due to the higher viscosity of the snow-rock-ice mixture of the avalanche, the inflow of the avalanche from the lateral moraines probably happens more gradually so that the abrupt inflow from the sides does not cause such a significant peak in the inflow hydrograph. Until models are developed that can easily and accurately represent two distinct fluids (in this case the mixture of snow, rock and ice of the avalanche and the water in the lake) combined with free surface flows, the limitations and irregularities of the model resulting from the representation of the avalanche fluid as water cannot be easily overcome.

There is a significant source of uncertainty in the mass-momentum source method due to the fact that the avalanche models were not run for the full time it takes all of the avalanche flow to enter the lake. Because of this, it is impossible to know what the tails of the inflow hydrographs look like. For the large avalanche scenario, 82% of the avalanche enters the lake within the simulation time in RAMMS, so the inflow hydrograph used in the mass-momentum source is likely a closer match to the actual inflow hydrograph. This problem is most exaggerated for the small scenario where a much smaller percentage (60%) of the flow enters the lake within the time of the RAMMS model run. There are multiple small peaks in the small avalanche model, and the implications of this in the lake model are uncertain. Because of limited information about the avalanche inflow conditions from the avalanche model, it is very difficult to say what the level of uncertainty is in the lake model due to the incomplete avalanche inflow hydrographs.

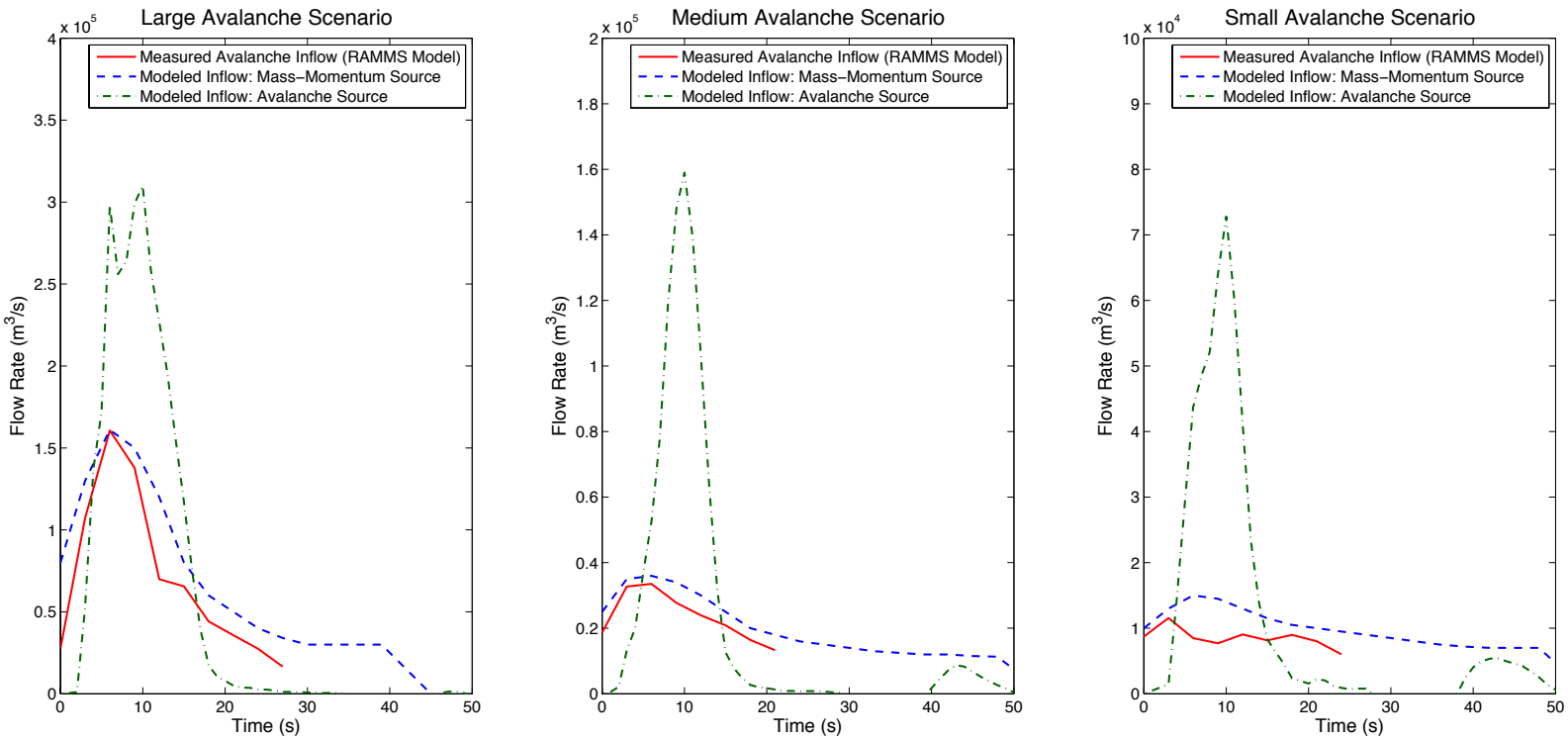

Figure 2.9- Inflow hydrographs for the avalanche as it enters the lake for the avalanche source and mass-momentum source boundary conditions as compared to the hydrograph extracted from the RAMMS avalanche mode

Although the avalanche source seems to have the most uncertainty, each of the boundary condition methods has its limitations. The complex nature of the interacting dynamic physical systems makes it extremely difficult to develop one comprehensive and precise method for simulating an avalanche-generated wave. The avalanche source has much higher peak inflow rates that may be unrealistically high, but it gives a better physical representation of the actual geometry of the terrain as the avalanche enters the lake. The avalanche source is also able to simulate the effects of avalanche material entering the sides of lake, whereas the mass-momentum source only simulates flow entering the lake from the end nearest to the glacier. The mass-momentum source better matches the peak flow rates from the avalanche model because that is how the method is designed; the flow rate of the avalanche inflow is a control parameter for the mass-momentum source. However, the mass-momentum source enters the lake horizontally, rather than at the angle of the steep incline of the terrain above the lake. Therefore, the mass-momentum source is likely underestimating the momentum transfer between the avalanche and the lake, as the avalanche can gain more momentum as it enters the lake at a downward angle. Despite the limitations of each representation of the boundary conditions and the significant uncertainty in the simulation of the wave generation from avalanche impact, the two boundary condition methods are potentially representing a range of possible outcomes, and we could consider the results from the avalanche source and mass-momentum source, respectively, as upper and lower bounds on the lake model results.

2.3.3 Wave Characteristics

Of the five phases for an avalanche-generated impulse wave presented in Section 2.1.3, this section focuses on the wave propagation and run-up, studying the wave characteristics during these phases. The wave generation was explored in Section 2.3.2, and the overtopping is investigated in Section 2.3.4.

As the avalanche impacts the lake, it generates a wave that propagates lengthwise along the lake towards the damming-moraine and attains its maximum height when it reaches the shallow portion at the western end of the lake (Figure 2.10). The characteristics for the waves generated for each avalanche scenario according to the Heller and Hager method are given in Table 2.7. Although the wave heights from FLOW-3D (Table 2.8) are of the same order of magnitude as those calculated from the empirical method (Heller and Hager), the FLOW-3D wave heights are all larger, with the difference in wave height up to 14% (5.8 m) over the empirically calculated wave height for the large avalanche. Without field measurements of lake dynamics or overtopping hydrographs from GLOF events, it is difficult to draw any definitive conclusions about the accuracy of the methods. However, the FLOW-3D simulations are able to reproduce the avalanche characteristics of the RAMMs model as the avalanche enters the lake and account for lake bathymetry, likely giving more accurate results than the empirical method. As expected, the FLOW-3D results show attenuation of the wave as it propagates along the lake; the maximum wave height is attenuated approximately 30% before it reaches the damming-moraine. Normally, there would be a significant increase in wave height with the run-up against the terminal moraine, but because of the high dissipation of energy on the western end of the lake where it becomes shallow, this effect is somewhat lessened.

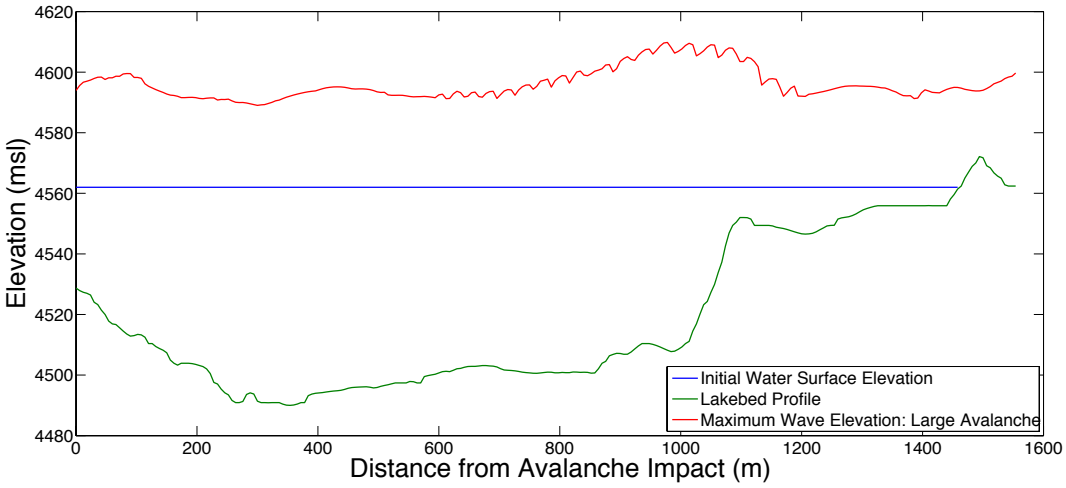

Figure 2.10- Profile of the maximum wave height as a function of distance along the lake for the large avalanche source scenario

Table 2.7- Characteristics of the impulse wave generated from each avalanche scenario calculated according to the Heller and Hager (2009) method

	Maximum wave height (m)	Wavelength (m)	Downstream distance to maximum wave height- x_m (m)
Large Event	42	793	392
Medium Event	21	468	254
Small Event	9	253	147

Looking in more detail at the wave propagation in the large avalanche scenario (Figure 2.10), there are two peaks in the wave height. The initial peak is near the avalanche impact, corresponding to the empirical equations, and a higher peak occurs when the wave encounters the shallow portion of the lake. The Heller and Hager empirical equations calculate the wave characteristics in the lake after wave generation but do not account for run-up impacts on the wave characteristics. Therefore, the peak wave height in the deeper portion of the lake can be considered to be the closest

comparison to the empirical equations. The increase in wave height as the wave makes contact with the shallow end of the lake cannot be easily represented in the Heller and Hager method. This is the beginning of the run-up process that culminates in the overtopping of the moraine, where the wave gains height as the water depth decreases.

There are some oscillations in the profile of the maximum wave height in Figure 2.10, and when investigating these oscillations, it is important to remember that the profile in Figure 2.10 gives the wave height as a function of distance along the lake, not as a function of time. The maximum wave height was calculated just for the water in the center of the lake to eliminate the effects of run-up onto the lateral moraines along the sides of the lake, but the run-up on the sides of the lake still seem to be influencing the wave in the center of the lake. The oscillations in the maximum wave height as a function of distance are most likely due to splashing from the run-up on the sides that is reflected off the lateral moraines and returns to the lake at irregular intervals.

Table 2.8- Maximum wave heights from the FLOW-3D model results as compared to the wave heights calculated according to the Heller and Hager (2009) method

	Max. Wave Height, empirical equations* (m above initial free surface)	Max. Wave Height, FLOW-3D simulations (m above initial free surface)	Distance of Peak Wave, FLOW-3D simulations (m from avalanche impact)
Large Avalanche Source	42	47.8	1080
Large Mass-Momentum Source	42	46.4	1039
Medium Avalanche Source	21	30.1	318
Medium Mass-Momentum Source	21	**	**
Small Avalanche Source	9	19.6	108
Small Mass-Momentum Source	9	**	**
* Heller and Hager 2010			
** water surface elevation data were not available for the small and medium mass-momentum source scenarios			

The run-up phase culminates with the overtopping of the lake-damming terminal moraine; the maximum wave heights above the crest of the drainage structure/artificial dam at the terminal moraine are given with the overtopping results in Table 2.8. The wave height above the moraine crest at the point of overtopping increases with lake lowering even though the total overtopping volumes and peak flow rates decrease. This may seem counterintuitive, but it can be explained by looking at how the lake dynamics are expected to change with lake lowering. First, as the water surface level is lowered, the total volume stored in the lake increases, thus the momentum transferred to the lake from the avalanches per unit volume should be higher. The avalanche characteristics do not change with the lake lowering scenarios but the total volume in the lake decreases with lake lowering, so the additional momentum relative to the lake volume can produce taller waves. Secondly, as the point of avalanche impact is at a lower elevation with lowered lake levels, there is more momentum in the avalanche fluid when it enters the lake. Although the increased overtopping wave heights for the lake lowering scenarios indicate that the waves may be larger when the lake is lowered, the amount of overtopping still decreases with lake lowering. This is most likely due to the lower initial water surface elevation; the lower free surface elevation means that more momentum is required for overtopping, and although the momentum transfer per unit volume to the lake from the avalanche is greater, more of this momentum is lost during the run-up and overtopping, and less water is actually able to pass over the crest of the terminal moraine.

2.3.4 Overtopping Hydrographs and Volumes

The wave run-up causes a significant amount of water to overtop the damming-moraine; the total overtopping discharge volume for each scenario is given in Table 2.9,

and the overtopping hydrographs are shown in Figure 2.11. For the large avalanche source, current lake level scenario, the results differ slightly from the hydrographs used for the sensitivity analysis (presented in Section 2.3.1). The original definition of the avalanche fluid region was resulting in overly high fluid depths; therefore, a second large avalanche source simulation was run with a more graduated release area for the initial fluid region that resulted in depths and velocities at the point of impact with the lake that more closely match those from the avalanche model. However, the simulations used for sensitivity analysis had already been run, and due to time limitations with the software license, it was not possible to repeat these simulations with the newly defined large avalanche initial fluid region.

Figure 2.11 shows that the large avalanche source results in an overtopping wave discharge hydrograph with a peak of about 63,000 m^3/s approximately 60 s after the avalanche fluid is released and a smaller peak of 6,000 m^3/s due to a reflected wave at about 200 s. The duration of the initial wave of the avalanche events is about 100 seconds (large avalanche), 70 seconds (medium avalanche), and 50 seconds (small avalanche). The total overtopping volume is 1.8×10^6 m^3 for the large avalanche source, and the medium and small avalanche sources result in overtopping volumes of 0.5×10^6 m^3 and 0.15×10^6 m^3 respectively; the mass-momentum source results in overtopping volumes of 1.64×10^6 m^3, 0.15×10^6 m^3, and 0.014×10^6 m^3 for the large, medium, and small avalanches respectively (Table 2.9). The overtopping volume for the large avalanche source is 60% of the avalanche volume, and for the medium and small avalanche sources, the overtopping volumes are 50% and 30% of the avalanche volumes respectively. The overtopping volume appears to decrease relative to the avalanche volume as the avalanche size decreases, indicating that the lake has much more capacity to dissipate smaller avalanche-generated waves, but a large wave is so large relative to the size of the

lake that the lake is overpowered, in a sense. Therefore, large avalanches may pose a greater threat of inundation relative to the magnitude of the event than smaller avalanches.

The mass-momentum source consistently results in lower overtopping flow rates and volumes, but the differences between the mass-momentum source and the avalanche source are more pronounced for the small and medium scenarios. For the large mass-momentum source, the peak overtopping flow rate is 14% less than the peak flow rate from the avalanche source, much less than the difference in peak inflow for the two types of boundary conditions; the peak inflow for the avalanche source was approximately twice the peak inflow for the mass-momentum source. The large mass-momentum source overtopping volume is 11% less than the avalanche source overtopping volume. For the medium mass-momentum source, the peak discharge and overtopping volume are respectively 65% and 70% less than the avalanche source, and the difference between the small avalanche source and mass-momentum source is 91% for both the peak discharge and overtopping volume. These differences for the medium and small scenarios are consistent with the more marked differences in the inflow hydrographs for the medium and small scenarios; the percent differences between the peak flow for the avalanche source and mass-momentum source for the overtopping flows do not deviate much from the differences in the inflow hydrographs. However, the more exaggerated differences between the avalanche source and mass-momentum source for the medium and small scenarios may be due more to weaknesses in the representation of the avalanche in the avalanche source model (discussed below) than in any fundamental differences between the various sizes of the avalanches.

The inflow hydrographs for the medium and small avalanche sources are markedly different from the inflow hydrographs for the medium and small mass-

momentum sources. This may be due to uncertainties in the conversion of the results of the RAMMS avalanche model to an inflow hydrograph, but it is likely that much of the difference is due to the shortcomings of the avalanche source model. The difficulties of getting a volume of water to behave exactly as the avalanche fluid would as it enters the lake despite the very different viscosities of the two fluids are discussed in Section 2.3.2, and these difficulties are compounded for the smaller scenarios that have lower avalanche depths and velocities entering the lake; because of this, the fluid must be released closer to the lake to get accurate depths and velocities, but this means that the fluid has less time to spread out as it flows into the lake, and so the inflow is more concentrated. The initial avalanche fluid region is defined manually through an iterative process, comparing the depths and velocities to the RAMMS avalanche parameters and then adjusting the heights and depths of the avalanche fluid region accordingly. The problems with the concentrated flow entering the lake (high peak inflows) could perhaps be improved with more iterations of the initial avalanche fluid region, but this is a manual process that is imprecise, at best, and the return on additional time invested in refining the initial avalanche fluid region becomes less with each iteration. This is a problem that is unlikely to be overcome without a model that can represent the mixing of two different fluids with free surface flow; most commercially available modeling software do not have this type of model that would allow for the avalanche region to flow as it naturally would with the characteristics of the avalanche fluid until it mixes with the water in the lake.

Table 2.9- Characteristics of Three Avalanche Events of Different Size as Simulated in RAMMS. Overtopping Volume, Flow Rate and Wave Height for Three Avalanche Events as Simulated in FLOW-3D for the Current Lake Level and Three Lake Mitigation Scenarios (after Somos-Valenzuela et al., 2016).

	Avalanche Event		
	Large	**Medium**	**Small**
0 m lower – Avalanche Source			
Overtopping volume (10^6 m^3)	1.8	0.50	0.15
Overtopping peak flow rate (m^3/s)	63,400	17,100	6,410
Overtopping wave height above artificial dam (m)	21.7	12.0	7.1
15 m lower – Avalanche Source			
Overtopping volume (10^6 m^3)	1.6	0.2	0.02
Overtopping peak flow rate (m^3/s)	60,200	6,370	1,080
Overtopping wave height above artificial dam (m)	38.4	27.5	25.1
30 m lower – Avalanche Source			
Overtopping volume (m^3)	1.3	0.05	0
Overtopping peak flow rate (m^3/s)	48,500	1,840	0
Overtopping wave height above artificial dam (m)	60.8	42.5	0
0 m lower – Mass-momentum Source			
Overtopping volume (10^6 m^3)	1.64	0.15	0.014
Overtopping peak flow rate (m^3/s)	54,600	6,000	592
Overtopping wave height above artificial dam (m)	15.9	*	*
15 m lower – Mass-momentum Source			
Overtopping volume (10^6 m^3)	0.83	0.034	0
Overtopping peak flow rate (m^3/s)	25,700	1,510	0
Overtopping wave height above artificial dam (m)	32.0	25.4	0
30 m lower – Mass-momentum Source			
Overtopping volume (m^3)	0.45	0	0
Overtopping peak flow rate (m^3/s)	15,100	0	0
Overtopping wave height above artificial dam (m)	46.1	0	0
* water surface elevation data were not available for the small and medium 0 m mass-momentum source scenarios			

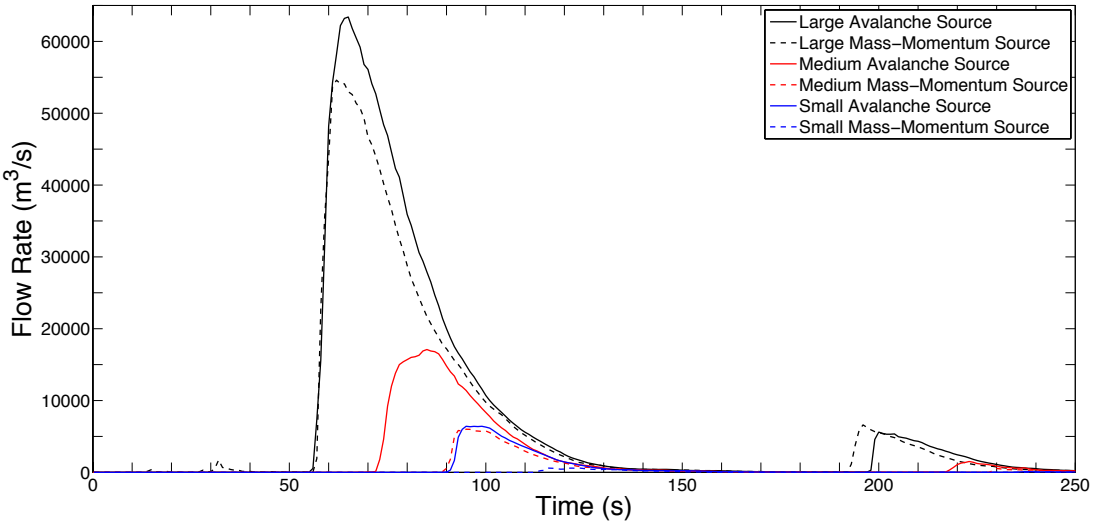

Figure 2.11- Overtopping wave discharge hydrographs for the three avalanche events and two types of boundary conditions with the lake at its current level.

2.3.5 Lake-lowering Scenarios

Two lake lowering or mitigation scenarios (with lake levels at 15 m and 30 m below the current water level) were simulated to determine the impact on the moraine overtopping. Simulations for all three avalanche sizes with both types of boundary conditions were repeated for each lake level, and the overtopping volume as well as the peak discharge of the wave are incrementally smaller as the lake is lowered (Table 2.9). The hydrographs for the overtopping discharge are shown in Figure 2.12. The overtopping volumes and peak flow rates decrease with incremental lowering of the lake, but the overtopping wave heights above the artificial dam increase. The reasons for this are discussed in Section 2.3.3.

Although overtopping cannot be entirely prevented for the large avalanche events, even by lowering the lake up to 30 m, overtopping can be prevented by lake-lowering for

the smaller avalanche scenarios. The scenarios with no overtopping are the small avalanche source, 30 m lowering; the small mass-momentum source, 15 m and 30 m lowering; and the medium mass-momentum source, 30 m lowering. The overtopping volume for the medium avalanche source with 30 m lowering is reduced by 90% compared to the current level scenario. Overtopping is not avoided entirely for most of the 15 m lake-lowering scenarios; however, the overtopping flow rates and volumes are reduced by about 60% and 80% for the medium and small avalanche sources, respectively, for 15 m lake lowering. The lake lowering appears to have the least impact with the large avalanche scenario, as significant overtopping still occurs for all lake-lowering scenarios for the large avalanche. However, the overtopping volume can be reduced by 28% for the avalanche source, 30 m lowering scenario and by up to 73% for the large mass-momentum source, 30 m lowering scenario. Any scenario that results in an overtopping volume less than 25,000 m^3 may be considered "safe" as defined in Section 2.2.4, and the categorization of each scenario according to this definition is given in Table 2.10.

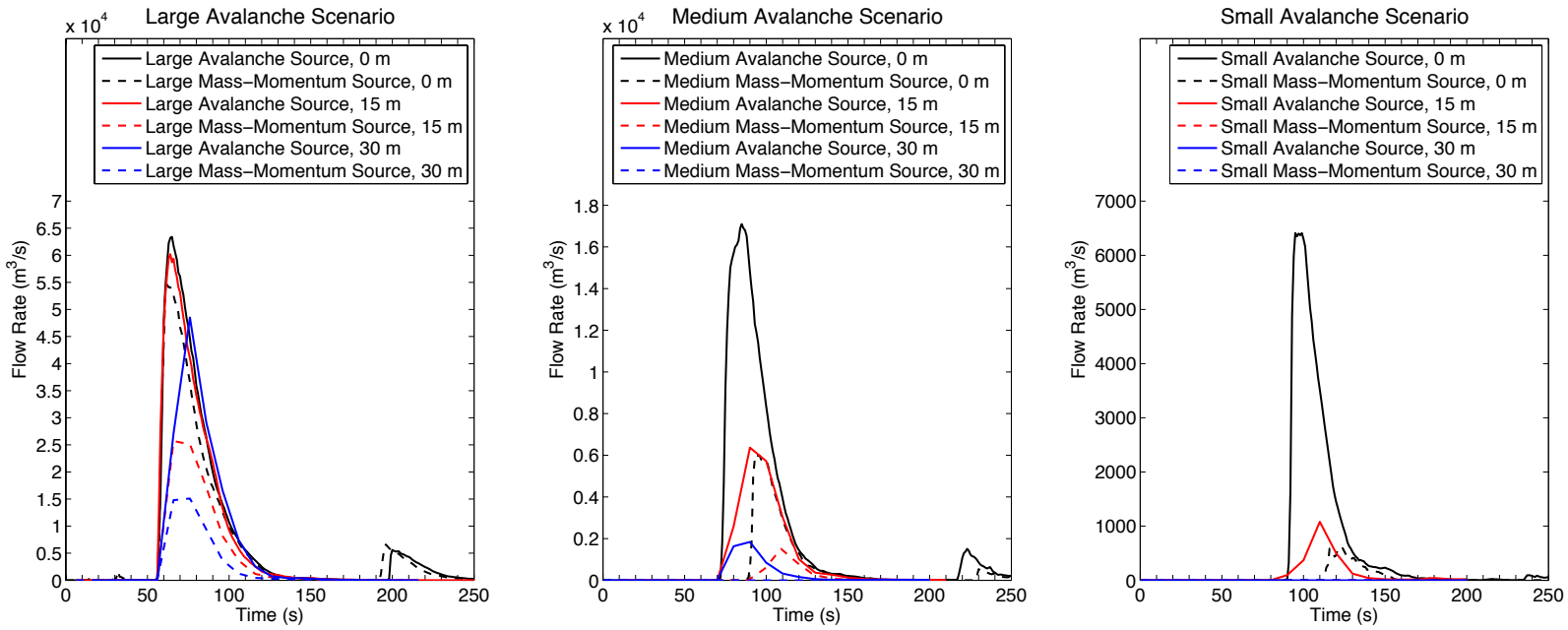

Figure 2.12- Overtopping hydrographs for lake lowering scenarios for a) large avalanche scenario, b) medium avalanche scenario, and c) small avalanche scenario

Table 2.10- Characterization of each simulation scenario as "safe" or "not safe" according to the minimum overtopping volume criterion.

Avalanche Scenario	Lake-lowering Scenario: Current Level	15 m Lower	30 m Lower
Large Avalanche Source	Not Safe	Not Safe	Not Safe
Large Mass-momentum Source	Not Safe	Not Safe	Not Safe
Medium Avalanche Source	Not Safe	Not Safe	Not Safe
Medium Mass-momentum Source	Not Safe	Not Safe	Safe
Small Avalanche Source	Not Safe	Safe	Safe
Small Mass-momentum Source	Safe	Safe	Safe

In examining the effect of lake lowering on flood volume, the question can be asked: *Is the relationship linear?* To investigate this relationship, the overtopping volume vs. lake lowering is plotted for the three avalanche scenarios in Figure 2.13. Although three data points (current level, 15 m lower and 30 m lower) cannot conclusively support the hypothesis of a linear relationship, the relationships in Figure 2.13 do appear to be linear. When linear regression equations are fitted to the data, the r^2 value is greater than 90% (with most greater than 95%) for all scenarios that do not reach the point of no overtopping. The slope of the relationship between lake level and overtopping volume is significantly different for each scenario and type of boundary condition, which suggests that each is unique. Therefore, the usefulness of a linear relationship between lake level and overtopping volume would be most suitable in investigating additional lake lowering scenarios that were not simulated. However, this must be done carefully because additional lowering was not simulated, and whether or not the linear relationship may continue to hold true for scenarios of extreme lake-lowering is unclear. If this relationship

is to be used, it is suggested that it only be applied for potential mitigation scenarios of lake lowering between 0 m and 30 m to estimate a potential overtopping volume.

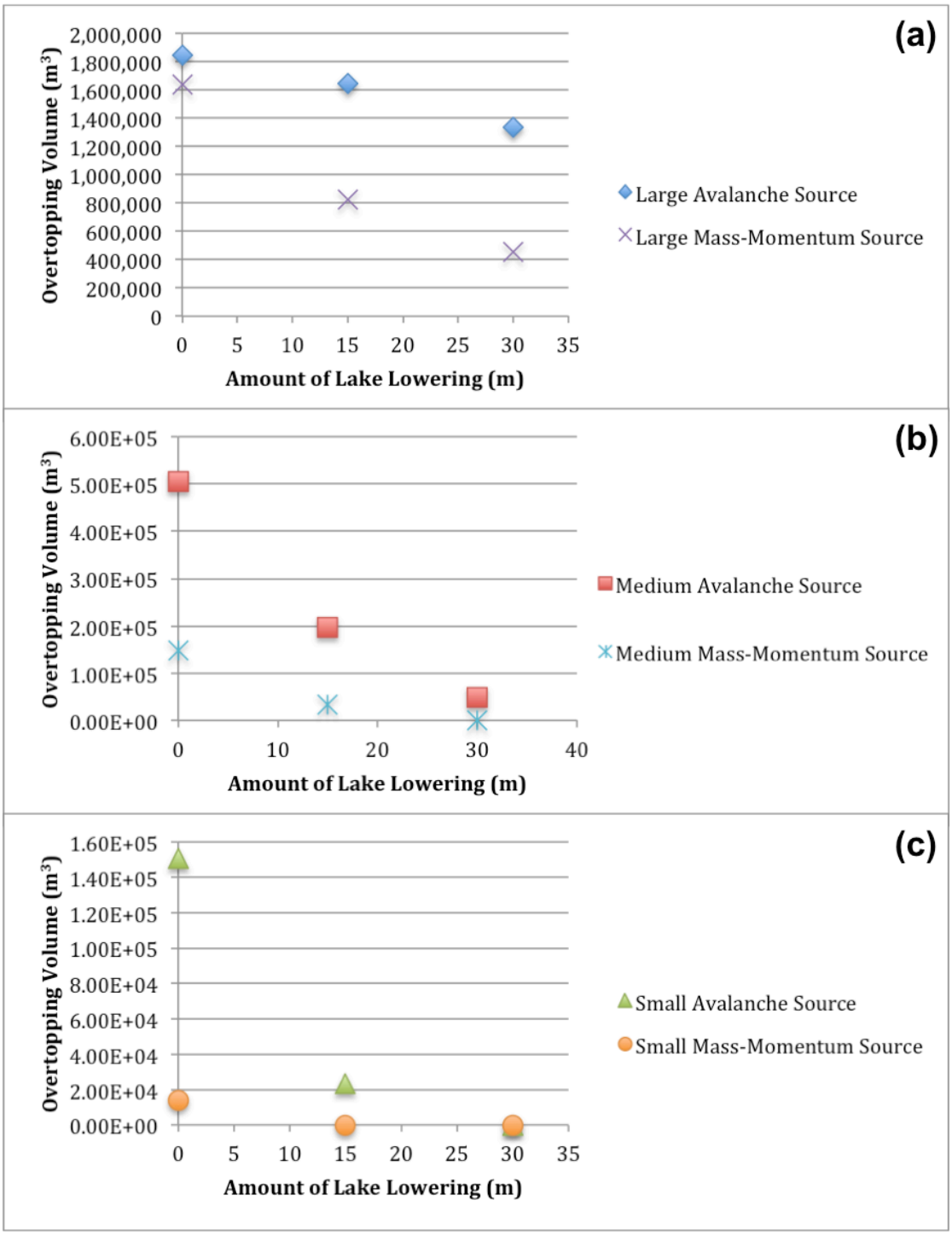

Figure 2.13- Relationship in the overtopping volume vs. lake level that appears to be linear for a) large avalanche, b) medium avalanche, and c) small avalanche scenarios.

The final step in assessing the lake-lowering mitigation scenarios is to look at the impact downstream on inundation intensities and hazard levels. As discussed in Section 2.1.4, only the avalanche source scenarios (and not the mass-momentum source) were simulated in the downstream inundation model because the avalanche source produced the most conservative results (highest flow rates and volumes) for a worst-case scenario hazard analysis. The resulting maps of inundation intensities are shown in Figure 2.14. For the large avalanche scenario, the total inundated area is reduced by 18% for 15 m lowering and 30% for the 30 m lowering; however, this does not completely represent the effect of lake lowering on hazard reduction. The reduction in area in the high-intensity flood zones for the large scenario is relatively higher than the reduction in total affected area, meaning that in the lake-lowering scenarios, a smaller percentage of the total inundated area is high-intensity.

The hazard level is a combination of the inundation intensity and the probability for each scenario. Because the large avalanche scenario has such high intensity levels, those results predominate in the hazard definition (areas in each hazard zone are given in Table 2.11); the hazard map for each lake-lowering scenario largely corresponds to the inundation intensities for the large avalanche. Because of this, the hazard zones do not necessarily reflect the complete picture of the impacts of lake lowering in the city. For the medium and small avalanche scenarios (the more likely scenarios according to the inverse relationship between avalanche size and likelihood) the inundated area can be significantly reduced by lake lowering. For the small avalanche, both the 15 m and 30 m lake-lowering scenarios result in no inundation in the city; any overtopping that does occur for the 15 m small avalanche source scenario is attenuated as it moves downstream such that the flow can be contained within the river channel. In addition, most of the inundated area for the medium avalanche, 30 m lowering scenario falls into the low-

intensity category, meaning that even if a significant area is flooded, the flood could be much less destructive. From the results in this work alone, it is difficult to reach any conclusions about the optimum lake-lowering scenario. Nonetheless, the results of the lake modeling do indicate that lowering the lake level can help mitigate the GLOF impacts downstream and reduce the hazard level in the city of Huaraz.

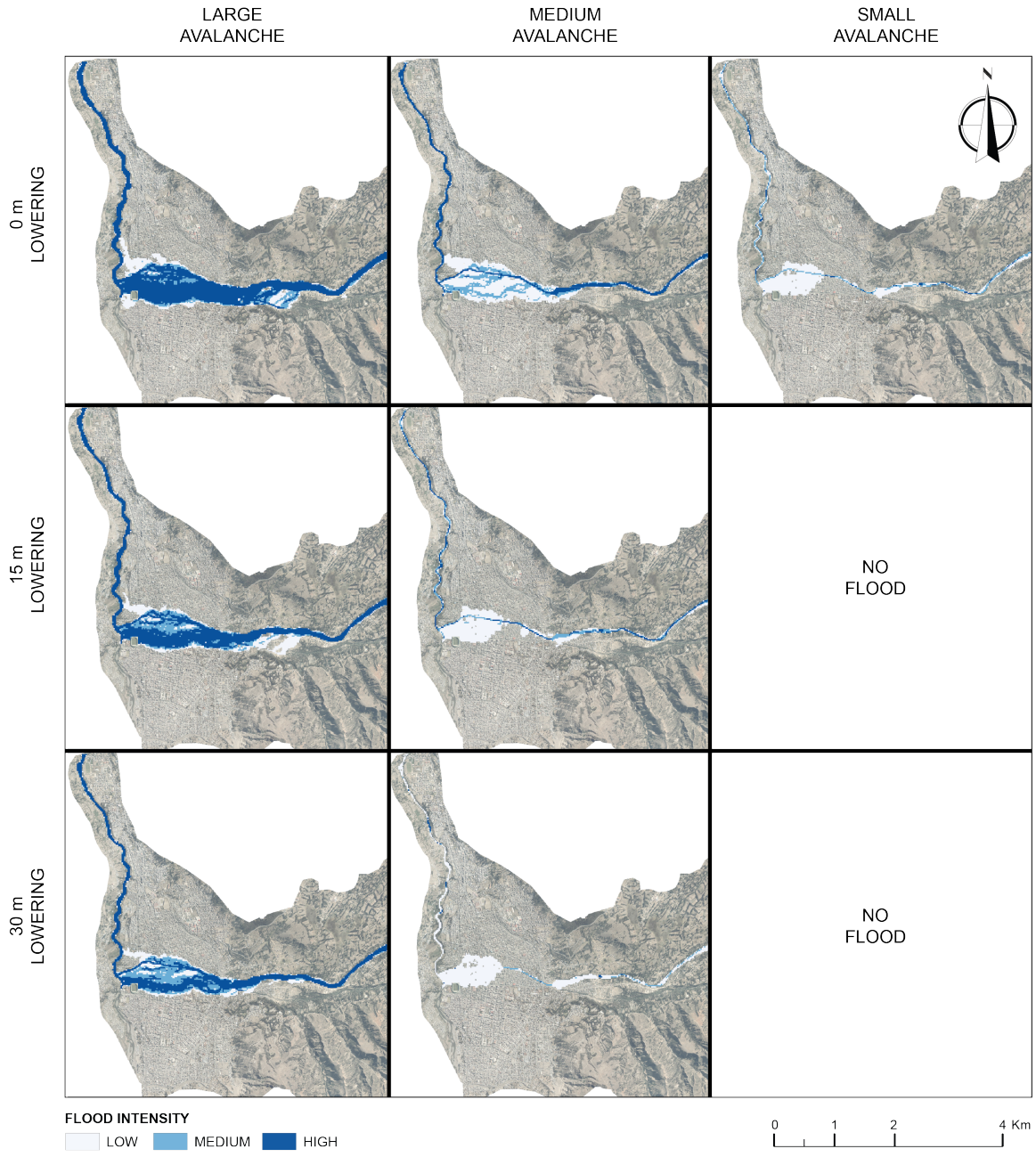

Figure 2.14- Flood intensity in Huaraz associated with a potential GLOF from Lake Palcacocha for scenarios of 0 m of lake lowering (current condition), 15 m lowering and 30 m lowering for small, medium and large avalanches (from Somos-Valenzuela et al., 2016).

Table 2.11- Areas of Each Hazard Level Corresponding to the Current Lake level and Two Lake Mitigation Scenarios (from Somos-Valenzuela et al., 2016).

Mitigation	Low hazard area (km^2)	Med. hazard area (km^2)	High hazard area (km^2)	Total affected area (km^2)
0 m lower	0.52	0.05	1.43	2.01
15 m lower	0.61	0.00	1.04	1.65
30 m lower	0.61	0.00	0.79	1.40

2.4 Discussion

This chapter presents simulations of an avalanche-generated wave, one step in the hazard process chain that could lead to inundation of Huaraz from a GLOF originating at Lake Palcacocha. The lake hydrodynamic model presented here is an advancement beyond what has been previously reported for GLOF hazard process chain simulations. The use of a fully three-dimensional hydrodynamic model for simulating wave generation, propagation, run-up and overtopping of the damming-moraine allows predictive modeling of the process chain through better representation of the physical processes. Other studies (e.g., Schneider et al., 2014) have used a past event to calibrate the models and then used those calibrations for predictive modeling of other scenarios using the two-dimensional shallow water equations (SWE). When data for past events are not available, the three-dimensional model can help overcome the limitations of two-dimensional SWE models. Better representation of the physical processes in the model (i.e., three-dimensional non-hydrostatic) makes the models useful for predictive purposes without a heavy reliance on calibration. Modeling for predictive purposes, such as that presented in here, is useful for analyzing potential GLOF impacts and mitigation strategies.

The general lack of field data regarding actual GLOF events leads to many unknowns about the processes, particularly processes related to avalanches, lake dynamics and moraine erosion. Previous simulations of GLOFs have focused on calibrating upper-watershed processes based on post-event observations (Schneider et al., 2014), but there is very little information on avalanche characteristics or magnitude of avalanche-generated waves (Kafle et al., 2016) on which to base validation of these simulated processes. For that reason, it is necessary to represent these processes more fully in simulations and minimize the approximations used in modeling. In this work, this is partially achieved through the use of three-dimensional simulations of lake dynamics.

To complement this work on three-dimensional lake modeling, another researcher in the group has run some two-dimensional SWE simulations with the BASEMENT model to determine if three-dimensional models are necessary for simulation of the wave dynamics in a dynamic erosion model of the lake-damming moraine (Somos-Valenzuela et al., 2016). Comparison of the results from a two-dimensional SWE model (BASEMENT) with the results presented here (FLOW-3D) indicate that the SWE approximation is not adequate to simulate waves generated by avalanches because of the large energy dissipation due to significant vertical accelerations (Somos-Valenzuela et al., 2016). The results from the BASEMENT simulations suggest that, without careful setting and adjustment of the model's boundary conditions, two-dimensional models might produce unrealistic results for wave driven phenomena that underestimate the magnitude of an event. Reference simulations, like those from three-dimensional hydrodynamic models, may help to overcome limitations of the two-dimensional models and turn them into more flexible and efficient tools for erosion and breach failure assessment (Somos-Valenzuela et al., 2016).

The characteristics of the wave as it propagates across the lake are significant indicators of the magnitude of the event that is being simulated. The wave heights are quite large (up to almost 50 m tall), especially when compared with the initial depths of the lake that range from 72 m to less than 10 m. Such large waves as compared to the lake depths indicate that vertical accelerations are likely to be significant enough that they should not be neglected; this hypothesis is validated by the simulations in BASEMENT that show that 2D SWE simulations are not adequate for this type of application (Somos-Valenzuela et al., 2016).

Another approach to using calibration to compensate for the limitations of 2D SWE models could be to use an empirical method for calculating wave characteristics, such as the Heller and Hager (2010) method, and then to use the wave characteristics to calibrate the hydrodynamic model so that the 2D SWE model more closely reflects the wave characteristics just before run-up, giving better overtopping results. To assess the potential for applying this type of approach if a fully three-dimensional model cannot be applied, the wave heights from the FLOW-3D simulations have been compared with the wave heights calculated with the Heller and Hager method. For the large avalanche scenario, both the avalanche source and mass-momentum source boundary conditions result in wave heights that are only 4.4-5.8 m higher than the wave height predicted by the empirical method. However, it is worth noting that the maximum wave height for the large avalanche source model occurs when the wave reaches the shallow portion of the lake and begins the run-up process, and the first wave peak in the deep portion of the lake is even closer to the height predicted by the Heller and Hager equations. The large differences between the empirical method and FLOW-3D wave heights for the medium and small scenarios may be due more to the shortcomings of the avalanche source model (as discussed in Section 2.2.2), and with the information available, it is difficult to say

which method is more accurate in predicting maximum wave heights. Nevertheless, the relatively close agreement between the empirical and hydrodynamic models for the large avalanche scenario indicates that the approach to using the empirical method as a calibration tool may be promising. However, 2D SWE models are still overly dissipative during the propagation and run-up phases, so the points of comparison between the hydrodynamic model and empirical equations should be chosen carefully if this tactic is to be employed. Further work is needed to thoroughly evaluate the feasibility of this type of modeling approach.

The primary limitation of the lake hydrodynamic model arises from representing an avalanche entering the lake as a volume of water, rather than a combination of rock, ice and snow (Kafle et al., 2016). The wave model calibration method involves controlling the height (above the lake) and depth of the release area in order to influence the fluid depth and velocity in the model as the avalanche enters the lake. This helps to overcome the limitations of substituting water for the avalanche fluid mixture, but the water representation does not dissipate the energy in the same way as the true avalanche mixture, and the mixing of the avalanche fluid with the lake is not accurately represented in the model. In addition, it is impossible to completely replicate the avalanche characteristics in the lake hydrodynamic model in this way, and there are significant differences in the inflow hydrographs of the RAMMS avalanche model (similar to the mass-momentum source) and the avalanche source model in FLOW-3D. The discrepancies between the avalanche source and mass-momentum source models are more pronounced for the smaller scenarios, but there is no obvious solution to overcome this difficulty in the avalanche source model.

Of all the sources of uncertainty in the lake model at Palcacocha (excluding uncertainties in other steps in the GLOF process chain that are not presented here), the

greatest uncertainty arises from the wave generation. Uncertainties due to the turbulence model and grid size are not negligible; but compared to the magnitude of uncertainty from the wave generation, these other sources of uncertainty are relatively insignificant. One way to attempt to portray the uncertainty in the wave generation is by using more than one method for representing the impact of the avalanche with the lake (the two methods for modeling the boundary conditions). Without any in-situ data from real events, it is impossible to quantify exactly the level of uncertainty, but given the range of overtopping flows and volumes from the two boundary condition methods, the uncertainty is considerable. Although there is no way to validate the results and say which type of boundary condition is more representative of the actual conditions likely to arise in an avalanche-triggered GLOF, it is possible that the avalanche sources are overestimating the momentum transfer while the mass-momentum sources are likely underestimating it. As discussed in the results section, the avalanche source could represent an upper bound for the simulation results while the mass-momentum source may be closer to a lower bound.

An important issue to consider when assessing the uncertainty of the model results is how this uncertainty should be conveyed and represented in the decision-making process. For GLOF hazards, worst-case scenarios should be presented so that the potential hazard is amply conveyed to the local populations and governing bodies. However, the results presented in this context should not be overly conservative to the point that they are unrealistic because it may cause people to take actions that are not cost-effective or to discount the results entirely because they are not satisfactorily representing the real hazard. In light of this, it is recommended to use the results from the large avalanche source simulations as the worst-case scenario. Given the significant differences between the small and medium avalanche source and mass-momentum source

simulations, results from both boundary condition methods should be provided for the small and medium avalanche scenarios if these scenarios and their likelihoods will be used in an economic or risk and vulnerability analysis of the mitigation alternatives.

Considering the lake-lowering scenarios, the only "safe" scenarios according to the minimum overtopping volume criterion (25,000 m^3) are the medium mass-momentum source with 30 m lowering, the small avalanche source with 15 m or 30 m lowering, and the small mass-momentum source for any lake level. All large avalanche scenarios and most of the medium scenarios resulted in significant overtopping, even with lake lowering. However, the definition of a "safe" scenario used here is not fully indicative of the effect of lake-lowering on hazard mitigation. For example, lake-lowering for the medium avalanche scenario can reduce the inundated area as well as the flood intensity level for the areas that are affected. This is significant because small and medium avalanches are much more likely than larger avalanches, so the real impact of lake-lowering given the probability of occurrence of these events may be greater than is immediately apparent. For the large avalanche scenario, while lowering the lake by 30 m only slightly reduces the inundated area, many areas that were previously in the high-intensity zone revert to the medium or low-intensity zones. It is clear that lowering the lake level can reduce flood intensities and hazard levels, but from the modeling results alone it is not possible to determine the optimum lake level. Further economic and vulnerability analyses are necessary to recommend an ideal mitigation alternative.

Finally, it must be noted that the work presented in this chapter focuses exclusively on the lake hydrodynamics and does not consider the question of dynamic erosion of the terminal moraine due to overtopping flows. The potential erosion of the terminal moraine is an important factor to consider when assessing the hazard level of any lake with a moraine dam. For Lake Palcacocha, this was assessed through a separate

hydromorphodynamic model run in BASEMENT, and the conclusion was that despite significant potential for erosion, the moraine is unlikely to fail completely (a complete failure is defined as a breach of the moraine opening a direct drainage channel with the lake) (Somos-Valenzuela et al., 2016). Simulations of erosion of the lake-damming moraine are much more computationally intensive than purely hydrodynamic simulations of the lake and are much more efficient with 2D SWE models than with three-dimensional non-hydrostatic models. Three-dimensional simulations of the lake hydrodynamics, such as the work presented in this chapter, can help advance our understanding of how avalanche-induced waves behave in the lake. The wave characteristics observed in 3D simulations can be used to calibrate 2D models of moraine erosion, as described in Somos-Valenzuela et al. (2016). This work provides a significant advancement in the area of lake modeling for GLOF hazard assessment with 3D non-hydrostatic simulations of avalanche-induced waves looking at multiple methods for representing wave generation.

Chapter 3: Hazard Assessment of an Emerging Lake at Artesonraju

This chapter explores the potential future hazard of an emerging lake at Artesonraju Glacier. Climate change is intrinsically a non-stationary process, so a forward-thinking approach to mitigating the impacts and hazards related to climate change should consider future conditions in addition to known current hazards. The Artesonraju Glacier, with an emerging lake at its terminus, is an ideal case study to look at how the hazard level might change in the future as the lake grows. This chapter seeks to address Research Question #3:

Research Question #3: What will emerging glacial lakes look like in the future, and how can we determine the level of hazard that they may pose?

This research question relates to the emergence and growth of glacial lakes and assessment of the evolving lake conditions and hazard levels. Because the lake at Artesonraju is just beginning to form, it presents an opportunity to make hypotheses about lake evolution and potential future impacts of climate change on glacial hazards. Within the context of climate resilient development and decision making in Peru, the motivation for looking ahead towards future hazard conditions rather than focusing exclusively on present conditions is to encourage decision makers to view climate change-related hazards as dynamic processes. Just because a hazard has been assessed at one point in time does not mean that the hazard level will always remain the same.

This chapter also presents simple analysis tools that can be used to build local capacity for GLOF hazard assessment in Peru. This objective motivates us to seek simple methodologies that are not overly difficult to employ yet are robust enough to produce

results that can be relied upon for decision-making purposes. With this objective in mind, the methods presented in this chapter use existing technologies, such as ground penetrating radar, in new ways. New methods of analysis have also been developed to meet the need for simple analysis tools where no existing method is sufficient. Before embarking on an in-depth assessment of GLOF hazards and their potential impacts (such as the study at Lake Palcacocha presented in Chapter 2), it is often expedient to determine if a lake is likely to produce a GLOF that could affect populated areas. The methods presented in this chapter provide a first-order hazard assessment to replace in-depth modeling studies when approximations of GLOF hazards are acceptable. This is a first step towards the primary objective of Part II of this dissertation: linking scientific research with practical applications for decision makers. With these simple analysis tools developed to build local capacity to evaluate GLOF hazards, we are not proposing to develop high-level modeling capabilities, but rather simpler approaches that can be a reasonable first order proxy for high-level modeling studies. Artesonraju is an ideal site to study a changing hazard environment and apply innovative methodologies to predict future hazard levels and seek adaptation solutions before the lake becomes dangerous.

Artesonraju is an interesting site with many characteristics that provide fodder for future research work. In addition to the interest in the emerging lake, Artesonraju is part of a series of glacial lakes. This work focuses on the upper watershed (the glacier and emerging lake). Although the scope of this work is limited to analysis of the emerging lake and the potential future conditions, there are many opportunities to continue this work at Artesonraju and further our understanding of the behavior of GLOF processes.

3.1 BACKGROUND

3.1.1 Emerging Lake at Artesonraju Glacier

Artesonraju Glacier is located in the Cordillera Blanca in the Paron watershed above the city of Caraz (Figure 3.1). The glacier ranges in elevation from 4684 to 5176 m amsl (above mean sea level) and spans an area of approximately 5.4 km^2 (Racoviteanu, 2007) (see Figure 3.2 for a map of the key features of the glacier). Snow and ice accumulate in the steeply sloped upper portions of the glacier. The tongue of the glacier is less steeply sloped and covers an area of approximately 0.5 km^2. The glacier has a northward facing aspect, which means that because of its location in the Southern Hemisphere it receives more direct solar radiation. Artesonraju Glacier has a small emerging lake at its terminus that may become dangerous as the lake approaches its full extent.

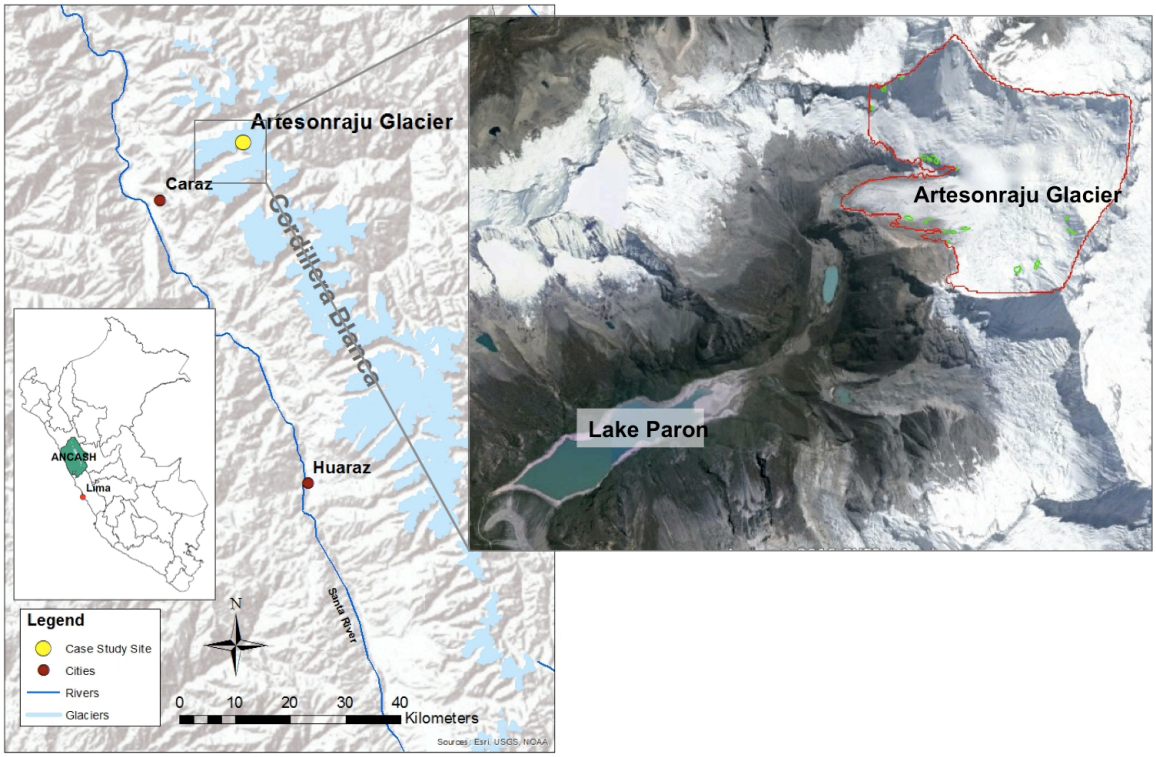

Figure 3.1- Location of Artesonraju Glacier in the Cordillera Blanca, Peru (inset background image from Google, 2013; glacier outline from Racoviteanu, 2007)

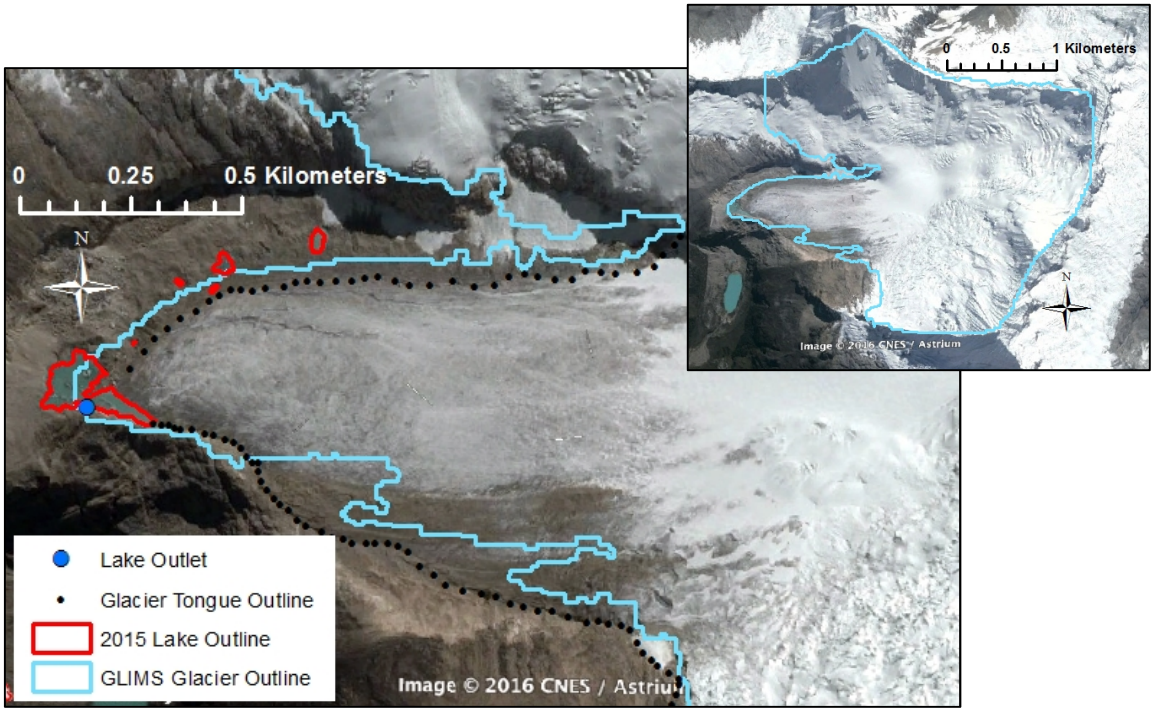

Figure 3.2- Artesonraju Glacier tongue with an inset showing the GLIMS outline for the whole glacier in the top right corner (images from Google, 2013; glacier outline from Racoviteanu, 2007)

A small lake began to form at the terminus of Artesonraju Glacier around 2003 and continues to grow as the glacier retreats. This lake is part of a system of three glacial lakes that includes Lake Paron, the largest glacial lake in the Cordillera Blanca, and Lake Artesoncocha, that has been known to produce outburst floods in the past (Lliboutry et al., 1977a) (see Figure 3.3). The discharge from the emerging lake at Artesonraju flows through Lake Artesoncocha and Lake Paron before discharging into the Paron River. If a GLOF were to occur at the emerging lake at Artesonraju Glacier, it would have to pass through this series of lakes (Lake Artesoncocha and Lake Paron) before reaching populated areas. The Paron River flows through a relatively steep canyon and eventually becomes the River Llullan that flows through the city of Caraz, approximately 15 km

from Lake Paron. A drainage system has been installed in Lake Paron now that controls the lake level to reduce the risk of flooding, but the operation of this drainage system does not take into account any changes that may happen in the upper lakes as a result of the retreat of Artesonraju Glacier. The drainage system at Lake Paron has been a source of controversy, and local communities took over control of the lake and operation of the drainage system in 2007. Since that time, the communities have been reluctant to relinquish control of the system and have at times allowed the lake level to exceed the level that was considered safe when the system was designed (Carey et al., 2012). If it is ultimately determined that the growth of the lake at Artesonraju may cause a GLOF that could produce discharge from Lake Paron, the topic must be approached very carefully with the local communities to explain the potential risk and the need to lower the lake level.

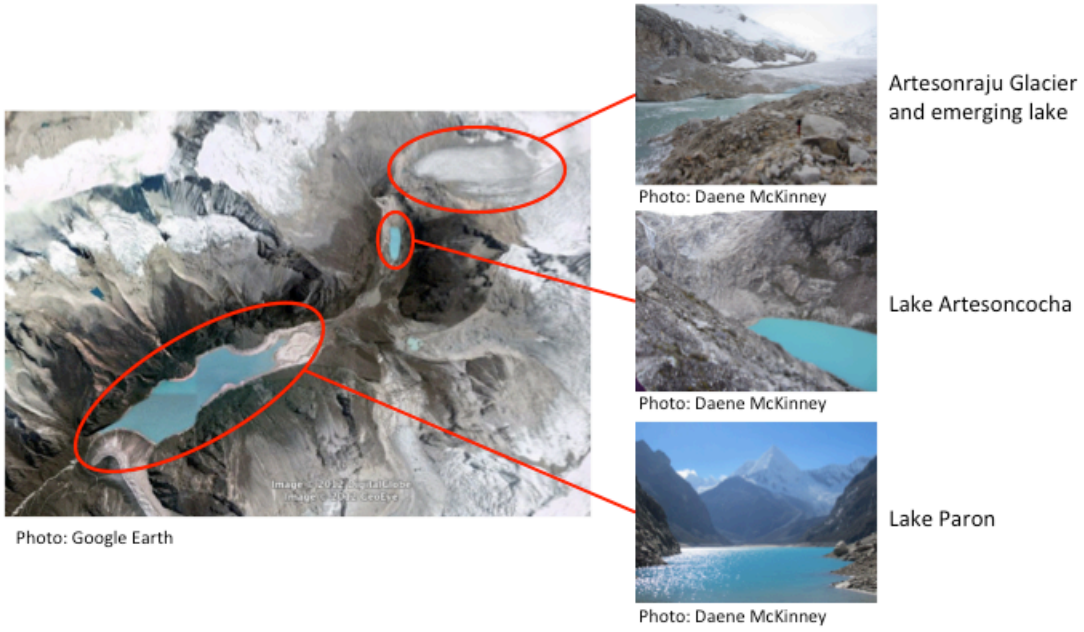

Figure 3.3- The glacial lake system of Artesonraju Glacier, Lake Artesoncocha, and Lake Paron

Since the emerging lake at Artesonraju began to form around 2003, it has continued to grow as the glacier retreats. The progressive evolution of the lake can be seen in Figure 3.4, showing the lake outlines in different years, and the surface areas are given in Table 3.1. Figure 3.4 shows that the lake began to form in the southwest corner of the glacier tongue and is expanding to the northeast. Although most of the Artesonraju Glacier is clean ice, there are portions near the glacier boundary that have a layer of debris on top of the ice, and much of the southern boundary of the glacier extending towards the accumulation zone appears to have characteristics of rock glaciers. The debris layer appears to influence the formation of melt ponds and the expansion of the lake. In addition to the main body of water comprising the emerging lake, small melt ponds have formed on top of the debris layer at different points in time. A melt pond appeared near the lake to the north sometime before 2012 and continued to grow (the

larger outline of this melt pond in 2013 can be seen in Figure 3.4) until it eventually coalesced into the main lake by 2015. Although this pond has joined with the main lake, there are still islands of debris and ice in the lake that are remnants of the debris-covered ice that once separated this melt pond from the lake (see Figure 3.5). The smaller melt ponds that have formed on top of the debris extend away from the lake towards the north along the edge of the glacier tongue. Many of these melt ponds seem to be transient. The precise locations of these melt ponds appear to change from year to year, as some have appeared in the images for certain years but disappeared again in subsequent years. The drainage point for the lake is on the southern boundary (Figure 3.2). The lake outlet was previously farther west (when the lake first began to form) until the lake grew to reach the current outlet point. The lake outlet seems to have remained the same since at least 2010. Although there has been northward expansion into areas with debris-covered ice, the more rapid direction of expansion appears to be towards the east. In this direction, the glacier ice near the lake is heavily crevassed (Figure 3.6). There is also overhanging ice from the glacier tongue (Figure 3.7), and the ice appears to be gradually calving into the lake, thus promoting lake expansion into the glacier tongue in the direction of the accumulation zone.

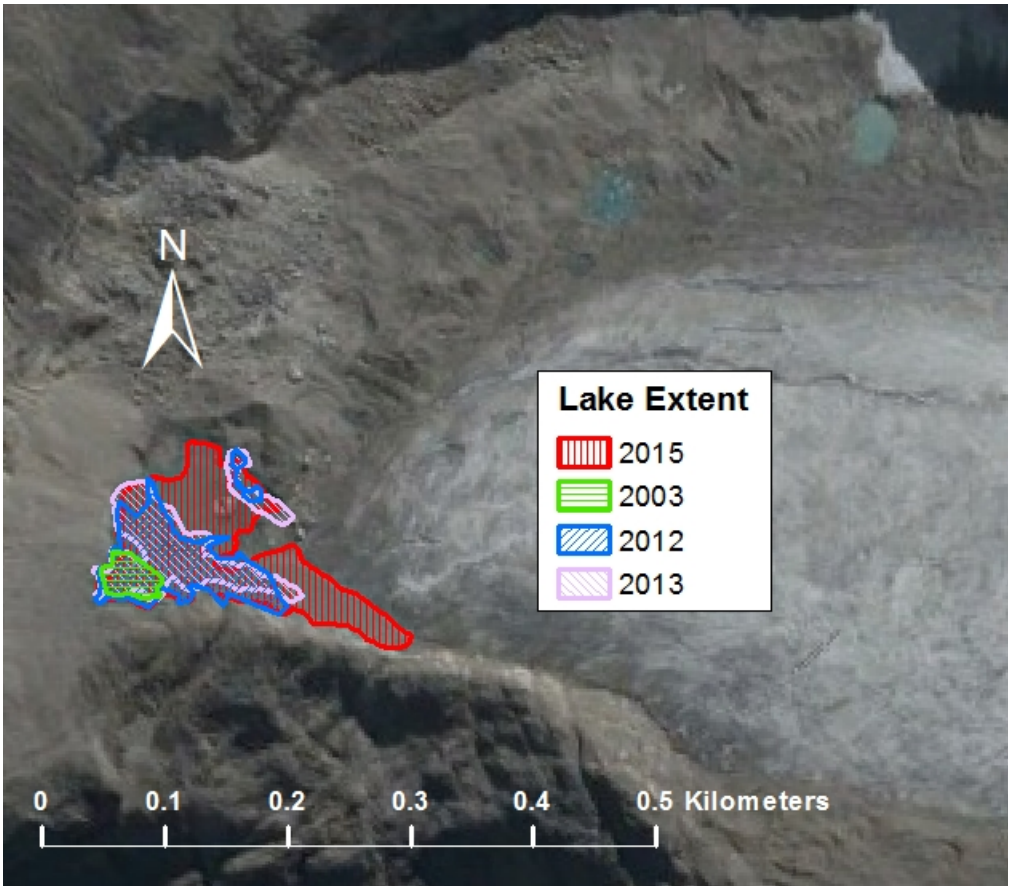

Figure 3.4- Outlines of the emerging lake at Artesonraju at four different points in time showing the lake growth and the formation of melt ponds through time. Outlines of the lake and melt ponds were delineated from Google Earth images (background image from Google, 2013).

Table 3.1- Approximate surface area of the emerging lake at Artesonraju Glacier at four different points in time

Year	Surface Area of the Emerging Lake (m^2)
2003	1305
2012	7,425
2013	7,453
2015	16,116

Figure 3.5- Debris covered ice to the north of the emerging lake and island boulders and debris in the middle of the lake at Artesonraju

Figure 3.6- Crevasses in the ice of the glacier tongue near the emerging lake at Artesonraju

Figure 3.7- Overhanging ice that appears to be calving into the emerging lake at Artesonraju. The clean ice along the vertical faces is an indicator that this overhanging ice is a calving front

3.1.2 Literature Review

Glacial Lake Formation and Future Lake Projections

During the Little Ice Age (LIA), many of the world's glaciers were advancing (Grove, 1979; Matthes, 1939). Since the LIA ended around the end of the 19th century, most glaciers have been retreating, causing the formation of many glacial lakes (Costa and Schuster, 1988). Most of the glacial lakes in the Cordillera Blanca, Peru are moraine-dammed lakes. This type of lake typically forms in overdeepenings in glacier beds as glaciers retreat after colder climatic periods (e.g., the LIA) and leave behind end

moraines that retain water (Clague and Evans, 1994a; 1994b; Costa and Schuster, 1988; Frey et al., 2010; Haeberli and Linsbauer, 2013). Debris-covered glaciers can have a slightly different mechanism of formation, as it is common for supraglacial melt ponds to form when the surface slope is small (<2˚), and the ponds gradually grow and coalesce into a glacial lake (Reynolds, 2000; Watanabe et al., 1994; Watanabe et al., 2009; Quincey et al., 2007). Large-scale models of future glacial retreat (e.g., Paul et al., 2007; Linsbauer et al., 2013) and methods for modeling bedrock topography and ice thickness (e.g., Farinotti et al., 2009; Linsbauer et al., 2009; Linsbauer et al., 2012) may be used to predict where future glacial lakes might form (e.g., Frey et al., 2010; Haeberli and Linsbauer, 2013). There are three key indicators of overdeepenings in the glacier bed: 1) abrupt transitions between steeply sloped area to areas with low slopes just below, 2) heavily crevassed areas immediately below areas with minimal crevassing, and 3) narrowing of the glacier as it flows downstream (Frey et al., 2010; Haeberli and Hohmann, 2008). Frey et al. (2010) propose a multi-level strategy with four steps of analysis for identifying overdeepened portions of glaciers where lakes may form. Frey et al. (2010) focus on the first two steps: identifying low-slope portions of glaciers from surface DEMs and identifying locations with overdeepening characteristics from satellite imagery. The third step involves more precise definitions of likely overdeepening locations from models of ice thickness such as the GlabTop model of Linsbauer et al. (2012); lake volumes can be estimated in this step, but these estimates carry a lot of uncertainty (Frey et al., 2010). In the final step of analysis, Frey et al. (2010) recommend using in-situ data collection (e.g. geophysical surveys or drillings) to confirm overdeepenings in the bedrock and get more precise estimates of future lake volumes, but this final step was not implemented in their study. GLOF hazards are influenced by rapidly changing glacial conditions, and there have been many calls for predictive

assessment of future lake conditions and potential GLOF hazard (Frey et al., 2010; Haeberli and Hohmann, 2008; Haeberli et al., 2010). So far, few studies have attempted to simulate future GLOFs, and most have focused on simulating downstream debris flow based on rough estimates of lake locations (Frey et al., 2010; Nussbaumer et al., 2014). Studies such as Frey et al. (2010) and Nussbaumer et al. (2014) can be helpful for determining if there is any possible threat to populated areas downstream but forgo assessment of the upper watershed processes that may help to determine if a GLOF is likely to happen in the first place.

Ground Penetrating Radar

Ground Penetrating Radar (GPR) is often used to characterize sub-surface features through the detection of electromagnetic radiation that is reflected at the interface between different materials below the surface. GPR has been used for a wide variety of applications ranging from the measurement of ice sheet thicknesses in Greenland and Antarctica (for which the technique was first developed in the 1950's) to groundwater detection in ice-free zones (Woodward and Burke, 2007; Reynolds, 2011). In Peru, Silva et al. (2010) used GPR to explore the composition of the moraine at Lake Palcacocha. While the technique has often been used in glaciological applications, it has rarely been applied to tropical glaciers. Peduzzi et al. (2010) and Salzmann et al. (2013) have used GPR to measure ice thickness of glaciers in Southern Peru, and Ramirez et al. (2001) have done the same in Bolivia.

Ice thickness values extracted from GPR measurements can be extrapolated to create three-dimensional maps of the glacier bedrock topography (e.g., Binder et al., 2009; Fischer, 2009; Fischer and Kuhn, 2013; Paul and Linsbauer, 2012; Saintenoy et al.,

2013; Ramirez et al., 2001). This is typically done through interpolation techniques that assume a null ice thickness at the glacier boundary (Fischer, 2009; Saintenoy et al., 2013). The most common interpolation methods are Kriging (Ramirez et al., 2001; Binder et al., 2009; Saintenoy et al., 2013) and the Topo2Raster tool in ArcGIS (Fischer, 2009; Fischer and Kuhn, 2013). Errors can result from GPR ice thickness measurements and interpolation of GPR data that are difficult to quantify. Many studies assume an error of 5% for GPR measurements of ice thickness (Gartner-Roer et al., 2014; Haeberli and Fisch, 1984; Yde et al., 2014; Fischer, 2009), but this error can be higher when there is not a clear basal reflection (Yde et al., 2014). In a detailed uncertainty analysis, Saintenoy et al. (2013) found that the total relative error was 11.9% of the ice volume, and errors from the ice velocity and use of non-migrated data were, respectively, 1.2% and 1.1% of the ice volume. The greatest errors in glacial bedrock maps interpolated from GPR measurements are in locations without ice thickness measurements (Fischer and Kuhn, 2013; Saintenoy et al., 2013).

The velocity of radar in glacier ice is used to convert the two-way travel times from GPR measurements to ice thicknesses. Many studies use a constant ice velocity, based on the assumption that the medium is homogeneous and isotropic. The ice velocity most commonly used for tropical glaciers is 0.16 m/ns (Peduzzi et al., 2010; Ramirez et al., 2001). The ice velocity can be more precisely determined for a particular site with a common midpoint (CMP) survey (Reynolds, 2011). Dix (1955) presents conceptual ideas used in CMP surveys and equations for calculating velocities. Neidell and Taner (1971) introduce the concepts of semblance and other coherence measures for determining radar velocities. Eisen et al. (2002) validate the CMP method by comparing it to dielectric profiling of ice cores; they find velocity differences between the two methods to be 2-8%. Methods for estimating errors in CMP velocities can include coherence analysis, Monte

Carlo simulation, and backshifting to account for wavelet bias (Barrett et al., 2007; Booth et al., 2010; Booth et al., 2011).

Tsunami Runup Models

An overview of the literature on avalanche or landslide-generated waves is given in Chapter 2 (Section 2.1.2), and the summary of previous work that is presented here focuses on research related to runup of tsunami waves with the intention of applying some of these principles to modeling the runup of avalanche-generated waves. Much research has been done in the field of tsunami wave runup. Early numerical simulations primarily used the Boussinesq equations (e.g., Pederson and Gjevik, 1983; Zelt, 1986; Kim et al., 1983; Hibberd and Peregrine, 1979; Heitner, 1969; Zelt, 1991; Shuto, 1972; Goto and Shuto, 1978; Goto, 1979; Goto, 1974; Liu et al., 1995). Other early research in tsunami runup focused on empirical runup relationships (e.g., Hall and Watts, 1953; Camfield and Street, 1969; Kishi and Saeki, 1966) and solitary wave theory (Stoker, 1957; Synolakis 1987; Synolakis 1990). Some tsunami models have simulated propagation and runup separately due to the large differences in scale during these processes (e.g., Kowalik, 2003). Recent computational advancements have allowed for more sophisticated numerical models to simulate tsunami propagation and runup. Behrens and Dias (2015) provide a good review of current tsunami modeling methods. Finite difference models (e.g., Titov and Gonzalez, 1997; Imamura et al., 2006) and finite volume models (e.g., Dutykh et al., 2011; George and LeVeque, 2006; LeVeque et al., 2011) have often been used for tsunami simulations. More general computational software such as Delft3D (Delft3D, 2014), OpenFOAM (OpenFOAM, 2016), and the Smoothed Particle Hydrodynamics (SPH) model (St-Germain et al., 2012; Xie et al.,

2012) can also be used to simulate tsunami impact (Behrens and Dias, 2015). Models of tsunami runup are now often used for hazard assessment and early warning (e.g., Behrens, 2010; Synolakis et al., 2008).

The motivation for considering tsunami runup literature in the context of GLOF hazard assessment is driven by the need for a simpler method for representing the wave dynamics within GLOF process chain modeling. It has been shown that 2D SWE models are insufficient for simulating avalanche-generated impulse waves (Heinrich, 1992; Zweifel et al., 2006; Somos-Valenzuela et al., 2016). Therefore, solitary wave theory and analytical approaches to tsunami runup have been explored as a possible substitute to approximate the results that might be expected from 3D hydrodynamic simulations of avalanche-generated wave overtopping. A good introduction to solitary wave theory can be found in Stoker (1957). Synolakis (1987) presented the first mathematical representation that adequately describes tsunami runup. Synolakis (1987) looked at both linear and non-linear theory of solitary waves and established a runup law and breaking criterion; the results were used to explain existing empirical relationships. Synolakis (1990) used results from laboratory and numerical simulations to demonstrate that linear theory is adequate for predicting maximum runup. Pelinovsky and Mazova (1991) also looked at analytical runup calculations, using them to identify control parameters that most influence wave characteristics. Pelinovsky and Mazova (1991) present non-dimensional runup calculations on various geometries, including runup on a vertical wall (an application that could be useful when assessing overtopping on various geometries for reinforced dam structures).

Previous Studies at Artesonraju Glacier and the Artesoncocha Watershed

There have been a number of previous studies at Artesonraju Glacier and the watershed below. Artesonraju is one of the more frequently studied sites in the Cordillera Blanca, and the Glaciology Unit of Peru's National Water Authority (UGRH, according to the initials in Spanish) has been monitoring the mass balance of this glacier for a number of years. Kaser and Osmaston (2002) show the retreat of Artesonraju Glacier from 1932-1994 and the formation of Lake Artesoncocha. Lliboutry et al. (1977a) describe two GLOF events at Lake Artesoncocha in 1951. A large icefall caused an initial breach of the moraine dam, lowering the moraine by 7 m, and resulting in a discharge of 1.13 million m^3. This discharge raised the water level in Lake Paron by 0.7 m. Three months later, progressive erosion of the terminal moraine at Lake Artesoncocha caused a second breach, releasing 3.52 million m^3 of water and raising the water level in Lake Paron by 2 m. Downstream flooding from this event was only avoided because it occurred during the dry season when the water level of Lake Paron was lower than normal. Lliboutry et al. (1997a) recommended a permanent system to lower the lake level by digging a tunnel. This work was later implemented and still controls the water level of Lake Paron. Lliboutry (1977b) describes the lake-damming terminal moraine at Lake Paron and the tongue of the Hatunraju Glacier that feeds this moraine, including descriptions of the ice mechanics and the structure of the glacier tongue, as determined by geophysical surveys.

Other research activities at this study location have focused on the Artesonraju Glacier. Pouyaud et al. (2005) and Juen (2006) used melt models and GCM projections to determine past and future streamflow contributions from glacial runoff. Suarez et al. (2008) modeled the water balance in the Paron basin and used local measurements at the glacier to calibrate the model. Moelg et al. (2009) and Winkler et al. (2009) investigated

the energy balance at Artesonraju Glacier using in-situ weather station and sublimation measurements. Hofer et al. (2010) proposed statistical methods for downscaling reanalysis weather data based on in-situ measurements at Artesonraju. Rabatel et al. (2012) showed from mass balance measurements at Artesonraju Glacier that the equilibrium line altitude for tropical glaciers can be reasonably approximated by the snow line during the dry season. Although a number of studies have looked at detailed short-term records of meteorological variables and mass balance, none of these studies (not even the mass-balance studies) have investigated mass balance as it relates to the rate of retreat of the glacier and growth of the emerging lake. Thus, the rate of retreat of Artesonraju Glacier is still unknown, and there are no existing projections for how quickly the emerging lake may grow.

3.2 METHODS

The emerging lake at the base of Artesonraju Glacier provides a unique opportunity to study the growth of the lake, make predictions about future growth, and see how projected lake evolution may impact the level of GLOF hazard. The first step in answering Research Question #3 was to determine the future extent of the emerging lake when it is fully formed. There are two underlying questions related to the growth of the emerging glacial lake and its potential hazard level that must be answered:

- What are the likely physical characteristics of the fully formed lake?
- If an outburst flood occurs at the fully formed lake, is it likely to produce a significant flood volume?

The first question is addressed in Sections 3.2.1 and 3.2.2. These sections focus on methods to characterize the volume and spatial extent of the lake. GPR measurements

of ice thickness were used to create a three-dimensional bedrock topography that was converted into the lakebed for the fully formed lake. The second question is addressed with the methods presented in Section 3.2.3, exploring ways to approximate the processes in the likely chain of events for an avalanche-triggered GLOF at Artesonraju and methodologies for characterizing potential avalanche-generated waves and their capacity for overtopping. For the purpose of this study, a significant overtopping volume has been defined as a volume equivalent to the overtopping volumes for the simulations of the current lake level scenarios at Lake Palcacocha (Section 2.3.4). This analysis did not include a full hazard assessment but was limited to the upper watershed. The methods presented in Section 3.2.3 were developed with the objective of approximating potential flood volumes that could be discharged at the lake outlet by an overtopping wave.

3.2.1 Ground Penetrating Radar

Determining the physical characteristics of the fully formed lake requires information about the topography of the glacial bedrock, glacier surface, and surrounding terrain. Ground penetrating radar (GPR) was used to measure ice thicknesses for the Artesonraju Glacier. GPR surveys in three separate years have been performed on the glacier's tongue with some transects extending into the accumulation area of the glacier. A common midpoint survey was performed to determine the radar velocity in the ice at Artesonraju Glacier. The bedrock elevations extracted from the GPR results were used as inputs to the interpolation presented in Section 3.2.2.

Equipment

Two different common-offset GPR units were used in the surveys of Artesonraju Glacier. The GPR unit owned by the University of Texas at Austin is a custom-built portable backpack unit that is described in Catania et al. (2010); this unit is henceforth referred to as the UT GPR unit. The UT GPR unit consists of a Kentech Instruments transmitter emitting a 4kV signal, a receiver that amplifies the reflected signal, a National Instruments USB-5133 digitizer, and a GPS receiver to measure geographic coordinates and surface elevations. 10 MHz antennae were connected to the transmitter and receiver with a separation distance of 25 m. A LabView program was used to log the GPR and GPS signals in a field computer. The GPR traces were stacked by computing an average waveform for every 512 traces, and the time, latitude, longitude, and elevation were recorded for every waveform. The second GPR unit is owned by the Glaciology and Water Resources Unit of Peru's National Water Authority (UGRH according to the initials in Spanish) and is henceforth referred to as the UGRH GPR unit. The UGRH GPR system is a commercially available Radar HF unit made by Unmanned Industrial that was operated with 10 MHz antennae at a separation distance of 15 m. The UGRH GPR unit emits a 900 V signal at a pulse rate of 1000 pps and has integrated GPS in both the transmitter and receiver. The receiver is connected to a hand-held computer device that controls the GPR and allows for visualization of the traces as they are being recorded.

With both GPR units, radar signals were transmitted and detected continuously at regular intervals as operators walked with the GPR system across the surface of the glacier. The antennae were connected to ropes to ensure that constant spacing was maintained. A minimum of three people were required to operate the GPS systems: one each to carry the transmitter and receiver, and a third person to carry the leading edge of

the transmitting antenna to ensure that it was fully extended (Figure 3.8). The leading edge of the receiving antenna was tied to the rope connecting the transmitter and receiver to ensure full extension.

Figure 3.8- UT GPR unit being deployed in the field (photo: Daene C. McKinney)

Transects

GPR surveys were undertaken in July 2012, 2013 and 2015. The specific dates and GPR units that were used for each survey are given in Table 3.2. The locations of the transects for each GPR survey are shown in Figure 3.9. All GPR data were measured between approximately 9 AM and 1 PM, so the ice conditions may be considered to be similar for all traces recorded; this justifies the use of a constant radar velocity for the glacier ice, as determined by the common midpoint survey.

Table 3.2- Date and equipment used for each GPR survey

Survey Date	**GPR unit(s) used**
July 18, 2012	UT
July 7, 2013	UT and UGRH
July 8, 2013*	UT
July 21, 2015	UGRH
* Common Midpoint Survey	

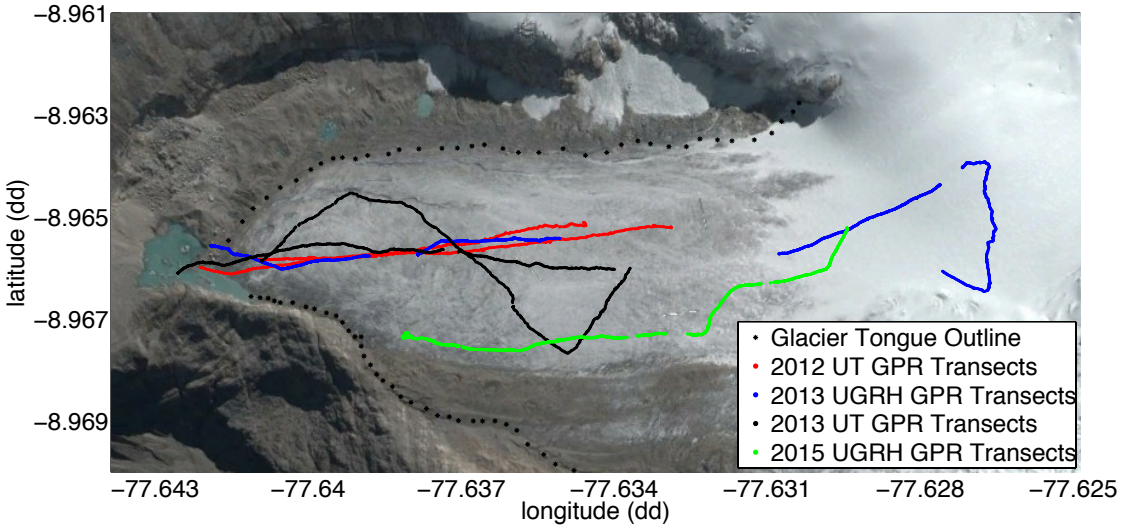

Figure 3.9- Location of transects recorded for each GPR survey (background image from Google, 2013)

Common Midpoint Survey

A common midpoint (CMP) survey was done on July 8, 2013 with the UT GPR unit to determine the radar velocity in the ice at Artesonraju Glacier. For the CMP survey, static measurements were taken with multiple distances of separation between the

transmitter and receiver, each with the same mid-point. For the CMP method, 2 points, P_1 and P_2, are needed with distances from the transmitter to the receiver of d_1 and d_2, respectively (see Figure 3.10 for an idealized sketch of the CMP setup). The vertical distance from the surface to the reflector point is constant, and the velocity in the medium (in this case, ice) is also assumed to be constant. Using the difference in two-way travel times for the signal returned from a common reflector (below the midpoint), the velocity of the radar in ice can be determined as outlined below.

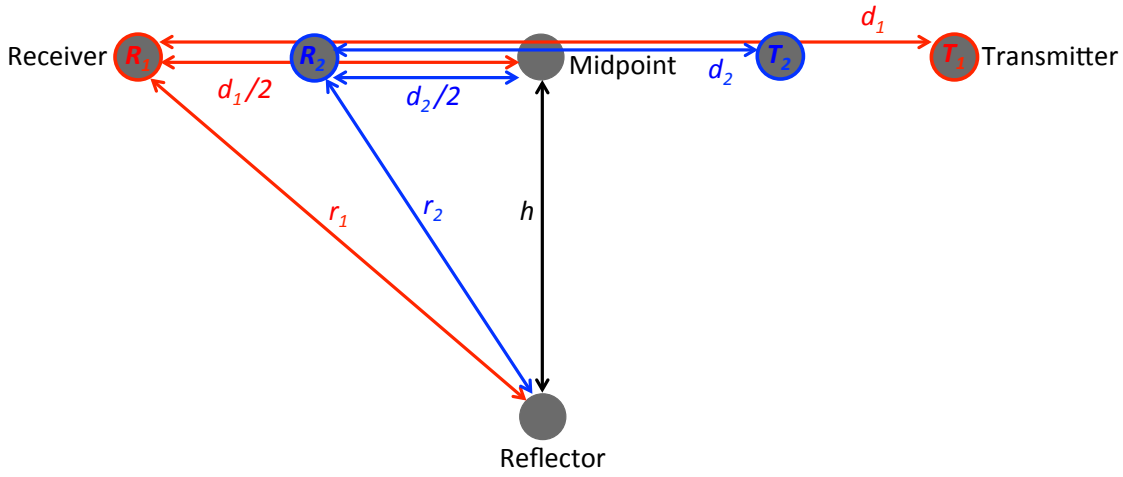

Figure 3.10- Schematic diagram of a common midpoint survey

The distance traveled by the reflected signal (r) is based on the velocity (v) and the two-way travel time (t):

(3.1) $$r = vt$$

Using the above equation and the Pythagorean theorem $\left[r^2 = (vt)^2 = h^2 + \left(d/2\right)^2\right]$, expressions for the depth to the reflector (h) were obtained:

$$h^2 = (vt_1)^2 - \left(d_1/2\right)^2 \tag{3.2}$$

$$h^2 = (vt_2)^2 - \left(d_2/2\right)^2 \tag{3.3}$$

The equations for the depth to the reflector were then combined to get an equation for the ice velocity:

$$v = \sqrt{\frac{\left(d_1/2\right)^2 - \left(d_2/2\right)^2}{(t_1)^2 - (t_2)^2}} \tag{3.4}$$

The CMP survey performed at Artesonraju Glacier used the 10 MHz antennae with separation distances of 20 m and 30 m. The two-way travel times were corrected based on the travel time for the initial airwave, and the resulting signal amplitudes were plotted as a function of two-way travel time. The difference in two-way travel times for the wave peaks corresponding to the reflector point were used to calculate the ice velocity according to equation 3.4.

Processing Steps

The data from the GPR transects were processed in Matlab and converted to Z-scope radargrams using a grayscale to represent the signal intensity. The first processing step was to remove pretrigger noise. With the UT GPR unit, a constant pretrigger cutoff of 5% was used. The pretrigger cutoff for the UGRH unit was not constant (ranging from 4% to 12%) and was determined for each transect by incrementally adjusting the pretrigger cutoff until the airwave signal was removed. Then, the following processing steps were performed: depth strip, demean, detrend, bandpass filter, and normalize by the maximum absolute value. The two-way travel times were converted to depths using an

ice velocity of 154 m/s (determined from the CMP survey). The processed data were plotted in radargrams used to visualize the subsurface.

After the raw GPR data were processed, a Matlab script was used to select points representing the interface between the ice and bedrock. Those points were interpolated to create a smooth line representing the bedrock for each GPR transect. Ice thickness, surface elevation, and bedrock elevation were then calculated at the location of each recorded waveform. Using the geographic coordinates of each waveform, the ice thicknesses and bedrock elevations were mapped and overlaid on a georeferenced satellite image of the glacier (from Google Earth).

3.2.2 Mapping 3D Bedrock Topography and Projecting Future Lake Bathymetry

The result of the GPR measurements was a set of point data of ice thicknesses and bedrock elevations for each transect (Section 3.3.1). These data were then interpolated over the glacier tongue to create a three-dimensional topographic model of the glacial bedrock. This topographic model was used to determine the potential future extent of the lake based on the elevation of the outlet of the emerging lake. Finally, the model of the bedrock topography was converted into a potential bathymetric model of the fully formed lake.

Since there is limited information on the melt rate and rate of retreat of Artesonraju Glacier, a simple assumption has been made that the glacial lake will continue to grow until the lake has reached its largest possible extent based on the bedrock topography. The assumption that there are no constraints on the extent of glacial retreat cannot be categorically validated; however, the current observations of rapid glacial retreat, the historical patterns of formation of other glacial lakes in the region and

the projection of continued warming trends from general circulation models support this assumption.

Bedrock interpolation from GPR traces

The interpolation of the bedrock topography was based on the bedrock elevations extracted from the GPR results as well as points representing the outlines of the glacier tongue and emerging lake. Even though there is ongoing ablation that may affect the ice thicknesses from year to year, the bedrock elevations are expected to remain the same. Therefore, the bedrock elevations measured from the 3 GPR surveys were combined to create a single set of point data representing the glacial bedrock. Surface elevations for points representing the outlines of the lake and tongue were extracted from an Aster GDEM (NASA LP DAAC, 2011) that has a 30 m horizontal resolution and a vertical error of 17 m at the 95% confidence level (Tachikawa et al., 2011). The ice thickness at the edge of the glacier tongue was assumed to be 0 (Fischer, 2009; Saintenoy et al., 2013). Based on this assumption, the bedrock elevations at the points around the glacier tongue were set to be equal to the surface elevation for the points representing the glacier tongue outline. The water depth at the edge of the lake (except at the interface between the lake and glacier ice) was also assumed to be zero; therefore the bedrock elevations at the points representing the lake outline were set to the current water surface elevation (4720 m.a.s.l.). Based on the ice thicknesses observed from the 2012 GPR survey, the bedrock at the location of the current interface between the lake and the glacier is approximately 10 m below the water surface elevation; consequently, bedrock elevations for the points representing the lake outline that correspond to the lake-ice interface were set to 4710 m.a.s.l. The points representing the lake and glacier outlines were combined

with the points from the GPR surveys, resulting in a set of points for which bedrock elevations were known. This set of points (shown in Figure 3.11) was used as an input for the bedrock interpolation.

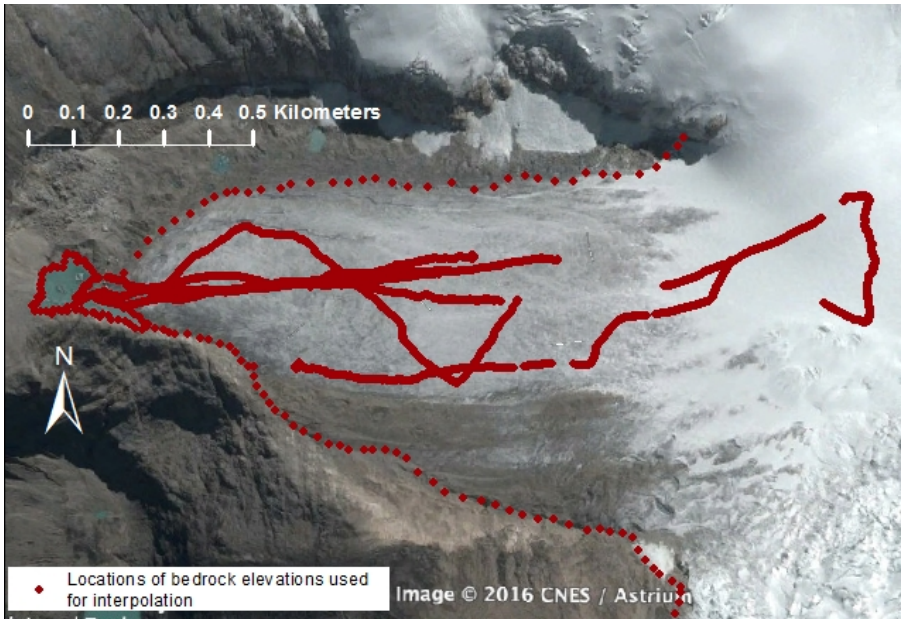

Figure 3.11- Locations of points where bedrock elevation was given as an input for interpolation of the bedrock topography (background image from Google, 2013)

Two different interpolation methods were used to create digital elevation models (DEMs) of the bedrock topography. The first interpolation method used the triscattered interpolation function in Matlab that is based on Delauney triangulation (Mathworks, 2011). The second interpolation method uses the "topo to raster" tool in ArcGIS, a map algebra tool that interpolates raster DEMs from elevation contours or points while maintaining hydrological connectivity (ESRI, 2014). Both interpolations were performed on a grid with a resolution of $3x10^{-5}$ degrees (approximately corresponding 3.3 m at the

location of study). The results of the two interpolation methods were compared by calculating the root mean square of the difference in elevation at each point (RMSD).

Lake Depth and Volume Calculations

The elevation of the current point of discharge for the current lake was used as the starting point for converting the bedrock topography into a model of the fully formed lake. At present, the emerging lake at Artesonraju drains into Lake Artesoncocha about midway along the southern end of the emerging lake (see Figure 3.2). The elevation of this drainage point was approximated from the Aster GDEM[3] (NASA LP DAAC, 2011), and the range of elevations measured at this location with a handheld GPS receiver were used to estimate the uncertainty in the water surface elevation. The water surface elevation derived from the Aster GDEM was determined from the points that correspond to the 2003 lake extent. The Aster GDEM v2 product was released in 2011 (v1 was released in 2009), and so the imagery used to produce the DEM were taken before the lake reached its current extent. Because the precise date of imagery acquisition for the DEM at the location of this study is unknown, it is likely that the more recently formed portions of the lake are represented in the Aster GDEM by the previous elevations of the glacier surface rather than the current water surface elevation. Therefore, the elevation corresponding to the location of the emerging lake at an early point in time (2003) was used to determine the water surface elevation; this resulted in a water surface elevation of 4720 m.a.s.l. The uncertainty in the water surface elevation was estimated with the maximum and minimum elevations measured near the location of the lake outlet from a track taken on July 18, 2012 with a handheld Garmin eTrex Legend HCx GPS receiver

[3] ASTER GDEM is a product of NASA and METI

that has an elevation accuracy of less than 10 m at the 95% confidence level (Garmin, 2007). The minimum and maximum elevations recorded near the lake outlet were 4712.8 m.a.s.l and 4729 m.a.s.l. This range of elevations gives an approximate range of uncertainty for the water surface elevation that was used to delineate the potential extent of the fully formed lake. As there is no point in the lateral moraine along the southern edge of the glacier tongue that is lower in elevation than the current lake outlet, it was assumed that the drainage point for the lake will remain the same as the lake continues to grow.

The future extent of the fully formed lake was considered to be the maximum potential extent of the lake, based on the assumption that the glacier will continue to retreat until the tongue disappears. It was conjectured that the lake growth will be proportionate to the glacier retreat so that any bedrock below the current elevation of the lake outlet that might be exposed by the retreating glacier will be covered by the lake. Therefore, the potential extent of the fully formed lake was defined by delimiting all areas where the interpolated bedrock elevation was below the elevation of the current lake outlet. Two different lake extents and bathymetries were calculated based on the two interpolated bedrock topographies (triscattered and "topo to raster" interpolation). The final estimated volume for the fully formed lake was calculated by averaging the volumes calculated from both interpolation methods with a water surface elevation of 4720 m.a.s.l. Because the RMSD in the interpolated bedrock elevations was significantly less than the GPR error and the error in the Aster GDEM, the interpolation error was ignored when calculating the range of uncertainty in the lake volume.

The bathymetry for the future lake was calculated by subtracting the interpolated bedrock elevation from the water surface elevation for all locations below the current water surface elevation. Finally, the lake volume was calculated by multiplying the area

of each grid cell (10.89 m^2) by the depth for each point of the raster grid within the delimited bounds of the future lake; the volumes for all grid cells inside the limits of the fully formed lake were summed to arrive at a final volume estimate for each interpolation method.

Estimating Uncertainty

The sources of uncertainty in lake volume projections include uncertainties in the GPR measurements, bedrock interpolation, and the water surface elevation used to delineate the lake boundary. As direct measurements (e.g., borehole drillings) are not available at Artesonraju, it is difficult to precisely quantify the uncertainty in the GPR measurements and the bedrock topography interpolated from these measurements. Therefore, comparisons between bedrock elevations at the same location were used to estimate the uncertainties in the GPR measurements and bedrock interpolation. These uncertainties were aggregated to give an overall uncertainty value for each lake definition (given the range of water surface elevations used to define the limits of the lake).

The uncertainty in the GPR measurements of bedrock elevation is influenced primarily by three factors: errors in the GPS, errors in the definition of the ice-bedrock interface, and uncertainty in the ice velocity. Errors in the GPS can include errors in the geographic coordinates as well as errors in the elevation of the glacier surface. GPS systems typically have higher accuracy for geographic coordinates than for elevations, so errors in the elevation of the glacier surface (thus affecting the elevation of the bedrock) are more likely to be of consequence than errors in the latitude or longitude of recorded points. Errors in the definition of the ice-bedrock interface can be the result of

uncertainties related to the resolution of the GPR signal (a function of the antenna frequency) as well as incorrect reading of the radargrams.

Following the example of Saintenoy et al. (2013), the errors in the GPR measurement, including errors in the GPS and bedrock delineation, were quantified by comparing points from intersecting transects that were less than 3 m apart. When the GPR surveys for all years were considered, there were a total of 29 intersections of transects and 1764 pairs of recorded data points with less than 3 m separation distance. The difference in measured bedrock elevation for each of these 1764 joined points was calculated, and the GPR measurement error was calculated as the root mean square of these differences in elevation (RMSD). This RMSD value was used to define the upper and lower bounds for the bedrock elevations used in the interpolation of the bedrock topography.

Best-practice methods for quantifying errors in ice velocity from CMP surveys (e.g. Booth et al., 2010; Booth et al., 2011) are quite complicated, involving analysis of coherence patterns and Monte Carlo simulations. It is likely that other errors in the GPR measurements supersede the error in ice velocity, so a simpler approach to estimating uncertainty in the radar ice velocity has been taken. A potential range of ice velocity values is taken from the literature, namely the values for temperate and cold ice: 150 x 10^6 m/s and 167 x 10^6 m/s, respectively (Woodward and Burke, 2007). The differences between the measured velocity (from the CMP survey) and the values in the literature for temperate and cold ice were calculated, and the maximum of these two values was taken to represent the maximum possible error for the ice velocity. With the measured ice velocity at Artesonraju of 154 x 10^6 m/s, this resulted in a maximum error of 8%. Given a maximum measured ice thickness of 175 m, this corresponds to an absolute maximum error in ice thickness of 14 m, with the error being much less in many locations where the

ice thickness is significantly less than 175 m. Since the maximum error is comparable to the error in GPR measurements calculated from paired points less than 3 m apart (with the error in most locations being much less), the uncertainty in ice velocity was ignored, based on the assumption that the GPR measurement error was greater.

In the interpolation of the measured bedrock elevations (from GPR) to a spatially distributed topographic model of the bedrock, additional errors and uncertainties are introduced. The errors in the bedrock interpolation originate from errors in the interpolation method and errors in the input data, including errors in GPR measurements and errors in the Aster GDEM used to define the surface elevations at the glacier boundary. The average vertical error for the DEM (Aster GDEM v2) that was used to define the boundary of the glacier tongue is -0.2 m, but the error is 17 m at the 95% confidence level (Tachikawa et al., 2011). This latter value (17 m) was used to determine the potential range of elevations for the bedrock at the glacier boundary used as input for the interpolation.

The interpolation error is difficult to quantify, as the highest errors will be at the locations that have no nearby GPR measurements. Therefore, the RMSD of the elevation between interpolation methods was used as a proxy for the uncertainty due to interpolation error. The RMSD calculated for the two forms of bedrock interpolation was less than the GPR measurement error; therefore, this error was ignored when calculating the final range of uncertainty in the lake volume, assuming that the GPR measurement error was more significant.

The maximum ranges of uncertainty in the input variables were used to calculate lower and upper bounds for the lake volume. First, to account for the errors in the GPR measurements and Aster GDEM (used to define the bedrock elevations at the glacier boundary), the triscattered interpolation was repeated twice. The uncertainty values for

the input points (12.4 m for the GPR points and 17 m for the Aster GDEM points) were subtracted from the original elevations of the interpolation points to give an interpolated bedrock that would result in the largest possible lake volume (bedrock interpolation #2). To calculate the maximum potential lake volume, the highest water surface elevation within the range of uncertainty (4729 m.a.s.l.) was used to define the lake extent with bedrock interpolation #2. The GPR and Aster uncertainty values were then added to the original elevations to give an interpolated bedrock topography that would give the smallest possible lake volume (bedrock interpolation #3). The minimum potential lake volume was calculated by using the lowest water surface elevation (2712.8 m.a.s.l.) to define the lake extent with bedrock interpolation #3.

This approach to estimating the range of uncertainty in the future lake volume is meant to be a conservative approach where the uncertainties in the bedrock elevations and uncertainty in the water surface elevation are compounded to give the largest potential range of lake volumes. It is unlikely that the maximum errors for each of the input elevations (GPR measurements, Aster points for the glacier outline, and water surface elevation of the lake) would occur simultaneously; therefore, the likelihood of the actual future lake volume being outside of this range is very low, and it is probable that the range of uncertainty given for the lake volume is much wider than the likely range of potential volumes of the fully formed lake. Although the method presented here for determining ice thicknesses and bedrock elevations has its uncertainties, because it relies on in-situ geophysical measurements it may be considered to be more accurate than other existing methods for approximating ice thicknesses and lake volumes such as the GlabTop model for ice thicknesses (Linsbauer et al., 2012) or volume-area scaling relationships of Huggel et al. (2002) and Cook and Quincey (2015).

3.2.3 Characterizing Avalanche-generated Waves and Potential Overtopping

After establishing the characteristics of the fully formed lake, the next step was to address the second component of Research Question #3: *How can we determine the level of hazard that emerging lakes may pose*? This question was addressed through the application of simplified assessment methodologies for a preliminary analysis of the potential for an outburst flood from the fully formed lake. Detailed models of the GLOF process chain such as the approach applied at Lake Palcacocha (Somos-Valenzuela et al., 2016) were beyond the scope of this work. The objective of this work is to show that it is possible to provide rough assessments of possible future hazard conditions to facilitate proactive approaches to GLOF risk management. For this purpose, a first-order hazard assessment using simplified calculations was considered sufficient to determine whether or not a lake might be dangerous.

This work focuses exclusively on the upper watershed processes associated with the emerging lake in its fully formed state, and three steps of the GLOF process chain have been considered: avalanche, wave generation, and wave overtopping. The downstream processes, including lake dynamics for Lake Artesoncocha and Lake Paron and potential downstream inundation, were not included in this analysis. The methods for analyzing each of the upper watershed processes and data inputs for the analysis are described in the following paragraphs. The final result of the analysis presented in this section was a range of estimates of potential overtopping volumes for several avalanche scenarios.

Avalanche

The avalanche assessment was centered on whether or not avalanches are likely to originate from the upper slopes of the glacier, the potential for these avalanches to reach

the lake, and possible parameters of the avalanche to be inputted into the wave generation model. The primary data input for this assessment was the topography of the glacier surface as represented by the Aster GDEM (shown in Figure 3.12).

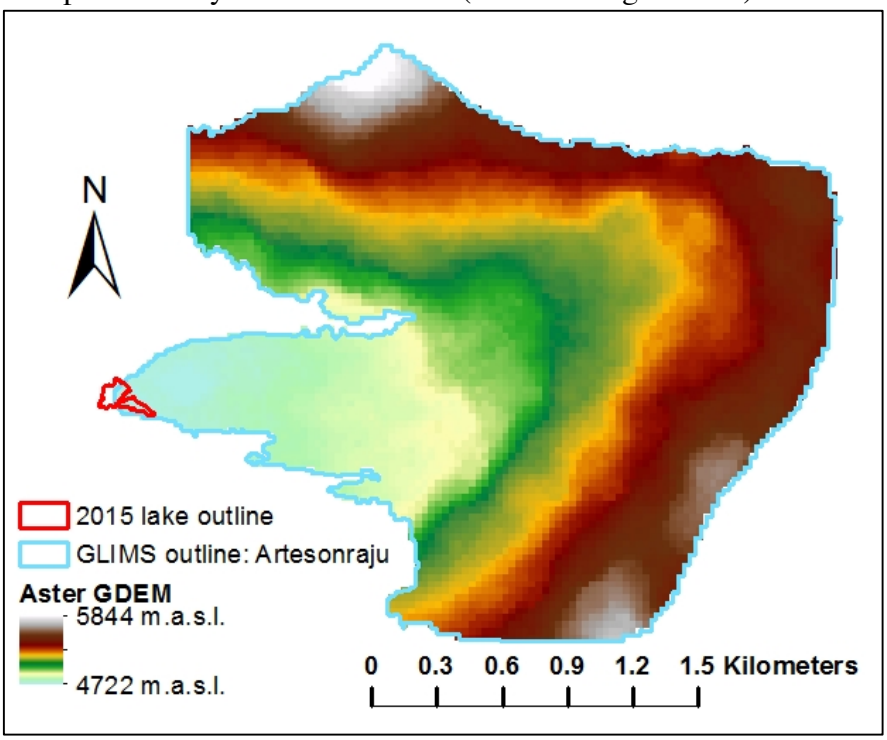

Figure 3.12- DEM of the glacier surface at Artesonraju (Aster GDEM from NASA LP DAAC, 2011; GLIMS outline from Racoviteanu, 2007)

First, the possibility of an avalanche being generated was determined by analyzing the slopes of the upper part of the glacier. The minimum slope that is likely to produce an avalanche for tropical glaciers is 24˚ (Huggel et al., 2004). The slopes above the future location of the fully formed lake range from approximately 20˚ to 45˚, and much of this area contains heavily crevassed or overhanging ice likely to produce avalanches (see Figure 3.13). Therefore, avalanches originating from the steeply sloped upper portion of the glacier are very likely.

After establishing the likelihood of an avalanche, the next step was to determine if an avalanche could reach the lake. According to Huggel et al. (2004), the maximum runout distance of an avalanche can be calculated by a regression equation relating the avalanche volume to the average slope of the runout:

(3.5) $$\tan\alpha = 1.111 - 0.118\log(V)$$

As long as the slope calculated from equation 3.5 is less than the average slope of the avalanche trajectory between the release point and the lake (approximately 25°), the avalanche should reach the lake. Following Somos-Valenzuela et al. (2016) and Schneider et al. (2014), three avalanche sizes were selected to represent a range of potential scenarios: 5 x 10^5 m^3, 1 x 10^6 m^3, and 3 x 10^6 m^3.

Figure 3.13- Upper slopes of the Artesonraju Glacier where crevasses and overhanging ice are prevalent.

The final result needed from the avalanche assessment was a set of avalanche characteristics to be used as inputs to the model of the wave generation. Because detailed avalanche modeling was not performed, approximate avalanche characteristics were taken from the RAMMS model at Lake Palcacocha presented in Somos-Valenzuela et al. (2016). These characteristics were the volume, density of avalanche material, and thickness entering the lake (Table 3.3).

Table 3.3- Avalanche characteristics used for calculations of the wave generation (from the RAMMS avalanche model in Somos-Valenzuela et al., 2016)

Avalanche Size	Large	Medium	Small
Volume (10^6 m^3)*	3	1	0.5
Thickness (m)*	20	15	6
Density of avalanche material (kg/m^3)*	900	900	900

The velocity entering the lake (V_s) was approximated from the drop in height from center of gravity of the slide (Δz_{sc}), the dynamic bed friction angle (δ), and the average slope of the avalanche path (α) (Heller et al., 2009):

$$V_s = \sqrt{2g\Delta z_{sc}\left(1-\tan\delta\cot\alpha\right)} \tag{3.6}$$

The dynamic bed friction angle was set to 20° according to the recommendation of Heller et al. (2009). An avalanche path along the longitudinal axis of the lake was taken as representative of the worst-case scenario because impact along this axis should generate waves with the least possible attenuation as they propagate along the lake. If an avalanche does not enter at a direct angle to the lake, the wave is likely to be reflected off the lateral moraines before it reaches the point of overtopping, thus dissipating energy and attenuating the wave. Based on this hypothetical avalanche trajectory, the initial

height of the center of gravity of the slide was estimated to be 5200 m.a.s.l., and the total drop in elevation was calculated as 480 m by subtracting the lake elevation (taken to be 4720 m.a.s.l., according to the elevation estimated in Section 3.2.2) from the initial avalanche elevation (5200 m.a.s.l.). The average slope of this avalanche path was approximated (from the Aster GDEM) to be 25˚.

Considerable uncertainty remains regarding the avalanche characteristics, but very little is known about the range of parameters for a potential avalanche. Nonetheless, the avalanche parameters can have a significant impact on the wave generation. Because there was not enough information to quantify the uncertainty in the avalanche parameters, a basic sensitivity analysis of the wave height to the avalanche thickness was performed. This was done by considering three different avalanche thicknesses for each avalanche scenario. The resulting wave heights were calculated for each avalanche thickness to explore the relationship between avalanche thickness and maximum wave height.

Wave Generation

The empirical method of Heller et al. (2009, 2010) was used to model the wave generation from avalanche impact and calculate maximum wave heights for the three avalanche scenarios. In addition to the avalanche characteristics presented above, the required inputs for this method are: the lake depth near the avalanche impact, the slide width and the slide impact angle. The still water depth of the lake was determined from the bathymetry (Section 3.2.2). The slide width entering the lake was assumed to be equal to the width of the lake (approximately 200 m). The slide impact angle was determined from the Aster GDEM to be approximately 25˚.

The characteristics of the avalanche-generated impulse wave were determined according to equations from Heller et al. (2009) outlined below. The slide Froude number (F), relative slide mass (M) and relative slide thickness (S) were calculated as:

$$F = \frac{V_s}{\sqrt{gh}} \tag{3.7}$$

$$M = \frac{\rho_s \forall_s}{\rho_w b h^2} \tag{3.8}$$

$$S = \frac{s}{h} \tag{3.9}$$

V_s = slide velocity (m/s)
h = still water depth (m)
ρ_s = bulk slide density (kg/m^3)
ρ_w = water density (kg/m^3)
$\forall_s$ = bulk slide volume (m^3)
b = slide width (m)
s = slide thickness (m)
α = slide impact angle (degrees)

The impulse product parameter was calculated according the following equation:

$$P = FS^{1/2}M^{1/4}\left\{\cos\left[\left(6/7\right)\alpha\right]\right\}^{1/2} \tag{3.10}$$

The impulse product parameter was used to determine the maximum wave height (H_m), distance from the slide impact to the maximum wave height (x_m), and the wave period for the maximum wave (T_m).

$$H_m = \left(5/9\right)P^{4/5}h \tag{3.11}$$

$$x_m = \left(11/2\right)P^{1/2}h \tag{3.12}$$

(3.13) $$T_m = 9P^{1/2}\left(h/g\right)^{1/2}$$

The wave amplitude is a function of the wave height above the equilibrium water level (h). The wave celerity (c) and period were used to calculate the wave length for the maximum wave (λ_m).

(3.14) $$a = \left(4/5\right)h$$

(3.15) $$c = \left[g\left(h + a\right)\right]^{1/2}$$

(3.16) $$\lambda_m = T_m c$$

The maximum wave height was the primary variable used to characterize the avalanche-generated wave, and it was used as an input to the method for estimating the wave overtopping volume presented below.

Wave Overtopping

The most commonly used method for calculating overtopping volumes from avalanche-generated impulse waves is that of Müller (1995) (this is also the method adopted by Heller et al. (2009) for the overtopping portion of their wave calculations). However, when this method was applied to Lake Palcacocha, the resulting volumes were in very poor agreement with the 3D modeling results and were often over an order of magnitude less than typical volumes that would be expected from outburst flood events involving overtopping waves. Huggel et al. (2004) state that when the ratio of the avalanche volume to the lake volume is between 1:1 and 1:10, it is possible for the lake to be completely emptied, but even for volume ratios between 1:10 and 1:100, overtopping is likely unless there is a high level of freeboard relative to the wave height. Considering

the projected volume of the fully formed lake, this general rule would imply that the large and medium avalanches could empty much or all of the lake. However, for the sake of argument (to allow for a more thorough demonstration of the method proposed here), the assumption has been made that the overtopping volume depends on the wave height and characteristics of the terminal moraine (freeboard height and approach angle). Waves generated by avalanche impacts are similar to tsunamis, especially as they approach the shore (large wave heights relative to the water depth, and significant changes in the wave height during runup). Therefore, analytical methods for calculating tsunami runup have been adapted for application to the problem of runup and overtopping of avalanche-generated waves in glacial lakes. The method proposed here for adapting tsunami runup equations to glacial lake environments is a new approach, and it is hoped that it will offer an improvement over existing empirical or analytical overtopping relationships to provide more accurate estimates of overtopping volumes.

The result from the adapted tsunami runup equations is an estimate of overtopping volume that does not require numerical simulations. The objective of this work is to present a method for first-order estimates of GLOF magnitudes. With this in mind, an estimate of overtopping volume (rather than a discharge hydrograph) was considered sufficient to determine if there is a potential for a significant outburst flood to originate from the fully formed lake at Artesonraju. The method presented here for estimating overtopping volumes from avalanche-generated waves has been validated against the results of the 3D simulations at Lake Palcacocha (presented in Section 2.3.4), resulting in overtopping volumes that were approximately 30% less than the overtopping volumes from the 3D model. The input parameters for Lake Palcacocha and comparisons of overtopping volumes between the methods are presented in Appendix B.

The method of tsunami runup calculations presented by Synolakis (1987) has been adapted here to calculate overtopping volumes for avalanche-generated waves in glacial lakes. The Synolakis (1987) method introduces a theory of solitary waves used to develop analytical equations for tsunami runup based on an assumption of linearity and the shallow water approximation. Synolakis (1987) uses a wave setup, such as that shown in Figure 3.14, to describe the water surface elevation and runup as a function of time. In this setup, the tsunami wave begins (t = 0) with an initial wave height of (H) at distance (X_1) from the shoreline that is far enough from the shore that the wave height is not affected by runup. The beach is partially submerged, and the runup height ($\Re$) represents the vertical distance above the initial shoreline position for maximum wave runup. The origin of this setup is at the initial shoreline position (x_0, y_0), and the horizontal distance (x) increases in the opposite direction of wave propagation.

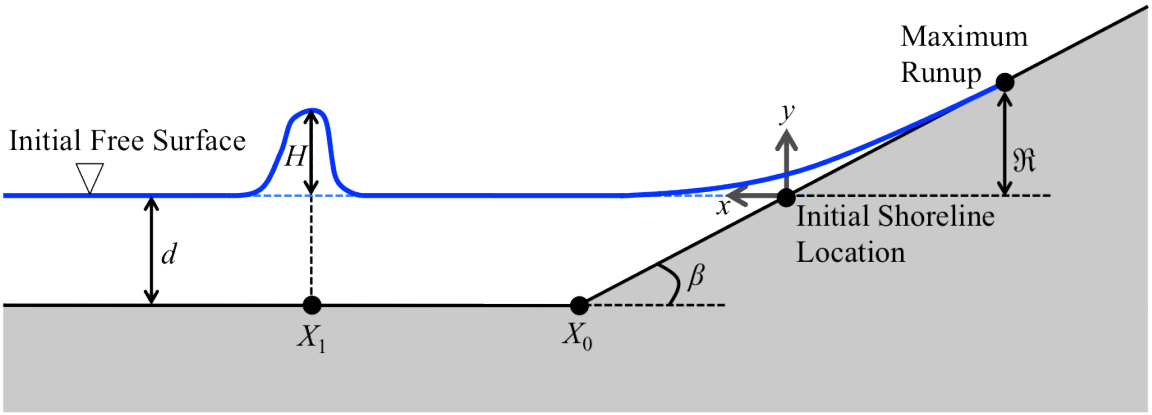

Figure 3.14- Schematic diagram of coordinate system and variables used for the tsunami runup equations (modeled after Figure 1 in Synolakis, 1987)

Synolakis (1987) introduces a runup law with the following equation used to calculate the tsunami runup height as a function of the initial wave height (H), still water depth before the beach (d), and shoreline slope (β):

$$\frac{\Re}{d} = 2.831(\cot\beta)^{\frac{1}{2}}\left(\frac{H}{d}\right)^{\frac{5}{4}} \tag{3.16}$$

In the system presented by Synolakis (1987), the free surface elevation is described as a function of horizontal distance and time:

$$\eta(x,t) = 2\int_{-\infty}^{\infty}\Phi(k)\frac{J_0\left(2k(xX_0)^{\frac{1}{2}}\right)e^{-ik(X_0+ct)}}{J_0(2kX_0)-iJ_1(2kX_0)}dk \tag{3.17}$$

where J_0 is a Bessel function of order 0 and $\Phi(k)$ is a function with the following form:

$$\Phi(k) = \frac{2}{3}k\,\mathrm{cosech}(\alpha k)e^{ikX_1} \tag{3.18}$$

To adapt this approach for calculation of GLOF overtopping, the assumption has been made that the theoretical runup height on a beach (with a continually increasing slope) can be converted to the momentum of the wave during runup and overtopping and can be used as a proxy variable to calculate overtopping. The setup has been altered slightly to represent a typical setup for a moraine-dammed lake (Figure 3.15). In the adapted setup, the slope of the beach (β) was replaced with the moraine slope on the lakeside face of the moraine, and the undisturbed water depth (d) was considered to be the still water depth near the moraine. The distance to the maximum wave (X_0) was calculated by subtracting the distance between the avalanche impact and the maximum wave from the wave generation calculations (x_m) from the total length of the lake. The theoretical tsunami runup height ($\Re$) was calculated according to the runup law (equation 3.16) assuming that the moraine slope continues with infinite height (preventing any overtopping).

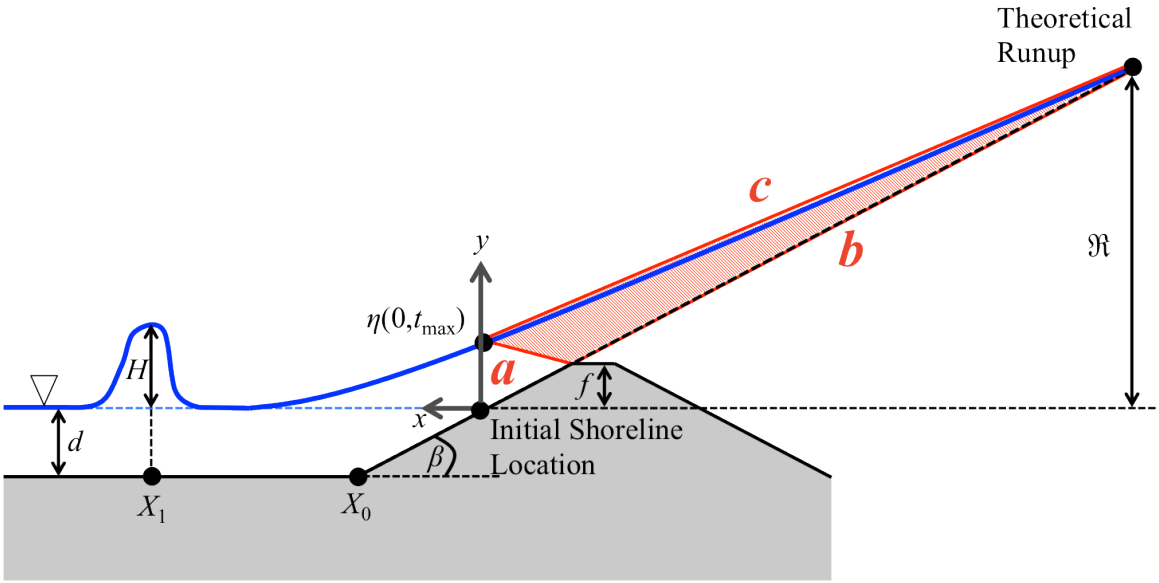

Figure 3.15- Schematic diagram of tsunami runup setup adapted for calculating GLOF overtopping volumes at the terminal moraine

The freeboard (f) of the lake-damming moraine is the key parameter (other than the wave characteristics) that controls the amount of overtopping. Using the theoretical runup height, a triangle can be drawn with the longest side (c) approximately following the free surface for the theoretical maximum runup and other the two sides extending from the moraine crest to the free surface (a) and from the moraine crest to the maximum runup point on the theoretical shoreline (b). The point where sides a and c of the triangle intersect was considered to be the free surface elevation directly above the initial shoreline position; equation 3.17 was integrated numerically (Matlab script is given in Appendix C) at $\eta(0, t_{max})$ to give the coordinates of this point. The area of this triangle can be used to represent the overtopping volume per unit length of the moraine crest (A_O). The length of the moraine crest (l) was assumed to be equal to the width of the lake at the

terminal moraine. The equations for the length of each side of the right triangle and the total area representing the overtopping volume (A_O) are given below.

$$a = \sqrt{\left(\eta - f\right)^2 + \left(\frac{f}{\tan\beta}\right)^2} \tag{3.19}$$

$$b = \sqrt{\left(\Re - \eta\right)^2 + \left(\frac{\Re}{\tan\beta}\right)^2} \tag{3.20}$$

$$c = \frac{\Re - f}{\sin\beta} \tag{3.21}$$

$$A_o = \sqrt{p\left(p-a\right)\left(p-b\right)\left(p-c\right)} \tag{3.22}$$

where

$$p = \frac{a+b+c}{2} \tag{3.23}$$

The total overtopping volume (V_O) was calculated by multiplying the overtopping area (A_O) by the length of the moraine crest (l):

$$V_O = A_O \cdot l \tag{3.24}$$

The input parameters for the method presented above describe the lake and moraine geometries as well as the characteristics of the avalanche-generated wave. The parameters of the lake geometry were taken from the lake extent and bathymetry, and the moraine geometry was characterized from the bedrock topography. The wave characteristics used to calculate the overtopping volumes were determined according to the Heller et al. (2009) method described in this section. The values for all input parameters are given in Table 3.4.

Table 3.4- Input parameters for the calculation of overtopping volumes based on the adapted tsunami runup equations

Still water depth near the moraine (d)	10 m
Freeboard (f)	5 m
Length of the moraine crest (l)	200 m
Moraine slope (β)	30˚
Distance to maximum wave height (X_1)	From Heller and Hager (2009) equations
Maximum wave height	From Heller and Hager (2009) equations

3.3 RESULTS

3.3.1 Ground Penetrating Radar

Common Midpoint Survey

The two-way travel times were corrected based on the travel time for the initial airwave, resulting in values for t_1 and t_2 of 4.47 x 10^{-7} s and 4.7 x 10^{-7} s (corresponding to separation distances of 20 m and 30 m, respectively) as indicated in the wiggle traces shown in Figure 3.16. The resulting radar ice velocity is 154 x 10^6 m/s which is reasonable when compared with values reported in the literature; Woodward and Burke (2007) report a radar velocity of 150 x 10^6 m/s for temperate ice and 167 x 10^6 m/s for cold ice.

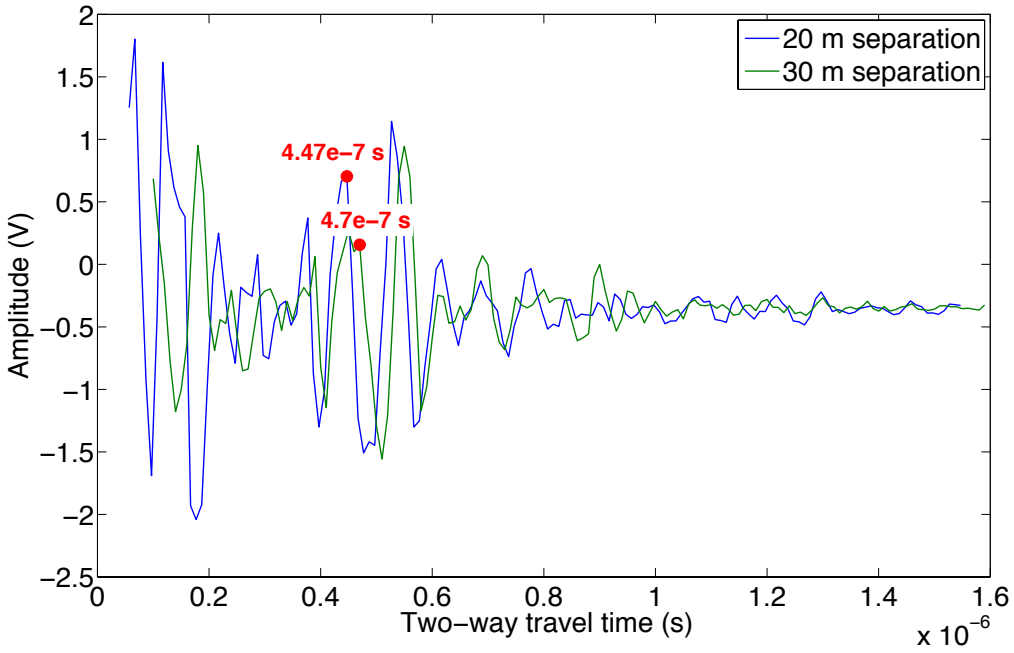

Figure 3.16- Wiggle traces for the CMP survey with the red dots indicating the travel times to the midpoint reflector

GPR Transects

In most of the GPR transects, the interface between the ice and bedrock was clearly visible. The GPR surveys showed an overdeepening in the bedrock near the glacier terminus that extends to the middle of the glacier tongue, indicating that the conditions are favorable for the growth of a glacial lake. The bedrock begins to slope upward near the transition from the ablation to accumulation zone, indicating that the glacial lake will likely be contained within the area that currently is the glacier tongue.

Radargrams for all transects taken at Artesonraju are given in Appendix A. Figure 3.17 shows the radargrams from the 2013 GPR survey with the UT system, indicating how the transects line up with common connecting points to produce a nearly continuous

line depicting the bedrock elevation (shown in Figure 3.18). To illustrate how the radargrams were interpreted to delineate the bedrock elevations, Figure 3.19 shows an example of a radargram from the 2012 GPR survey along with an annotated version of the same figure showing the interpretation of the bedrock location used to determine the ice thickness.

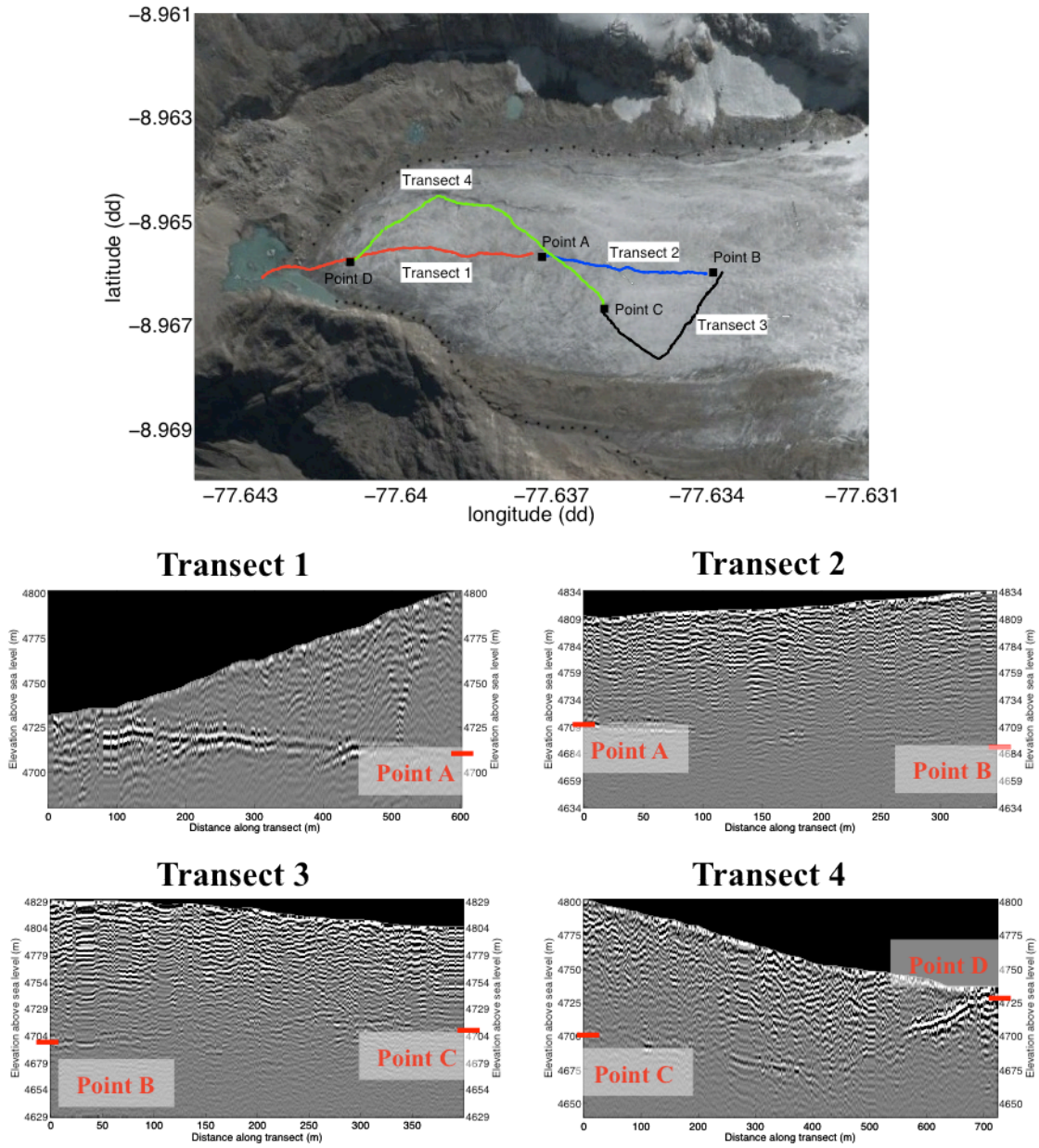

Figure 3.17- 2013 GPR transects measured with the UT GPR unit: top image shows the locations of the transects, and the bottom four images show the radargrams from these transects with the bedrock elevations at the common connecting points between transects indicated in red. Locations of these points are shown in the top figure (background image from Google, 2013).

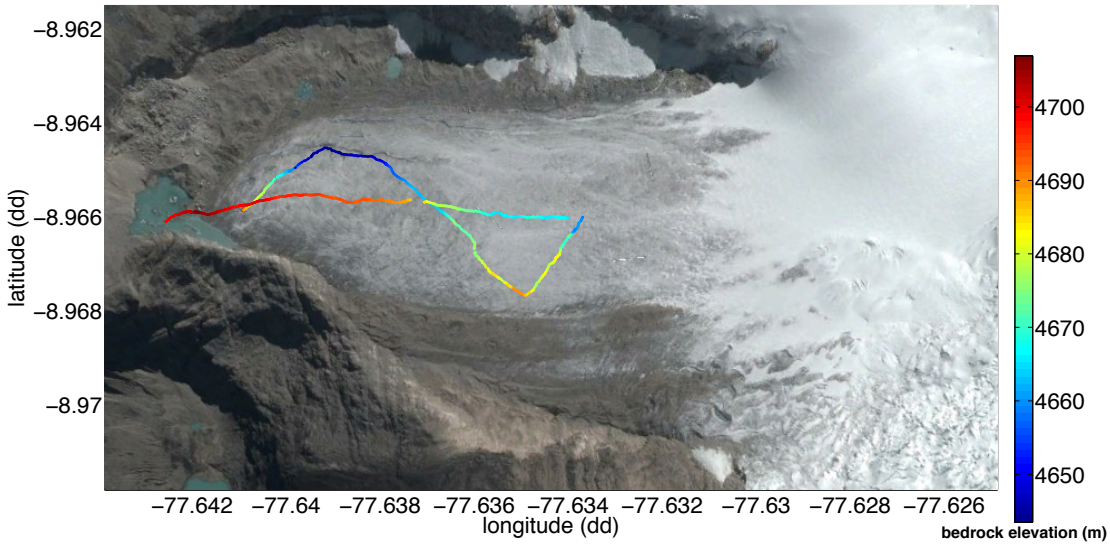

Figure 3.18- Bedrock elevations delineated from the 2013 UT GPR transects shown in Figure 3.17 (background image from Google, 2013)

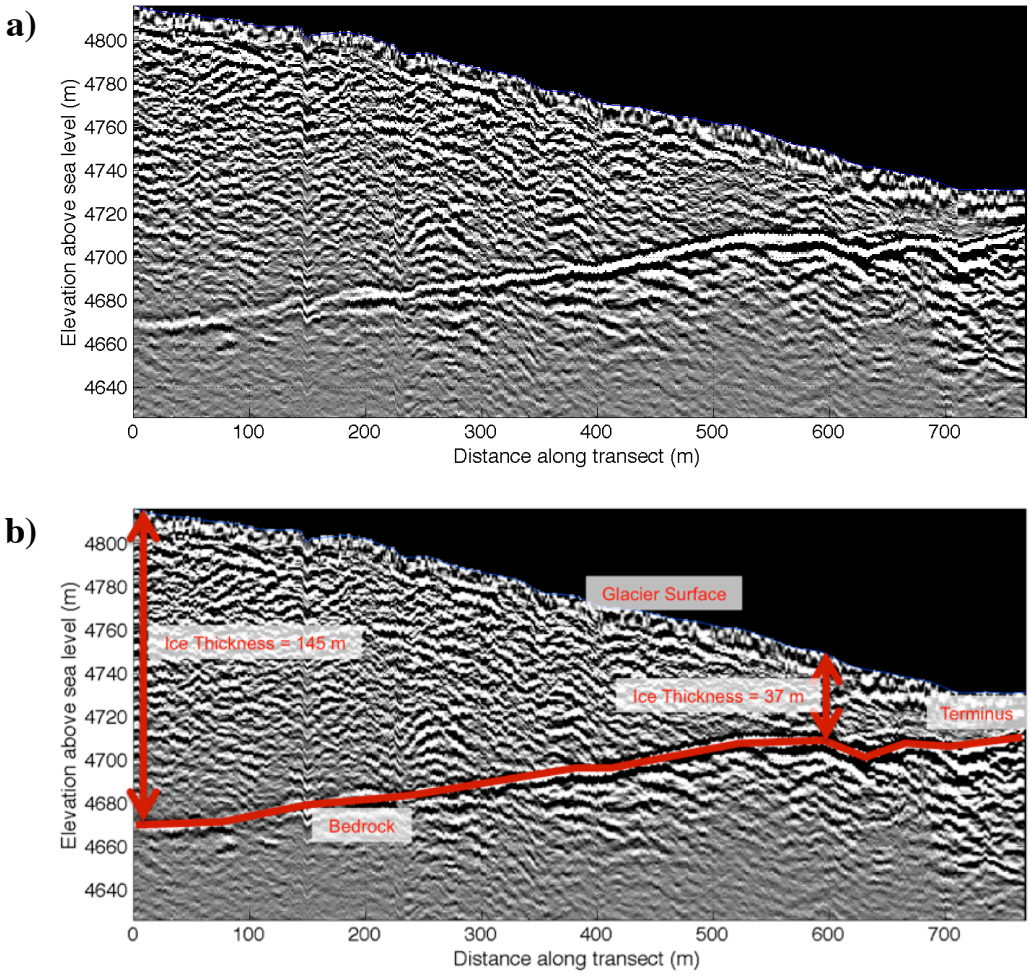

Figure 3.19- a) Z-scope radargram of a GPR transect from the July 2012 GPR survey at Artesonraju; b) the same radargram in a), annotated to show ice thicknesses and the location of the bedrock.

The ice thicknesses, calculated from the bedrock picks of the radargrams shown in Appendix A, are mapped over an image of the glacier in Figure 3.20. These thicknesses were converted to bedrock elevations based on the glacier surface elevations measured by the GPR systems (Figure 3.21). The minimum measured ice thickness was approximately 11 m, and the maximum was approximately 175 m. The measured bedrock

elevations ranged from approximately 4634 m.a.s.l. to 4893 m.a.s.l. The RMSD of the difference in elevation for intersecting transects was 12.4 m, and this value was used to represent the uncertainty in the GPR measurements.

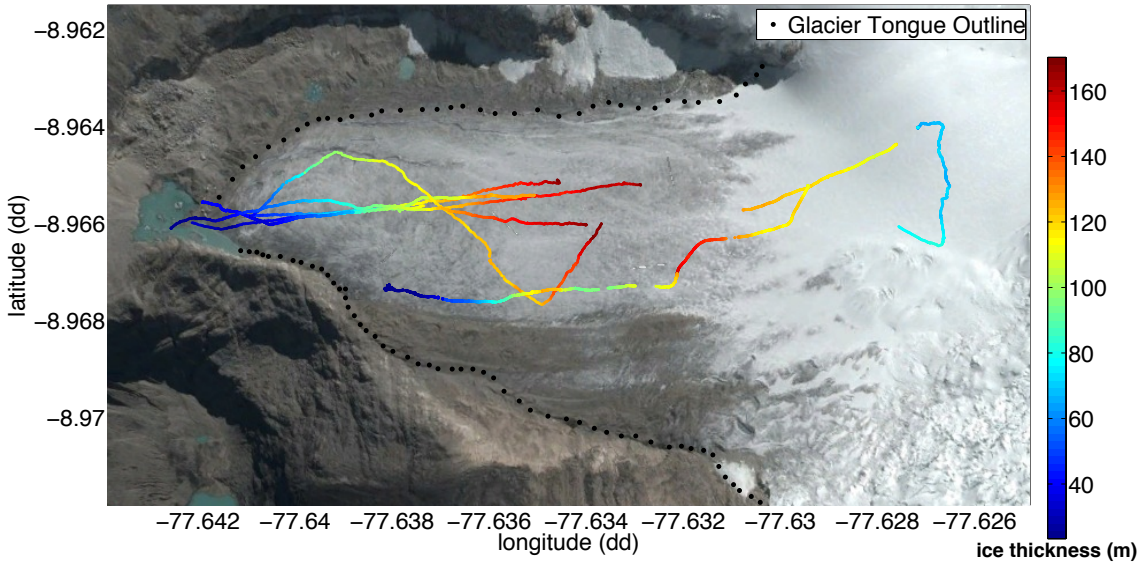

Figure 3.20- Ice thicknesses measured from all GPR surveys at Artesonraju Glacier (background image from Google, 2013)

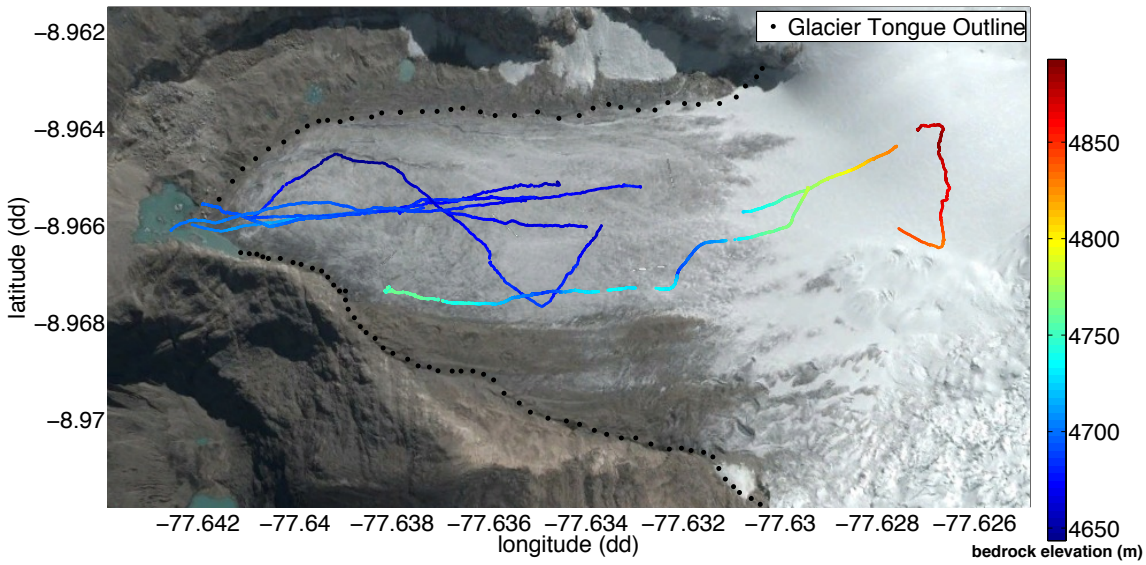

Figure 3.21- Bedrock elevations measured from all GPR surveys at Artesonraju Glacier (background image from Google, 2013)

3.3.2 Mapping 3D Bedrock Topography and Projecting Future Lake Bathymetry

Bedrock Interpolation

The interpolated bedrock topographies (shown in Figures 3.22 and 3.23) followed roughly the same patterns as the bedrock elevations in the GPR transects, but the "topo to raster" interpolation was slightly smoother than the triscattered interpolation. There was also very little difference in the range of elevations for the interpolated bedrock topographies. Both interpolations resulted in a maximum bedrock elevation (for the interpolated area) of 5011-5012 m.a.s.l. The triscattered interpolation gave a minimum bedrock elevation (4636 m.a.s.l.) very nearly the same as the minimum measured elevation (4634 m.a.s.l., from Section 3.3.1). The "topo to raster" interpolation gave a slightly higher minimum bedrock elevation (4643 m.a.s.l.), most likely due to the

smoothing technique that creates hydrologically correct topographies. Most of the differences in elevation between the two bedrock topographies (Figure 3.24) were small, but there were a few areas where the differences were quite large. The RMSD between the two interpolated bedrock topographies was 4.8 m.

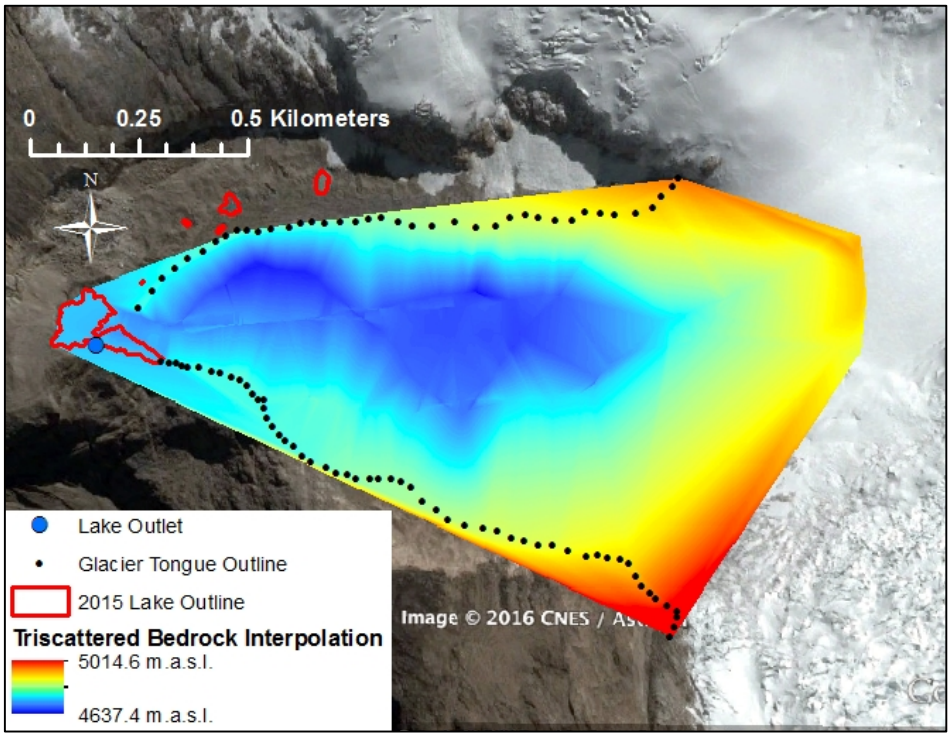

Figure 3.22- Bedrock elevations interpolated from GPR data using the Triscattered Interpolation function in Matlab (background image from Google, 2013)

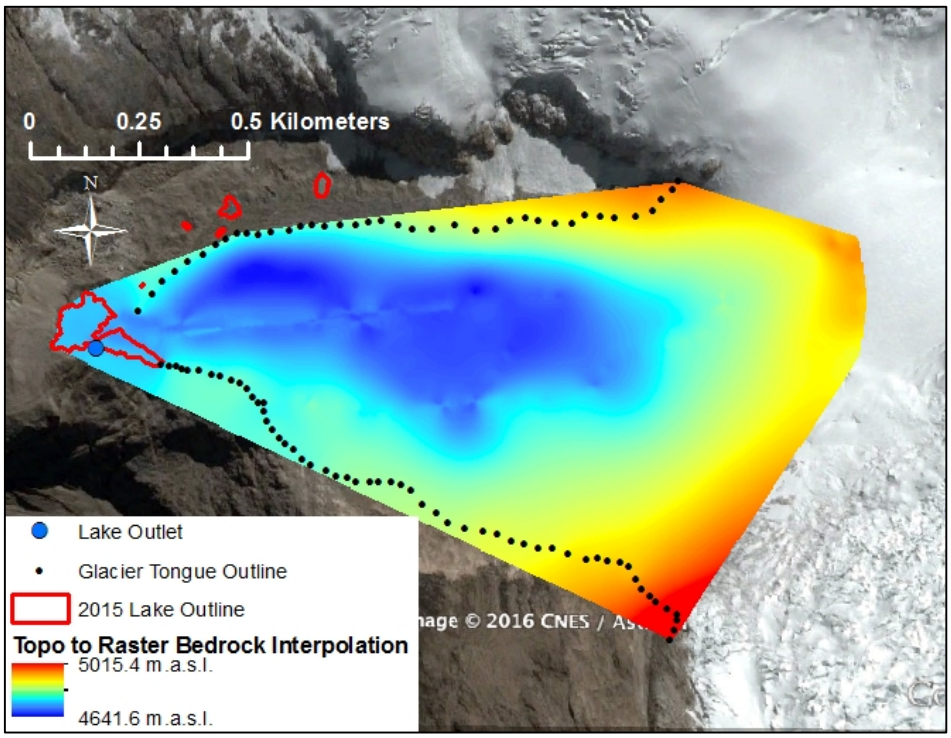

Figure 3.23- Bedrock elevations interpolated from GPR data using the "topo to raster" tool in ArcGIS (background image from Google, 2013)

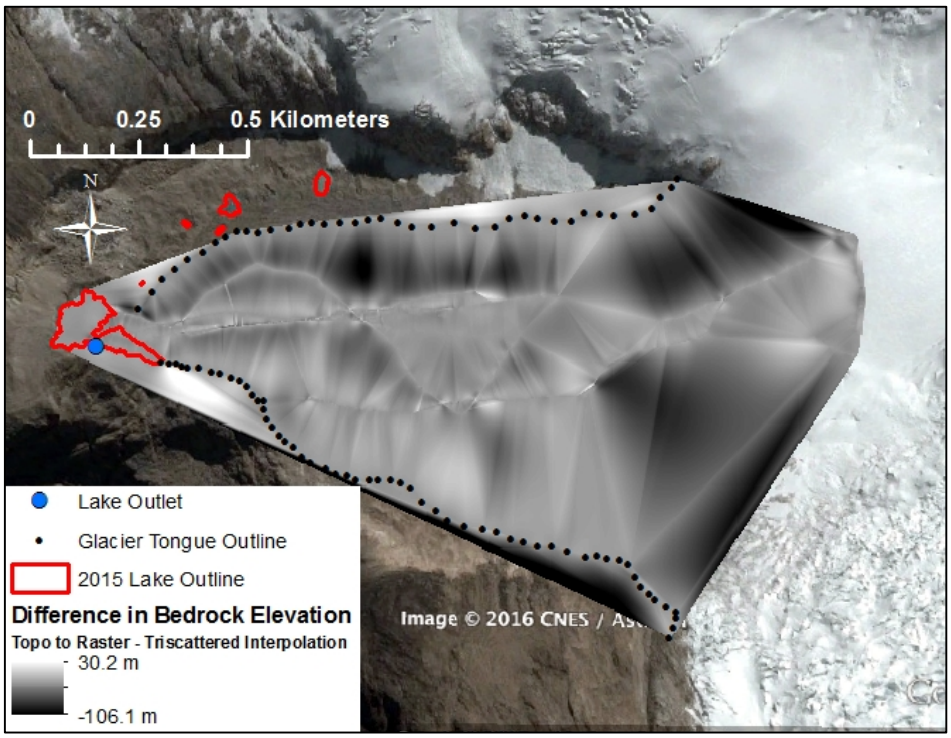

Figure 3.24- Difference in elevation between the "topo to raster" interpolated bedrock topography and triscattered interpolated bedrock topography (background image from Google, 2013)

Lake Depth and Volume Calculations

The projected surface extent and water depths for the fully formed lake are shown for each of the two interpolation methods in Figures 3.25 and 3.26. The maximum depth and total lake volume for each lake definition are given in Table 3.5. The maximum depth for the lake delineated from the triscattered interpolation was higher than the maximum depth from the "topo to raster" interpolation, reflecting the lower minimum bedrock elevations in the "topo to raster" interpolated topography. This difference in maximum depth was relatively small ~5%. The difference in maximum depth was not reflected in the projected lake volumes, and the "topo to raster" interpolation resulted in a

projected lake volume that was ~15% higher than the volume from the triscattered interpolation. Averaging the projected volumes for each of the interpolation methods resulted in an estimated volume of 10.3 million m^3 for the fully formed lake. A treatment of the uncertainties in the lake volume projections follows.

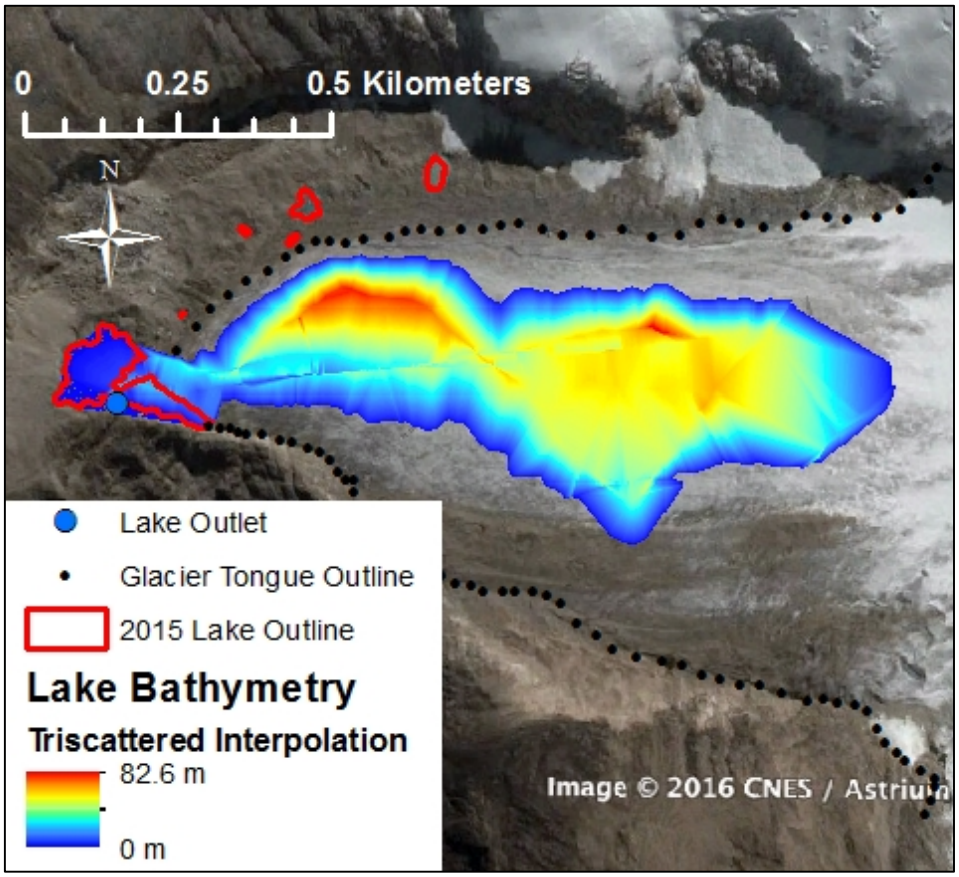

Figure 3.25- Projected lake extent and bathymetry for a water surface elevation of 4720 m.a.s.l. delineated according to bedrock elevations from the triscattered interpolation (background image from Google, 2013)

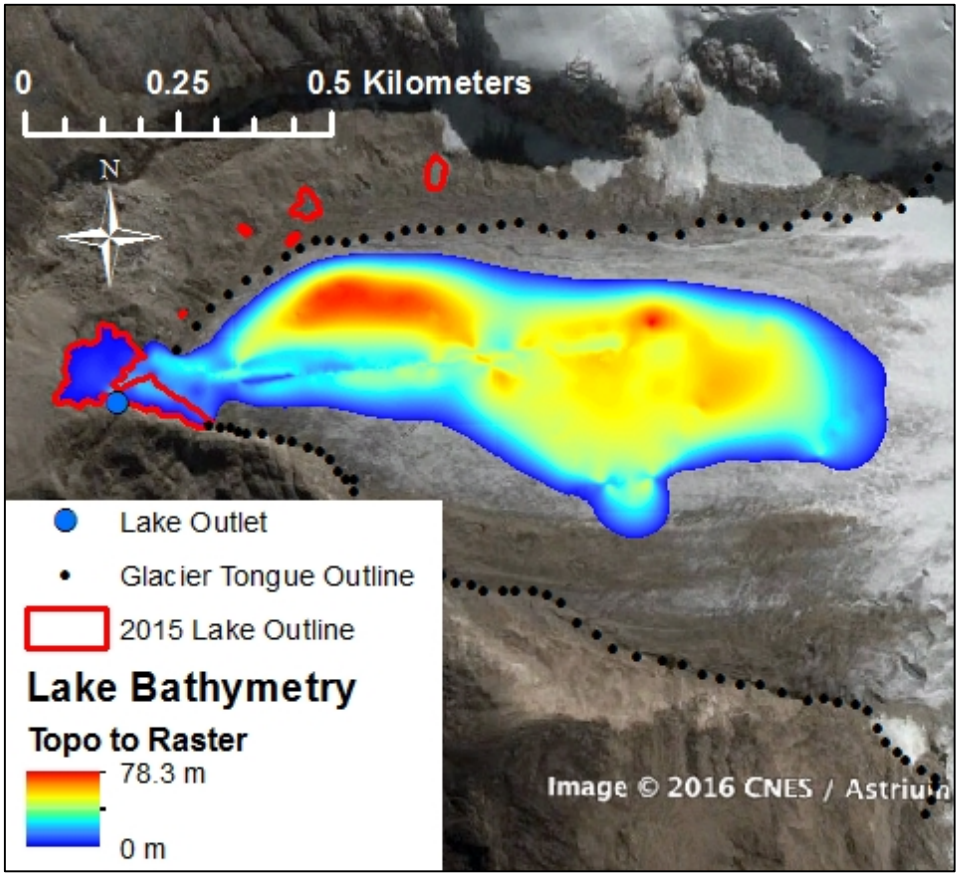

Figure 3.26- Projected lake extent and bathymetry for a water surface elevation of 4720 m.a.s.l. delineated according to bedrock elevations from the "topo to raster" interpolation (background image from Google, 2013)

Table 3.5- Maximum depth and total volume projections for the fully formed lake

Interpolation Method	**Water Surface Elevation (m.a.s.l.)**	**Maximum Depth (m)**	**Projected Lake Volume (10^6 m^3)**
Triscattered	4720	82.6	9.56
Topo to Raster	4720	78.4	11.0

Uncertainty

The calculations of uncertainty for the individual variables have been given with the results for each step of analysis and are summarized in Table 3.6. The ranges of uncertainty in the GPR measurements, elevations of the glacier boundary, and water surface elevation were used to calculate the range of uncertainty in the volume of the fully formed lake (Table 3.7). The uncertainty in the lake volume was considerable: 56% of the projected volume for the lower bound and 67% of the projected volume for the upper bound. It is possible that the volume of the fully formed lake could be anywhere from 4.5 million m^3 to 17 million m^3, but it is most likely that the actual volume (if the lake ever reaches its fullest extent) will be much closer to the projected value of 10.3 million m^3.

Table 3.6- Summary of uncertainty values for intermediate calculations and input variables used to calculate the lake volume

Variable	**Range of Uncertainty**
GPR Measurements*	± 12.4 m
Aster GDEM*	± 17 m
Ice Velocity	± 8% (corresponding to a maximum error in ice thickness of 14 m)
Bedrock Interpolation	± 4.8 m
Water Surface Elevation*	4712.8 m.a.s.l – 4729 m.a.s.l. (upper and lower bounds)
* Variables used to calculated upper and lower bounds of the lake volume	

Table 3.7- Range of uncertainty in the projected volume of the fully formed lake

Lower Bound (10^6 m^3)	**Lake Volume (10^6 m^3)**	Upper Bound (10^6 m^3)
4.5	**10.3**	17.3

3.3.4 Characterizing Avalanche-generated Waves and Potential Overtopping

Avalanche

Three avalanche sizes have been considered for estimating the potential magnitude of a GLOF generated from an avalanche falling into the lake. The minimum runout slope for each avalanche (calculated according to equation 3.5) is given in Table 3.8. The minimum runout slopes for all avalanche sizes were less than the estimated average slope between the avalanche release point and the lake (25˚), so it can be assumed that all avalanches could reach the lake. The avalanche characteristics (apart from the volume, depth and density that are given in Table 3.3, Section 3.2.3) were approximated based on an avalanche originating at an elevation of approximately 5200 m.a.s.l., following a direct path along the longitudinal axis of the lake. The vertical drop in elevation and average slope used to calculate the slide impact velocity were: Δz_{sc} = 480 m and α = 25˚. The resulting velocity of the avalanche as it enters the lake was V_s = 45 m/s.

Table 3.8- Average slope for maximum runout of the three avalanche scenario volumes

Avalanche Size	Avalanche Volume (10^6 m^3)	$\tan\alpha$	Average Slope for Maximum Runout
Large	3	0.347	19˚
Medium	1	0.403	22˚
Small	0.5	0.439	24˚

Wave Generation

Using the avalanche characteristics in Table 3.3 as input parameters results in significant wave heights for all three avalanche sizes (Table 3.9). The maximum wave heights ranged from approximately 20 m for the small scenario to approximately 46 m for

the large scenario. However, there remains a lot of unquantifiable uncertainty regarding the avalanche characteristics, and the maximum wave height was quite sensitive to the avalanche thickness. Table 3.10 gives the maximum wave heights for a range of avalanche thicknesses. For the large avalanche, a 50% reduction in the avalanche thickness (10 m) resulted in a 24% reduction in the maximum wave height, and reducing the thickness to 5 m resulted in a 43% reduction in the maximum wave height. Given the wide range of uncertainty in the avalanche characteristics, it may be possible for each avalanche size to generate any of the corresponding wave magnitudes given in Table 3.10.

Table 3.9- Characteristics of the maximum wave generated for each avalanche scenario

Avalanche Size	**Maximum wave height, H_m (m)**	**Distance to maximum wave height, x_m (m)**	**Period of maximum wave, T_m (s)**
Large	45.8	310.3	29.6
Medium	33.4	255.0	24.3
Small	19.8	183.5	17.5

Table 3.10- Maximum wave heights for a range of avalanche thicknesses entering into the lake

Avalanche Size	**RAMMS avalanche thickness (m)**	**H_m, RAMMS thickness (m)**	**H_m, 10 m thickness (m)**	**H_m, 5 m thickness (m)**
Large	20	45.8	34.7	26.3
Medium	15	33.4	28.4	21.6
Small	6	19.8	24.2	15.0 (3 m thickness)**
** **3 m avalanche thickness**: Because the 5 m thickness was very close to the original avalanche thickness (6 m), a 3 m avalanche thickness was used to illustrate the effect of reducing the avalanche thickness for the small avalanche				

Wave Overtopping

Using the input parameters described in Section 3.2.3 (Table 3.4), the overtopping volumes have been calculated according to the analytical method adapted from tsunami runup equations; these overtopping volumes are shown in Table 3.11. The overtopping volumes ranged from approximately 1 million m^3 for the large avalanche to approximately 130,000 m^3 for the small avalanche. The difference in volume between the small and large avalanche scenarios was almost an order of magnitude; this difference is not surprising given that the difference in avalanche volumes was of comparable magnitude, and the 3D hydrodynamic simulations at Lake Palcacocha (Chapter 2) produced a similar range of overtopping volumes. The overtopping volumes calculated by this method can be very sensitive to the input parameters. To demonstrate this sensitivity, the input parameters (still water depth near the moraine, moraine slope, and freeboard) have been varied to show the range of volumes that may result if the input parameters are not precisely the initial values estimated for Artesonraju (Table 3.12). The still water depth and moraine slope seem to have much more of an impact on the overtopping volume than the freeboard. This is an interesting finding, as increasing freeboard is one of the most common mitigation alternatives for glacial lakes in Peru. Yet, these results must be interpreted carefully. This method for calculating overtopping volumes does not account for changes in slope of the terminal moraine (e.g. if the slope is higher above the water surface than for the subsurface portion of the moraine), and reinforced moraine structures are likely to have higher slopes than the natural slope of the moraine below the surface. These effects are discussed further in Section 3.4. Nonetheless, given all the uncertainties, the overtopping volumes calculated from the adapted tsunami wave equations are high enough to draw attention to the possible hazard of a GLOF originating from Artesonraju.

Table 3.11- Results of the runup and overtopping calculations at Artesonraju using the adapted tsunami runup equations of Synolakis (1987) and the input parameters in Table 3.4

Avalanche Size	**Maximum wave height, H_m (m)**	**Free surface elevation at x=0, $\eta(0, t_{max})$ (m)**	**Theoretical runup height, $\Re$ (m)**	**Total overtopping volume, V_O (m^3)**
Large	45.8	25.4	249.6	1.08×10^6
Medium	33.4	17.2	168.2	4.86×10^5
Small	19.7	8.9	87.0	1.27×10^5

Table 3.12- Sensitivity of overtopping volume calculations to input parameters. Each parameter has been varied while maintaining the same values as in Table 3.4 for all other parameters. For each parameter, the initial value (from Table 3.4) is shown in bold.

	Large Avalanche	**Medium Avalanche**	**Small Avalanche**
Still water depth			
5 m	3.04E+06	1.37E+06	3.60E+05
10 m	**1.08E+06**	**4.86E+05**	**1.27E+05**
15 m	5.88E+05	2.65E+05	6.91E+04
20 m	3.82E+05	1.72E+05	4.49E+04
30 m	2.09E+05	9.42E+04	2.45E+04
40 m	1.36E+05	6.14E+04	1.60E+04
Moraine slope			
15˚	4.99E+06	2.25E+06	5.92E+05
30˚	**1.08E+06**	**4.86E+05**	**1.27E+05**
45˚	3.62E+05	1.63E+05	4.24E+04
60˚	1.23E+05	5.54E+04	1.44E+04
Freeboard			
5 m	**1.08E+06**	**4.86E+05**	**1.27E+05**
10 m	1.06E+06	4.71E+05	1.19E+05
15 m	1.03E+06	4.56E+05	1.11E+05
20 m	1.01E+06	4.41E+05	1.04E+05
25 m	9.89E+05	4.26E+05	9.60E+04

The volumes in Table 3.11 are high enough to be of concern, as volumes of similar magnitudes discharged from Lake Palcacocha resulted in inundation in the city of Huaraz according to hydrodynamic simulations of potential GLOF impacts (Somos-Valenzuela et al., 2016). However, to provide a complete context for interpreting these results, several factors must be noted. First, until this method for calculating overtopping volumes can be further validated, these overtopping volumes should be considered as estimates and not precise values to be used for hazard mapping purposes. Second, the geometry of the emerging lake at the outlet may somewhat mitigate overtopping because the outlet is along the lateral moraine at an angle approximately perpendicular to the longitudinal axis of the lake. With avalanche-generated impulse waves, there is generally significant runup along the lateral moraines as well as the lake-damming terminal moraine. Therefore, it is still likely that significant overtopping will result from an avalanche-generated wave in the fully formed lake. However, because the momentum would not be carrying the wave in the direction of the lake outlet, it is likely that the overtopping would be less than what is indicated by the volumes in Table 3.11. Finally, no definite conclusions about downstream impacts can be made with the available information. All that can be said at the moment is that there is the potential for significant overtopping volumes from an avalanche entering the fully formed lake. Further studies are needed to determine if there is a potential hazard to populated areas in the Paron valley, but the results presented here indicate that the emerging lake could be prone to outburst floods when it reaches its fully formed state.

3.4 DISCUSSION

Steps have been presented in this chapter for a progressive analysis of future conditions and hazard potential for emerging and growing glacial lakes, starting from field surveys of the glacier in its existing state and ending with calculations of potential GLOF scenarios based on bathymetric projections for the fully formed lake. While the use of GPR to observe ice thicknesses and bedrock topographies is not a new application, using the results of GPR for projections of future conditions with continued glacier retreat is an innovative concept. If climate change is to be viewed as a non-stationary process within GLOF hazard planning, it is time that hazard assessments and mitigation measures begin to consider future hazard conditions rather than exclusively assessing present conditions. The methods presented here show that it is a relatively straightforward process to go from GPR surveys to projections of future lake extent. With these future lake projections, it is possible to perform a simple GLOF hazard assessment in the same way it would be done if the lake were already fully formed.

Uncertainty

The methods for creating 3D bedrock topographies from GPR measurements have considerable uncertainty that is subsequently transmitted to the estimates of lake volume. Nonetheless, even uncertainty in the lake volume of up to 60-70% does not prevent a first-order assessment of the potential for an outburst flood from the emerging lake in its fully formed state. The uncertainties in the lake extent and bathymetry could be reduced with a more accurate, higher resolution DEM of the glacier surface and surrounding topography as well as more GPR transects that cover a larger portion of the glacier. Additionally, more precise GPS measurements in the GPR systems (such as a differential GPS incorporated into the GPR) could reduce uncertainties in the geographic coordinates

and especially in surface elevations used to determine the bedrock elevations. A more accurate surface topography would reduce the errors in the surface elevation of the edge of the glacier (used to constrain the interpolated bedrock topography) and in the elevation of the lake outlet. The elevation of the lake outlet is a parameter that has a significant impact on the lake volume, and reducing the uncertainty of this parameter would significantly reduce the uncertainty in the lake volume projections. However, the additional cost and time investment needed to reduce these uncertainties may not produce an equivalent return on investment. If interpolated bedrock topographies and the lake bathymetries linked to these elevations were used for more precise hydrodynamic models to produce official hazard maps or to evaluate specific mitigation alternatives (e.g. lake lowering scenarios), then it would be desirable to reduce the current uncertainties. However, errors within the existing range of uncertainty in the projections of lake depth and volume would not significantly affect the outcome (the potential range of overtopping volumes) and final conclusion of this work (that the fully formed lake may be prone to outburst floods).

In addition to the uncertainty in the projected lake volumes, there are also considerable uncertainties in the steps of the GLOF process chain that have been analyzed in this chapter. These uncertainties come primarily from the input variables that are not precisely known, but there are also uncertainties in the assessment methods themselves. The former type of uncertainty is somewhat easier to quantify by looking at the sensitivity of the results to a possible range of input parameters (such as the results shown in Table 3.12 for the overtopping volume calculations). However, as the potential GLOF considered here is comprised of a complex chain of processes whose connections are not precisely known, a thorough assessment of how the uncertainty in each individual parameter influences the overall uncertainty is beyond the scope of this work. Therefore,

the uncertainty in the projected lake volumes is the only uncertainty estimate that is precisely stated. All other discussions of uncertainty are limited to qualitative assessments of the sensitivity of individual calculations to input parameters.

Limitations

There are a number of limitations with the methodology presented in this chapter that must be considered when interpreting the results. Beyond the uncertainties discussed above, the results of this assessment are limited by two factors: 1) the limitations of the methods, and 2) this analysis is restricted to the upper portion of the watershed and does not consider potential impacts below the emerging lake.

The limitations of the methods presented in this chapter result from the simplified analysis approach that does not include numerical simulations. The avalanche parameters are very rough estimates, and the wave generation model can be quite sensitive to the avalanche characteristics, particularly the slide thickness and slide impact velocity. Without an avalanche simulation (that itself carries a considerable amount of uncertainty) and a more detailed analysis of avalanche release points, it is not possible to get any more precise estimates of these parameters. The method used here for representing wave generation by calculating maximum wave characteristics is an established method that has been applied to other studies of glacial lakes (e.g., Schneider et al., 2014; Baer et al., 2016). Therefore, the limitations of the wave calculations are not discussed here.

The primary limitation of the method for calculating overtopping volumes is that it has not been sufficiently validated to understand the errors and uncertainties. The foundational article on the tsunami runup equations (Synolakis, 1987) is one of the most recognized works in the tsunami literature, but the application of this approach to GLOF

hazard assessment is new, and the effects of these differences should be further analyzed before this approach can be applied for anything beyond a first-order assessment of the potential for a significant outburst flood. Specifically, this approach relies on tsunami equations based on a non-linear SWE approximation (Synolakis, 1987). It is reasonable to question whether or not these approximations are valid for glacial lakes where the distance traveled and differences in water depth between wave generation and runup are much less than for tsunamis. In addition, overtopping wave calculations do not account for changes in slope between the submerged portion of the moraine and the portion above water. For example, if an artificial dam is built with a higher slope above the water surface, and the moraine has a much gentler slope below the surface, this could result in errors in the runup calculations. The exact conditions of the lake's geometry influence what effects this limitation may have. For example, if the slope of the submerged portion of the moraine is gentle enough, it may be accounted for in the still water depth near the moraine; in this case, the slope used as an input parameter for the overtopping volume calculation would be the slope of the upper portion of the moraine. This example resembles the case for the fully formed lake at Artesonraju and for Lake Palcacocha (overtopping calculations in Appendix B). However, there are other lakes in the Cordillera Blanca that do not have this type of gentle slope leading up to the terminal moraine but rather have a more bowl-like shape to the bedrock topography (e.g. the rock-dammed Lake 513). It is unclear how well the method presented in this chapter could represent overtopping volumes for this type of lake. On the one hand, the submerged and above water slopes would likely be similar. On the other hand, the slopes for this type of lake could be high enough that the overtopping would be less like tsunami runup and more like a wave striking a vertical obstruction. Further assessment of the method presented here should be undertaken in lakes with a variety of bathymetric geometries.

This method appears to be promising in its ability to estimate overtopping volumes to within an order of magnitude (or less), but it should be used with caution until the validity of this method can be established for the application to GLOF hazard assessment.

The final limitation is that this analysis has focused on the upper watershed and does not include any potential downstream impacts, not a trivial limitation. Downstream inundation depends highly on the topography of the terrain between the lake and populated areas. Although steep slopes are prevalent between Lake Paron and the city of Caraz, the series of glacial lakes that a GLOF must pass through before reaching downstream areas makes this problem a very complex one. There currently is insufficient information about how a flood would propagate through Lake Artesoncocha and Lake Paron to be able to say whether a hazard for the city of Caraz exists. The steep drop in elevation between the emerging lake at Artesonraju and Lake Artesoncocha could potentially add a lot of energy into the overtopping flow as it enters Lake Artesoncocha. Conversely, there is the potential for energy loss as the flood passes over the very flat terrain between Lake Artesoncocha and Lake Paron. Without a detailed assessment of the cascading GLOF through this series of glacial lakes, it is difficult to assess whether or not the freeboard at Lake Paron (usually ~ 20 m) could contain the flow; the discharge at Lake Paron is the key factor that would influence inundation further downstream and potential impacts to populated areas. With the available information and the results presented in this chapter, it is only possible to state that there is a significant potential for a substantial volume of water to be discharged from the emerging lake if glacier retreat continues and the lake is allowed to reach its fullest extent.

Implications and Broader Impact

This work shows how field surveys can be used for projections of future hazard conditions so that decision-makers can have the information they need to take proactive steps towards addressing hazard before it becomes imminent. The methods presented in this chapter are intended to be simple enough that they can be useful analysis tools for local Peruvian institutions that are interested in evaluating potential GLOF hazards but do not have the resources to perform detailed simulations of the GLOF process chain. For this purpose, a first-order analysis (such as what has been presented in this chapter) is sufficient to determine if there might be a future hazard. This work only considers whether or not a significant outburst flood from the emerging lake is possible. As hazard involves the potential for an event to occur as well as the potential for the event in question to affect people or livelihoods, a complete watershed assessment is needed to determine if there may be any hazard for populated areas. If a potential hazard is identified, a more detailed analysis of the potential impacts of a GLOF is recommended before implementing mitigation works. The further analysis should include process chain simulations to assess the potential GLOF impacts for downstream populations.

Simulating a hypothetical GLOF for a lake that is not yet formed is something that has never been done before. Peru's approach to lake safety systems has traditionally been more reactive than proactive, and systems are typically designed for current rather than future lake conditions. However, the newly formed Glaciology Institute (INAIGEM, per the Spanish initials) has a vision for more proactive management of GLOF hazards, The methods presented here could advance their ability to assess future hazard conditions, thus enabling preemptive GLOF hazard management. For this type of anticipatory hazard assessment to be implemented at the regional level by the competent local agencies in Peru, methodologies are needed that are much simpler than the

prevailing approach that involves detailed simulations of each step in the GLOF process chain. The method for calculating overtopping volumes that was presented in this chapter is intended to meet this need for more simplified methodologies that can be broadly applied without too much difficulty. If this method can be adequately validated, it could prove to be a very useful tool for GLOF hazard assessment. This could enable Peruvian technical specialists working in INAIGEM to replicate the assessment performed at Artesonraju on a much broader geographic scale and assess many lakes without a significant investment of time and resources.

For the present, the work presented here provides an evaluation of future conditions and outburst flood potential for the emerging lake at Artesonraju Glacier. The GPR surveys and bedrock interpolations show that the conditions at Artesonraju are favorable for lake growth. Furthermore, the results of simple models of potential GLOF scenarios indicate that it will be possible for the fully formed lake to produce a significant flood volume in the event of an avalanche falling into the lake. If it can be shown that an emerging lake has the potential to be dangerous in the future, perhaps it will encourage a progressive and forward-thinking mentality for adaptation and mitigation of climate change related hazards in Peru.

Chapter 4: Climate Indices as a Tool for Climate-Resilient Infrastructure

This chapter addresses the data needs for public investment projects (PIPs) to be able to effectively incorporate climate change into the analysis of risk and vulnerability of projects. The analysis of climate data presented here is intended to address *Research Question #4*. This chapter is meant to serve as a proof of concept to show how scientific studies (if they are oriented towards the development needs of a local population) can be used to inform public investment project decisions and designs to make them more climate-resilient. This chapter explores the types of data analyses needed to improve understanding of the localized behavior of climate change and how to synthesize the results into information or conclusions that may be useful to PIP formulators. The work presented here is not meant to be a definitive climate change analysis but rather as a launching point to explore the possibility of developing standard analyses of climate data for irrigation projects in the Sierra Ancash.

Research Question #4: How can the gap between science and policy in the context of climate change and adaptation in Ancash be breached by simplifying methodologies for vulnerability analysis without losing validity of results?

Methods of analysis of climate data related to agriculture or irrigation projects are presented as a case study demonstrating the types of analyses that could be used for PIP proposals. This chapter presents analysis of precipitation data in ways that might affect crop productivity with an emphasis on the variability of precipitation in the rainy season. Potential applications of this type of analysis include assessing the supply and demand

for agricultural projects. In regions such as the Sierra of Ancash that rely heavily on rainfall to meet crop water requirements, intermittent droughts can have a large effect on crop productivity (Bodner at al., 2015). Agricultural water demand is very closely linked with precipitation, and periods of time when rainfall is less than expected result in increased irrigation demand to make up for the shortfall in precipitation. Sanabria et al. (2014) investigated the potential impacts of climate change on crop production in the Cusco and Apurimac Departments in Southern Peru and determined that there may be increased risk of crop failure, earlier harvest dates and shorter growing seasons in the future; however, they concluded that there is a need for better understanding of changes in precipitation patterns to be able to effectively evaluate adaptation options. Climate-resilient agricultural projects should have mechanisms in place (through project design) that give them the flexibility to adapt to a range of potential weather and climate conditions. Information on the range of potential conditions is needed for fully-informed design decisions that consider this added level of flexibility. For example, if an agricultural project is implemented in an area that is seeing increasingly common dry spells during the rainy season, then the project design should incorporate irrigation infrastructure that can supplement the water from precipitation in the absence of rain; this type of option is especially important if the project only intends for crops to be cultivated in the rainy season, and water storage for irrigation use during the dry season would not typically be considered as part of the project. The operation and management plan for the project should also include contingency plans for irregularities in climate conditions that might occur so that operators know how to use the infrastructure to compensate for weather anomalies.

Lack of in-situ data is a problem that must addressed for most projects or studies in developing countries. The Peruvian government allows project formulators to use data

on people's perceptions of climate change and vulnerability as a substitute for measured data (MEF, 2015), but there are currently no protocols for how to incorporate perceptions of climate change into a vulnerability analysis for a project. In addition, there has been very little analysis of the accuracy of the qualitative information gathered from local populations as compared to quantitative measurements of climate variables (Vergara Rodriguez, 2011); this type of comparison is needed to be able to gauge the efficacy of using perceptions of climate change in lieu of gauged data in cases of the absence of the latter. With this in mind, the analysis in this chapter is oriented towards comparisons of historical gauged data with results from a study of perceptions undertaken in several communities of the Sierra Ancash (Vergara Rodriguez, 2011; 2015).

The data analysis presented here uses precipitation data, although similar analyses could be performed with temperature data. This work focuses on precipitation data for two reasons: 1) water is the primary resource or input for irrigation projects and 2) precipitation variability and trends have not been well characterized for the Sierra Ancash. Additionally, longer records of daily precipitation data were available, whereas temperature data for periods longer than 20 years could not be obtained for this study; a minimum of 30 years of data are needed for any meaningful analysis of trends. Finally, the results of the study of perceptions of change were much more heterogeneous for precipitation related variables than for temperature, making an analysis of corresponding climate data much more interesting. The study of perceptions showed somewhat conclusively that the population has perceived an increase in temperature, and it would not be difficult to show that trend in the data if they were available; however, the perceptions of changes in precipitation and reliability of the rainy season were much more mixed. Vergara Rodriguez (2011) hypothesizes that the heterogeneity in perceptions of changes in precipitation reflects a highly variable system. This is a theory

that merits further investigation, and a thorough analysis of the variabilities in the precipitation data could either prove or disprove this hypothesis.

The concept of climate indices involves analysis of climate data to determine thresholds at which projects could be impacted (critical values for climate variables) and to quantify probabilities or how often those thresholds might be surpassed. This concept could be applied to temperature and precipitation data as well as a number of secondary climate variables. Of especial interest to the agricultural sector are changes in the variability of precipitation and changes in the rainy season (delays in the onset, duration, reliability of rainfall, etc.), thus motivating the focus on precipitation data in this chapter. The analysis of trends in the precipitation data should also provide information about how climate change has impacted precipitation patterns. It is necessary to have this type of fundamental understanding of the relationship between climate change and precipitation (that is still not very well understood from a climatological perspective) before assessing secondary impacts of climate change that could influence the vulnerability of PIPs (such as streamflow and irrigation demand). Because atmospheric circulation models and principles of physical climatology are not yet able to predict precipitation patterns and variability with the level of certainty (or lack of uncertainty) needed for long-term planning and climate change vulnerability assessment, statistical analysis of historical data is needed to gain a better understanding of climatic trends, variability and uncertainty. This approach of using historic conditions and variability to characterize the range of probable future conditions is similar to the use of historical streamflow data for flood frequency analysis in the field of stochastic hydrology. Characterizing variability in climatic variables is a first step towards estimating future uncertainty of those same variables. PIP proposals can then use the knowledge of uncertainty to create more resilient and sustainable projects.

Background information is presented in Section 4.1, including previous work on climate and drought indices and information about the study area and data. The methodological framework, developed to address the research question presented above, is outlined in Section 4.2. The results of the data analysis are presented in Section 4.3, and a discussion of the implications of these results, possible next steps in the development of specific climate indices, and possible applications to PIPs follows in Section 4.4.

4.1 BACKGROUND

4.1.1 Climate and Climate Change in the Sierra Ancash

The climate in the Sierra Ancash is primarily driven by tropical atmospheric circulation patterns with easterly trade winds carrying moisture across the mountains from the Atlantic Ocean and Amazon River Basin (Aceituno, 1987; Garreaud, 2009). Because of the orographic lifting that occurs when the easterly winds reach the mountains, the eastern side of the mountains in Ancash is typically wetter than the western side, and the precipitation decreases in the westward direction (Garreaud, 2009; Espinoza Villar et al., 2009). The seasons in the Sierra Ancash are the rainy season and dry season. The rainy season is caused by the proximity of the Intertropical Convergence Zone around December – March, and the dry season (June – August) corresponds to austral winter (Kaser and Osmaston, 2002; Garreaud, 2009). There are several months of transition between the rainy and dry seasons (September – November and April – May) that have intermittent precipitation. The temperature in the Sierra Ancash is highly correlated to elevation. Microclimates in the Sierra Ancash are often delineated by altitudinal zones, and many crops only grow in specific elevation bands owing to the

climatic characteristics that are needed for optimal growth. In the tropical high mountains, the combination of low atmospheric density and high incoming solar radiation causes high diurnal variability in temperature with diurnal temperature swings that can exceed the range of seasonal variability (Kaser and Osmaston, 2002). Temperature can also be linked to precipitation to a certain degree, as cloud cover can influence the levels of incoming and outgoing radiation. During the rainy season, cloud cover can moderate temperature variability. Daytime cloud cover limits the daily maximum temperatures, and nighttime cloud cover limits the loss of heat through outgoing longwave radiation. Because of this effect, if there is a delay in the onset of the rainy season, the lack of cloud cover can result in higher daytime temperatures and more frequent frosts during the transition months (due to clear nighttime skies that can cause lower than normal nighttime temperatures). Therefore, a better understating of precipitation variability can also enhance understanding of potential variability in temperatures.

The interannual climate variability in the Sierra Ancash is heavily influenced by the El Niño Southern Oscillation (ENSO) cycle. Still, the impacts of El Niño and La Niña events on precipitation in the Sierra Ancash are not very well understood. El Niño, the warm phase of ENSO, causes a weakening of the easterly trade winds. In El Niño years, temperatures in the Sierra Ancash are generally warmer, and more of the moisture that causes precipitation originates from the Pacific than in normal years (Lavado-Casimiro and Espinoza, 2014; Garreaud, 2009). The cold phase of ENSO, La Niña, is characterized by stronger easterly trade winds that accentuate the typical atmospheric circulation patterns. In the Sierra Ancash, La Niña typically causes colder than normal temperatures (Lavado-Casimiro and Espinoza, 2014). The effects of both phases of the ENSO cycle on precipitation are highly spatially variable, and the mechanisms that cause increases or decreases in precipitation in El Niño or La Niña years are not well understood. It is

possible that climate change is influencing the magnitude of El Niño events. An increasing trend in ENSO amplitude has been observed, but it is uncertain whether this trend should be attributed to climate change or natural variations (Christensen et al., 2013). There is a high degree of uncertainty about the impacts of climate change on the frequency of future ENSO events (Christensen et al., 2013).

In recent history, a general warming trend has been observed in the Andes with an increase of around 0.1 °C per decade since 1939 and greater rates of increase in recent decades (about 0.33 °C per decade since 1975) (Vuille and Bradley, 2000). Most global circulation models (GCMs) predict an increase in temperature for the Andes, but the magnitude varies with the model. The GCM projections for increase in temperature in the Peruvian Andes are given in Table 4.1. In general, the projected increase in temperature is more pronounced in the winter than in the summer months. The regional climate model (RCM) of Urrutia and Vuille (2009) projects that the greatest high-elevation warming in the tropical Andes will be in the Cordillera Blanca, and these temperature increases may be several degrees greater than the GCM projections.

Table 4.1- Predicted increases in temperature relative to 1986-2005 for the Peruvian Andes based on the 50th percentile results of the medium-low RCP4.5 and high RCP8.5 emissions scenarios (IPCC, 2013: Annex I)

Years	RCP4.5 increase for June, July and August (austral winter)	RCP4.5 increase for December, January and February (austral summer)	RCP8.5 increase for June, July and August (austral winter)	RCP8.5 increase for December, January and February (austral summer)
2016-2035	0.5-1 ˚C	0.5-1 ˚C	0.5-1.5 ˚C	0.5-1 ˚C
2046-2065	1.5-2 ˚C	1-1.5 ˚C	2-3 ˚C	1.5-3 ˚C
2081-2100	2-3 ˚C	1.5-2 ˚C	3-5 ˚C	3-4 ˚C

Predicted changes in precipitation are much more uncertain, but the ensemble prediction based on the medium-low emissions scenario (RCP4.5) is a 0-10% increase in precipitation in the Andes; the highest emissions scenario (RCP8.5) projects a 0-20% increase in precipitation (IPCC, 2103: Annex I). GCM predictions also indicate that seasonal variability in precipitation will be enhanced with increased precipitation in the wet season and decreased precipitation in the dry season (Vuille et al., 2008), and this projection is confirmed in the RCM for the tropical Andes (Urrutia and Vuille, 2009). There are very few long-term records of in-situ data recorded in the Cordillera Blanca, and for this reason the only analyses looking at trends have been done at the regional scale and not for local sites (e.g., Espinoza Villar et al., 2009; Vuille and Bradley, 2000).

A few studies have looked at gridded data products in the tropical Andes (e.g., Mourre et al., 2016; Condom et al., 2011b; Hofer et al., 2010). This region has a high level of spatial variability in climate due to the extremely variable topography (Espinoza Villar et al., 2009), and because of this, most studies have concluded that large-scale gridded datasets do not adequately represent the local weather patterns without correction. Hofer et al. (2010) proposed a statistical downscaling method for correcting NCEP/NCAR reanalysis data based on in-situ observations at Artesonraju Glacier. Condom et al. (2011b) compared TRMM precipitation data to in-situ weather station data and concluded that TRMM underestimates precipitation in the rainy season and overestimates it in the dry season; they therefore proposed a correction algorithm for the use of TRMM data at high elevations in the Peruvian Andes. Mourre et al. (2016) assessed several precipitation datasets for potential use in glacio-hydrologic models, investigating the effectiveness of the type of product and spatial resolution for reproducing precipitation patterns during one hydrologic year. Mourre et al. (2016) compared Kriging-interpolated in-situ data with TRMM and results from a WRF regional

climate model. They concluded that while none of these produces precipitation estimates with the level of accuracy at the time scales needed for glacio-hydrological models, the coarse-gridded products could be useful as indicators of the spatial patterns of variability.

The Peruvian government has recognized the importance of climate change and the potential consequences of climate change impacts. As a result, the Ministry of Economy and Finances (MEF) now requires that all PIP proposals consider climate change in the project's vulnerability assessment (MEF, 2016). Yet, this is very difficult given the limited local information on climate change, sparse historical climate records and uncertainty in climate change impacts. To compensate for the lack of in-situ data, the MEF allows for local perceptions of climate change to be used in lieu of gauged data. However, this policy was put in place without considering the accuracy and usefulness of data on local perceptions of change. Studies on the local population's perceptions of climate change (Vergara Rodriguez, 2011; 2015) are used in this chapter as a point of comparison with the climate data analysis to assess the accuracy of perceptions of change as they relate to PIPs.

4.1.2 Climate and Drought Indices in the Literature

The use of climate indices to quantify shifts or trends in meteorological variables due to climate change is not a new concept, and discussions of climate indicators are intertwined with the discussion about climate change itself. A number of groups have developed specific indicators for a variety of climate variables (e.g., ETCCDI, 2009; Peterson et al., 2001). The CCI/CLIVAR/JCOM Expert Team on Climate Change Indices from the World Climate Research Programme (ETCCDI) has identified 27 core indices

of climate extremes looking at various aspects of temperature and precipitation data (ETCCDI, 2009). A list of these indices is given in Appendix D.

Temperature Indices

Of the ETCCDI temperature indices, the index that seems to be most readily applicable to agriculture projects in the Cordillera Blanca is the *number of frost days*. Other potentially useful temperature indices in the context of PIPs in the Sierra Ancash are the *monthly maximum and minimum temperatures*, the *daily temperature range*, the *percentage of days when the minimum temperature is less than the 10th percentile* and *percentage of days when the daily maximum temperature is greater than the 90th percentile* (compared to a baseline period of 1961-1990). The first three indices are indicators of normal temperature variability, and the latter two indices are indicators of changes in the frequency of temperature extremes. Peterson et al. (2001) suggest 10 key indices to monitor climatic extremes at a global scale (also presented in Appendix D), and most of the indicators in this list also appear on the ETCCDI list.

Precipitation & Drought Indices

Because this dissertation is principally about water security, the analysis of climate data in this chapter focuses exclusively on precipitation. The Sierra Ancash region has regular precipitation patterns (i.e., a rainy season and a dry season with rain more common in the afternoons and evenings than in the morning), but there can be a lot of variability within the typical patterns. For instance, the start of the rainy season and the amount of rainfall during the rainy season can vary from year to year. Because of the seasonal nature of precipitation, drought takes on a different meaning in the region than

many other places in the world. It is normal for there to be little to no precipitation in the months of June, July and August, and the streamflow typically decreases accordingly (although there is some amount of baseflow in many streams and rivers supplied by groundwater and glacial melt). Therefore, lack of rain in the dry season should not be considered a drought. In the context of agricultural projects, problems arise when the typical precipitation patterns break down and rain fails to come at the normal times of year.

There are numerous definitions of drought, and many depend on the application and geographic region. Drought typically describes conditions when precipitation is less than normal, with the shortfall in precipitation resulting in water shortages that fail to meet the local needs. Wilhite and Glantz (1985) have divided drought definitions into four categories: meteorological, agricultural, hydrological, and socio-economic. Meteorological droughts are defined based on precipitation deficits and are linked exclusively to the amount of rainfall, and the latter three drought categories are related to the impacts of precipitation shortfalls. Agricultural droughts relate precipitation deficits to impacts on soil moisture and crop productivity. Hydrological droughts are typically defined over longer timescales and describe effects on streamflow and groundwater. Socio-economic drought definitions link droughts with their impacts on human societies; droughts may be considered much more significant if they affect vulnerable populations and have lasting economic impacts that continue beyond the time of the shortfall in water availability. In the context of precipitation data analysis for agricultural PIPs, meteorological and agricultural droughts are most relevant. The precipitation data analysis in this chapter is meant to be a precursor to a region-specific definition of drought for the Sierra Ancash. The subsequent paragraphs present a review of

precipitation climate indices and the most common drought indices with discussions of their potential applicability to the Sierra Ancash.

Agricultural projects can be affected by both too much and too little rainfall. Of the precipitation related indices presented in Appendix D, the ones most likely to be applicable to agricultural projects are related to rainfall intensities and dry spells. The indices related to intensity include the *monthly maximum 1-day precipitation*, the *simple daily intensity index* and the annual *count of days when the precipitation exceeds nn mm*. The threshold *nn* for the latter index should be determined based on what intensities are considered normal for a particular area and what level of daily precipitation is likely to cause significant damage; because of the spatial heterogeneity of weather and climate patterns, it is best to determine this threshold at the local scale (for each microclimate). In the 27 ETCCDI core indices, the only precipitation index related to insufficient rainfall is the *maximum length of dry spell*. This can be useful in the Sierra Ancash because significant periods of time without rain can affect crops (in the absence of irrigation to compensate for precipitation deficits), but the usefulness is limited because this index does not distinguish between dry season and rainy season. More significant in the Sierra Ancash are aberrations from normal precipitation behavior, particularly dry spells that occur during the wet season. The *maximum length of dry spell* index will most likely be dominated by dry periods in the dry season, but dry spells in the rainy season are more significant for agricultural projects because farmers more often rely on rain to water their crops in the rainy season. There is a need to develop indicators of drought or dry spells that are specific to the Sierra Ancash region.

Heim (2002) describes the evolution of drought indices from simplified definitions based on precipitation data (that have limited links to hydrologic impacts) to more complex calculations involving water balance, soil moisture, streamflow, vegetation

cover, and other impacts of precipitation deficits. Indices based on precipitation data can be useful, as they are the simplest to calculate, but many of the early precipitation-based definitions of drought were not sufficiently validated against historic climate conditions. There has been very little study on the links between precipitation, dry spells and agricultural and hydrologic impacts in the Sierra Ancash. Therefore, the best approach to a drought index for the Sierra Ancash may be to study historic climate patterns, including typical dry spells, to determine precipitation thresholds that can be considered abnormally dry.

The most widely used drought index in the United States is the *Palmer Drought Index*, also known as the Palmer Drought Severity Index (PDI or PDSI) (Palmer, 1965). The PDI uses a water balance approach for an algorithm that calculates theoretical soil moisture conditions, and the index typically has a lag between meteorological drought and hydrologic drought (Heim, 2002). The PDI works best at longer time scales and can identify droughts of durations of several months or more but is not as good at indicating droughts lasting on the order of weeks (Hayes, 2016). The *Percent of Normal* index is a simple means of comparing rainfall to normal conditions and can be useful for assessing drought in a single region or an individual season; it is calculated by comparing the measured precipitation in a given year, month or season to the normal precipitation as a percentage of the 30-year mean (Hayes, 2016). The *Standardized Precipitation Index* (SPI) calculates a probability for measured precipitation using frequency distributions and then converts the cumulative probabilities to a standardized scale using an inverse normal distribution (McKee et al., 1993). Although it does not use standardized precipitation in its calculation, the SPI is based on the concept of standardized precipitation, which is the precipitation with the mean subtracted and divided by the standard deviation (mean and standard deviation are calculated for the given time of year)

(McKee et al., 1993). *Precipitation deciles* are another simple way to quantify drought, an approach used by the government of Australia to determine when to supply aid to farmers (Gibbs and Maher, 1967). The use of deciles as a drought index involves grouping monthly precipitation into deciles (levels of non-exceedance in groups of 10%). When the 3-month cumulative precipitation is in the first or second decile (levels not exceeded more than 20% of the time), drought conditions exist, with severe droughts being defined as 3-month totals in the first decile (Wilhite and Glantz, 1985). Other common drought indicators include the *Crop Moisture Index* (CMI) that assesses short-term crop conditions (Palmer, 1968); the Surface Water Supply Index (SWSI), a supplement to the PDI for mountainous regions, particularly regions with snowpack (Shafer and Dezman, 1982); and the Reclamation Drought Index (RDI) that calculates drought at a basin level with snowpack, streamflow and reservoir levels as inputs in addition to climate data (Hayes, 2016).

Of the major drought indices, the SPI (McKee et al., 1993, 1995) is one of the indices that could most easily be applied in the Sierra Ancash because it only requires precipitation data as an input. The SPI is generally calculated using monthly precipitation data and can be assessed for a range of time scales. The user-defined time scale (period of i months) is the period of time for which historical data are used to determine a precipitation deficit or surfeit, and this is done by calculating a running average for the previous i months before calculating the cumulative probability of the time-averaged rainfall. An inverse normal distribution (mean 0, standard deviation 1) is then applied to the standardized precipitation value, resulting in the value of the SPI for a given month. Thus, the monthly precipitation averaged over the period corresponding to the time scale determined by the user is compared to normal values for the given time of year and converted to an easily comparable scale. The thresholds for defining a drought and its

severity depend on the application, but in general SPI values between -1 and -1.99 indicate mild to severe droughts, and values less than -2 correspond to extreme droughts. The periods of time that would be defined as a drought changes with the time scale, and for longer time scales, droughts tend to be less frequent and of longer duration (McKee et al., 1993). Guttman (1999) gives some recommendations on standard procedure for calculating the SPI, including using the Pearson Type III distribution for calculating the cumulative probability and a maximum time scale of 24 months. Guttman (1999) also concludes that the SPI is less reliable for small sample sizes. There is a wide variety of existing drought indices, many tailored to a specific application, type of drought, or location. None of the drought indices are universally applicable. The unique climate and patterns of variability of the Sierra Ancash require a region-specific drought index, but the precipitation patterns of the region must first be characterized so that the drought index can adequately quantify departures from the normal.

4.1.3 Data and Study Area

The analyses presented in this chapter are meant to illustrate the concept of climate data analysis and were therefore calculated for precipitation data at one weather station. These analyses could be repeated at other weather stations where a sufficiently long record (30+ years) of daily data is available. The data used for this study were the data used in Vergara Rodriguez (2011) and were provided to Vergara Rodriguez by the Servicio Nacional de Meteorología y Hidrología del Perú (SENAHMI). The weather station data were collected at Cachicadan, located at an elevation of 2890 amsl in the Region of La Libertad, just north of Ancash in the Santa River basin (see Figure 4.1). Daily precipitation data from the weather station at Chachicadan were available from

September 1963 through December 2010 with data gaps from May 1982 – December 1984 and in February 2004. There are also daily precipitation data for similar time periods available from weather stations located at Mollepata (2580 msl) and Sihuas (3375 msl), and it would be possible to repeat the data analysis in this chapter with the data from these stations.

Data availability in Peru is a critical problem that should be addressed at the regional level in order to facilitate analysis of climate and weather patterns and trends. These types of studies are essential to the analysis of vulnerability of PIPs to climate change. The data available for this work were limited to the data used in the climatological analysis in Vergara Rodriguez (2011); therefore all of the weather stations with available data are located near the Campesina Community of Conchucos where the local surveys, interviews and workshops were undertaken. The climate data analysis of Vergara Rodriguez (2011) focuses primarily on measures of central tendency to characterize the climate and the application of the SPI (calculated annually) to identify abnormally dry or wet years. This work is not meant to repeat the analysis in Vergara Rodriguez (2011) but rather to build upon that work, particularly in the areas of analysis of variability and extreme events.

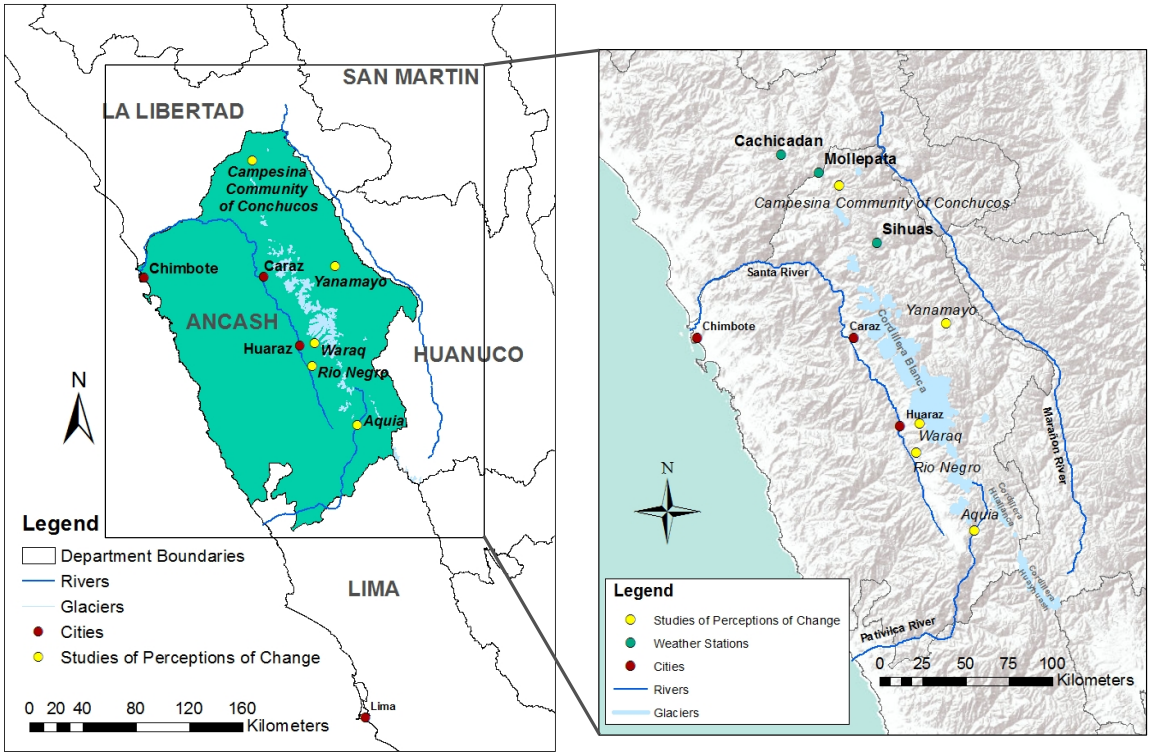

Figure 4.1- Map showing the locations of the weather stations and studies of perceptions of change in Vergara Rodriguez (2011, 2015)

The results of the study of perceptions of climate change from Vergara Rodriguez (2011, 2015) that are relevant to this work are presented in Appendix E. The people's perceptions of changes in temperature, precipitation quantity, and precipitation intensity were documented from interviews in the Campesina Community of Conchucos, the district of Aquia (headwaters of the Pativilca River basin), the subbasin of the Rio Negro (tributary to the Santa River), the Waraq Commonwealth (the Auqui and Paria catchments in the Cordillera Blanca as well as the towns of Santa Cruz and Wilcacocha in the Cordillera Negra), and the Yanamayo Commonwealth (the Yanamayo River is a tributary to Marañon River and part of the greater Amazon Basin). The general trends

observed were an increase in temperature (Table E.1, observed by 91% of all people surveyed), a decrease in the amount of rainfall (Table E.2, observed by 73% of all people surveyed), and a decrease in rainfall intensity (Table E.3, observed by 52% of all people surveyed). Additionally, perceptions of changes in seasonality for the rainy and dry seasons (Table E.5 and E.6, respectively) were recorded for Aquia, Rio Negro, Waraq, and Yanamayo. The most common observation about the rainy season is that the seasonality is out of sync compared to patterns 30 years ago (observed by 51% of all people surveyed), and the most common response about the dry season is that it is longer than it was 30 years ago (observed by 46% of all people surveyed). The responses to changes in rainfall intensity and seasonality were more varied than the other variables that people were questioned about; this may be an indication of greater uncertainty or variability in rainfall intensity and seasonal precipitation patterns. Nonetheless, very few people (less than 4%) have observed a longer rainy season or a shorter dry season, implying that if there have been changes in seasonality, they are more likely to be have a tendency towards drier conditions.

Regarding perceptions of droughts, the people of Aquia, Rio Negro, Waraq, and Yanamayo were questioned about how they define droughts. This was an interesting exercise concerning the wide-ranging definitions of drought, and while the responses were varied, most were related to precipitation shortfalls or generally dry conditions of the land. The responses are shown in Table E.7 (Appendix E). The survey participants in Conchucos were questioned about the occurrence of droughts, and the majority (81%) have observed increased frequency and intensity of droughts compared with 20 years ago; this is greater than the percentage of participants who have observed a decrease in the quantity of precipitation, implying that the timing of precipitation (as well as the quantity) influences droughts.

4.2 METHODS

In context of the USAID steps for climate-resilient development presented in the introduction, this chapter focuses on the following stages: (1) *scope* and (2) *assess*, as well as the preliminary phase of analysis of climate trends and projections (*phase 0*) that was proposed in the introduction as an addition to the climate-resilient development protocol proposed by USAID.

Research Question #4 is related to linking scientific knowledge to policy and decision-making, and this will be discussed in Section 4.4. However, to guide the methodological framework in this chapter, it seems expedient to propose a research question and hypotheses related to precipitation patterns. The most important aspect of precipitation patterns for the agricultural sector is the regularity and quantity of rain in the rainy season. Therefore, the research question formulated for this chapter is:

Research Question #5: Have the character and reliability of the rainy season changed in recent decades?

The work presented in this chapter is oriented towards answering this research question about changes in the precipitation patterns in the rainy season. To answer this question, data analysis should include assessment of intensities, heteroscedasticity, dry periods in the rainy season, and the start and end dates of the rainy season. Both climate (long-term trends and patterns) and weather (short-term conditions) are considered in this chapter. Based on qualitative observations of the local population (summarized in Section 4.1.3), the following working hypotheses have been formulated:

Hypothesis #1: The amount of precipitation in the rainy season has decreased over the period of record for precipitation data (1963-2010).

Hypothesis #2: Variability in precipitation has increased for all months of the year.

Hypothesis #3: The start of the rainy season has been delayed in recent years compared to several decades earlier.

Hypothesis #4: Dry spells during the rainy season and transition months leading into the rainy season have become more frequent and of longer duration in recent years.

Hypothesis #5: Rainfall intensities have decreased in recent years compared to several decades earlier.

The methodology for precipitation data analysis used in this chapter was developed with the following key aspects in mind:

- Typical precipitation patterns
- Trends
- Changes in variability and seasonality
- Dry spells
- Rainfall intensities

Section 4.2.1 addresses the climatology of Cachicadan (the location of the weather station where the data analyzed in this chapter were collected). Section 4.2.2 presents methods to evaluate the data for trends and variability in the seasonal precipitation patterns. Section 4.2.3 describes ways to evaluate the data for variables that may be indicators of droughts and precipitation intensities. The methods presented in this chapter are intended to illustrate climate data analysis procedures that can be used to better understand the climate as well as patterns of climate change of a region. Characterization of climate and climate change patterns is fundamental knowledge that is a prerequisite to developing climate indices to quantify potential future climate trends and variability.

4.2.1 Seasonal Precipitation Patterns

Seasonal precipitation patterns (what can be considered typical for each season or month of the year) are analyzed with group statistics calculated on monthly precipitation totals for the period of record (1963-2010). The mean and standard deviation were calculated to get an idea of "normal precipitation" for each month and what may be a normal amount of variability; trends in these variables are assessed separately in Section 4.2.2. In addition, the monthly precipitation data were converted into a box plot, a non-parametric analysis of central tendency and variability for each month that is less affected by outliers. Box plots show the monthly median, interquartile range, range of variability (values within 1 step of the interquartile range, where a step is defined as 1.5 times the interquartile range), and outliers (more than 1 step beyond the interquartile range). Frequency histograms of total precipitation for each month were calculated to show what values of monthly precipitation within the range of variability are most common.

4.2.2 Trends and Shifts in Seasonality

Regarding changes in precipitation patterns, two topics must be addressed: trends and heteroscedasticity. Analysis of trends assesses whether there is an upward or downward tendency in precipitation; or, on the contrary, no trend implies that there is no tendency towards change in the magnitude of precipitation. If there are trends detected, the direction of the trend can give an indication if climate change is generally providing more or less rainfall in a given season. Trends detected in the rainy season or dry season can indicate whether the typical seasonal rainfall patterns are enhanced or diminished. Trends detected in the transition months can possibly be indicators of the regularity of the onsets of the rainy and dry seasons and if there have been any changes in these seasonal transitions. Another possible indicator of the reliability of the seasonal precipitation

pattern is heteroscedasticity. Homoscedasticity means that there is no change in the variability of the variable of interest (in this case, precipitation), and the converse, heteroscedasticity, signifies that the variance is not constant. Analysis of the time dependence of the variance of precipitation can give an idea of both the normal amount of variability and whether or not variability has increased or decreased.

To look at trends in precipitation and changes in seasonality, two key questions must be answered:

1) Has precipitation increased, decreased or stayed relatively consistent for each month of the year?
2) Has the variability of precipitation for each month remained constant, increased, or decreased (i.e., is precipitation for each month homoscedastic or heteroscedastic)?

Trends in the monthly precipitation data were analyzed with two different methods. The Mann-Kendall test was run at the 5% significance level on the time series of precipitation totals for each month; the result is either acceptance or rejection of the null hypothesis of no trend in a month as well as values for Kendall's *S* statistic (positive values signify increasing trends and negative values signify decreasing trends) and the p-value that indicates the probability of the resulting *S* statistic if the null hypothesis is true (lower p-values indicate that a trend is more likely). The *S* statistic for each month was also used in the seasonal Kendall test to calculate an overall *S* value for the whole year according to the method outlined in Helsel and Hirsch (1992). The seasonal Kendall test served to determine if there is an overall trend in precipitation (if the annual total precipitation has an increasing or decreasing tendency). The Mann-Kendall test is a non-parametric test that is a simple greater than/less than comparison between a given value

and subsequent data points, and this test is not affected by the magnitude of precipitation. The argument can be made that the magnitude is important for detecting trends; if higher monthly precipitation is more common with climate change, the increase in magnitude implies an increasing trend. To account for the magnitudes in monthly precipitation trends, a 10-year moving average was calculated for each month (the mean monthly precipitation calculated over moving windows of 10 years each). To determine if there is a trend in the 10-year moving averages, the Mann-Kendall test was run on the 10-year moving average precipitation with a 5% significance level.

The data were analyzed for heteroscedasticity with the 10-year moving standard deviation; this was calculated in the same way as the moving averages, with the standard deviation calculated on the data for each 10-year window. Trends were detected in the 10-year moving standard deviation with the monthly Mann-Kendall test at a 5% significance level. Any trend detected in the moving standard deviation implies that the data for that month are heteroscedastic, but of interest here are primarily the months with increasing standard deviations. An increasing standard deviation indicates that there is more variability now than 20-50 years prior, and this can be considered a metric of decreasing reliability; an increasing standard deviation means that the amount of precipitation for that month is less predictable than it used to be.

To assess the reliability of the rainy season, a quantitative metric for the start of the rainy season must first be defined. Although it is common to qualitatively discuss when the rainy season starts, few researchers have looked at the start of the rainy season in a quantitative way. If you ask the average person in the Sierra Ancash when the rainy season starts (this is a question I am constantly asking people), some will say September, more will say October or November, some will say December, and a few will even say January (this answer is more common with people living in the drier Cordillera Negra).

There is a similar variability in responses to the question of when the rainy season ends. In general, September – November and April – May are considered transition months, and the months of December – March are more reliably part of the rainy season. However, the date of onset of persistent, reliable precipitation can be highly variable from year to year. Before analyzing the variability in the start of the rainy season, the question must be asked: How do we quantitatively define the start of the rainy season? Very much tied up with this question is: what factors should be considered in defining the rainy season dates? The most important factors to consider for the start date of the rainy season are the amount of precipitation and the number of days with rain. To facilitate analysis of rainy season precipitation, *the water year is defined in this dissertation as September – August*. The simplest way to define the start of the rainy season is to look at accumulated precipitation: once a certain threshold of total precipitation for the water year has been reached, the rainy season has officially started. Another way to define the start of the rainy season is to look at a combination of the accumulated precipitation and a minimum number of consecutive days without rain. This type of definition would have to be determined retroactively, thus making it slightly more complex to evaluate in the context of water planning and management. The minimum number of consecutive dry days should be based on historic rainfall patterns, and the prior analysis needed to determine this threshold could be quite complex. In this dissertation, the first method for defining the start of the rainy season (accumulated precipitation threshold) is applied.

The next question is how to determine the threshold for accumulated precipitation that can be used to define the start of the rainy season. A clear place to start is to look at the mean and median precipitation for each of the three transition months (September – November). The mean and median values for each month are given in Table 4.2 (Section 4.3.1). The sum of the mean and median precipitation values for September – November

were used as a starting point to determine possible thresholds for accumulated precipitation to define the start of the rainy season. To look at the effect of varying this threshold on the rainy season start date, thresholds of 100 mm, 150 mm, and 200 mm were chosen to define three different start dates for each year. The mean and median start date was calculated for each threshold to facilitate comparison between the different accumulated precipitation thresholds, and the standard deviation of the start date was calculated for each threshold to characterize the amount of variability typically seen in the initiation of the rainy season. Trend analysis on the start date of the rainy season was performed with the Mann-Kendall test (5% significance level) applied to the dates calculated with all three thresholds. Detection of a positive trend would imply a tendency towards a delayed start of the rainy season in later years, and a negative trend would indicate that the rainy season has started earlier in more recent years.

The analysis of trends and changes in seasonality presented in this section provides a foundation for assessing climate change impacts on precipitation and assessing the reliability of precipitation in the rainy season, the time of year when agricultural workers are most dependent on reliable rainfall to water their crops. This analysis also presents first steps towards quantifying future uncertainty that can be used to propose potential ranges of precipitation values for each month that should be considered when assessing supply and demand for an agricultural project.

4.2.3 Climate Extremes: Dry Periods and Rainfall Intensities

The methods in this section focus on data analysis related to droughts and extreme precipitation events. Developing a regional drought index goes beyond the scope of this work, but the analysis of variables related to droughts presented here can be considered a

precursor to a drought index. The primary variable of interest related to droughts is the number of dry days. A dry day is defined as a calendar day in which no measurable precipitation is recorded. The precipitation data used in this chapter has some daily rainfall records of trace amounts of rainfall (too little to be measured accurately), and those data points were converted to 0 mm of rainfall for the purpose of data analysis. The number of dry days for each month in the dataset were calculated and plotted as a function of time. The time series of dry days/month was analyzed for trends to determine if dry days are becoming more or less frequent with time. The Mann-Kendall test for trends (at a 5% significance level) was performed on the time series for each month of the number of dry days. Additionally, the 10-year moving average of dry days/month was calculated for each monthly time series. Finally, to assess the variability over time, the 10-year moving standard deviation of the number of dry days/month was calculated for each monthly time series. Trends in the 10-year moving standard deviation of dry days/month were detected by the Mann-Kendall test at the 5% significance level.

In addition to the absolute number of dry days in each month, the length of each dry spell (consecutive dry days) was calculated. The water year was divided into three seasons: (Season 1) September – December, (Season 2) January – April, and (Season 3) May – August. These seasonal delineations are not completely aligned with the rainy, dry and transition months defined in Section 4.1.1; however, this definition of three seasons was selected to have seasons of equal duration that roughly align with the transition months (Season 1), the rainy months (Season 2), and the dry months (Season 3). The maximum number of dry days in each season was plotted as a function of time. The assessment of the maximum number of consecutive dry days by season was necessary because the seasonal nature of rainfall means that longer dry spells are more common in the dry season (Season 3) than in other seasons. If the maximum number of consecutive

dry days per year were calculated, then the results would be dominated by the dry season, thus concealing important information about the length of dry spells in the transition months and the rainy season. Complications in the calculation of maximum seasonal dry spells arise when dry spells span multiple seasons, as they often do. If the longest dry spell in a given season is continued into the next season, it is most accurate to reflect that dry spell in both seasons; showing the dry spell only in the latter season would incorrectly imply that the preceding season was wetter than it actually was. At the same time, to consider the magnitude of the dry spell duration, it is important that the total number of days in the dry spell be reflected in the data. Therefore, for dry spells that spanned multiple seasons, the final count at the end of the first season is considered in the maximum number of consecutive dry days for that season. For the subsequent season, the count of consecutive dry days is added to the final count from the preceding season (the count for the season that the dry spell extends into is carried over from the previous season).

The full Standardized Precipitation Index (SPI) was not calculated for the precipitation data at Cachicadan because it would require a thorough analysis of precipitation distributions at various time scales, something that was beyond the scope of this work. Yet, the standardized precipitation (that forms a conceptual basis for the SPI) was calculated to give an idea of the range of standardized precipitation values. The standardized precipitation (*SP* in the equation below) is the monthly total (for the specific month and year) minus the mean for that month divided by the standard deviation for that month; the mean and standard deviation for each month are calculated over the entire period of record (Section 4.2.1). The standardized precipitation plotted as a time series shows both the general dispersion of *SP* values and periods of time with consecutive months that were abnormally wet or abnormally dry. The mean and median values of the

SP were calculated to determine if the central tendency is more or less than 0 (mean and median of 0 would be expected for a normal distribution).

$$SP_{ij} = \frac{P_{ij} - \bar{P}_j}{\sigma_j}$$

SP_{ij} = standardized precipitation for year i and month j

P_{ij} = monthly precipitation for year i and month j

$\bar{P}_j$ = mean precipitation for month j

σ_j = standard deviation of precipitation for month j

The final assessment of climate extremes relates to rainfall intensities and whether higher intensity events are more or less common than they used to be. It was not possible to do a full analysis of extreme precipitation events due to the frequency of the data. Because the duration of a storm is as important as the total amount of precipitation, hourly data would be needed to do a probability analysis of extreme precipitation events and their magnitudes (e.g., the magnitude of a 100-year storm) as well as analysis of the impact of climate change on the magnitude and frequency of extreme precipitation events. Therefore, the analysis presented here is limited to analysis of daily precipitation totals. The data were divided into two time periods; Period 1 (1964-1989) represents historic intensity distributions and Period 2 (1990-2010) represents changes (if there are any) in intensity distributions. For each of the two time periods, the data of total daily precipitation for all wet days (days with measurable precipitation) in each month were selected. The cumulative distributions for each month were determined by ordering the daily precipitation values from smallest to largest and calculating the Weibull plotting position (Helsel and Hirsch, 2002) for each data point. The exceedance probabilities were calculated by using the same Weibull plotting positions on the data ordered from largest to smallest. For each time period, the cumulative probabilities and exceedance

probabilities were plotted as functions of daily precipitation amount for each month of the year. Finally, the Simple Daily Intensity Index (SDII), the total precipitation on wet days divided by the number of wet days, was calculated by month for each time period. The SDII is one of the 27 core climate indices defined by ETCCDI (Appendix D). The SDII values for each month facilitated comparison of rainfall intensities between Period 1 and Period 2.

Although the methods of data analysis presented in this chapter do not arrive at a completed drought index that could be used in the Sierra Ancash, they do provide the foundation for a better understanding of patterns of dry spells that is a necessary precursor to the development of a drought index. Additional steps that could be taken to develop a drought index for this region are discussed in the section on future work in the Conclusions chapter (Section 5.4.3). This work also begins to investigate precipitation intensity, but extreme rainfall events and their relationship with floods are complex enough that the scope of this work does not allow for a thorough flood frequency analysis. Nonetheless, the frequency histograms of daily precipitation intensities could be used to assess the impact of heavy rainfall on crops. This could be done by determining the field capacity for the location of a potential project and comparing the capacity of the soil to retain water to the amount of precipitation in a day (or several consecutive days). When the precipitation greatly exceeds the field capacity, then concerns may be raised about too much rainfall having negative impacts; in this case, measures to protect crops from oversaturated soil (such as raised beds and swales that promote infiltration) could be considered to reduce vulnerability of the crops to extreme rainfall events. The methods presented in this section are intended as a first step towards developing simple analysis tools for PIP formulators to consider extreme events related to precipitation (deficits or excess precipitation).

4.3 RESULTS

4.3.1 Seasonal Precipitation Patterns

The seasonal precipitation patterns, analyzed through measures of central tendency and dispersion, can be considered as a characterization of the local climate. The monthly mean, median and standard deviation of precipitation for each month are given in Table 4.2, and the mean and standard deviation (as error bars) are plotted in Figure 4.2. The box plot shown in Figure 4.3 plots the mean, interquartile range, and outliers. As expected, the rainy season months have the highest mean and median precipitation; March generally has the highest precipitation, followed by February and January. July is the month with the lowest precipitation, but June and August also have very low precipitation; this is consistent with the categorization of June – August as dry season months. The transition months (September – November and April – May) typically have precipitation levels between the central tendency values for the rainy and dry seasons. However, it must be pointed out that precipitation in April is very similar to December precipitation (mean, median and standard deviation all have less than 10% difference between the two months). The similar precipitation characteristics for December and April imply that they should be considered to be part of the same season; either December should be considered a transition month, or April part of the rainy season. If the seasonal definitions are changed to include April in the rainy season, the rainy season (Dec – Apr) precipitation accounts for approximately 75% of the annual total; the dry season (Jun – Aug) accounts for approximately 3%, and the transition months (Sep – Nov, Apr – May) account for approximately 22% of the total annual precipitation.

Regarding the variability in precipitation, the standard deviation is higher in the months with higher mean precipitation values, signifying more absolute variability in the rainy season than in the dry season. The variability may be better understood in relation

to the amount of precipitation in each month. Therefore, the standard deviation is also presented as a percentage of the mean in Table 4.2. In the dry season months, the standard deviation exceeds the mean, and the difference is most significant for the month of June when the standard deviation is nearly twice as much as the mean. The rainy season months still have a relatively high variability, but the standard deviation is generally around 60% (or less) of the mean. According to the box plot in Figure 4.3, there is a wider range of variability in precipitation for values greater than the median, indicating that it is more common to get precipitation values much higher than the median than to have much lower values. This effect is partly influenced by the lower limit for precipitation (it is not possible to have precipitation values less than 0), but the pattern is also present for rainy season months that had no monthly precipitation values of 0 (January – March). All outliers are on the upper end of the spectrum (high precipitation levels), and outliers are most frequent in the dry season months; the higher frequency of outliers in the dry season may be due in part to the fact that the median for those months is so low that any significant precipitation is an outlier. The variability is high for all months (no month has a standard deviation less than 54% of the mean), and the major implication of this is that there is a high level of uncertainty in total monthly precipitation. For long-term planning purposes, the range of potential precipitation values for each season should be taken into account.

Table 4.2- Mean, median, standard deviation and relative standard deviation (presented as a percentage of the mean) of precipitation at Cachicadan for each month

	Mean (mm)	Median (mm)	Standard Deviation (mm)	Relative Standard Deviation (% of the mean)
January	135.2	120.9	81.2	60.1
February	155.9	131.4	92.0	59.0
March	180.0	176.8	98.6	54.8
April	106.1	104.3	65.0	61.2
May	33.7	32.8	24.5	72.8
June	15.0	7.9	26.2	174.6
July	6.9	3.1	9.5	136.6
August	8.1	4.7	10.2	125.8
September	27.7	17.6	27.7	100.0
October	69.1	56.3	47.4	68.6
November	63.0	51.8	45.4	72.1
December	96.4	95.0	61.5	63.8

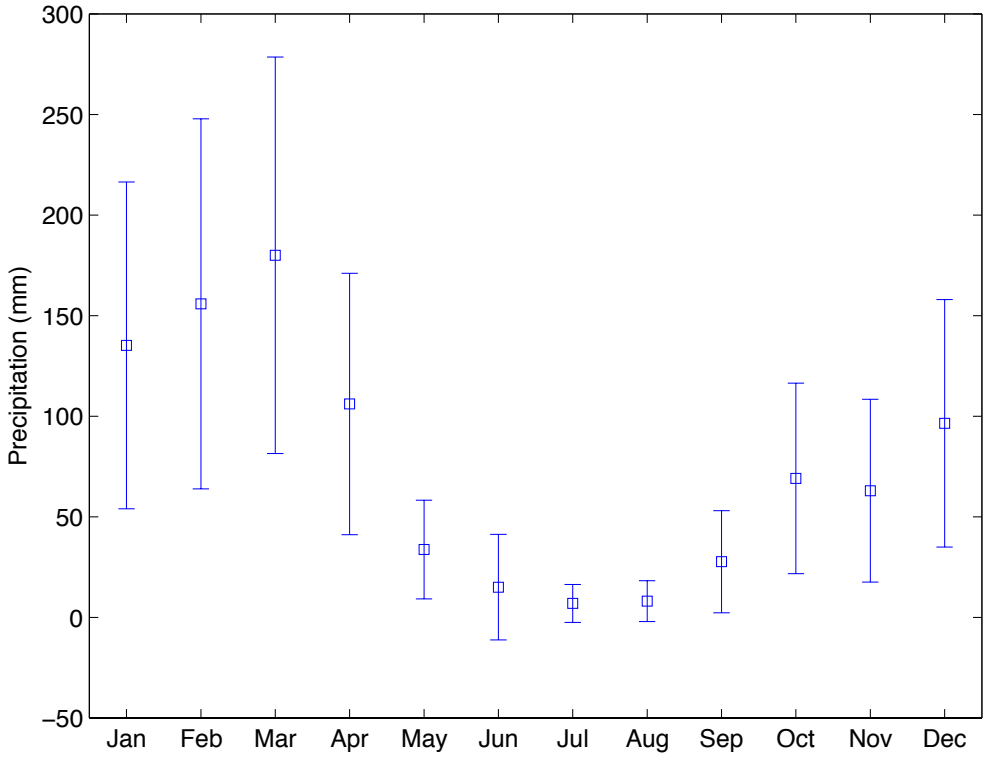

Figure 4.2- Mean and standard deviation (shown as error bars) of monthly precipitation

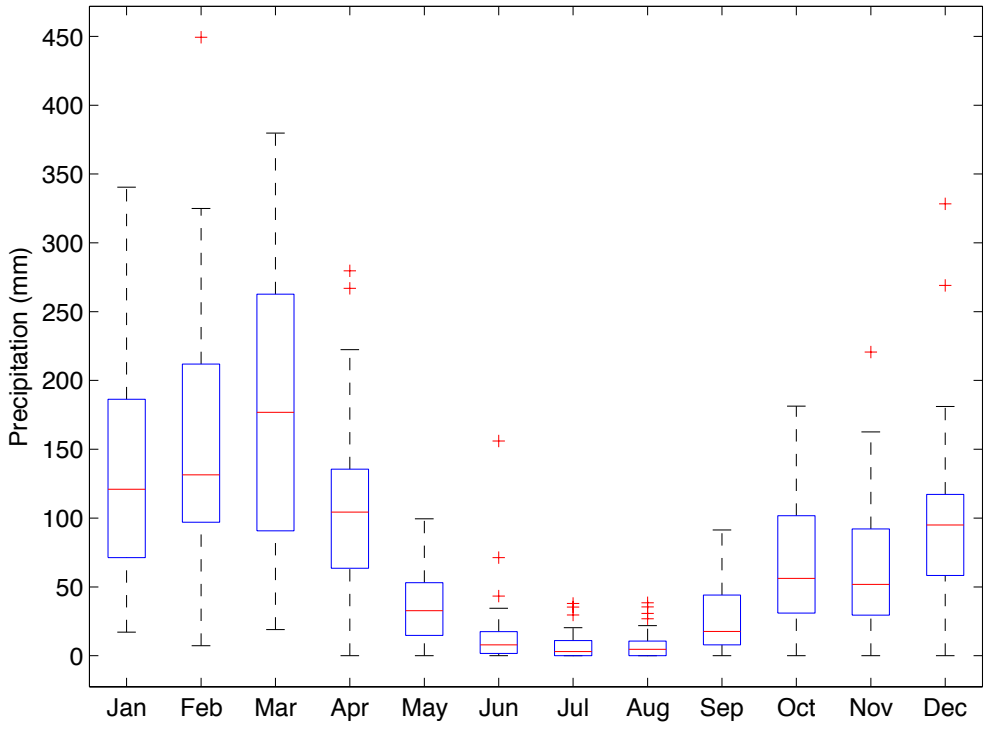

Figure 4.3- Boxplot showing central tendency and dispersion of monthly precipitation values. The red line in the center of each box indicates the median, the box delimits the interquartile range, and the whiskers represent the values within 1 step of the interquartile range (1 step = 1.5 times the interquartile range). Outliers (more than 1 step beyond the interquartile range) are denoted by red + signs.

The distributions of monthly precipitation are presented in frequency histograms for each month (Figure 4.4). The months of June – September are heavily positively skewed with the low monthly precipitation values occurring most frequently. The transition months of October – November and April – May have a more even distribution for values up to about 60% of the maximum, and the higher values of monthly precipitation are much less frequent. The frequencies in the rainy season months of January – March appear to be a little more evenly distributed, but the highest values are still less frequent. There is a lot of variability in the distribution patterns from month to

month, and there does not seem to be a standard pdf distribution that would describe the distribution for all months.

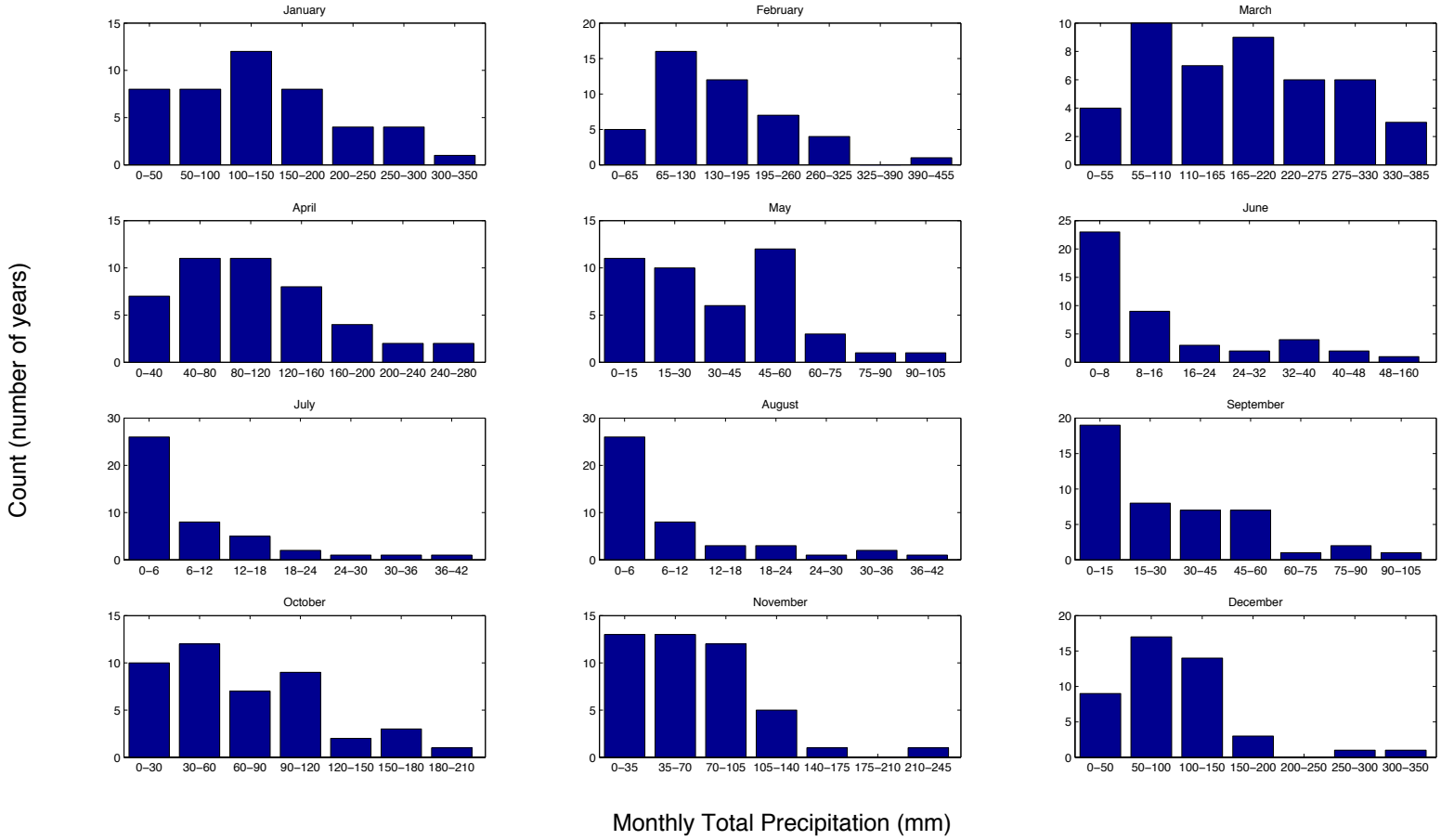

Figure 4.4- Frequency histograms of monthly precipitation at Chachicadan (1964-2010)

5.3.2 Trends and Shifts in Seasonality

Trends and Heteroscedasticity

The time series of monthly precipitation for each month are shown in Figure 4.5 along with the 10-year moving averages and moving standard deviations. In addition, the colors in Figure 4.5 indicate the results of the trend analyses. The results of the Mann-Kendall tests for trends are presented in Tables 4.3-4.5. For the Mann-Kendall test on the original time series data (not the 10-year moving averages), only the months of July and August showed trends, and both trends were decreasing. This test is a non-parametric test that does not account for magnitudes of precipitation and only indicates if subsequent values tend to be more or less than preceding values. When magnitudes were considered (with the 10-year moving averages), increasing trends were detected for the months of February, April and November, and a decreasing trend was detected for precipitation in September in addition to the decreasing trends detected for July and August (further confirmation of the trends detected with the original time series data).

According to the results of the trend tests the only months with decreases in precipitation were dry season months (July and August) and September. The decreasing trends for July and August imply that the seasonality of the dry season may be more enhanced than it used to be (a drier dry season or more frequent years with little to no precipitation). The moving standard deviation for the dry season months had no trend for June and July and a decreasing trend in August. This implies that in conjunction with decreasing precipitation in the dry season, the variability is also decreasing; less variability with a decreasing mean signifies that there have been fewer occasions with abnormally high precipitation in recent years. There have been several years with measurable precipitation (up to 150 mm in June and almost 40 mm in July and August),

and many of the years with higher dry season precipitation occurred before 1990; this implies that it has never been abnormal to have some amount of precipitation in the dry season. While significant precipitation in the dry season may still be an outlier, it is most likely not due to climate change. There have been many years with no precipitation in the dry season months, and dry season precipitation is not reliable enough to supply crops with their water requirement without irrigation. Some people consider September as part of the end of the dry season rather than the beginning of the transition to the rainy season, and the decreasing trend for September may mean that it is has more dry seasonal characteristics than it used to. The decreasing trend for September could also be interpreted as a delay in the onset of the rainy season. The decreasing trend in the moving standard deviation for September indicates that the amount of precipitation for that month is less variable than it used to be. So, not only has the amount of precipitation in September decreased, but years when precipitation in September differs significantly from the mean are less frequent as well. In particular, deviations from the norm on the upper end have been less frequent in recent years, meaning that if that trend holds true in the future, the probability of high precipitation in September is decreasing.

Although they were not detected in the original time series, increasing trends were detected with the 10-year moving averages for the months of February, April and November. All three of these months are either transition or rainy season months, and from October – May, no month had a decreasing trend detected. Although there is not enough information to draw definitive conclusions about changes in the seasonality and reliability of the rainy season from these results, it may be said that rainy season precipitation is not decreasing; if anything, it may be increasing. Additionally, with the exception of September (that had a decreasing trend), none of the transition months had decreasing precipitation. From these results, it is not possible to completely disprove the

hypothesis that the start of the rainy season has been delayed in recent years, but the validity of this hypothesis can be called into question. If the rainy season were delayed, then this change would most likely be reflected in the data with a decrease in the precipitation during the transition months of October – November.

In the analysis of variability to determine if monthly precipitation is homoscedastic or heteroscedastic, increasing trends in the moving standard deviation were detected for January, February, March, May, and November (indicating an increase in variability). Decreasing trends were detected in the moving standard deviation for the months of August and September (indicating heteroscedasticity but decreasing variability), and no trends were detected for April, June, July, October and December (indicating homoscedasticity in monthly precipitation for those months). All of the months with increasing variability are rainy season or transition months, and the three months with the highest average precipitation (January – March) all had increasing variability. The heteroscedasticity in many of the rainy season and transition months may be an indicator that the rainy season is less reliable than it used to be; there may be more years with more precipitation, but there also may be more years with significantly less rainfall than normal during these months. Increasing variability means that the range of possible rainy season precipitation levels is widening, making the task of planning for all possible outcomes in PIP proposals potentially more difficult. This also means that projects would have to plan for both scenarios of higher than normal precipitation and precipitation deficits. The results in Section 4.3.3 are also related to the implications of increased variability in rainy season precipitation, and further discussion is reserved for Section 4.4 after all results have been presented.

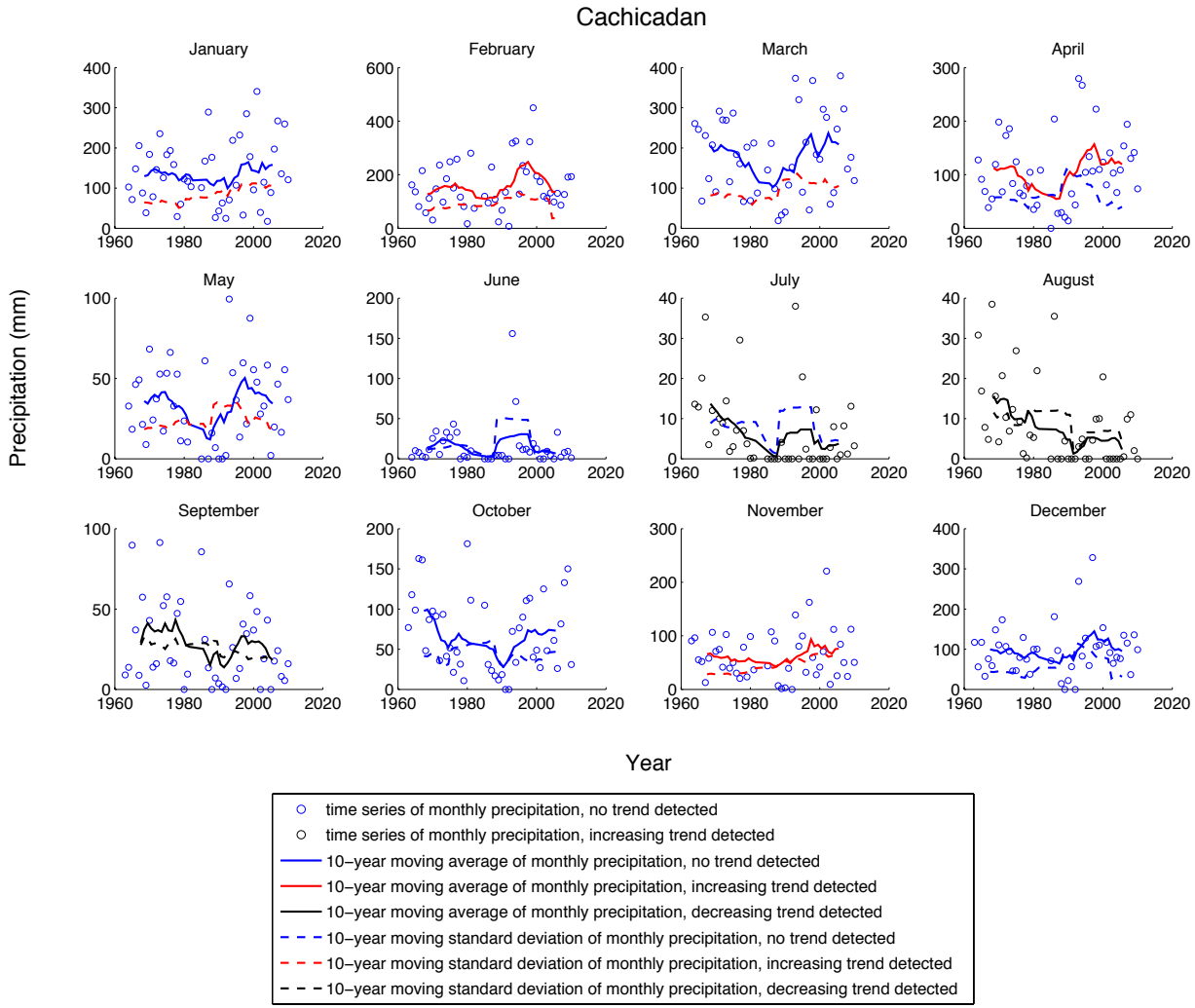

Figure 4.5- Time series plots of monthly precipitation at Cachicadan, 10-year moving average, and the 10-year moving standard deviation. Different colors are used to indicate the results of the Mann-Kendall tests for trends.

Table 4.3- Results of the Mann-Kendall test for trends on the original time series data of monthly precipitation

	H*	p-value	S
January	0	0.6317	50
February	0	0.4396	80
March	0	0.8988	14
April	0	0.2141	128
May	0	0.8874	15
June	0	0.4184	-81
July	1	0.0096	-257
August	1	0.0016	-313
September	0	0.2251	-125
October	0	0.3316	-97
November	0	0.8833	-16
December	0	0.5313	65
Seasonal Kendall Test	**0**	**0.063**	**-537**
*** H = 0 indicates failure to reject the null hypothesis (no trend), H = 1 indicates rejection of the null hypothesis (a trend was detected)**			

Table 4.4- Results of the Mann-Kendall test for trends on the 10-year moving average values for monthly precipitation at Cachicadan

	H*	p-value	S
January	0	0.3615	68
February	1^{+}	0.0229	168
March	0	0.236	88
April	1^{+}	0.0185	174
May	0	0.4432	55
June	0	0.6292	-35
July	1^{-}	2.47E-05	-298
August	1^{-}	3.78E-09	-416
September	1^{-}	6.61E-04	-251
October	0	0.3942	-61
November	1^{+}	0.0283	162
December	0	0.1238	114
*** H = 0 indicates failure to reject the null hypothesis (no trend), H = 1 indicates rejection of the null hypothesis (a trend was detected)**			
$^{+}$ Positive trend detected			
$^{-}$ Negative trend detected			

Table 4.5- Results of the Mann-Kendall test for trends on the 10-year moving standard deviation values for monthly precipitation at Cachicadan. Positive trends indicate increasing variability, and negative trends indicate a decrease in variability.

	H*	p-value	S
January	1^{+}	6.82E-10	454
February	1^{+}	1.45E-04	280
March	1^{+}	0.0137	182
April	0	0.8169	-18
May	1^{+}	0.0309	153
June	0	0.8424	15
July	0	0.8203	-17
August	1^{-}	0.0152	-172
September	1^{-}	5.37E-07	-369
October	0	0.7764	-21
November	1^{+}	1.89E-12	518
December	0	0.0744	132
*** H = 0 indicates failure to reject the null hypothesis (no trend), H = 1 indicates rejection of the null hypothesis (a trend was detected)**			
$^{+}$ Positive trend detected			
$^{-}$ Negative trend detected			

Start of the Rainy Season

The start of the rainy season has been defined in this chapter as the date on which the cumulative precipitation for the water year (September 1 – August 31) first exceeds a certain threshold. Before calculating the rainy season start dates for a range of threshold levels, the accumulated precipitation for each water year was plotted as a function of the number of days since the start of the water year (Figure 4.6). This cumulative precipitation plot gives an idea of the range of values of accumulated precipitation that have been recorded for any given day of the year. The values of accumulated precipitation on August 31 are the totals for each water year. Because the purpose of the

figure is to illustrate the range of accumulated precipitation values, the years that correspond to each measurement are not indicated.

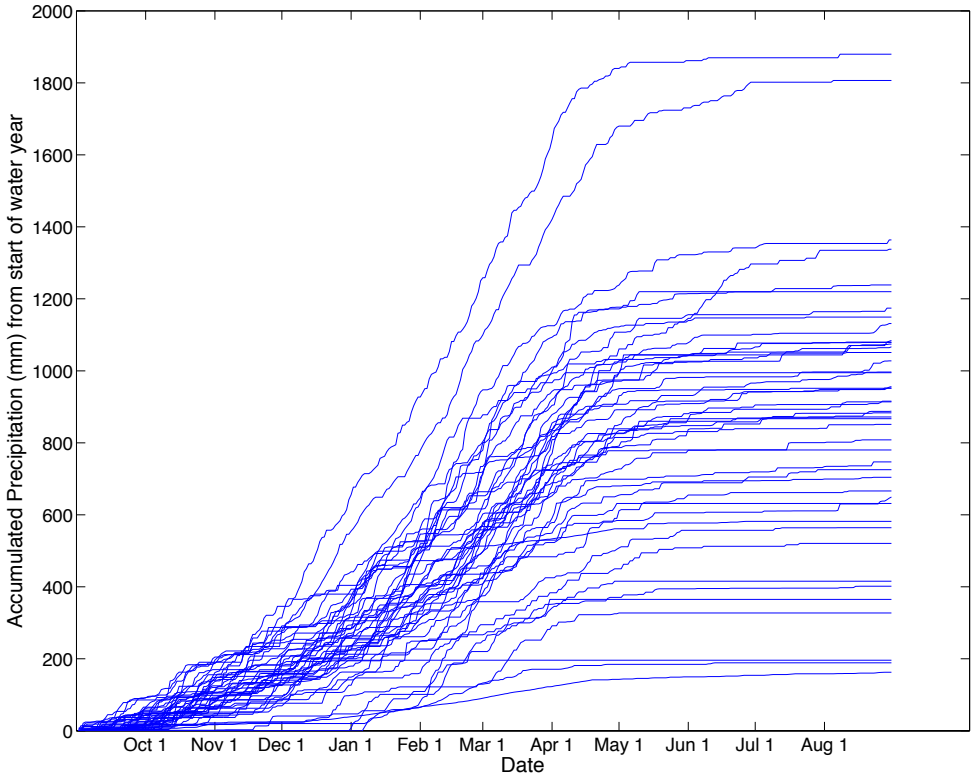

Figure 4.6- Accumulated precipitation from the start of the water year (September 1) for all years with data recorded at Cachicadan.

The start date of the rainy season (Figure 4.7) was calculated for three different thresholds of accumulated precipitation. As expected, for higher thresholds, the rainy season starts later, but the number of days between the three start dates varies from year to year. The mean and median rainy season start date for each threshold are given in Table 4.6. The median start date is earlier than the mean for all three thresholds, indicating that earlier start dates are more common, but late start dates can differ more significantly from the mean (more of the outliers are late start dates). However, the mean

and median tend to converge as the threshold increases. The mean start date for the 150 mm threshold (Dec. 6) is 20 days later than for the 100 mm threshold (Nov. 16), and the mean start date for the 200 mm threshold (Dec. 16) is one month (30 days) later than the mean 100 mm start date. The difference between median start date for the 150 mm threshold and 100 mm threshold is 22 days, and the difference in median start dates between the 200 mm and 100 mm thresholds is 37 days. The 200 mm threshold for the start of the rainy season appears to be too high because there were several years for which this threshold was never reached (implying that there was no rainy season in those years). Although there were some abnormally dry years for which this type of index may not be appropriate (e.g., water years between 1988-89 and 1992-93), this method for defining the start of the rainy season appears to be a reasonable approach for most years. It has the advantage of being simple and easy to apply, and it does not need to be evaluated retroactively (as an additional criterion about minimum consecutive dry days would).

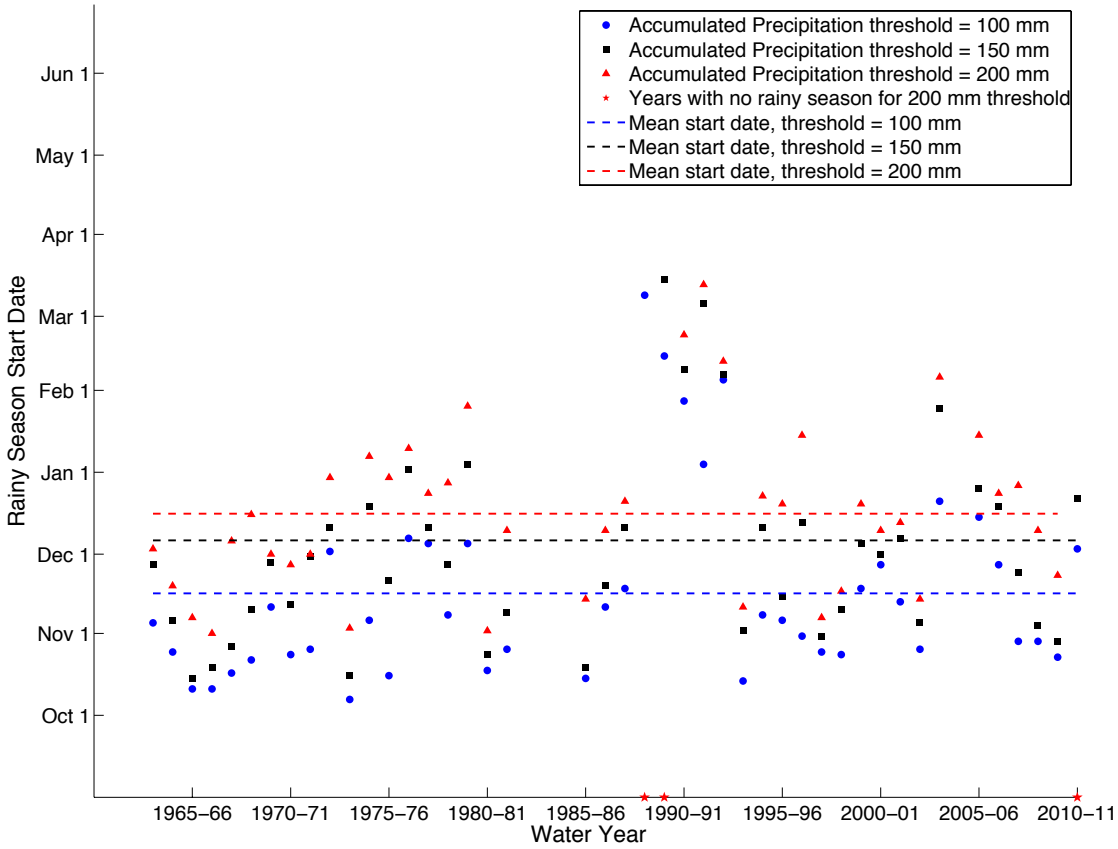

Figure 4.7- Rainy season start date for all water years that have recorded data at Cachicadan, calculated according to three different accumulated precipitation thresholds

Table 4.6- Mean and median start dates for the rainy season for each threshold of accumulated precipitation

Threshold	**100 mm**	**125 mm**	**150 mm**	**200 mm**
Mean rainy season start date	Nov. 16	Nov. 26	Dec. 6	Dec. 16
Median rainy season start date	Nov. 6	Nov. 19	Nov. 28	Dec. 13

The question that follows is: *What is an appropriate threshold?* The selection of the threshold should have some basis in the historic data. If September – November are considered transition months, the sum of the mean or median for those months could be an appropriate threshold. The threshold of 150 mm is slightly less than the sum of the

mean values for September – November (159.69 mm). However, the argument can be made that the median is a more appropriate indicator because it is a non-parametric measure of central tendency (less affected by outliers). The sum of the median values for September – November is 125.65 mm. To evaluate the difference between using the mean to determine the threshold (corresponding to the 150 mm threshold) and using the median precipitation in transition months (corresponding to the 125 mm threshold), the rainy season start date for each year was determined for both the 125 mm and 150 mm thresholds, shown in Figure 4.8.

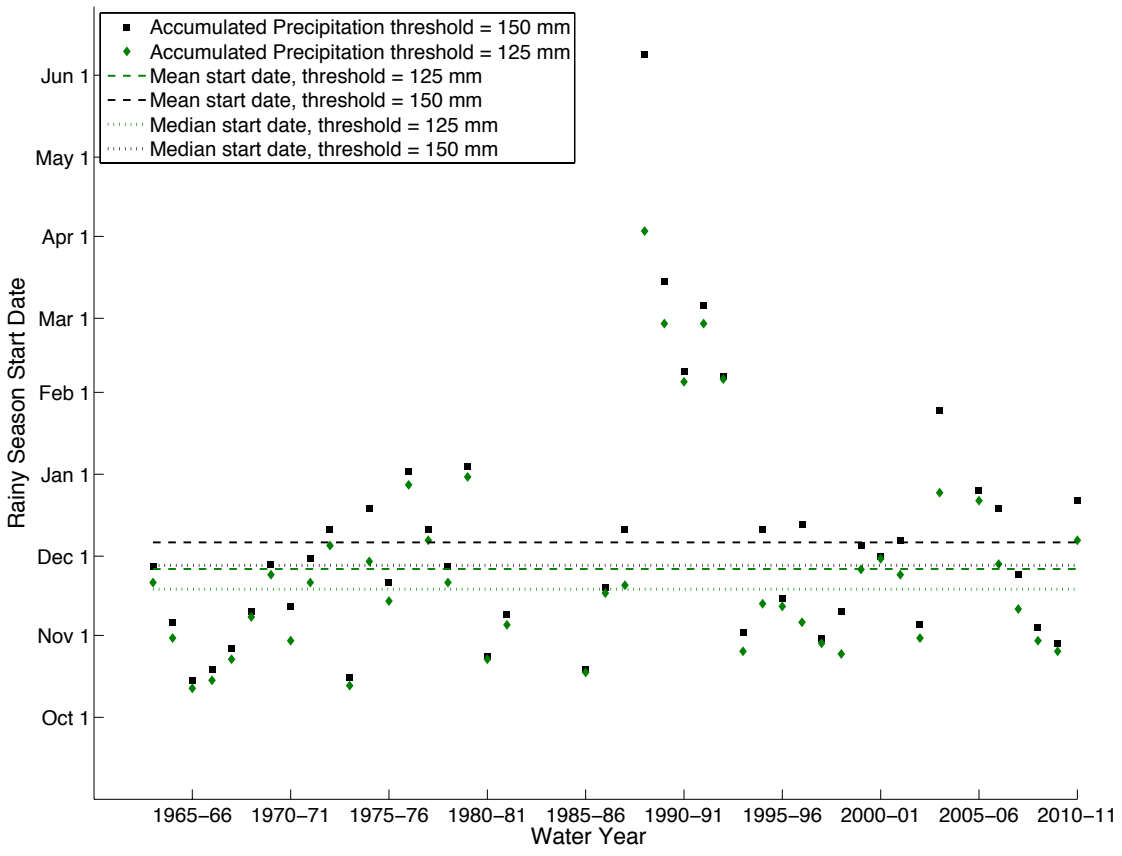

Figure 4.8- Rainy season start date at Cachicadan for accumulated precipitation thresholds of 125 mm and 150 mm (corresponding to the median and mean precipitation, respectively, for September – November)

Finally, to determine if there is a trend in the start date of the rainy season, the Mann-Kendall test for trends was run for the start dates calculated according to each of the accumulated precipitation thresholds. Results of the trend tests are presented in Table 4.7. There was no trend detected except at the 100 mm threshold, and even the trend of increasing (later) rainy season start dates detected for the 100 m threshold is a weak trend that would not be detected at the 1% significance level. These results indicate that there has not been a trend towards delay in the start of the rainy season. This conclusion is consistent with the analysis of trends in monthly precipitation that did not show a decreasing trend for most transition months.

Table 4.7- Results of the Mann-Kendall test for trends on the start date of the rainy season

Threshold	H	p-value	S	z
100 mm	1	0.0431	201	2.0229
125 mm	0	0.2287	120	1.2036
150 mm	0	0.1078	160	1.6082
200 mm	0	0.157	127	1.4152
*** H = 0 indicates failure to reject the null hypothesis (no trend), H = 1 indicates rejection of the null hypothesis (a trend was detected)**				

4.3.3 Climate Extremes: Dry Periods and Rainfall Intensities

This section explores data analysis related to extreme precipitation events, droughts and heavy rainfall. The character of droughts in the Sierra Ancash is explored through the number of dry days in each month (Figure 4.9) and the number of consecutive dry days (i.e., the length of dry spells, calculated seasonally in Figure 4.10).

The daily rainfall intensities are explored through frequency histograms of daily precipitation totals for two time periods (Figure 4.12).

Dry Periods

The number of dry days per month (shown in Figure 4.9) was assessed for trends to determine if the number of dry days in a specific month is increasing. An increasing trend may be an indicator of more frequent droughts. The months of May, July, August, and October showed strong increasing trends in the number of dry days per month that were detected in both the original time series data and with the 10-year moving averages (results of the Mann-Kendall tests are shown in Table 4.8 and 4.9). The trend analysis on the 10-year moving average (Table 4.9) shows increasing trends for the months of January, June, September, November and December in addition to the months for which an increasing trend was detected with the original data. There was no change in the number of dry days/month for February, March, and April. No negative trends were detected for either the original data or the moving average of dry days/month (all months had either no trend or an increasing trend); this is an indicator that number of wet days has not increased for any season, and some seasons (particularly the dry season) seem to be increasingly drier.

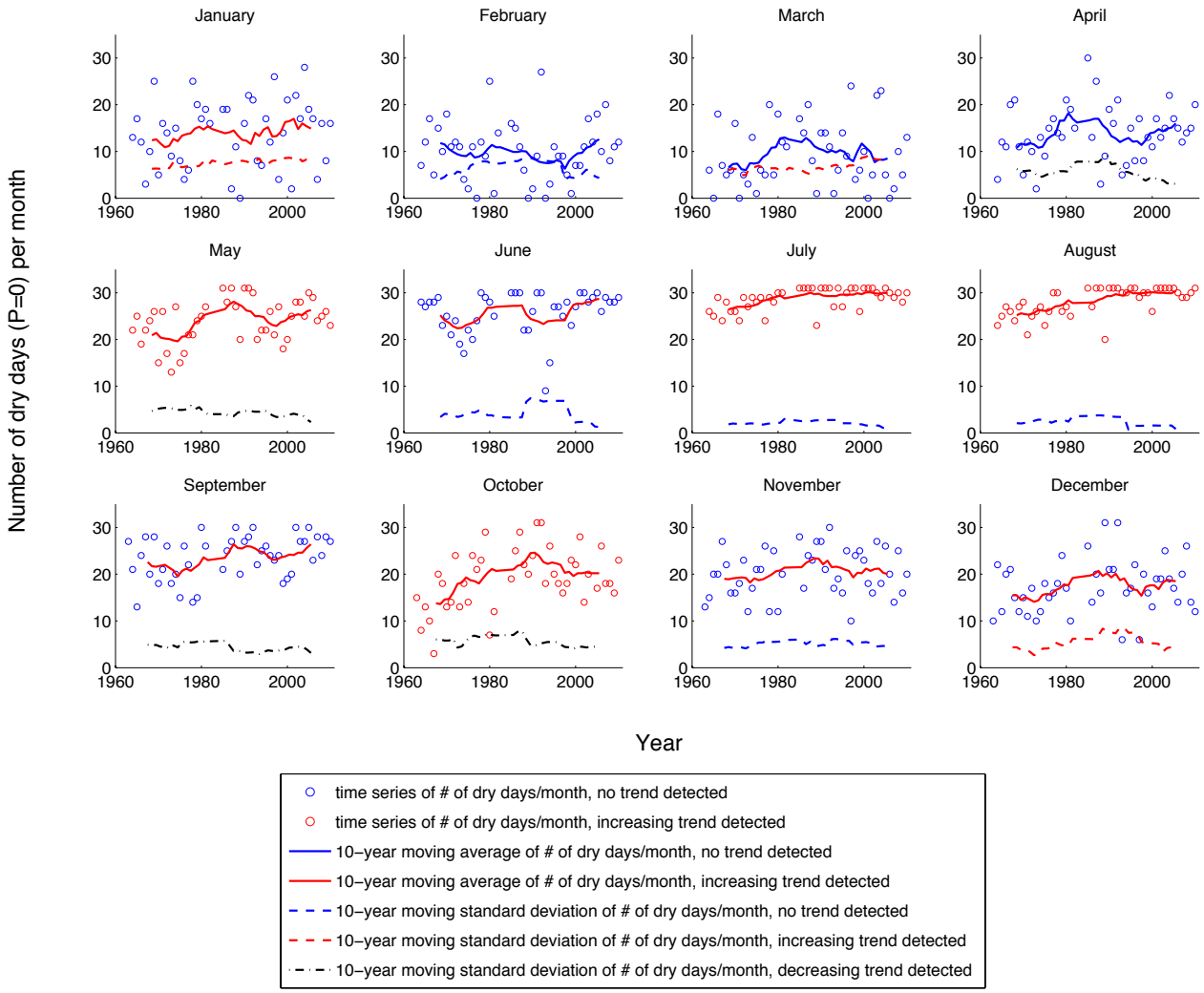

Figure 4.9- Time series of the number of dry days per month at Cachicadan along with values of the 10-year moving average and the 10-year moving standard deviation

The moving standard deviation is a means of assessing the data for homoscedasticity, and the results of the trend tests on the moving standard deviation (Table 4.10) represent a range of trends, both positive and negative. Increasing trends (increasing variability) were detected for January, March, and December (all rainy season months). Decreasing trends were detected for April, May, September, and October (all transition months). No trend was detected for February, June, July, August, and November. In the dry season months, the number of dry days appears to be increasing, but the variability is relatively constant; the dry season is getting drier and more consistently dry. The transition months of May and October seem to have the most significant changes, increasing trends in the number of dry days as well as decreasing variability. The decreasing variability is an indicator of decreasing uncertainty in the more frequent dry days during those months. Although the number of dry days could be considered an indicator of the reliability of the rainy season, it is difficult to draw any conclusions about the number of dry days in the rainy season months. It may be said that the increased variability in December, January and March is an indicator that the uncertainty (or unpredictability) in the number of dry days in the rainy season is increasing. This would imply that projects should have the ability to compensate for more frequent days without rain (e.g., through irrigation), but these measures may not be necessary in all years. Increased variability in the number of dry days during the rainy season may make more difficult the task of cost benefit analysis for alternatives to reduce vulnerability to precipitation deficits.

Table 4.8- Results of the Mann-Kendall test for trends on the original time series data of monthly precipitation

	H	p-value	S
January	0	0.4281	82
February	0	0.9766	4
March	0	0.8449	21
April	0	0.1345	154
May	1^{+}	0.0452	199
June	0	0.0784	175
July	1^{+}	0.002	307
August	1^{+}	8.34E-05	390
September	0	0.0504	201
October	1^{+}	0.0312	214
November	0	0.3681	93
December	0	0.2524	118
*** H = 0 indicates failure to reject the null hypothesis (no trend), H = 1 indicates rejection of the null hypothesis (a trend was detected)**			
$^{+}$ **Positive trend detected**			

Table 4.9- Results of the Mann-Kendall test for trends on the 10-year moving standard average values for number of dry days/month at Cachicadan.

	H	p	S
January	1^{+}	2.62E-04	269
February	0	0.25	-85
March	0	0.31	76
April	0	0.07	134
May	1^{+}	0.002	219
June	1^{+}	4.59E-05	288
July	1^{+}	3.45E-10	443
August	1^{+}	6.67E-13	507
September	1^{+}	1.22E-04	283
October	1^{+}	5.30E-04	245
November	1^{+}	0.0086	194
December	1^{+}	0.0033	217
*** H = 0 indicates failure to reject the null hypothesis (no trend), H = 1 indicates rejection of the null hypothesis (a trend was detected)**			
$^{+}$ **Positive trend detected**			

Table 4.10- Results of the Mann-Kendall test for trends on the 10-year moving standard deviation values for monthly precipitation at Cachicadan. Positive trends indicate increasing variability, and negative trends indicate a decrease in variability.

	H	p	S
January	1^{+}	4.34E-09	432
February	0	0.7853	21
March	1^{+}	1.78E-05	316
April	1^{-}	0.0041	-212
May	1^{-}	1.11E-06	-344
June	0	0.3634	-65
July	0	0.371	-64
August	0	0.0938	-119
September	1^{-}	0.0255	-165
October	1^{-}	0.003	-210
November	0	0.1271	113
December	1^{+}	0.0246	166
*** H = 0 indicates failure to reject the null hypothesis (no trend), H = 1 indicates rejection of the null hypothesis (a trend was detected)**			
$^{+}$ Positive trend detected			
$^{-}$ Negative trend detected			

Perhaps more useful than the absolute number of dry days/month is the length of dry spells. The number of consecutive dry days in each season is plotted in Figure 4.10 as a function of water year. For dry spells that span more than one season, the method outlined in Section 4.2.3 was used to account for the dry spells in all seasons during which each dry spell occurred. In Figure 4.10, there appears to be significantly more variability in the lengths of dry spells after 1985 than before, and there were a few dry spells that were significantly longer in duration than the longest pre-1985 dry spell (2-3 times as long). Thus, very long periods of consecutive dry days seem to be more common after 1985. There were several years around 1989-1993 that had extremely long dry spells (more than 100 consecutive days); these years seem to align with the years that had a

later start to the rainy season (Figure 4.7). To examine this pattern more closely, the mean, median, and standard deviation were calculated for the period before 1985 as well as for the period of time from 1985 onwards (Table 4.11). The mean, median, and standard deviation increased in all seasons for the period of 1985-2010 compared with the values for the period of 1963-1982 (there was a gap in the data from 1982-1985). This validates the observation that the variability and magnitudes of dry spell durations have increased since 1985.

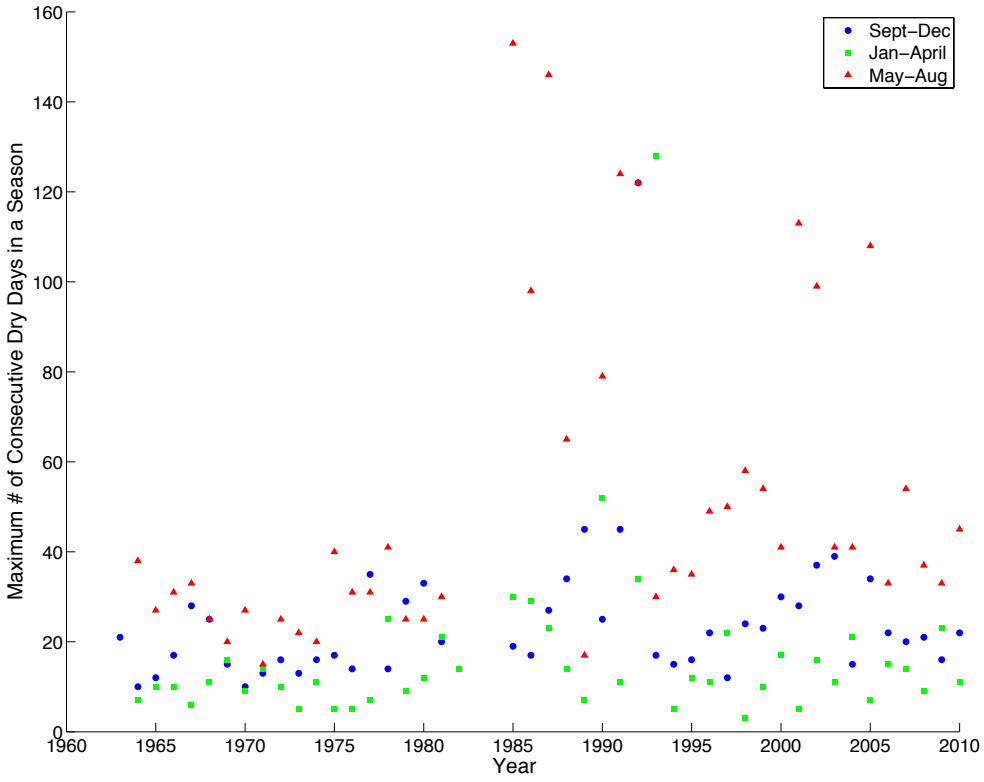

Figure 4.10- Time series of the number of consecutive dry days in each season

Table 4.11- Mean, median and standard deviation of the dry spell duration (number of consecutive dry days) in each season for the entire period of record, and the two data subsets for periods before 1985 and from 1985 to 2010

	Season 1 (Sep – Dec)	**Season 2 (Jan – Apr)**	**Season 3 (May – Aug)**
Mean (# of consecutive dry days) (All data: 1963-2010)	25	17	52
Median (# of consecutive dry days) (All data: 1963-2010)	21	11	38
Standard Deviation (# of consecutive dry days) (All data: 1963-2010)	17	19	36
Mean (# of consecutive dry days) (1963-1982)	19	11	28
Median (# of consecutive dry days) (1963-1982)	16	10	27
Standard Deviation (# of consecutive dry days) (1963-1982)	8	5	7
Mean (# of consecutive dry days) (1985-2010)	29	21	68
Median (# of consecutive dry days) (1985-2010)	23	14	52
Standard Deviation (# of consecutive dry days) (1985-2010)	21	24	39

Some of the dry spells after 1985 were so much longer than the maximum pre-1985 dry spell that it raises the question of whether or not there are other external influences (e.g., El Niño or La Niña events) that may be increasing the duration of dry spells. To examine specific years when long dry spells occurred, thresholds for abnormally long dry periods were set for each season and compared to the years when El Niño or La Niña events occurred (Climate Prediction Center, 2015). The thresholds for abnormally long dry spells are: 25 days for Season 1 (transition months), 15 days for Season 2 (rainy months), and 60 days for Season 3 (dry months). Before 1985, Season 1

had 5 abnormally long dry spells, Season 2 had 3, and Season 3 had 0 abnormally long dry spells. Between 1985 and 2010, the number of abnormally long dry spells increased to 11 in Season 1, 11 in Season 2, and 10 in Season 3 (normalized for the number of years, the number of abnormally dry spells would be 8.3, 8.3, and 7.6 relative to the pre-1985 period for Seasons 1, 2, and 3, respectively). Of these abnormally long dry periods, there seemed to be no connection to El Niño or La Niña events; in all three seasons, some abnormally dry periods occurred in weak to moderate years of El Niño or La Niña, and many occurred in years with no El Niño or La Niña event. Of the four longest dry spells (all concluding in the dry season and exceeding 120 days in duration), one occurred in a weak La Niña year (1985), two occurred during moderate El Niño years (1987 and 1992), and one happened in a year with no El Niño or La Niña event (1991). With the exception of one abnormally long dry spell in Season 1 that occurred during the 1988-89 La Niña event (strong magnitude), none of the abnormally long dry spells corresponded with strong or very strong El Niño or La Niña events. If there were a correlation between dry spell duration and Niño/a events, then strong or very strong events would most likely cause abnormally long dry spells for either El Niño or La Niña years. This, however, is not the case, signifying that there is likely a cause other than the ENSO cycle for the increase in dry spell duration since 1985.

The standardized precipitation is a way to normalize precipitation for the time of year to facilitate identification of abnormally wet and dry months. Although calculated somewhat differently, the SPI drought index is based on the concept of standardized precipitation; the SPI uses pdfs fitted to the data rather than the mean and standard deviation for the given time of year. To give an idea of the range of variability in monthly precipitation, the standardized precipitation is shown in Figure 4.11. Most of the outliers appear to be in the upper end of the range of standardized P values, and there is more

dispersion in the positive standardized precipitation values (wetter than normal) than with the negative values. The minimum value of standardized precipitation is -1.63, and the maximum is 5.38. As expected, the mean of all standardized precipitation values is 0 (the values are normalized with the mean for each month), but the median of all standardized precipitation values is -0.2543. The median value less than 0 implies that negative standardized precipitation values have been more frequent than positive values, and the data are positively skewed.

Figure 4.11- Standardized monthly precipitation at Cachicadan (monthly mean subtracted from the monthly precipitation and divided by the standard deviation for that month)

Precipitation Intensities

Although daily rainfall data are insufficient to do a full flood frequency analysis (hourly data are needed), the daily precipitation intensities can be analyzed to determine if there has been any shift in the data. The daily precipitation data were divided into two time periods: Period 1 = 1963-1989, Period 2 = 1990-2010. The cumulative distributions and distributions of exceedance probability for the daily precipitation intensities were calculated by month for each time period (Figures 4.12 and 4.13). The cumulative distributions for most months (except the dry season months of June – August) appear to have the shape of an exponential distribution, so an exponential distribution fit may be appropriate for rainy season months. In general, days with the lowest daily precipitation intensities are less frequent in Period 2 while the frequency of higher precipitation intensities is slightly greater in Period 2 (compared to Period 1). In the rainy season months, the greatest increase in frequency for Period 2 compared to Period 1 is in the range of 10-15 mm. Similar patterns in frequencies for Period 2 compared to Period 1 were exhibited for the rainy season and transition months, but the dry season months display different behavior in daily intensities. During the dry season months, low daily precipitation intensities were less frequent in Period 2 than in Period 1 (as is the case for all months), but the distribution no longer appears to be exponential for Period 2. In Period 2, higher intensity rainfall days (> 3 mm) were more frequent in the dry season than the low intensity days (< 3 mm); this was not the case for any other month outside of the dry season.

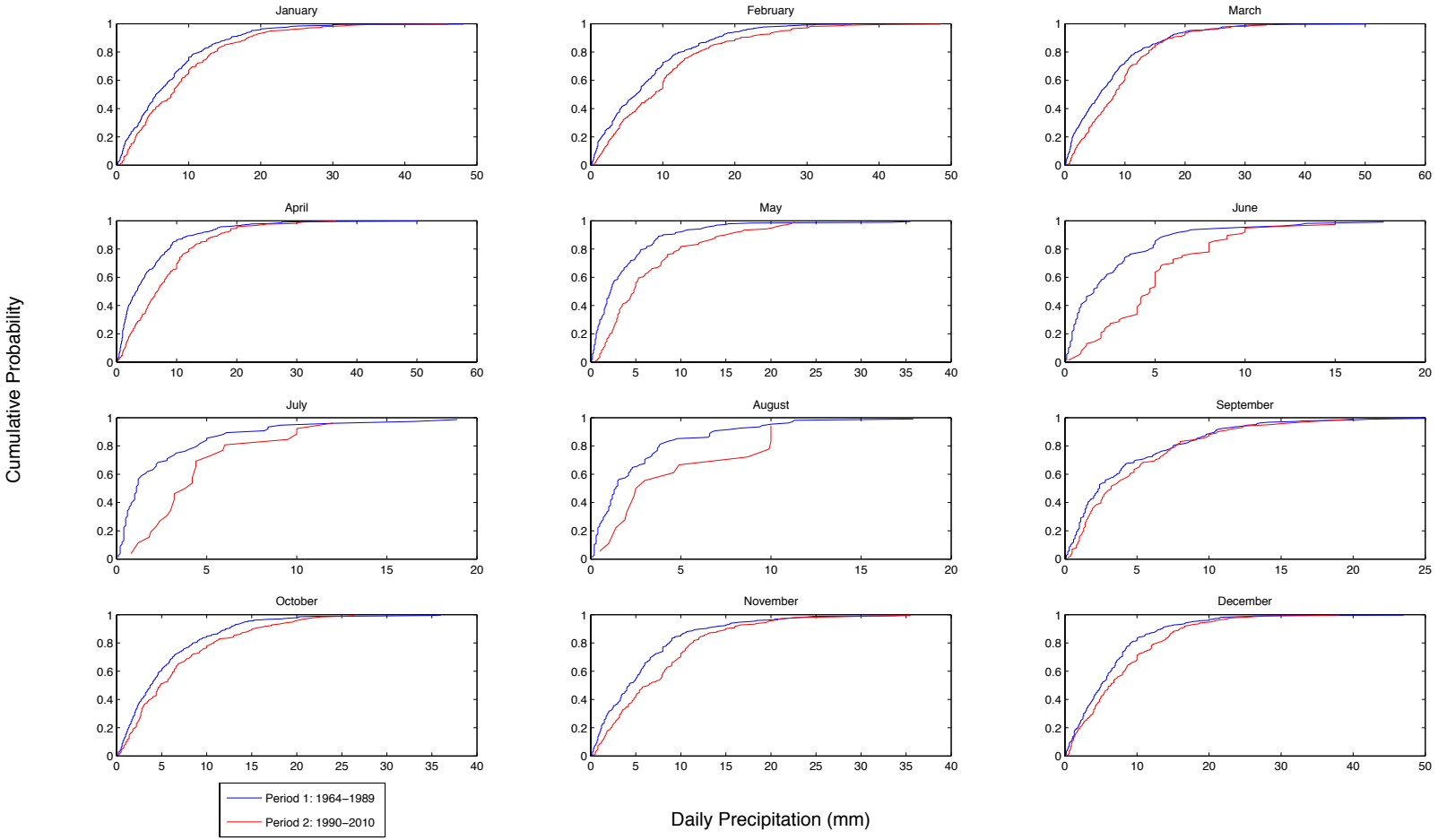

Figure 4.12- Cumulative distribution of total daily precipitation for each month at Cachicadan, shown for two time periods: Period 1 = 1964-1989, Period 2 = 1990-2010

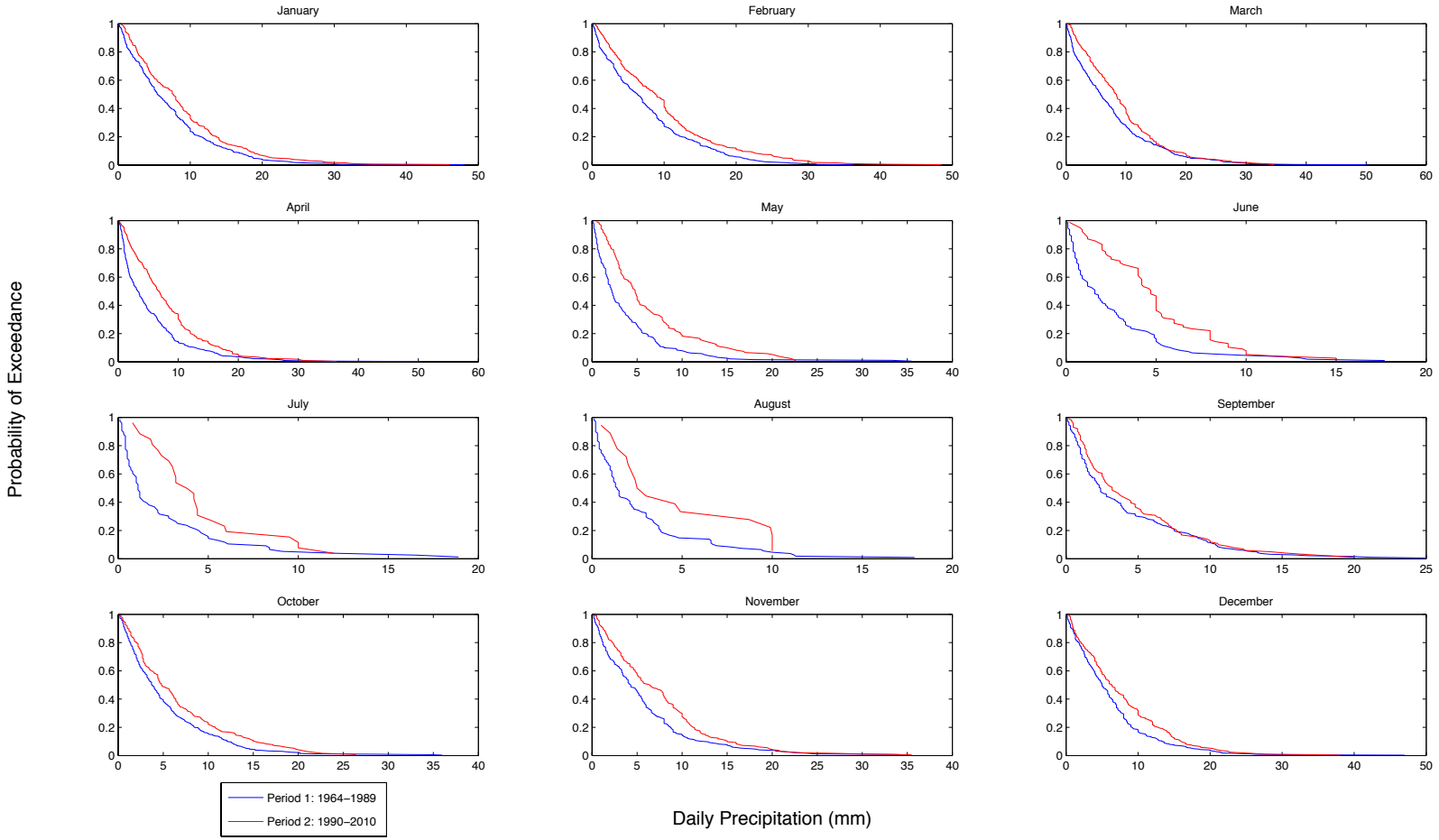

Figure 4.13- Probability of exceedance for total daily precipitation for each month at Cachicadan, shown for two time periods: Period 1 = 1964-1989, Period 2 = 1990-2010

The Simple Daily Intensity Index (SDII) was calculated by month for both time periods as a simple measure of change in daily precipitation intensity (Table 4.12). All months had higher SDII values in Period 2 than in Period 1, and the greatest relative increases in the SDII from Period 1 to Period 2 were in the months of May – August (all > 40% increase). In April, the SDII increased 34% in Period 2 compared to Period 1, and the increases in all other months were between 10% and 25%. The higher SDII values for all months are another indicator that rainfall intensities may have increased in recent years.

Table 4.12- SDII for each month (total precipitation on wet days divided by the number of wet days) calculated for two time periods: Period 1 = 1964-1989, Period 2 = 1990-2010

	Period 1 (mm)	**Period 2 (mm)**
January	7.2	8.8
February	7.6	9.9
March	7.5	9.2
April	5.3	8.2
May	3.7	6.4
June	2.6	5.0
July	2.6	4.4
August	2.6	4.5
September	4.2	4.7
October	5.3	6.7
November	5.7	7.5
December	6.3	7.8

An attempt was made to fit pdfs to the daily precipitation data for each time period so that they could be used to calculate probabilities of events of a given intensity and possible shifts in those probabilities. While it was possible to fit an exponential distribution to the data, it was not possible to distinguish between the two time periods in the fitted distributions. Therefore, it is only possible to draw qualitative conclusions about changes in frequencies of daily precipitation intensities, but with the available data it is not possible to quantify these probabilities for planning purposes. One of the most significant potential impacts of high-intensity precipitation on agricultural projects is the potential for floods. However, it is not possible to analyze extreme events and intensities with daily precipitation data because inundation depends on how quickly the precipitation falls as well as the total amount of rainfall. Hourly precipitation data or streamflow records would be needed to do a thorough flood frequency analysis. Based on the data analysis presented here, there are indications that the hypothesis that rainfall intensities have decreased is not true, but further analysis and additional data are needed to categorically disprove this hypothesis.

4.4 DISCUSSION

This section addresses two principal points: (1) assessment of the validity of the working hypotheses, and (2) potential applications of the findings to PIPs. The working hypotheses formulated for this chapter have their basis in the results of the study of perceptions of climate change (Vergara Rodriguez, 2011 and 2015). The five working hypotheses identified for this chapter all are related to trends and changes in seasonality of precipitation. Brief assessments of each hypothesis based on the results presented in Section 4.3 are presented below. Note that the evaluation of the hypotheses presented

here is only valid for Cachicadan, and it does not necessarily hold true that the trends, variabilities and seasonalities detected in the data at Cachicadan are consistent for the entire Sierra Ancash region. Further analysis is needed with representative data that cover a larger portion of the full spatial extent of the Sierra Ancash for conclusions to be drawn about changes in precipitation patterns for the region as a whole. However, since no other analyses of local-scale climate anomalies and change have been made, this work represents a first attempt to quantify climate trends and variability for the region, even with quite limited data.

Hypothesis #1: The amount of precipitation in the rainy season has decreased over the period of record for precipitation data (1963-2010).

This hypothesis appears to be untrue. The dry season precipitation has decreased, but the precipitation in the rainy season months was shown to either be increasing or to have no trend. The seasonal Kendall test was used to detect trends in precipitation for all seasons while accounting for the natural seasonal variability, and no trend was detected with the seasonal Kendall test.

Hypothesis #2: Variability in precipitation has increased for all months of the year.

This hypothesis is only true for certain months but is not categorically true for all months of the year. Although variability has increased for some months of the year, this is not true for all months. The only months with increased variability were the typically wettest months of January – March as well as May and November. Variability has decreased for August and September, and all other months had no change in the variability of precipitation.

Hypothesis #3: The start of the rainy season has been delayed in recent years compared to several decades earlier.

This hypothesis does not appear to be true. For rainy season start dates calculated according to an accumulated precipitation threshold, most thresholds did not result in a detectible trend. No trend was detected for the two thresholds tied to past monthly precipitation levels (125 mm and 150 mm – corresponding to the median or mean precipitation, respectively), nor for the 200 mm threshold. The weak trend detected for the 100 mm threshold may be an indicator that precipitation in the early transition months may be decreasing (as seen with the decreasing trend for September precipitation), but when a threshold is chosen to correspond with all of the months that are considered transition months in this chapter (September – November), there is no detectable change in the start date of the rainy season.

Hypothesis #4: Dry spells during the rainy season and transition months have become more frequent and of longer duration in recent years.

This hypothesis appears to be true. There appears to be an abrupt shift in the length of dry spells starting in 1985 (it also may be true for 1982-1985, but data are missing for that period of time). The mean and median length of dry spells has increased for all seasons for the period from 1985-2010 compared with the data before 1985. There was a significant increase in the number of abnormally long dry spells for this period (1985-2010) as well as a significant increase in the variability of dry spell duration for all seasons.

Hypothesis #5: Rainfall intensities have decreased in recent years compared to several decades earlier.

This hypothesis does not appear to be true. Although a complete rainfall intensity analysis is not possible without hourly data, the data analysis presented in Section 4.3.3

indicates that if anything, rainfall intensities may have increased. Daily precipitation intensity calculated by the SDII increased for the period of 1990-2010 compared to 1963-1989, and the frequency histograms for both time periods show a decrease in the frequency of the lowest daily precipitation intensities.

In general, the dry season has become drier (less total precipitation, more dry days, and longer dry spells), but there was no detectable change in the overall amount of precipitation over the course of the year. Of all the precipitation-related observations in the perceptions of the local populations, decrease in the amount of precipitation was the most consistently identified trend. This trend, however, could not be identified in the precipitation data. There does seem to be an increase in the variability of the amount of precipitation during the rainy season as well as an increase in the length of dry spells (a possible drought indicator), which may explain the perception of decrease in precipitation (even though the data analysis indicates that this is not true). Although the results of the survey of perceptions of change in rainfall quantity do not reflect the reality, the local population may be identifying a separate but related problem with the reliability of rainfall. Increasingly more frequent and longer dry spells may have as much (if not more) of an impact on the agricultural sector as deficits in overall precipitation. It is possible that the local people were trying to express an observation of increase in droughts without having the ability to articulate it. The survey participants in Conchucos (near the weather station at Cachicadan) were asked specifically about droughts, and the majority (81%) responded that they had observed an increase in drought frequency. The observation of decrease in rainfall intensity (in the study of perceptions) also appears to be false, and the reason for this may be partly an inability to distinguish between intensity and quantity of rainfall. Although surveys of people's perceptions of climate change may yield useful

data in regions of data scarcity, the results of surveys should be interpreted carefully; they may not always correlate with the data, or they may reflect climate change patterns other than what is specifically stated in the question. This is important in the context of the government allowing this kind of qualitative information about perceptions of change (as a proxy for quantitative data) in PIPs.

If no other data are available, interpretation of studies of perceptions of change should err on the side of a conservative approach to project design and sustainability. For example, even though the perceived decrease in precipitation seems to be incorrect, if an irrigation project were to include a decrease in precipitation when assessing potential future water supply, this should result in a project that is more resilient to droughts; the potential effects of underestimating the precipitation could likely outweigh the potential negative impacts of overestimating it. If projects use perceptions of climate change in lieu of gauged data, the sensitivity to uncertainty in climate data for each type of analysis (e.g., assessment, design parameters, vulnerability) should be considered as part of the plan for PIP proposals. The discrepancy between the people's perceptions of change and the data indicate that local perceptions should be used with caution when designing PIP proposals and assessing projects for vulnerability to climate change.

The observations of changes in seasonality in the study of perceptions of climate change are more difficult to verify with data analysis, but some of the monthly tendencies can be used as indicators of seasonality. From the trends in the transition months, there were no clear signs that the rainy season is shorter or out of step with patterns 30 years ago (as many people said in the perceptions study). There was either no trend or an increasing trend detected for the months of October, November, April, and May, and increased variability was only seen in the transition months of November and May. The decreasing trend for September may be an indicator that September is exhibiting more

characteristics of the dry season than before. Thus, the perception of a longer dry season than 30 years ago (observed by 46% of survey participants) may be accurate. The increasing number of dry days in many transition months and longer dry spell durations in the transition and rainy seasons may be indications that the rains in the transition and rainy months are less reliable (more sporadic) or that the variability in daily precipitation has increased. However, because the total precipitation in those months has not decreased, this does not necessarily reflect a change in seasonality but rather an increase in the frequency and intensity of droughts.

Without a standard definition of the seasons (based on precipitation patterns), it is difficult to quantify changes in the timing of the seasons. There is justification for establishing standard protocols for defining the seasons; this could facilitate analysis of seasonal patterns and the impacts of aberrations from typical seasonal patterns on PIPs. The method for defining the start of the rainy season according to a threshold of accumulated precipitation may be a reasonable definition for the rainy season. Historically, there have been standard times of year to plant and harvest certain crops based on when the rains typically start and end. It is common to hear farmers talk about the failure of the rainy season in relation to the timing of their crops. For example, if crops are planted in October or November, and the precipitation in those months is much less than average, it could have drastic effects on productivity. Before standard protocols are set for defining the start of the rainy season, the definitions of the seasons should be linked with agricultural studies that investigate the quantity and frequency of rainfall needed to sustain crops without irrigation and the water requirements for crops at different growth stages.

There remains a question about what months should be considered as typically part of the rainy season. In this dissertation, the rainy season has been defined as

December – March, based in part on the months of austral summer (from the summer solstice to the autumnal equinox in the Southern Hemisphere). However, the precipitation in December and April are remarkably similar (similar mean and standard deviation with precipitation in April slightly higher than December, see Table 4.2). The similar rainfall characteristics in December and April suggest that either December should be considered a transition month or April should be considered part of the rainy season. When the participants in the study of perceptions of change were questioned about what months are part of the rainy season and dry season (Tables E.8 and E.9), the responses varied, but the majority said that the rainy season is October – April and the dry season is June – August. The highest percentages of responses were for the months of December – March for the rainy season and June – August for the dry season (coinciding with the seasonal definitions used in this dissertation). To resolve this question about the months that make up each season, it would perhaps be useful to question the local population about why they include certain months in the rainy and dry seasons. This question is likely related to how people interact with their environment. A better understanding about how the seasons and climatic variability affect people's activities and livelihoods can help project formulators improve PIP proposals so that they are more climate-resilient and better meet the needs of the project's beneficiaries.

Drought is perhaps the climate phenomenon that could have the greatest impact on agricultural projects. Definition of drought is not standard (as evidenced by the range of definitions provided by the local population shown in Table E.7), and most of the common drought indices are not really applicable in the Sierra Ancash where droughts are more likely to be short-term incidents rather than something that happens over the course of one or more years. The SPI has potential for evaluating droughts in the Sierra Ancash if applied at shorter time scales because it compares precipitation to normal

values for a given time of year. Similarly, rainfall deciles could be a useful approach to drought definition in the Sierra Ancash. To be truly useful, the SPI should be further adapted to the climate patterns of the region. For example, if monthly precipitation data are used, even a time scale of 3 months could smooth out short-term dry spells that might have significant local effects. Three months could include the transition between seasons so that even comparing to normal values for the time of year might not reflect important aberrations from normal rainfall behavior. Daily data could be used to define droughts over a period of several weeks, but this would be very time-intensive because a large number of probability distributions would have to be fitted to the data to cover the seasonal distribution for the whole year at a time scale of days to weeks. Once the distributions have been fitted, future calculations of the SPI would not be very difficult. However, because of the high level of spatial variability in the Sierra Ancash, the distributions for precipitation are location-specific, so the process of distribution fitting would have to be repeated for each new location. A drought index like the SPI that requires a large amount of analysis as an input to the calculation is unlikely to be used in the Sierra Ancash. The SPI is one of the simpler drought indices, but something even less complex is needed for the Sierra Ancash if quantification of droughts is to be considered as part of climate change vulnerability analysis for PIPs. Some possible ways to quantify drought in an index for the Sierra Ancash include an accumulated precipitation deficit (e.g., % below normal for the water year), consecutive dry days, or a combination of the two. The development of a region-specific drought index for the Sierra Ancash goes beyond the scope of this work, yet some of the variables analyzed in this chapter (i.e., number of dry days/month, dry spell duration, accumulated precipitation, and standardized precipitation) can be considered as possible indicators of drought.

Another way to view droughts and dry spells in the context of agricultural PIPs is by comparing precipitation deficits to crop water requirements. To illustrate this concept, a hypothetical scenario is outlined below:

A crop with a root depth of 1 ft., a maximum allowable depletion (MAD) of soil water of 50%, and an evapotranspiration rate (ET_{crop}) of 4 mm/day is planted in a loamy soil with an available water capacity (AWC) of 0.17 mm/mm (Ross et al., 1997). If the soil is initially saturated, the maximum amount of time that could elapse between irrigation or rainfall events and meet the water requirement without stressing the crop is 6 days $\left(\frac{AWC \times root\_depth \times MAD}{ET_{crop}} \right)$.

This means that the crop must be provided with water (via precipitation or irrigation) at least every 6 days. Considering that the mean duration of the maximum annual dry spell during the rainy season (from 1985-2010) is 21 days, it is very likely that the crop could become extremely water stressed if it relies exclusively on rainfall to meet the water requirement. Dry spells long enough to cause extreme water stress may not necessarily occur in all years, but the frequency of dry spells longer than 6 days is high enough that it would be unwise to implement a project with this particular crop and soil conditions without some way to supplement rainfall during long dry spells.

Based on the analysis of the length of dry spells during the rainy season (Figure 4.10), even agricultural projects that produce crops only during the rainy season should consider either supplemental irrigation or very water-resistant crops (or both). For climate change vulnerability assessment of agricultural projects, particular attention should be paid to the range of variability in precipitation and duration of dry spells during the critical growth stages for each crop.

Although temperature analysis was not included in this chapter, a discussion of potential impacts of temperature changes on PIPs is included here to illustrate how climate data analysis could be translated into concrete and simple metrics to be applied in PIP vulnerability assessments. Analysis of temperature variability in the context of risk and vulnerability assessment for PIPs should be relatively straightforward if data are available for a long enough period of time to be able to consider climate change. The most direct impacts of temperature variability on agriculture projects are frosts and shifts toward warmer temperatures. The most problematic adverse effect of frosts is potential damage to crops, but more persistent below-freezing temperatures could also affect the durability of infrastructure and introduce the potential for pipes to freeze in irrigation distribution systems. Warmer temperatures can have both positive and negative consequences. Increased temperatures could allow new blights or diseases to flourish. On the other hand, consistently warmer temperatures in a given zone could allow farmers to grow different crops that previously could only be produced at lower altitudes. Increased occurrences of frosts and warmer daytime temperatures are not necessarily mutually exclusive. Observations of the local population indicate that temperatures are warmer than they were 20-30 years ago, but many of the local people surveyed also have said that frosts are more common (Vergara Rodriguez, 2011; 2015).

The potential impacts of temperature changes on agriculture projects do not necessarily mean that projects cannot be successful. Nonetheless, the potential climate risks should be taken into account in the project design and operation and maintenance plans so that adverse impacts can be mitigated, resulting in more sustainable projects. The range of potential temperatures should be taken into account in the selection of crops to be planted, measures to protect crops from frosts and diseases, as well as in the calculation of potential evapotranspiration in the water balance study. If there is

considerable uncertainty in future temperature patterns, PIP proposals could include contingency plans, each tailored to a possible scenario of temperature ranges. This would require continued monitoring of climate conditions (i.e., data collection) and projects that have the flexibility to adapt to a wide range of conditions. For example, if temperatures increase, crops that thrive in warmer temperatures could replace crops that are better suited for colder temperatures if the project has the ability to change crops from year to year. Alternatively, crops could be shifted to higher altitudinal zones in the case of increased temperatures, but only if project beneficiaries have land available at higher altitudes and if the irrigation infrastructure (if applicable) is transportable. If it is possible that frosts may be more common in the future, agricultural PIP proposals could include plans to protect crops from frosts that would only be implemented if necessary. Since this chapter focuses on analysis of precipitation data and does not include analysis of temperature, all of these possibilities for future climate variability are hypothetical at this point. The potential considerations for PIPs are meant to illustrate the types of things that should be considered when assessing agricultural project proposals for vulnerability to climate change.

The type of analysis presented in this chapter requires data that may not be available at all potential project locations. Therefore, to develop a truly useful tool, the logical next step would be to compile all of the available data for the region. Then, building on the analyses presented in this chapter, the data could be analyzed at a regional level and synthesized into a regional climatic characterization that describes both the spatial and temporal patterns and variability for the Sierra Ancash. If the analyses presented in this chapter were applied to all the data available at the regional level, they could allow for broader conclusions to be drawn about climate change impacts and the secondary impacts that climate change could have on agricultural projects.

Chapter 5: Conclusions

The objective of this dissertation was to assess the impact of climate change on water security in the Sierra of Ancash with a focus on GLOF hazards and water availability. Specific emphasis has been placed on the following topics:

- Studying avalanche-generated impulse waves to improve understanding of lake dynamics during GLOF events
- Examining an emerging glacial lake, projecting future lake volumes, and evaluating future hazard conditions
- Analyzing precipitation data to determine if local perceptions of precipitation trends and variability are reflected in the data

The motivation for all of this work has been a desire to advance our understanding of high mountain glacial watershed systems as well as to develop tools to analyze climate change impacts that may be used to promote climate-resilient development.

The following sections give a summary of how the research questions were addressed, the major findings for each chapter, and how this work fits into the broader context of climate-resilient development. This is followed by a discussion of future work, describing directions this research could take to advance our knowledge about climate change impacts on water resources in the Sierra of Ancash.

5.1 Hydrodynamic Modeling at Lake Palcacocha

The first research question in Chapter 2 focused on the dynamics of avalanche-generated waves and the resulting overtopping flows during GLOF events:

Research Question #1: What would the lake dynamics be during a GLOF event, and how would they influence the outflow hydrograph and GLOF hazard?

This question has been addressed by studying a potential GLOF event at Lake Palcacocha with 3D modeling of avalanche-generated waves, including wave generation, propagation, runup and overtopping of the terminal moraine. These 3D simulations produced waves of considerable magnitude. The avalanche characteristics and the shape of the inflow hydrographs seemed to have the most influence on the overtopping volumes. The results of the lake model at Palcacocha indicated that the large avalanche scenario poses the greatest threat to the city of Huaraz, but all three avalanche scenarios could generate significant overtopping discharges, resulting in considerable inundation in the city of Huaraz.

The second research question related to the evaluation of lake-lowering scenarios to mitigate GLOF hazard:

Research Question #2: What impact would lowering the lake level have on the magnitude of a GLOF event, and how can we determine a "safe" lake level?

The simulations of the lake-lowering scenarios showed that lowering the lake level may reduce the hazard level and inundated area for the large avalanche scenario, but it is not possible to entirely eliminate the potential for overtopping. For the small and medium avalanche scenarios, it may be possible for the wave to be contained in the lake if the lake is lowered. However, given the range of uncertainty in the model results, it cannot be conclusively stated that lowering the lake level would prevent overtopping for smaller-

sized avalanches. Even though the precise reduction in hazard level due to lake lowering cannot be quantified, it is reasonable to conclude that lowering the level of Lake Palcacocha can reduce the hazard levels in the city of Huaraz.

The three-dimensional (3D) modeling at Lake Palcacocha provides a significant advancement beyond simulations that are typically performed for avalanche-generated waves. The 3D modeling approach was intended as an alternative to partially overcome the absence of field data from a GLOF event at the location of the study. This is not to say that this model is free from significant uncertainties, but as a 3D model provides better mechanisms to represent the underlying physical phenomena, uncertainties move from the model engine to the physical initial and boundary parameters, reducing the amount of physical or empirical assumptions.

Nonetheless, the lake dynamics still remain a problematic part of the GLOF process chain. The 2D SWE models that are typically applied in GLOF process chain modeling do not appear to represent the wave propagation and overtopping adequately. These models have dissipative effects that can cause significant wave attenuation and may result in greatly underestimated overtopping volumes (Somos Valenzuela et al., 2016). But, 3D models require more computational and human resources. It is possible that the empirical method of Heller et al. (2009, 2010) may be a more accurate alternative to 2D SWE models for representing wave generation when 3D modeling is not feasible. However, for empirical equations to replace numerical simulations of the lake dynamics in GLOF process chain modeling, an alternative method must be found to calculate overtopping volumes and determine discharge hydrographs for the overtopping waves (Chapter 3 presents a first attempt at this).

The avalanche simulation seems to be the step of the GLOF process chain that carries the greatest uncertainty, and much of that uncertainty is carried into the lake model. We do not currently have the means to know precisely how the avalanche behaves, and so it is equally impossible to say how well the lake model reproduces the avalanche characteristics as it enters the lake. Because the lake model is so heavily influenced by the avalanche characteristics, any attempt at quantifying the uncertainty due to the methods used for the lake model is very difficult. More simulations are needed to gain a better understanding of the magnitudes and sources of uncertainty in the 3D lake model (see Section 5.4.1).

Understanding and communicating uncertainty of these results is especially important because the downstream inundation simulations that have been produced from the results of this work are currently being adapted to create official hazard maps for the city of Huaraz. These results may also help inform decisions about implementing an early warning system (EWS) as well as providing justification for implementing an improved lake safety system. While an EWS is a less expensive alternative to a large construction project to lower the lake level, it is only able to give people sufficient warning to evacuate. If implemented with an effective evacuation plan, it can save lives. However an EWS cannot protect against damage to property and infrastructure. For this, additional measures are needed to control the lake level, and the results of the lake-lowering scenarios may be used to evaluate mitigation alternatives. It is important to clarify that the work proposed here is not a risk analysis. This research can only demonstrate what may happen if a GLOF were to occur, but this analysis of the physical processes in the GLOF chain of events can lay the necessary foundation to enable a risk assessment.

In communicating uncertainty, the first priority is clear communication. There is little doubt that there is a significant GLOF hazard from Lake Palcacocha; the important

question is rather what flood magnitudes are likely if a GLOF does occur. A conservative approach has been taken, and the worst-case scenarios have been presented to local authorities to represent the potential hazard in Huaraz due to a GLOF at Lake Palcacocha. For the lake modeling results, this means that the results from the avalanche source simulations have been used. It is possible that the differences between the boundary condition methods (especially in the small and medium scenarios) could be significant enough to influence the optimal amount of lowering when the lake-lowering scenarios are evaluated. However, it is more likely that the maximum amount of lake lowering will be limited by cost and engineering feasibility so that uncertainty in the lake model would have a minimal influence on the optimum lake level. Even with the uncertainties in the lake model, the following can be concluded with reasonable confidence: 1) In the event of a GLOF, the current conditions at Lake Palcacocha are likely to produce significant overtopping discharges, and 2) Lowering the level of Lake Palcacocha may reduce the hazard potential for Huaraz but cannot guarantee the prevention of overtopping.

5.2 Projecting Future Lake Conditions and GLOF Hazard at Artesonraju Glacier

Chapter 3 addressed the need to have a future-oriented outlook when evaluating GLOF hazards. Glacial hazards are heavily influenced by the warmer temperatures brought about by climate change, and new lakes are still emerging and continue to grow as climate change persists. Therefore, new methods are needed for evaluating future lake conditions to ensure that any actions to mitigate GLOF hazard may be robust to the variable circumstances brought about by climate change. The research question for this chapter was:

Research Question #3: What will emerging glacial lakes look like in the future, and how can we determine the level of hazard that they may pose?

This question has been answered by using geophysical measurements of current glacier conditions to make projections of the future bathymetry for a fully-formed lake. The volume of the lake when it reaches its fullest extent was projected to be approximately 10 million m^3 (± 6/7 million m^3). To assess the hazard potential of the fully formed lake, simplified methods were used to simulate the upper-watershed portion of the GLOF process chain, from avalanche to overtopping of the terminal moraine. The estimated overtopping volumes ranged from approximately 0.13 million m^3 for the small avalanche scenario to 1.8 million m^3 for the large avalanche scenario. Although no conclusions can be made about downstream GLOF impacts and hazard potential from the research in Chapter 3, it is reasonable to conclude that there is the potential for an avalanche-generated wave to produce significant overtopping volumes. Therefore, the emerging lake at Artesonraju could potentially be dangerous if it is allowed to reach its full extent.

Chapter 3 presented a novel application of existing technology to project future lake depths and volumes. Ground penetrating radar (GPR) was used to project the future lakebed characteristics that may be expected as the lake grows. The truly innovative aspect of the research in Chapter 3 is that it uses those projections to anticipate potential future hazard conditions. GLOF modeling with a hypothetical future lake extent is something that has rarely been done before. Previous studies that modeled GLOFs based on future lake extent (e.g., Frey et al., 2010; Nussbaumer et al., 2014) have only simulated downstream debris flows while ignoring the upper watershed processes that were the focus of Chapter 3.

The new method for calculating overtopping volumes from avalanche-generated waves (adapted from the tsunami runup equations) that was presented in Chapter 3 could potentially fill in a key missing link in the simplified methodologies used to assess the GLOF process chain. This method is promising, but it needs further validation before it can be used for reliable assessments of the GLOF process chain. One limitation of this method is that it does not address the issue of possible breaches of lake-damming moraines due to wave-induced erosion. However, the major shortcoming of this method is that it does not produce discharge hydrographs. If this method proves to give reasonable enough estimates of overtopping volumes so that it can be used in place of hydrodynamic simulations, a method for converting discharge volumes to hydrographs (a necessary input to downstream inundation simulations) must be developed.

The research in Chapter 3 demonstrates the possibility of using simple analysis methods for a first-order assessment of GLOF hazard without investing a significant amount of time and resources. This type of approach can be used to determine the likelihood for a glacial lake to produce a high-magnitude GLOF and prioritize sites for more detailed studies. The work in Chapter 3 also shows that it is possible to take an anticipatory approach to GLOF hazard assessment. If these methods are accepted by Peruvian technical specialists and authorities, it may be possible to evaluate and implement measures to reduce GLOF hazard before lakes become dangerous. This type of preemptive approach to lake safety systems could be more economically efficient while also preventing the possibility of a time lag between when a lake becomes dangerous and when a lake safety system can be implemented. In the case of Artesonraju, a tunnel could be constructed in the lateral moraine to control the lake level before the lake reaches the tunnel location. Construction would be easier (potentially reducing costs), and the lake would never be allowed to reach a dangerous level.

Chapter 3 demonstrates that it is possible to extrapolate the results of field studies to project future lake conditions and hazard potential for emerging lakes. Furthermore, if the simplified modeling techniques for representing the GLOF process chain can be validated, this could prove to be a useful tool in promoting proactive approaches to risk management, especially in developing countries with limited resources.

5.3 CLIMATE INDICES

Chapter 4 sought to bridge the gap between science and policy in climate-resilient development by promoting simple yet robust methods of climate data analysis that are relevant to public investment projects (PIPs), as proposed by Research Question #4:

Research Question #4: How can the gap between science and policy in the context of climate change and adaptation in Ancash be breached by simplifying methodologies for vulnerability analysis without losing validity of results?

To be effective, the simplified methodologies must be grounded in good science and quantitative analysis. Therefore, analysis of precipitation data was undertaken as part of an effort to develop climate indices that quantify changes in climate variables with the objective of improving understanding of climate change by examining trends and variability in precipitation patterns. However, long-term records of meteorological data are very scarce in the Sierra of Ancash, and not all PIPs may have access to the data required for a thorough analysis of climate trends and variability. Thus, a simple approach was used: people's perceptions of climate change may be used as a proxy for gauged precipitation data. The validity of this approach was evaluated through

comparison of a study of climate change perceptions by Vergara Rodriguez (2011) to an analysis of historical data at the same geographic location, a weather station at Cachicadan. Of five specific hypotheses about the character and reliability of the rainy season that were tested, only one appears to be categorically true (Table 5.1): the hypothesis related to droughts. The local people surveyed indicated that droughts have increased. Dry spells during the rainy season appear to have increased both in duration and frequency, which may imply that droughts have become more frequent. Most of the hypotheses formulated from people's perceptions appear to be incorrect when compared with historic data analysis, indicating that people's perceptions of change do *not* represent the actual trends and variability seen in historical data.

Table 5.1- Assessment of the five specific hypotheses for Chapter 4 about the character and reliability of the rainy season

#	**Statement**	**True/False**
1	*The amount of precipitation in the rainy season has decreased*	False
2	*Variability in precipitation has increased for all months of the year*	Partially true, only in rainy months
3	*The start of the rainy season has been delayed in recent years compared to several decades earlier*	False
4	*Dry spells during the rainy season and transition have become more frequent and of longer duration in recent years*	True
5	*Rainfall intensities have decreased in recent years compared to several decades earlier*	False

If we can develop an effective methodology for the technical aspects of climate change vulnerability analysis, then it will not only promote advancement of the state of knowledge about climate change and impacts, but it will also lay the foundation for better adaptive capacity in decision-making and policy contexts. A solid foundation of data

analysis is the first step towards promoting climate-resilient development, and this work shows that it is possible to draw a number of conclusions from basic precipitation data (if the data are available for sufficiently long periods of record). With this knowledge, links may be made to impacts on PIPs, and this could enable more efficient use of the water resources of the region.

5.4 Future Work

This dissertation provided a solid foundation for an improved understanding of the high mountain glacial watershed systems of the Sierra of Ancash. Yet, the scope of this work was limited, and there are countless research activities that could build upon this work and strengthen our knowledge about the impacts of climate change on water security in the Cordillera Blanca. This section describes future work that would be a natural continuation of the research in this dissertation.

5.4.1 Three-Dimensional Lake Modeling

The simulations at Lake Palcacocha show that 3D hydrodynamic modeling can be a useful tool in understanding the dynamics of avalanche-generated waves, especially at sites where there are no observations in the field to assist with calibration. However, additional simulations are needed to fully assess the added benefits of 3D models over 2D models and to determine the sensitivity of the model to boundary conditions and initial conditions. With detailed comparisons of a variety of 2D and 3D simulations, the optimal balance between model complexity and accuracy may be determined. It is known that the 2D SWE are overly dissipative and do not represent wave propagation and overtopping effectively (Somos Valenzuela et al., 2016). However, it is not clear whether this is due

to the shallow water approximation or the 2D nature of the model. The following comparisons may help to determine what level of model complexity is needed to effectively simulate avalanche-generated impulse waves:

- 2D SWE vs. 2D non-hydrostatic

  This comparison will help to determine the significance of vertical accelerations in the generation and propagation of avalanche-generated waves.

- 2D vs. 3D (both non-hydrostatic)

  This comparison will determine whether a 3D model is necessary to accurately represent the dynamics of avalanche-generated waves.

The models can be compared by calculating the difference in maximum wave heights in the middle of the lake (before runup). The dissipation of energy for each model may be determined by the attenuation in wave height as the wave propagates across the lake and during runup. Finally, the overtopping volumes and hydrographs should be compared for each model to determine the sensitivity of these key model outputs to the type of model. By separately comparing 2D vs. 3D and hydrostatic vs. non-hydrostatic models, it will allow us to determine which of these two simplifications most influences the results. It may be the case that the difference between the 2D and 3D models is negligible if both are non-hydrostatic, but it also may transpire that a 3D non-hydrostatic model is necessary to fully capture the dynamics of avalanche-generated impulse waves.

The largest source of uncertainty in the Palcacocha lake model is the representation of the impact of the avalanche with the lake. To better understand this

process, additional simulations may be run with slight variations on the two types of boundary conditions presented in Chapter 2. To get a more direct comparison between the boundary conditions, the inflow hydrographs should be the same for each method. The inflow hydrographs measured from the avalanche source method may be used as inputs to the mass-momentum source so that an absolute difference between the boundary condition methods may be determined; this may be determined by comparing wave heights, overtopping hydrographs, and total overtopping volumes.

The uncertainty in the avalanche parameters is still the greatest overall source of uncertainty, and the avalanche characteristics have a large influence on the lake dynamics. More research on the dynamics of ice-rock avalanches is needed to be able to reduce this uncertainty. However, analysis of sensitivity of the lake model to the inflow depth and hydrograph may help to understand how much the avalanche characteristics influence the results further downstream. Various simplified inflow hydrograph shapes could be used to determine how much the peak flow and duration of the avalanche might influence overtopping. The height and width of the inflow area could also be varied to determine the effect of avalanche height and width. These simulations may help to quantify the uncertainty in the lake model. This may, in turn, make it easier to determine a potential range of outcomes that could facilitate economic and vulnerability analyses.

5.4.2 Analytical Overtopping Calculations

As discussed in Chapter 3, further validation of the new method for calculating overtopping volumes from avalanche-generated waves is needed before it can be considered a reliable method. 3D hydrodynamic simulations should be run at a variety of glacial lakes to determine how waves behave with different bathymetric conditions and

runup geometries. In the absence of data from field observations, these 3D simulations must serve as the best available data for comparison to the analytical calculations of overtopping volumes proposed in Chapter 3. The runup and overtopping calculations are quite sensitive to the lake depth near the moraine and the slope of the terminal moraine. Therefore, it is important to evaluate how these calculations compare to 3D model results with a variety of lakebed geometries. The following bathymetric characteristics may test how the model behaves in extreme circumstances: deep lakes with a bowl-like shape (Lake 513 is a good example of this type of lake), lakes with abrupt changes in slope of the terminal moraine (e.g., lakes with vertical dam structures), and lakes of varying freeboard heights.

The lake dynamics remain a difficult step in the GLOF process chain to simulate, and GLOF process chain modeling could be greatly assisted if it is possible to replace hydrodynamic lake models with simplified calculations of the wave and overtopping characteristics (i.e., a combination of the Heller et al. (2009) method for wave generation and the method presented in Chapter 3 for calculating overtopping volumes). If this is the case, it will be necessary to develop a method for approximating the shape of the discharge hydrograph. Before hydrograph shapes can be approximated, more information is needed on the potential ranges of peak flow and flow duration that may be expected from overtopping waves. A large number of 3D simulations may help us understand what factors influence the shape of overtopping hydrographs, and these may be used to develop empirical relationships between wave characteristics and moraine geometries and the peak flow and duration of the overtopping hydrograph. It may be possible to adapt some of the concepts of the synthetic unit hydrograph to establish protocols for determining the hydrograph shape. Even if it is not feasible to completely replace hydrodynamic lake simulations with simplified calculations, the new method for

calculating overtopping volumes could still be a useful tool for first-order GLOF hazard assessment.

The simplified analysis methods in Chapter 3 could also be used as part of a hierarchy of levels of analysis. A preliminary analysis of all glacial lakes in a geographic region can be done with remotely sensed data and satellite images to identify lakes that have characteristics indicative of potential GLOF triggers and filter out lakes that are not likely to produce a GLOF[4]. A first-order model of the GLOF process chain (i.e., the methods in Chapter 3) could then be undertaken for all the lakes identified in the previous step as potentially dangerous. The lakes that might produce significant flood volumes could be selected for further study and identified as high hazard or very high hazard, and the lakes for which preliminary modeling studies indicate that a significant GLOF is unlikely could be demoted to a low or medium hazard level. This type of hierarchical GLOF hazard assessment would be an efficient use of time and resources and would ensure that sites are prioritized based on their real hazard potential.

5.4.3 Climate Indices

Chapter 4 provided a thorough analysis of precipitation trends and variability at one site, something that has never been done before in the Sierra of Ancash. Yet, for this work to be more broadly applicable, the analysis must be repeated at other sites. This work on climate indices has been presented to several local government agencies in Ancash, and the hope is that these methods for climate data analysis can be repeated for other locations where long-term data are available, resulting in a regional climatic

[4] This study has been undertaken for the Cordillera Blanca by a Peruvian student intern at The Mountain Institute under my supervision and with the assistance of graduate students at the University of Texas at Austin.

characterization that can be used to develop guidelines for PIP formulators. If this can be done, then it may be possible to develop standard protocols to account for climate change in the analysis of risk and vulnerability of PIP proposals.

Long-term records of climate data in the Sierra of Ancash are scarce, and access to these data is even more limited. Nonetheless, there are a few sites in the region for which long-term precipitation records are available. Precipitation data analysis carried out at multiple locations would allow us to draw more general conclusions about climate change and precipitation patterns in the Sierra of Ancash and to determine if the trends and patterns of temporal variability observed at Cachicadan are localized or if they hold true for the whole geographic region. It is well known that precipitation in the Sierra of Ancash is highly spatially variable, but the exact nature of this spatial variability is poorly understood. Data analysis at additional weather stations could help characterize this spatial variability in precipitation.

There are many additional analyses that could give added value to the work on climate indices. One specific feature that could be further investigated is the length of the rainy season. The end of the rainy season could be determined in a similar way to the method for determining the start date of the rainy season. The date of the end of the rainy season could be defined as the date on which the accumulated precipitation for the water year surpasses a certain percentage of the annual total precipitation (for the water year). This can only be determined on a post factum basis, but it would be useful for analyzing historical patterns and trends. In this way, it may be determined if the rainy season has become shorter or if there is more variability in the timing of the rainy season than there used to be (as indicated in the studies of Vergara Rodriguez, 2011; 2015).

The usefulness of a drought index was discussed in Chapter 4, and the development of such an index for the Ancash region could be done in future work. The

first step in developing a drought index would be to look at "normal" precipitation patterns throughout the year. This could be done through analysis of probability density functions (pdfs) for precipitation over different time periods (i.e., different lengths of time and times of the year). From these pdfs, an optimal time span for analyzing precipitation in this region may be determined (e.g., days, weeks, months). This analysis of pdfs could be a precursor to a percent of normal type of drought index. Ideally, a drought index for this region would consider frequency and duration of dry spells as well as shortfalls in total precipitation. The assessment of dry spells in Chapter 4 focused on the maximum length of dry spell for each season, but this ignores all dry spells in a given season that were not the longest. If a frequency-duration curve were determined for all the dry spells during the rainy season, it may contain additional information that could be useful in developing a drought index.

The final step in applying the precipitation data analysis of Chapter 4 to PIPs is to develop standard protocols for incorporating quantitative analysis of climate change into analysis of risk and vulnerability for these projects. With the major findings from the data analysis, indices may be developed to quantify possible changes and ranges of variability. For example, a frequency analysis of dry spell duration may make it possible to determine a standard length of dry spell (at a given persistence/confidence level) that should be considered for all agricultural projects. Similar guidelines may be developed to quantify the expected value and uncertainty for other aspects of precipitation that may have implications for public investment projects. If these guidelines are based on solid analysis of historical data, they may provide precisely the type of tool that is needed for climate change vulnerability assessment in the context of development projects.

5.5 FINAL REMARKS

The research in this dissertation has investigated climate change and water security in the Sierra of Ancash and improved our understanding of several specific aspects of climate change impacts on high mountain glacial watershed systems. The three-dimensional lake model in Chapter 2 is an improvement over the typical lake model used in GLOF process chain simulations. The 3D hydrodynamic model can give us a better understanding of the likely outcomes than models that require extensive calibration (e.g., 2D SWE models). Chapter 3 presented innovative ways to use field data at glaciers to project future conditions of emerging lakes and perform simple GLOF hazard assessments. Chapter 4 demonstrated that it is possible to extract a lot of information about trends and variability of precipitation patterns through straightforward analysis of climate data; the precipitation data analysis also showed that perceptions of climate change may not be a reliable way to account for climate change in PIP proposals. These advancements in the state of knowledge about climate change impacts in the Sierra of Ancash are just one piece of the puzzle needed to promote sustainable development that is resilient to climate change.

The second objective of this research was to bridge the gap between scientific research and local planning and policy. This has been attempted by: 1) adapting the research to fit the needs of the people, and 2) developing simple analysis methods that are grounded in solid research methodology. The research findings will be presented to local institutions in the Sierra of Ancash in a straightforward way so that the applications for decision-makers are easily understood. A thorough understanding of the potential impacts of climate change combined with the transfer of this knowledge to decision-makers and technical personnel in government agencies could make great strides in promoting adaptation solutions geared towards mitigating the impact of climate change on water

resources in the Sierra of Ancash. If this is successfully accomplished, the technical methods developed with this dissertation can be used to promote a progressive and proactive mentality to climate change adaptation rather than the reactive approach that has traditionally been used in Ancash.

Appendix A: GPR Radargrams

Radargrams for all GPR transects measured at Artesonraju Glacier are presented in the following figures. Each figure shows an image of the z-scope radargram and an inset map of the glacier showing the location of the transect.

2012 Radargrams

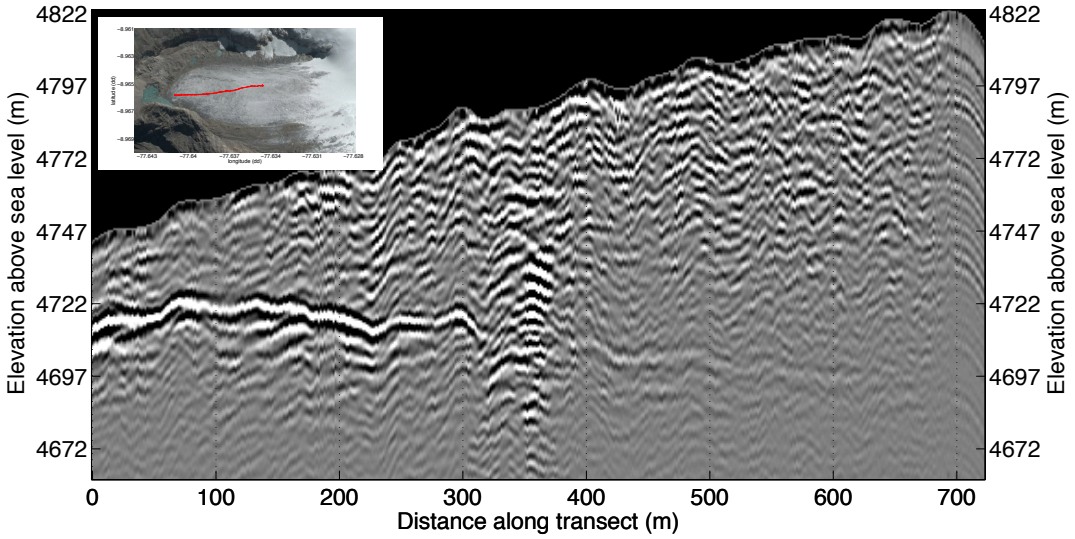

Figure A.1- Radargram for 2012 Transect 1, taken with the UT GPR unit

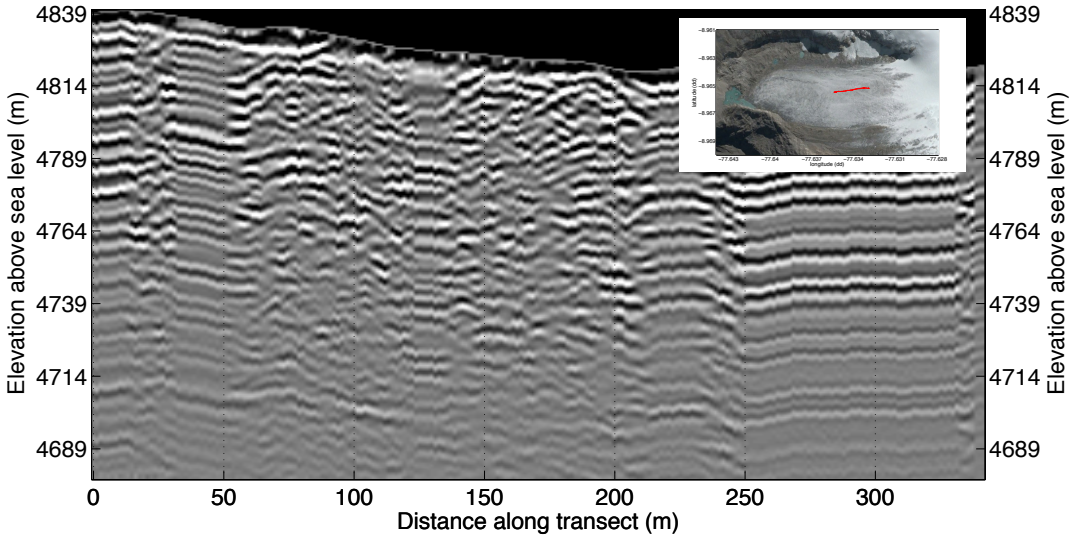

Figure A.2- Radargram for 2012 Transect 2, taken with the UT GPR unit

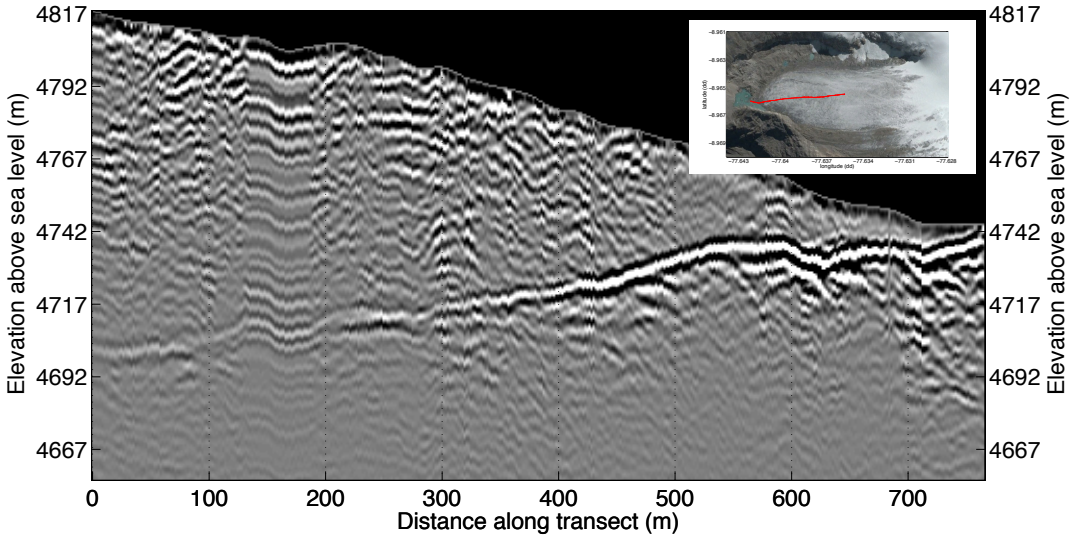

Figure A.3- Radargram for 2012 Transect 3, taken with the UT GPR unit

2013 UT Radargrams

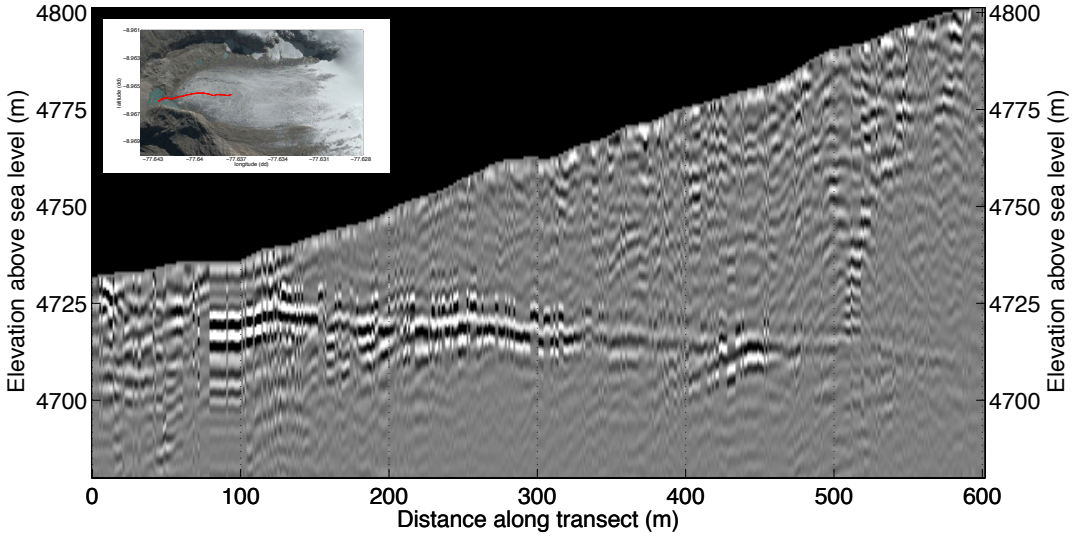

Figure A.4- Radargram for 2013 UT Transect 1, taken with the UT GPR unit

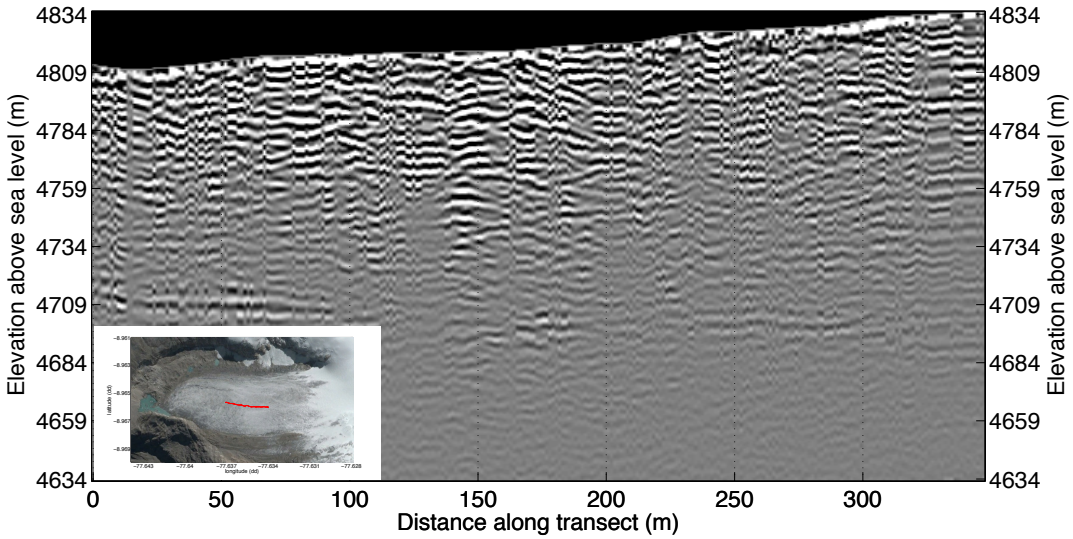

Figure A.5- Radargram for 2013 UT Transect 2, taken with the UT GPR unit

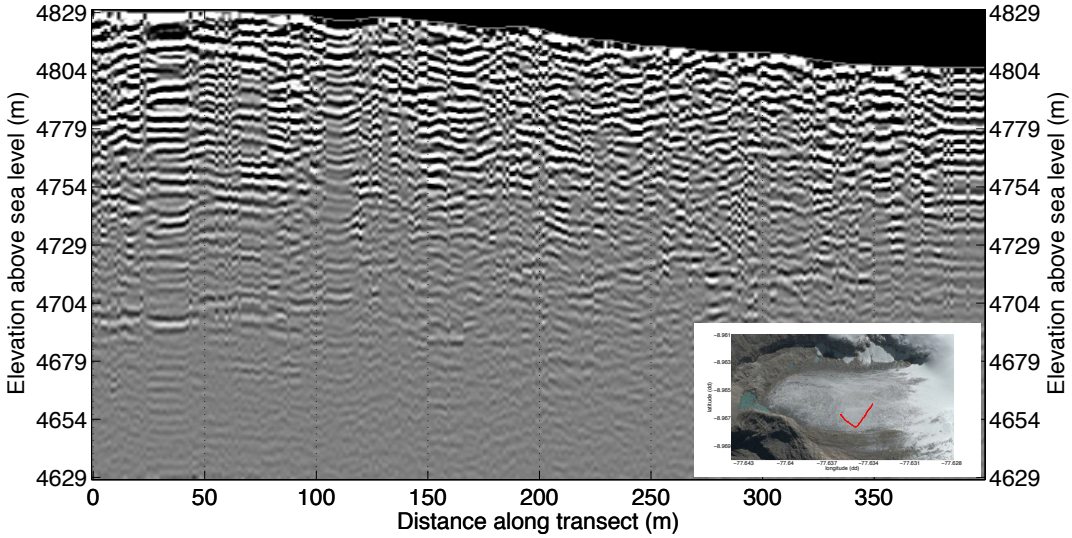

Figure A.6- Radargram for 2013 UT Transect 3, taken with the UT GPR unit

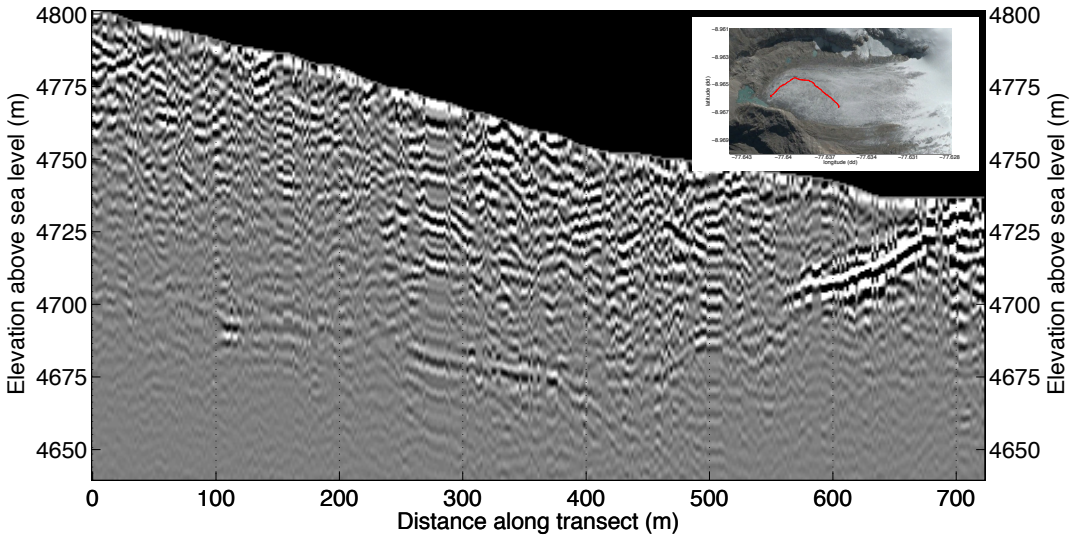

Figure A.7- Radargram for 2013 UT Transect 4, taken with the UT GPR unit

2013 UGRH Radargrams

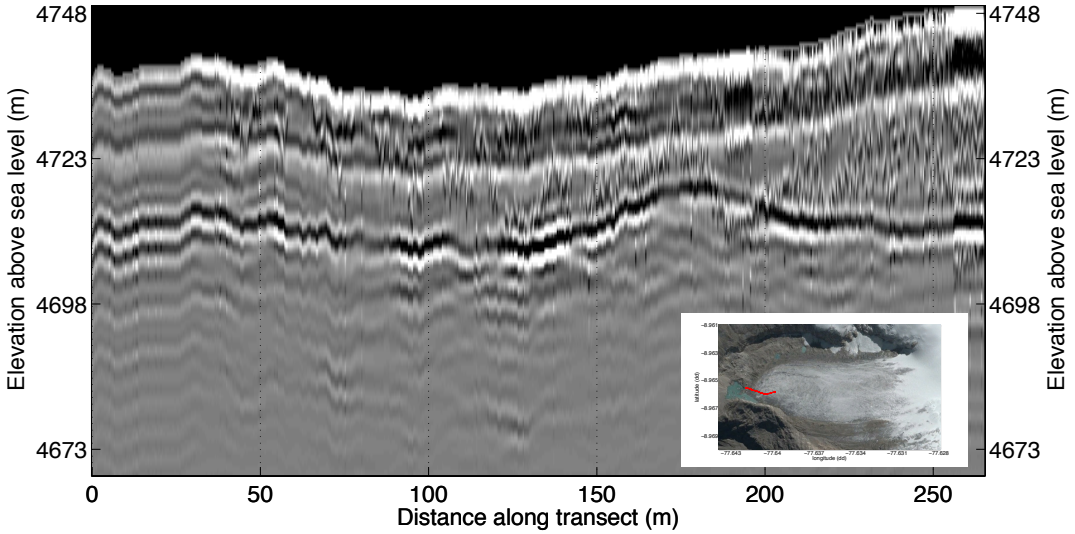

Figure A.8- Radargram for 2013 UGRH Transect 1, taken with the UGRH GPR unit

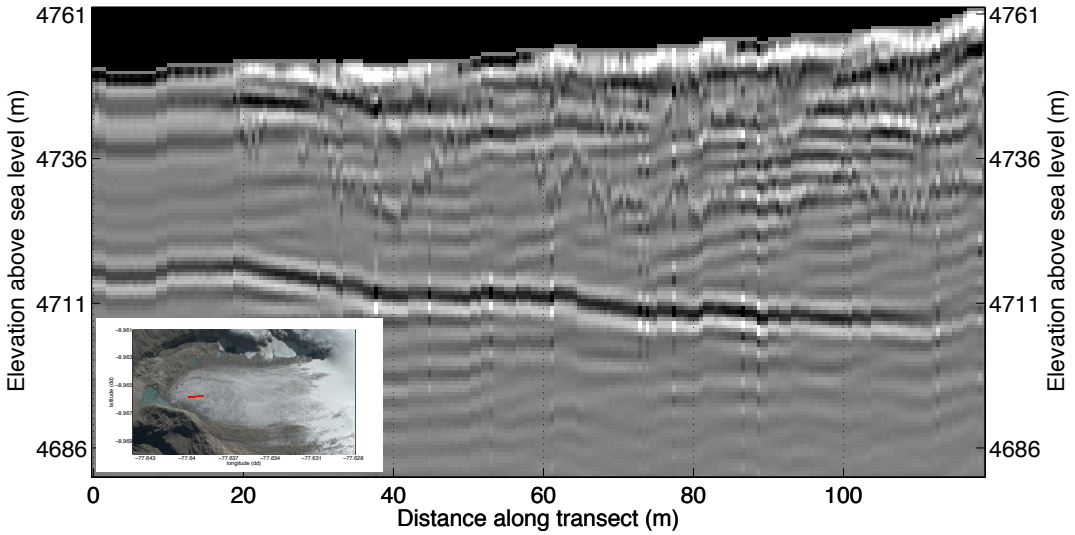

Figure A.9- Radargram for 2013 UGRH Transect 2, taken with the UGRH GPR unit

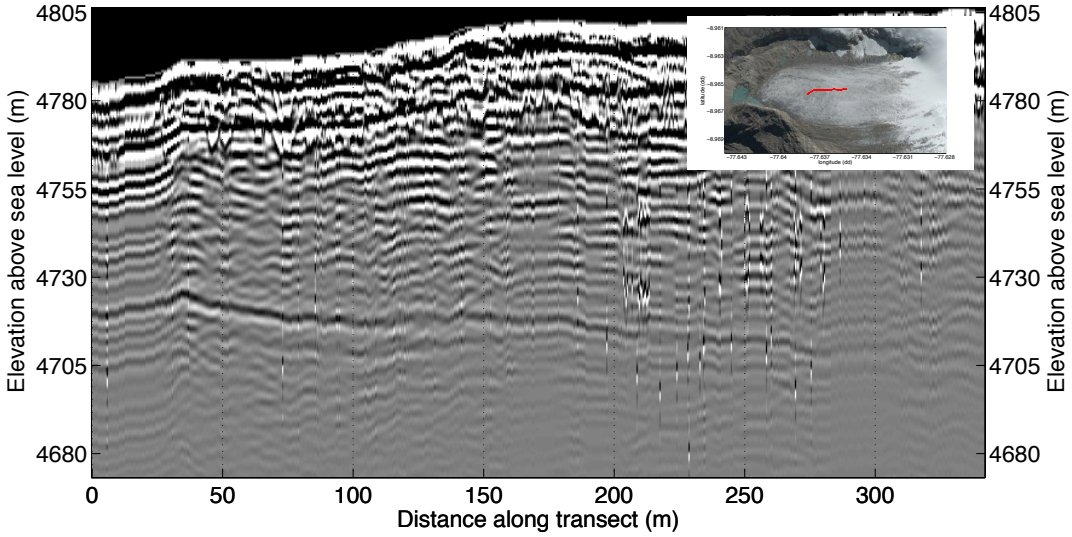

Figure A.10- Radargram for 2013 UGRH Transect 3, taken with the UGRH GPR unit

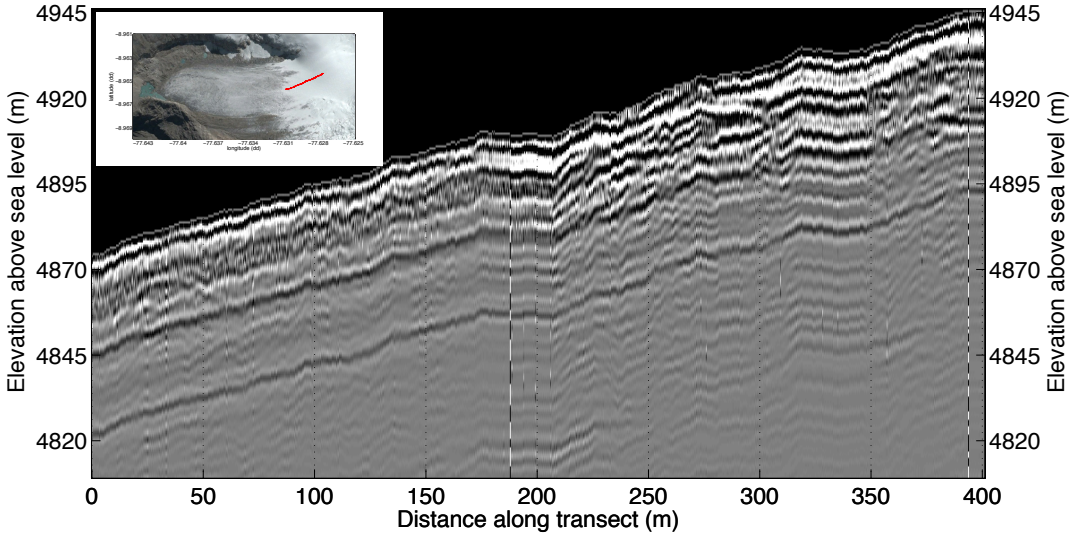

Figure A.11- Radargram for 2013 UGRH Transect 4, taken with the UGRH GPR unit

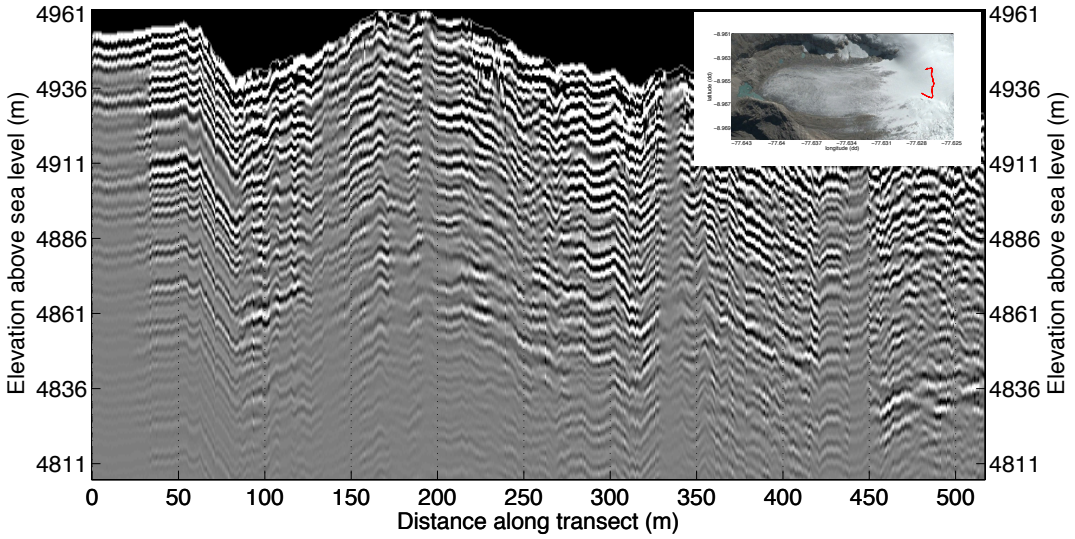

Figure A.12- Radargram for 2013 UGRH Transect 5, taken with the UGRH GPR unit

2015 Radargrams

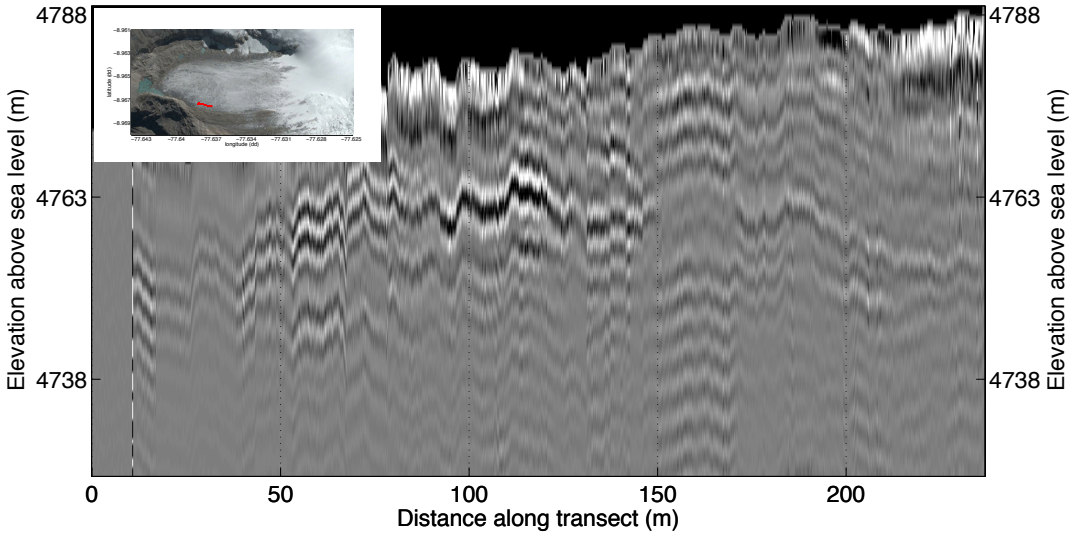

Figure A.13- Radargram for 2015 Transect 1, taken with the UGRH GPR unit

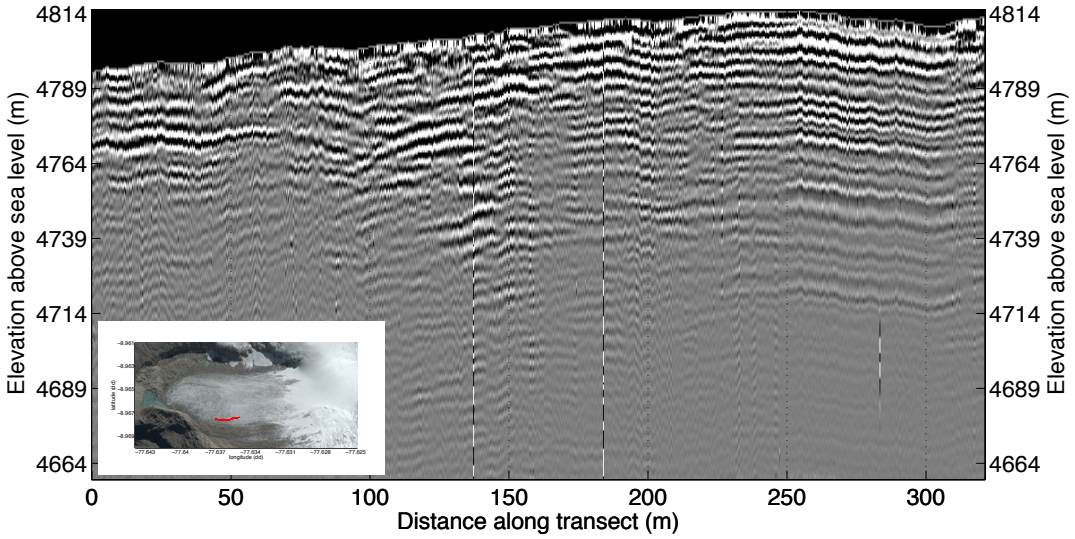

Figure A.14- Radargram for 2015 Transect 2, taken with the UGRH GPR unit

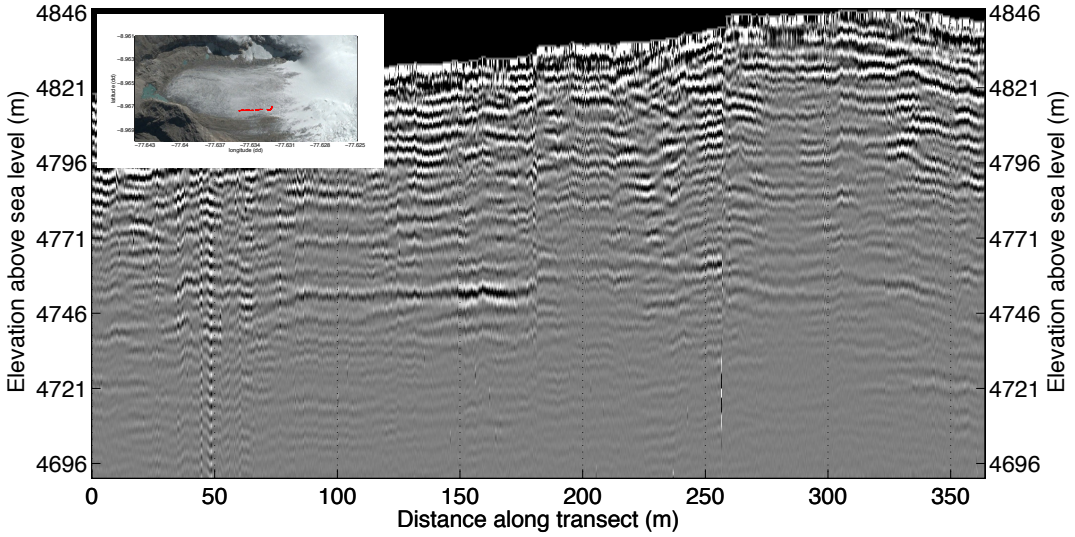

Figure A.15- Radargram for 2015 Transect 3, taken with the UGRH GPR unit

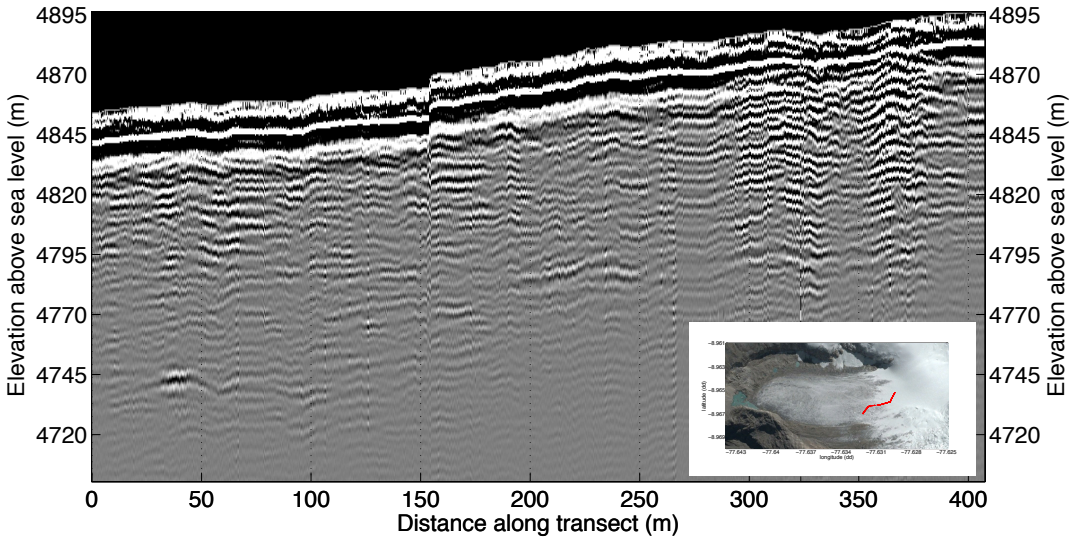

Figure A.16- Radargram for 2015 Transect 4, taken with the UGRH GPR unit

Appendix B: Validation of Overtopping Wave Equations at Lake Palcacocha

A summary of the results of the 3D hydrodynamic simulations at Lake Palcacocha from Chapter 2 is given in Table B.1. The input parameters used to calculate approximate overtopping volumes according to the adapted tsunami runup method are summarized in Table B.2. Table B.3 gives a summary of the results of the analytical overtopping calculations, and the results from the two methods are compared in Table B.4. The overtopping volumes calculated with the analytical equations are approximately 30% less than the FLOW-3D overtopping volumes.

Table B.1- Maximum wave heights and overtopping volumes from the FLOW-3D simulations at Lake Palcacocha (results from Chapter 2)

	Max. Wave Height, empirical equations* (m)	**Max. Wave Height, FLOW-3D simulations (m)**	**Overtopping Volume (10^6 m^3)**
Large Avalanche Source	42	47.8	1.8
Large Mass-Momentum Source	42	46.4	1.64
Medium Avalanche Source	21	30.1	0.5
Medium Mass-Momentum Source	21	--	0.15
Small Avalanche Source	9	19.6	0.15
Small Mass-Momentum Source	9	--	0.014
** Heller and Hager (2010)*			

Table B.2- Input parameters used to calculate overtopping volumes at Lake Palcacocha from the adapted tsunami runup equations described in Section 3.2.3

Still water depth near the moraine (d)	5 m
Freeboard (f)	8 m
Length of the moraine crest (l)	200 m
Moraine slope (b)	45°
Distance to maximum wave height (X_1)	300 m
Maximum wave height: small avalanche (m)	19.6
Maximum wave height: medium avalanche (m)	30.1
Maximum wave height: large avalanche (m)	47.8

Table B.3- Results of the runup and overtopping calculations at Palcacocha using the adapted tsunami runup equations of Synolakis (1987) and the input parameters in Table B.2

Avalanche Size	**Maximum wave height, H_m (m)**	**Free surface elevation at x=0, $\eta(0, t_{max})$ (m)**	**Theoretical runup height, $\Re$ (m)**	**Total overtopping volume, V_O (m^3)**
Large	47.8	48.7	238.0	1.12×10^6
Medium	30.1	27.5	133.5	3.45×10^5
Small	19.6	16.2	78.1	1.13×10^5

Table B.4- Comparison between FLOW-3D overtopping results and the analytical calculations from the adapted tsunami runup equations

Scenario	**Wave Height (m)**	**Calculated Overtopping Volume (analytical equations), 10^6 m^3**	**Simulated Overtopping Volume (FLOW-3D), 10^6 m^3**
Large Avalanche Source	47.8	1.12	1.8
Large Mass-Momentum Source	46.4	1.04	1.64
Large Empirical Equations*	42	0.81	---
Medium Avalanche Source	30.1	0.35	0.5
Medium Empirical Equations*	21	0.14	---
Small Avalanche Source	19.6	0.11	0.15
Small Empirical Equations*	9	0.013	---

** Heller and Hager (2010)*

Appendix C: Matlab Script for Analytical Overtopping Volume Calculations

```
% Wave Runup and overtopping calculations

H = 19.6; %maximum wave height in the middle of the lake
d = 10; %water depth next to the terminal moraine
beta = 30; %slope angle of terminal moraine in degrees
X1 = 300/d;
X0 = cotd(beta);
w = 200; %width of the lake (m)
f = 5; %freeboard height (m)

R_ht = d*2.831*(cotd(beta)^0.5)*((H/d)^(5/4));

gamma = ((3*H)/(4*d))^0.5;
alpha = pi/(2*gamma);
tmax = (X0 + X1 - (0.366/gamma));


eq_int = @(k) ((2/3).*k.*(1./sinh(alpha.*k)).*exp(i.*k.*X1)).*(exp(-
i.*k.*(X0+tmax))./(besselj(0,(2.*k.*X0))-i*besselj(1,(2.*k.*X0))));
eta_2 = integral(eq_int,-Inf,Inf);
eta = 2*eta_2;

% a, b, and c are lengths of the triangle that represents two-dimensional
% overtopping volume (total volume will be area of the triangle x lake
% width)
a = sqrt((real(eta)-f)^2+(f/tand(beta))^2);
b = sqrt((R_ht-real(eta))^2 + (R_ht/tand(beta))^2);
c = (R_ht - f)/sind(beta);

p = (a + b + c)/2; % 1/2 perimeter of the triangle
A = sqrt(p*(p-a)*(p-b)*(p-c)); % Heron's formula for area of triangle
V = A*w; % Total overtopping volume
```

Appendix D: Existing Climate Indices

The following indices are summaries of some of the references mentioned in Chapter 5 (not a comprehensive list of all the existing climate indices). Indices highlighted in blue are the 10 key indices recommended by Peterson et al., 2001.

CLIMDEX/ETCCDI Indices

Indices in bold are ones identified in this dissertation as most likely to be applicable in the Sierra Ancash

Table D.1- Core Precipitation Indices (from ETCCDI, 2009 and Peterson et al., 2001)

Name of Index	**Abbreviation**	**Explanation**
Monthly maximum 1-day precipitation	**Rx1day**	
Monthly maximum consecutive 5-day precipitation	Rx5day	
Simple daily precipitation intensity index	**SDII**	**Total precipitation divided by the number of wet days (days with precipitation > 1 mm) for a given period**
Annual count of days when Precipitation ≥ 10 mm	R10mm	
Annual count of days when Precipitation ≥ 20 mm	R20mm	
Annual count of days when Precipitation ≥ nn mm	**Rnnmm**	**nn is a user defined threshold**
Maximum length of dry spell	**CDD**	**Maximum number of consecutive days with precipitation < 1mm (dry days)**
Maximum length of wet spell	CWD	Maximum number of consecutive days with RR ≥ 1mm
Annual total Precipitation when daily precipitation > 95p	R95pTOT	Annual total of precipitation on days when the daily precipitation exceeds the daily precipitation amount corresponding to the 95th percentile of precipitation on wet days for the period 1961-1990
Annual total Precipitation when daily precipitation > 99p	R99pTOT	Annual total of precipitation on days when the daily precipitation exceeds the daily precipitation amount corresponding to the 99th percentile of precipitation on wet days for the period 1961-1990
Annual total precipitation in wet days	PRCPTOT	Total annual precipitation
**Fraction (%) of annual total precipitation due to events exceeding the 1961-90 95th percentile*	*R95T	
**One of the 10 key indices in Peterson et al. (2001) but not one of the ETCCDI/CLIMDEX indices*		

Table D.2- Core Temperature Indices (from ETCCDI, 2009 and Peterson et al., 2001)

Name of Index	**Abbreviation**	**Explanation**
Number of frost days	**FD**	**Annual count of days when daily minimum temperature < 0°C**
Number of summer days	SU	Annual count of days when daily maximum temperature > 25°C
Number of icing days	ID	Annual count of days when daily maximum temperature < 0°C
Number of tropical nights	TR	Annual count of days when TN (daily minimum temperature) > 20°C
Growing season length	GSL	Year for growing season is defined as 1st Jan to 31st Dec in Northern Hemisphere (NH), 1st July to 30th June in Southern Hemisphere (SH). Annual count between first span of at least 6 days** with daily mean temperature > 5°C and first span after July 1st (Jan 1st in SH) of 6 days** with daily mean temperature < 5°C
Monthly maximum value of daily maximum temperature	**TX_x**	
Monthly maximum value of daily minimum temperature	TN_x	
Monthly minimum value of daily maximum temperature	TX_n	
Monthly minimum value of daily minimum temperature	**TN_n**	
Percentage of days when daily minimum temperature < 10th percentile	**TN10p**	**Percentage of days when the daily minimum temperature is less than the calendar day 10th percentile daily minimum temperature centered on a 5-day window for the base period 1961-1990 (recommend use of bootstrapping procedure from Zhang et al. 2005 to calculate base period percentiles)**
Percentage of days when daily maximum temperature < 10th percentile	TN10p	Percentage of days when the daily maximum temperature is less than the calendar day 10th percentile daily maximum temperature centered on a 5-day window for the base period 1961-1990 (recommend use of bootstrapping procedure from Zhang et al. 2005 to calculate base period percentiles)
Percentage of days when daily minimum temperature > 90th percentile	TN90p	Percentage of days when the daily minimum temperature is greater than the calendar day 90th percentile daily minimum temperature centered on a 5-day window for the base period 1961-1990 (recommend use of bootstrapping procedure from Zhang et al. 2005 to calculate base period percentiles)
Percentage of days when daily maximum temperature > 90th percentile	**TN90p**	**Percentage of days when the daily maximum temperature is greater than the calendar day 90th percentile daily maximum temperature centered on a 5-day window for the base period 1961-1990 (recommend use of bootstrapping procedure from Zhang et al. 2005 to calculate base period percentiles)**

*Warm spell duration index****	WSDI	Annual count of days with at least 6 consecutive days when the daily maximum temperature > 90th percentile
Cold spell duration index	CSDI	Annual count of days with at least 6 consecutive days when the daily minimum temperature < 10th percentile
Daily temperature range	**DTR**	**Monthly mean of the difference between the maximum and minimum temperature for each day**
**Intra-annual Extreme Temperature Range*	*ETR	Difference between the highest temperature observation of any given calendar year and the lowest temperature reading of the same calendar year
**One of the 10 key indices in Peterson et al. (2001) but not one of the ETCCDI/CLIMDEX indices*		
***Peterson et al. (2001) use periods of 5 days in their definition*		
**** Peterson et al. (2001) use a slightly different definition based on the maximum period (greater than 5 consecutive days) when the daily maximum temperature is more than 5˚C above the normal daily maximum temperature for the baseline period of 1961-1990*		

Appendix E: Results from Studies of Perceptions of Climate Change

Table E.1- Perceptions of changes in temperature. From Vergara Rodriguez, 2011 (Conchucos) and Vergara Rodriguez, 2015 (Aquia, Rio Negro, Waraq, and Yanamayo)

	Conchucos	Aquia	Rio Negro	Waraq	Yanamayo	**Total for all locations (%)**
Increase (% of responses)	91	84	96	89	95	**91.15**
Decrease (%of responses)	3	13	2	10	1	**5.31**
No change (% of responses)	6	3	2	1	3	**3.34**
No response (% of responses)	0	0	0	0	1	**0.20**

Table E.2- Perceptions of changes in quantity of precipitation. From Vergara Rodriguez, 2011 (Conchucos) and Vergara Rodriguez, 2015 (Aquia, Rio Negro, Waraq, and Yanamayo)

	Conchucos	Aquia	Rio Negro	Waraq	Yanamayo	**Total for all locations (%)**
Increase (% of responses)	2	11	10	11	34	**12.99**
Decrease (% of responses)	93	63	81	74	47	**73.05**
No change (% of responses)	5	21	8	15	16	**12.25**
Irregular compared to 20/30 years ago (% of responses)	0	5	1	0	2	**1.51**
No response (% of responses)	0	0	0	0	1	**0.20**

Table E.3- Perceptions of changes in precipitation intensity. From Vergara Rodriguez, 2011 (Conchucos) and Vergara Rodriguez, 2015 (Aquia, Rio Negro, Waraq, and Yanamayo)

	Conchucos	Aquia	Rio Negro	Waraq	Yanamayo	**Total for all locations (%)**
Increase (% of responses)	15	17	12	26	37	**20.94**
Decrease (% of responses)	74	54	65	34	24	**52.43**
No change (% of responses)	8	27	22	40	33	**24.03**
Varied compared to 20/30 years ago (% of responses)	3	2	1	0	4	**2.19**
No response (% of responses)	0	0	0	0	2	**0.41**

Table E.4- Perceptions of changes in drought frequency and intensity in Conchucos (from Vergara Rodriguez, 2011)

Increase (% responses)	81
Decrease (% responses)	7
No change (% responses)	11
Don't know (% responses)	1

Table E.5- Perceptions of changes in seasonality of the rainy season (from Vergara Rodriguez, 2015)

	Aquia	Rio Negro	Waraq	Yanamayo	**Total for all locations (%)**
Out of step compared to 30 years ago (% of responses)	42	57	42	62	**51.44**
Shorter rainy season (% of responses)	19	18	19	2	**13.99**
Longer rainy season (% of responses)	2	3	3	7	**3.86**
No change (% of responses)	23	15	36	21	**23.12**
Irregular compared to 30 years ago (% of responses)	4	7	0	6	**4.49**
Other (% of responses)	10	0	0	2	**3.10**

Table E.6- Perceptions of changes in seasonality of the dry season (from Vergara Rodriguez, 2015)

	Aquia	Rio Negro*	Waraq	Yanamayo	**Total for all locations (%)**
Out of step compared to 30 years ago (% responses)	30	12	15	20	**19.43**
Shorter dry season (% responses)	2	1	3	4	**2.51**
Longer dry season (% responses)	48	57	35	44	**46.46**
No change (% responses)	10	22	39	23	**22.81**
Irregular compared to 30 years ago (% responses)	3	8	8	7	**6.45**
Other/no response (% responses)	7	0	0	2	**2.33**

Table E.7- Drought, as defined by the local population (from Vergara Rodriguez, 2015)

	Aquia	Rio Negro	Waraq	Yanamayo
Shortage of water (% of responses)	39	32	29	25
Shortage of water for crops or irrigation (% of responses)	4	2	5	2
Shortage of water and dry grass (% of responses)	0	2	1	0
Shortage of rainfall (% of responses)	29	49	47	47
Shortage of water and rainfall (% of responses)	0	4	6	3
Shortage of rainfall in the summer (% of responses)	2	0	0	0
Decrease in water (% of responses)	6	1	0	0
Dry plants and grass (% of responses)	8	5	4	2
Production shortage/famine/bad years (% of responses)	4	1	0	0
Shortage of grass (% of responses)	4	1	0	0
Summer/dry season (% of responses)	3	0	0	4
Heat (% of responses)	1	0	0	3
Water in crisis (% of responses)	0	0	0	2
Dry (% of responses)	0	0	0	1
Don't know/no opinion (% of responses)	0	0	8	5
No response (% of responses)	0	3	0	6

Table E.8- Months that are part of the rainy season according to local surveys. Numbers indicate the percentage of participants who indicated that a given month is part of the rainy season (from Vergara, Rodriguez 2015).

	Sep.	Oct.	Nov.	Dec.	Jan.	Feb.	Mar.	Apr.	May
Aquia (% of responses)	26.14	50.00	73.86	90.91	92.05	94.32	95.45	69.32	31.82
Rio Negro (% of responses)	33.71	66.29	92.13	96.63	95.51	98.88	95.51	61.80	19.10
Waraq (% of responses)	41.10	80.82	94.52	95.89	95.89	95.89	93.15	75.34	24.66
Yanamayo	18.56	71.13	89.69	91.75	92.78	92.78	92.78	78.35	28.87

Table E.9- Months that are part of the dry season according to local surveys. Numbers indicate the percentage of participants who indicated that a given month is part of the dry season (from Vergara Rodriguez, 2015).

	Apr.	May	Jun.	Jul.	Aug.	Sep.	Oct.
Aquia (% of responses)	11.36	25.00	48.86	59.09	47.73	18.18	11.36
Rio Negro (% of responses)	11.24	51.69	92.13	96.63	92.13	51.69	21.35
Waraq (% of responses)	8.22	52.05	94.52	97.26	80.82	42.47	8.22
Yanamayo (% of responses)	10.31	55.67	92.78	94.85	91.75	72.16	20.62

References

Abadie, S., et al. (2010). Numerical simulation of waves generated by landslides using a multiple-fluid Navier–Stokes model. *Coastal Engineering, 57,* 779–94.

Aceituno, P. (1987). On the functioning of the southern oscillation in the South American sector. Part II. Upper-air circulation. *J. Climate*, *116*, 505–524. doi:10.1175/1520-0442(1989)002<0341:OTFOTS>2.0.CO;2

Alean, J., (1985). Ice Avalanches: Some Empirical Information About Their Formation and Reach. *Journal of Glaciology*, *31*(109), 324-333.

Alley, W. M. (1984). The Palmer Drought Severity Index: Limitations and assumptions. *J. Climate Appl. Meteor., 23*, 1100–1109.

ANA – Autoridad Nacional del Agua. (2013). Informe Tecnico Colegiado sobre las Acciones, Actividades, y Proyectos Que Deben Ejecutarse, Para Disminuir el Riesgo de Desastre por Desembalse de la Laguna Palcacocha (Huaraz – Ancash). *Autoridad Nacional del Agua, Instituto Geofísico del Peru, Instituto Geológico Minero y Metalúrgico, Instituto Nacional de Defensa Civil, Centro Nacional de Estimación Prevención y Reducción de Riesgos de Desastres*. Huaraz, Peru. Annan, A.P. (2001). Ground Penetrating Radar Workshop Notes. Sensors & Software Inc.

Annan, A.P., & Davis, J.L. (1976). Impulse radar sounding in permafrost. *Radio Science*, *11*, 383–394.

Ataie-Ashtiani, B., & Nik-Khah, A. (2008). Impulse Waves caused by Subaerial Landslides. *Environmental Fluid Mechanics, 8*, 263-280.

Ataie-Ashtiani, B., & and Yavari-Ramshe, S. (2011). Numerical simulation of wave generated by landslide incidents in dam reservoirs. *Landslides*. *8*(4), 417-432.

Awal, R., et al. (2008). An integrated approach to predict outflow hydrograph due to landslide dam failure by overtopping and sliding. *Annual Journal of Hydraulic Engineering, JSCE*. *52*, 151-156.

Awal, R., Nakagawa, H., Fujita, M. K., Baba, Y., & Zhang, H. (2010). Experimental study on Glacial Lake Outburst Floods due to waves overtopping and erosion of moraine dam. *Annuals of Disas*. *Prev*. *Res Inst*. Kyoto University, *53B*, 583-594.

Awal, R., et al. (2011). Study on moraine dam failure and resulting flood/debris flow hydrograph due to waves overtopping and erosion. *Proceedings of the international conference on debris-flow hazards mitigation: mechanics, prediction, and assessment,* Padua, Italy.

Baer, P., Huggel, C., Frey, H., Chisolm, R., McKinney, D., Mcardell, B., Portocarrero, C., & Cochachin, A. (2016). Modelling Cascading and Erosional Processes for

GLOFs in the Quillcay Catchment, Huaraz, Cordillera Blanca, Peru. [Poster # EGU2016-6536]. *Poster presented at the European Geosciences Union Meeting*. Vienna, Austria.

Bahr, D.B., Meier, M.F., & Peckham, S.D. (1997). The physical basis of glacier volume–area scaling. *J. Geophys. Res.*, *102*(B9), 355–362. http://dx.doi.org/10.1029/97JB01696.

Bajracharya, B., Shrestha, A. B., & Rajbhandari, L. (2007a). Glacial Lake Outburst Floods in the Sagarmatha Hazard assessment using GIS and Hydrodynamic Modeling. *Mountain Research and Development*, *27*, 336–344.

Bajracharya, S. R., Mool, P. K., & Shrestha, B. R. (2007b) Impact of Climate Change on Himalayan Glaciers and Glacial Lakes Case Studies on GLOF and Associated Hazards in Nepal and Bhutan. International Centre for Integrated Mountain Development (ICIMOD), Kathmandu.

Baraer, M., et al. (2012). Glacier Recession and Water Resources in Peru's Cordillera Blanca. *Journal of Glaciology*, *58*(7), 134-150.

Barnett, T.P., Adam, J.C., & Lettenmaier, D.P. (2005). Potential impacts of a warming climate on water availability in snow dominated regions. *Nature*, *438*(7066), 303–309.

Barrett, B. E., Murray, T., & Clark, R. (2007). Errors in radar CMP velocity estimates due to survey geometry, and their implication for ice water content estimation. *Journal of Environmental and Engineering Geophysics*, *12*(1), 101-111.

Bartelt, P., Salm, B., & Gruber, U. (1999). Calculating dense-snow avalanche runout using a Voellmy-fluid model with active/passive longitudinal straining. *Journal of Glaciology*, *45*(150), 242-254.

Bartelt, P., Bühler, Y., Buser, O., Christen, M. & Meier, L. (2012). Modeling mass-dependent flow regime transitions to predict the stopping and depositional behavior of snow avalanches. *Journal of Geophysical Research*, *117*(F01015).

Bartelt, P., Buehler, Y., Christen, M., Deubelbeiss, Y., Salz, M., Schneider, M., & Schumacher, L. (2013) RAMMS: Rapid Mass Movement Simulation: A numerical model for snow avalanches in research and practice. User Manual v1.5 – Avalanche. Swiss Federal Institute for Forest, Snow and Landscape Research WSL. Birmensdorf.

Basu, D., Das, K., Green, S., & Janetzke, R. (2010). Numerical Simulation of Surface Waves Generated by a Subaerial Landslide at Lituya Bay Alaska. *Journal of Offshore Mechanics and Artic Engineering, 132*, 1-11.

Behrens, J. (2010). Numerical methods in support of advanced tsunami early warning. In *Handbook of geomathematics* (eds W Freeden, MZ Nashed, T Sonar). Berlin, Germany: Springer.

Behrens J. & Dias, F. (2015). New computational methods in tsunami science. *Phil. Trans. R. Soc. A, 373*(20140382). DOI:10.1098/rsta.2014.0382

Benn, D.I., Owen, L.A., Osmaston, H.A., et al. (2005). Reconstruction of equilibrium-line altitudes for tropical and sub-tropical glaciers. *Quaternary International, 138*, 8-21.

Benn, D. I. & Evans, D. J. A. (Eds.). (2010). *Glaciers and Glaciation*, 2nd ed., London: Hodder Education.

Binder, D., Brueckl, E., Roch, K. H., et al. (2009). Determination of total ice volume and ice-thickness distribution of two glaciers in the Hohe Tauern region, Eastern Alps, from GPR data. *Annals of Glaciology*. *50*(51), 71-79.

Bindoff, N.L., Stott, P.A., AchutaRao, K.M., Allen, M.R., Gillett, N., Gutzler, D., Hansingo, K., Hegerl, G., Hu, Y., Jain, S., Mokhov, I.I., Overland, J., Perlwitz, J., Sebbari, R., & Zhang, X. (2013). Detection and Attribution of Climate Change: from Global to Regional. In: Climate Change 2013: *The Physical Science Basis. Contribution of Working Group I to the Fifth Assessment Report of the Intergovernmental Panel on Climate Change* [Stocker, T.F., Qin, D., Plattner, G.-K., Tignor, M., Allen, S.K., Boschung, J., Nauels, A., Xia, Y., Bex, V., & Midgley, P.M. (Eds.)]. Cambridge University Press, Cambridge, United Kingdom and New York, NY, USA.

Bingham, R. G. & Siegert, M. J. (2007). Radio-Echo Sounding Over Polar Ice Masses. *Journal of Environmental Engineering & Geophysics*, *12*, 47-62.

Birkeland, K. W. & Landry, C. C. (2002). Power-laws and snow avalanches, *Geophys. Res. Lett*. 29(11), 49-1–49-3. DOI: 10.1029/2001GL014623

Biscarini, C. (2010). Computational Fluid Dynamics Modelling of Landslide Generated Water Waves. *Landslides, 7*, 117-124.

Blumenstock, G., Jr. (1942). Drought in the U.S. analyzed by means of the theory of probability. *USDA Tech. Bull. 819*, GPO, Washington, D.C.

Bogorodsky, V.V, Bentley, C.R., & Gudmandsen, P.E. (1985). *Radioglaciology*. Dordrecht, Holland: Reidel Pub. Co. 254 pp.

Bolch, T., Buchroithner, M. F., Peters, J., et al. (2008). Identification of glacier motion and potentially dangerous glacial lakes in the Mt. Everest region/Nepal using spaceborne imagery. *Natural Hazards and Earth System Sciences*, *8*(6), 1329-1340.

Booth, A.D., Clark, R., & Murray, T. (2010). Semblance response to a ground-penetrating radar wavelet and resulting errors in velocity analysis. *Near Surface Geophysics, 8*(3), 235–246.

Booth, A.D., Clark, R., & Murray, T. (2011). Influences on the resolution of GPR velocity analyses and a Monte Carlo simulation for establishing velocity precision. *Near Surface Geophysics, 9*(5), 399–411.

Bradley, R.S., Keimig, F.T., & Diaz, H.F., (2004). Projected temperature changes along the American cordillera and the planned GCOS network. *Geophysical Research Letters*, *31*(L16210).

Bradley, R.S., Vuille, M., Diaz, H.F., & Vergara, W. (2006). Threats to water supply in the tropical Andes. *Science, 312*(5781), 1755–1756.

Bühler, Y., Christen, M., Kowalski, J., & Bartelt, P. (2011). Sensitivity of snow avalanche simulations to digital elevation model quality and resolution. *Annals of Glaciology*. *52*(58), 72-80.

Burroughs, S. M., & Tebbens, S. F. (2005). Power law scaling and probabilistic forecasting of tsunami runup heights. *Pure Appl. Geophys.*, *162*, 331–342.

Bury, J., Mark, B., McKenzie, J., French, A., Baraer, M., Huh, K., Luyo, M., & Gómez, J. (2011). Glacier recession and human vulnerability in the Yanamarey watershed of the Cordillera Blanca, Peru. *Climatic Change*. *105*, 179-206.

Byers, A.C., Cuellar, A.D., & McKinney, D.C. (2015). HiMAP Local Adaptation Plans of Action: Case Studies and Lessons Learned in Nepal and Peru. High Mountains Adaptation Partnership Technical Report, U.S. Agency for International Development, Washington, DC.

Camfield, F. E. & Street, R. L. (1969). Shoaling of solitary waves on small slopes. *Proc. ASCE*, *WW95*, 1-22.

Capel, A. (2015). Wave run-up and overtopping reduction by block revetments with enhanced roughness. Coastal Engineering, 104, 76-92. DOI:10.1016/j.coastaleng.2015.06.007

Capone, T., Panizzo, A., Monaghan, J. J. (2010). SPH modelling of water waves generated by submarine landslides. *Journal of Hydraulic Research*, *48*(SI), 80-84.

Carey, M. (2005). Living and Dying With Glaciers: People's Historical Vulnerability to Avalanches and Outburst Floods in Peru. *Global and Planetary Change, 47*(2-4), 122-134.

Carey, M. (2008). The Politics of Place: Inhabiting and Defending Glacier Hazard Zones in Peru's Cordillera Blanca. In Orlove, B., Wiegandt, E., & Luckman, B. (Eds.). *Darkening Peaks: Glacier Retreat, Science, and Society*, Berkeley: University of California Press, 229-240.

Carey, M. (2010). *In the Shadow of Melting Glaciers: Climate Change and Andean Society*. New York: Oxford Univ. Press.

Carey, M., Huggel, C., Bury, J., Portocarrero, C., & Haeberli, W. (2012). An integrated socio-environmental framework for glacier hazard management and climate change adaptation: Lessons from Lake 513, Cordillera Blanca, Peru. *Climatic Change*, *112*, 733–767.

Carrier, G. F., Wu, T. T., & Yeh, H. (2003). Tsunami run-up and draw-down on a plane beach. *Journal of Fluid Mechanics, 475*, 79-99.

Casteller, A., Christen, M., Villalba, R., et al. (2008). Validating numerical simulations of snow avalanches using dendrochronology: the Cerro Ventana event in Northern Patagonia, Argentina. *Nat. Hazards Earth Syst. Sci.*, *8*, 433–443.

Catania, G., Hulbe, C., & Conway, H. (2010). Grounding-line basal melt rates determined using radar-derived internal stratigraphy. *Journal of Glaciology*, *56*(197).

Cenderelli, D. A. & Wohl, E. E. (2003). Flow hydraulics and geomorphic effects of glacial-lake outburst floods in the Mount Everest region, Nepal. *Earth Surface Processes and Landforms*, *28*, 385-407.

Changnon, S. A. (1980). Removing the confusion over droughts and floods: The interface between scientists and policy makers. *Water Int., 5*, 10-18.

Chang, C. & Wang, K. (2011). Generation of Three-Dimensional Fully Nonlinear Water Waves by a Submerged Moving Object. *Journal of Engineering Mechanics, 137*, 101-112.

Charvet, I., Eames, I., & Rossetto, T. (2013). New tsunami runup relationships based on long wave experiments. *Ocean Modelling, 69*, 79-92.

Chen, J., & Ohmura, A., (1990). Estimation of Alpine Glacier Water Resources and Their Change Since the 1870s. *Hydrology in Mountainous Regions*, IAHS-AISH Publ, *I 193*, 127–135.

Chevallier, T., Pouyaud, B., Suarez, W., et al. (2011). Climate change threats to environment in the tropical Andes: glaciers and water resources. *Regional Environmental Change*, *11*(Supplement: 1), S179-S187.

Christen, M., Bartelt, P., & Gruber, U. (2002). AVAL-1D: An Avalanche Dynamics Program for the Practice. International Congress INTERPRAEVENT 2002, In *The Pacific Rim – MATSUMOTO / JAPAN Congress publication*, *2*, 715-725.

Christen, M., Bartelt, P., & Gruber, U. (2005). Numerical calculation of snow avalanche runout distances. In: Soibelman, L., & Pena-Mora, F. (Eds.). *Computing in Civil Engineering*. Cancun, Mexico: Proc. of the 2005 International Conference, July 12-15, 2005.

Christen, M., Bartelt, P., Kowalski, J., & Stoffel, L. (2008). Calculation of dense snow avalanches in three-dimensional terrain with the numerical simulation programm

RAMMS. In: International Snow Science Workshop 2008, Proceedings. September 21-27. Whistler, BC, CAN, 709-716.

Christen, M., Kowalski, J., & Bartelt, P. (2010). RAMMS: numerical simulation of dense snow avalanches in three-dimensional terrain. *Cold Regions Science and Technology*, *63*, 1–14.

Christen, M., Bühler, Y., & Bartelt, P. (2012). Integral Hazard Management Using a Unified Software Environment: Numerical Simulation Tool "RAMMS" for Gravitational Natural Hazards. *12th Congress INTERPRAEVENT 2012 – Grenoble / France Conference Proceedings*, Grenoble.

Christensen, J.H., Kumar, K. K., Aldrian, E., An, S.-I., Cavalcanti, I.F.A., de Castro, M., Dong, W., Goswami, P., Hall, A., Kanyanga, J.K., Kitoh, A., Kossin, J., Lau, N.-C., Renwick, J., Stephenson, D.B., Xie, S.-P. and Zhou, T. (2013). Climate Phenomena and their Relevance for Future Regional Climate Change. In: *Climate Change 2013: The Physical Science Basis. Contribution of Working Group I to the Fifth Assessment Report of the Intergovernmental Panel on Climate Change* [Stocker, T.F., Qin, D., Plattner, G.-K., Tignor, M., Allen, S.K., Boschung, J., Nauels, A., Xia, Y., Bex, V., & Midgley, P.M. (Eds.)]. Cambridge University Press, Cambridge, United Kingdom and New York, NY, USA.

Clague, J. J., & Evans, S. G. (2000). A Review of Catastrophic Drainage of Moraine-Dammed Lakes in British Columbia. *Quaternary Science Reviews*, *19*, 1763–1783.

Climate Prediction Center. (2015, November). *Historical El Nino and La Nina Episodes (1950-Present): Cold and Warm Episodes by Season*. Retrieved from NOAA/National Weather Service website http://www.cpc.ncep.noaa.gov/products/analysis_monitoring/ensostuff/ensoyears.shtml

Cogley, J.G., Hock, R., Rasmussen, L.A., Arendt, A.A., Bauder, A., Braithwaite, R.J., Jansson, P., Kaser, G., Möller, M., Nicholson, L., & Zemp, M. (2011). Glossary of Glacier Mass Balance and Related Terms. *IHP-VII Technical Documents in Hydrology No. 86*, IACS Contribution No. 2. Paris: UNESCO-IHP.

Collins, M., et al. (2010). The impact of global warming on the tropical Pacific ocean and El Nino. *Nature Geosci., 3*, 391–397.

Collins, M., Knutti, R., Arblaster, J., Dufresne, J.-L., Fichefet, T., Friedlingstein, P., Gao, X., Gutowski, W.J., Johns, T., Krinner, G., Shongwe, M., Tebaldi, C., Weaver, A.J., & Wehner, M. (2013). Long-term Climate Change: Projections, Commitments and Irreversibility. In: *Climate Change 2013: The Physical Science Basis. Contribution of Working Group I to the Fifth Assessment Report of the Intergovernmental Panel on Climate Change* [Stocker, T.F., Qin, D., Plattner, G.-K., Tignor, M., Allen, S.K., Boschung, J., Nauels, A., Xia, Y., Bex, V., &

Midgley, P.M. (Eds.)]. Cambridge University Press, Cambridge, United Kingdom and New York, NY, USA.

Cook, S. J. & Quincey, D. J. (2015). Estimating the volume of Alpine glacial lakes. *Earth Surf. Dynam. Discuss.*, *3*, 909–940.

Condom, T., Coudrain, A., Sicart, J. E., et al. (2007). Computation of the space and time evolution of equilibrium-line altitudes on Andean glaciers (10 degrees N-55 degrees S). *Global and Planetary Change*, *59*(1-4), 189-202.

Condom, T., Escobar, M., Purkey, D., et al. (2011a). Modelling the hydrologic role of glaciers within a Water Evaluation and Planning System (WEAP): a case study in the Rio Santa watershed (Peru). *Hydrol. Earth Syst. Sci. Discuss.*, *8*, 869–916.

Condom, T., Rau, P., & Espinoza, J. C. (2011b). Correction of TRMM 3B43 monthly precipitation data over the mountainous areas of Peru during the period 1998–2007. *Hydrol. Process.*, *25*, 1924– 1933. doi:10.1002/hyp.7949

Costa, J. E., & Schuster, R. L. (1988). The formation and failure of natural dams. *Geological Society of America Bulletin*, *100*, 1054-1068.

Coudrain, A., Francou, B., & Kundzewicz, Z. W. (2005). Glacier shrinkage in the Andes and consequences for water resources. *Hydrological Sciences Journal-Journal des Sciences Hydrologiques, 50*(6), 925-932.

Cremonesi, M., Frangi, A., & Perego, U. (2011). A Lagrangian finite element approach for the simulation of water-waves induced by landslides. *Comput. Struct.*, *89* 1086–93 .

Daniels, D.J. (Ed.). (2007). *Ground Penetrating Radar* (2nd ed.). London: The Institution of Engineering and Technology.

Davis, J.L., & Annan, A.P. (1989). Ground-penetrating radar for high-resolution mapping of soil and rock stratigraphy. *Geophysical Prospecting*, *37*(5), 531–551.

Dean, R. G., & Dalrymple, R. A. (1991). *Water wave mechanics for engineers and scientists*. Singapore: World Scientific.

de Carvalho, R. F., & Antunes do Carmo, J. S. (2007). Landslides into reservoirs and their impacts on banks. *Environmental Fluid Mechanics*, *7*(6), 481-493.

Delft3D. (2014). *Delft3D- Functional Specifications, Version: 2.20.33337*. Delft, Netherlands: Deltares.

Diario La Republica. (2010, April). Declaran en emergencia la laguna Palcacocha en Huaraz. *La republica*. Retrieved from www.larepublica.pe/regionales/20/04/2010/declaran-en-emergencia-la-laguna-palcacocha-en-huaraz

DiNezio, P. N., Clement, A. C., Vecchi, G. A., Soden, B. J., & Kirtman, B. P. (2009). Climate response of the equatorial Pacific to global warming. *J. Clim., 22*, 4873–4892.

Di Risio, M., Bellotti, G., Panizzo, A., et al. (2009). Three-dimensional experiments on landslide generated waves at a sloping coast. *Coastal Engineering*, *56*(5-6), 659-671.

Dix, C. H. (1955). Seismic velocities from surface measurements. *Geophysics, 20*(1), 68-86.

Doesken, N.J., McKee, T.B., & Kleist, J. (1991). Development of a surface water supply index for the western United States. *Climatology Report Number 91–3*, Fort Collins, CO: Colorado State University.

Durbin, P.A. & Pettersson Reif, B.A. (2001). *Statistical Theory and Modeling for Turbulent Flows*. Chichester, England: John Wiley & Sons.

Dutykh, D., Poncet, R., & Dias, F. (2011). The VOLNA code for the numerical modeling of tsunami waves: generation, propagation and inundation. *Eur. J. Mech. B/Fluids, 30*, 598–615. DOI:10.1016/j.euromechflu.2011.05.005

Dracup, J. A., Lee, K. S., & Paulson, E. G. (1980). On the statistical characteristics of drought events. *Water Resour. Res., 16*, 289–296.

Eisen, O., Nixdorf, U ., Wilhelms, F., et al. (2002). Electromagnetic wave speed in polar ice: validation of the common-midpoint technique with high-resolution dielectric-profiling and gamma-density measurements. *Annals of Glaciology*, *34*, 150-156.

Emmer, A., & Cochachin, A. (2013). Causes and mechanisms of moraine- dammed lake failures in Cordillera Blanca (Peru), North American Cordillera and Central Asia, *AUC Geographica*, *48*(2), 5-15.

Emmer, A., & Vilimek, V. (2013). Review Article: Lake and breach hazard assessment for moraine-dammed lakes: an example from the Cordillera Blanca (Peru). *Natural Hazards and Earth System Sciences*, *13*(6), 1551-1565.

Emmer, A., & Vilímek, V. (2014). New method for assessing the susceptibility of glacial lakes to outburst floods in the Cordillera Blanca, Peru. *Hydrol. Earth Syst. Sci.*, *18*, 3461–3479.

Emmer, A., Vilímek, V., & Zapata, M. L. (2016). Hazard mitigation of glacial lake outburst floods in the Cordillera Blanca (Peru): the effectiveness of remedial works. *Journal of Flood Risk Management*, 13 pp. DOI: 10.1111/jfr3.12241

Espinoza, E. S. (2013). Identificación de los Riesgos Relacionados con la Laguna Palcacocha. *Institución en Clima para la Accion (INCLIMA*). Lima, Peru.

Espinoza, J. C., Chavez, S. P., Ronchail, J., Junquas, C., Takahashi, K., & Lavado, W. (2015). Rainfall hotspots over the southern tropical Andes: spatial distribution,

rainfall intensity and relations with large-scale atmospheric circulation. *Water Resour. Res.*, *51*, 3459–3475. doi:10.1002/2014WR016273

Espinoza Villar, J. C., Ronchail, J., Guyot, J. L., Cochonneau, G., Naziano, F., Lavado, W., De Oliveira, E., Pombosa, R., & Vauchel, P. (2009). Spatio-temporal rainfall variability in the Amazon basin countries (Brazil, Peru, Bolivia, Colombia, and Ecuador). *Int. J. Climatol.*, *29*, 1574–1594. doi:10.1002/joc.1791

ESRI – Environmental Systems Research Institute. (2014). ArcGIS Desktop Help 10.2.2: How Topo to Raster works.

ETCCDI – Expert Team on Climate Change Detection and Indices. (2009). *Climate Change Indices: Definitions of the 27 Core Indices*. Retrieved from ETCCDI/CRD Climate Change Indices, Climate Research Division, Environment Canada http://etccdi.pacificclimate.org/list_27_indices.shtml

Etemad-Shahidi, A., Shaeri, S., & Jafari, E. (2016). Prediction of wave overtopping at vertical structures. Coastal Engineering, 109, 45-52. DOI:10.1016/j.coastaleng.2015.12.001

Evans, S. G., & Clague, J. J. (1994). Recent climatic change and catastrophic geomorphic processes in mountain environments. *Geomorphology*, *10*, 107–128.

Evans, S. G., & Clague, J. J. (1988). Catastrophic rock avalanches in glacial environments. *Proc. Fifth Int. Symp. on Landslides*, *2*, 1153-1158.

Evans, S. G., Bishop, N. F., Smoll, L. F., Valderrama-Murillo, P., Delaney, K. B., & Oliver-Smith, A. (2009). A re-examination of the mechanism and human impact of catastrophic mass flows originating on Nevado Huascarán, Cordillera Blanca, Peru in 1962 and 1970. *Engineering Geology*, *108*, 96–118.

Fah, R. (2005). Numerik an der VAW: Entwicklungen und Beispiel des Triftgletschers, In: Festkolloquium VAW 75 JAHRE, edited by: Minor, H.-E., Versuchsanstalt für Wasserbau, Hydrologie und Glaziologie ETH-Zentrum CH-8092 Zürich, 187–200.

Farinotti, D., Huss, M., Bauder, A., Funk, M., & Truffer, M. (2009). A method to estimate the ice volume and ice-thickness distribution of alpine glaciers. Journal of Glaciology, 55(191), 422–430.

Favier, V., Wagnon, P., Chazarin, J.P., et al. (2004). One-year measurements of surface heat budget on the ablation zone of Antizana Glacier 15, Ecuadorian Andes. *Journal of Geophysical Research- Atmospheres*, *109*(D18).

Favier, V., Wagnon, P. & Ribstein, P. (2004). Glaciers of the outer and inner tropics: a different behavior but a common response to climatic forcing. *Geophysical Research Letters*, *31*(L16403).

FEMA – Federal Emergency Management Agency. (2003). *Guidelines and specifications for flood hazards mapping partners, Appendix G: Guidance for alluvial fans*

flooding analyses and mapping. Washington, DC. Retrieved from http://www.fema.gov/mit/ft_alfan.htm

Fernandez, B., & Salas, J. D. (1999a). Return period and risk of hydrologic events. I: Mathematical formulation. *ASCE J. Hydrol. Eng., 4*, 297–307.

Fernandez, B., & Salas, J. D. (1999b). Return period and risk of hydrologic events. II: Applications. *ASCI J. Hydrol Eng., 4*, 308–316.

Fiebiger, G. (1997). Hazard Mapping in Austria. *Journal of Torrent, Avalanche, Landslide and Rockfall Engineering,* 134(61).

Fischer, A. (2009). Calculation of glacier volume from sparse ice-thickness data, applied to Schaufelferner, Austria, *J. Glaciol.*, *55*, 453–460.

Fischer, L., Purves, R. S., Huggel, C., Noetzli, J., & Haeberli, W. (2012). On the influence of topographic, geological and cryospheric factors on rock avalanches and rockfalls in high-mountain areas. *Nat. Hazards Earth Syst. Sci.*, *12*, 241–254.

Fischer, A., & Kuhn, M. (2013). Ground-penetrating radar measurements of 64 Austrian glaciers between 1995 and 2010. *Annals of Glaciology*, *54*(64), 179-188.

Flato, G., Marotzke, J., Abiodun, B., Braconnot, P., Chou, S.C., Collins, W., Cox, P., Driouech, F., Emori, S., Eyring, V., Forest, C., Gleckler, P., Guilyardi, E., Jakob, C., Kattsov, V., Reason, C., & Rummukainen, M. (2013). Evaluation of Climate Models. In *Climate Change 2013: The Physical Science Basis. Contribution of Working Group I to the Fifth Assess- ment Report of the Intergovernmental Panel on Climate Change* [Stocker, T.F., Qin, D., Plattner, G.-K., Tignor, M., Allen, S.K., Boschung, J., Nauels, A., Xia, Y., Bex, V., & Midgley, P.M. (Eds.)]. Cambridge University Press, Cambridge, United Kingdom and New York, NY, USA.

Flow Science. (2012). *FLOW-3D Documentation: Release 10.1.0*, Flow Science, Inc.

Flow Science. (2013). Selecting Convergence Criteria. *CFD 101: The basics of computational fluid dynamics modeling*. Retrieved from http://www.flow3d.com/cfd-101/cfd-101- convergence-criteria.html

Francou, B., Vuille, M., Wagnon, P., Mendoza, J., & Sicart, J.E. (2003). Tropical climate change recorded by a glacier in the central Andes during the last decades of the 20th century: Chacaltaya, Bolivia, 16°S. *Journal of Geophysical Research, 108*(D5), 4154-4165.

Francou, B., Vuille, M., Favier, V., & Cáceres, B. (2004). New evidence for an ENSO impact on low latitude glaciers: Antizana 15, Andes of Ecuador, 0°28'S. *Journal of Geophysical Research*, *109*(D18106), 18 pp.

Fraser, B. (2012). Goodbye Glaciers. *Nature*, *491*(7423), 180-182.

Fread, D. L. (1988). *DAMBRK: The NWS DAMBRK Model: Theoretical Background/User Documentation*. Silver Spring, MD: Hydrologic Research Laboratory, National Weather Service, Office of Hydrology.

Frey, H., Haeberli, W., Linsbauer, A., Huggel, C., & Paul, F. (2010). A multi-level strategy for anticipating future glacier lake formation and associated hazard potentials. *Nat. Hazards Earth Syst. Sci.*, *10*, 339–352.

Frich, P., Alexander, L. V., Della-Marta, P., Gleason, B., Haylock, M., Klein Tank, A., & Peterson, T. (2002). Observed coherent changes in climatic extremes during the second half of the twentieth century. *Climate Research, 19*, 193-212.

Friedt, J.-M., Tolle F., Bernard, E., Griselin, M., Laffly, D., & Marlin, C. (2012). Assessing the relevance of digital elevation models to evaluate glacier mass balance: Application to Austre Lovénbreen (Spitsbergen, 79o N). *Polar Record, 48*(244), 2–10.

Fritz, H. M., Hager, W. H., & Minor, H. (2001). Lituya Base Case: Rockslide Impact and Wave Run-up. *Science of Tsunami Hazards, 19*(1), 3-22.

Fritz, H. M. (2002). Initial Phase of Landslide Generated Impulse Waves (PhD Dissertation). Swiss Federal Institute of Technology, Zurich.

Fritz, H. M., Hager, W. H., & Minor, H. (2003). Landslide Generated Impulse Waves. 1. Instantaneous Flow Fields. *Experiments in Fluids, 35*, 505-519.

Fritz, H. M., Hager, W. H., & Minor, H. E. (2004). Near Field Characteristics of Landslide Generated Impulse Waves. *Journal of Waterway, Port, Coastal, and Ocean Engineering, 130*, 287-302.

Fuchs, H., Heller, V., & Hager, W. H. (2010). Impulse wave run-over: experimental benchmark study for numerical modeling. *Experiments in Fluids*, *49*(5), 985-1004.

Fuchs, H., & Hager, W. H. (2012). Scale Effects of Impulse Wave Run-Up and Run-Over. *Journal of Waterway Port Coastal and Ocean Engineering-ASCE*, *138*(4), 303-311.

Gades, A., Conway, H., Nereson, N. (2000). Radio echo-sounding through supraglacial debris on Lirung and Khumbu Glaciers, Nepal Himalayas. *Debris-Covered Glaciers Workshop Proceedings*, *IAHS Publ. no. 264*. Seattle, Washington, USA,

Gaertner-Roer, I., Naegeli, K., Huss, M., et al. (2014). A database of worldwide glacier thickness observations. *Global and Planetary Change*, *122*, 330-344.

Garcia, R., López, J. L., Noya, M., et al. (2003). Hazard mapping for debris flow events in the alluvial fans of northern Venezuela. *Third International Conference on Debris-Flow Hazards Mitigation: Mechanics, Prediction and Assessment*. Davos, Switzerland.

García, R., López, J. L., Noya, M. E., Bello, M. E., González, N., Paredes, G., & Vivas, M. I. (2002). Hazard maps for mud and debris flow events in Vargas State and Caracas. *Avila Project Report*. Caracas, Venezuela (In Spanish).

García-Martinez, R., & Lopez, J. L. (2005). Debris flows of December 1999 in Venezuela, Chapter 20. In Jakob, M., & Hungr, O. (Eds). *Debris-flow Hazards and Related Phenomena*. Praxis, Springer, Berline and Heidelberg, pp. 519-538.

Garmin. (2007). *eTrex HC Series Owner's Manual*. Olathe, Kansas: Garmin, Ltd.

Garreaud, R. D. (2009). The Andes climate and weather. *Adv. Geosci.*, *22*, 3–11, doi:10.5194/adgeo-22-3-2009

Geist, E. L., & Parsons, T. (2006). Probabilistic Analysis of Tsunami Hazards. *Natural Hazards, 37*(3), 277-314.

George, D. L. & LeVeque, R. L. (2006). Finite volume methods and adaptive refinement for global tsunami propagation and local inundation. *Sci. Tsunami Hazards, 24*, 319–328.

Georges, C. (2004). 20th-century glacier fluctuations in the tropical Cordillera Blanca, Peru. *Arctic Antarctic and Alpine Research*, *36*(1), 100-107.

Ghimire, M. (2005). Review of Studies on Glacier Lake Outburst Floods and Associated Vulnerability in the Himalayas. *The Himalayan Review*, (35–36)49–64.

Ghozlani, B., Hafsia, Z., & Maalel, K. (2013). Numerical study of surface water waves generated by mass movement. *Fluid Dynamics Research*, *45*(5), Article Number: 055506.

Gibbs, W.J., & Maher, J. V. (1967). Rainfall deciles as drought indicators. *Bureau of Meteorology Bulletin No. 48*, Melbourne: Commonwealth of Australia.

Giese, B., & Ray, S. (2011). El Niño variability in simple ocean data assimilation (SODA), 1871–2008. *J. Geophys. Res. Oceans, 116*, DOI: 10.1029/2010JC006695.

Glantz, M. H., & Katz, R. (1977). When is a drought a drought? *Nature*, *267*, 192-193.

Google (2013). Google Earth (Version 7.1.2.2041) [Software]. CNES/Astrium 2016. Available from http://www.earth.google.com

Gopalakrishnan, T. C., & Tung, C. C. (1981). Run-up of non-breaking waves—A finite-element approach. *Coastal Engineering, 4*, 3-22.

Goto, C. & Shuto, N. (1978). Numerical simulation of tsunami run-up, *Coastal Engrg. Japan, 21*, 13-20.

Goto, C. (1979). Nonlinear equation of long waves in the Langrangian description, *CoastalEngrg. Japan,* 22, 1-9.

Goto, C. (1974), Nonlinear waves in a channel of variable section, *Coastal Engrg. Japan* 17, 1-12.

Greenshields, C. J. (2015). *Open Foam - The Open Source CFD Toolbox, User Guide*. Reading, UK: Open Foam Foundation.

Grilli, S. T., Svendsen, I. A., & Subramanya, R. (1997). Breaking criterion and characteristics for solitary waves on slopes. *Journal of waterway, port, coastal, and ocean engineering, 123*(3), 102-112.

Groot, A., Hollaender, K., & Swart, R. (2014). *Productive Science-practice Interactions in Climate Change Adaptation. Lessons from practice*. A CIRCLE-2 research policy brief. Lisbon, Portugal: Foundation of the Faculty of Sciences.

Grove, J. M. (1979). The glacial history of the Holocene. *Progress in Physical Geography*, *3*, 1-54.

Gurgiser, W., Moelg, T., Nicholson, L., et al. (2013). Mass-balance model parameter transferability on a tropical glacier. *Journal of Glaciology*, *59*(217), 845-858.

Guttman, N. B. (1993). The use of L-moments in the determination of regional precipitation climates. *J. Climate, 6*, 2309-2325.

Guttman, N. B. (1998). Comparing the palmer drought index and the standardized precipitation index. *Journal of the American Water Resources Association*, *34*(1), 113-121.

Guttman, N. B. (1999). Accepting the standardized precipitation index: A calculation algorithm1. *Journal of the American Water Resources Association*, *35*(2), 311-322.

Haeberli, W., & Fisch, W. (1984). Electrical resistivity soundings of glacier beds: a test study on Grubengletscher, Wallis, *Swiss Alps*. *J. Glaciol*., *30*(106), 373–376.

Haeberli, W., Alean, J.-C., Müeller, P., & Funk, M. (1989). Assessing Risks from Glacier Hazards in High Mountain Regions: Some Experiences in the Swiss Alps. *Annals of Glaciology*, *13*, 96–102

Haeberli, W. (2013) Mountain permafrost — research frontiers and a special long-term challenge. *Cold Regions Science and Technology*, *96*, 71–76

Haeberli, W. & Hohmann, R. (2008). Climate, Glaciers and Permafrost in the Swiss Alps 2050: Scenarios, Consequences and Recommendations. *Proceedings of the 9th International Conference on Permafrost 2008*, Fairbanks, Alaska, USA.

Haeberli, W. & Linsbauer, A. (2013). Brief communication 'Global glacier volumes and sea level - small but systematic effects of ice below the surface of the ocean and of new local lakes on land'. Cryosphere, 7(3), 817-821.

Haeberli, W., Noetzli, J., Arenson, L., Delaloye, R., Gärtner-Roer, I., Gruber, S., Isaksen, K., Kneisel, C., Krautblatter, M., & Phillips, M. (2010). Mountain permafrost:

development and challenges of a young research field. *Journal of Glaciology*, *56* (200), 1043–1058 (special issue).

Hafeez, H. (2008). Inundation of Tsunami Waves and its Relation to the Tsunami Runup. *Pakistan Journal of Meteorology,* 5.9.

Hall, J. & Watt, S. J. (1953) Laboratory investigation of the vertical rise of solitary waves on impermeable slopes. *Tech. Memo., 33*, Beach Erosion Board, US Army Corps of Engineers. 14PP.

Hartmann, D. L. (1994). *Global Physical Climatology*. San Diego: Academic Press.

Hartmann, D. L., Klein Tank, A.M.G., Rusticucci, M., Alexander, L.V., Brönnimann, S., Charabi, Y., Dentener, F.J., Dlugokencky, E.J., Easterling, D.R., Kaplan, A., Soden, B.J., Thorne, P.W., Wild, M., & Zhai, P.M. (2013). Observations: Atmosphere and Surface. In: *Climate Change 2013: The Physical Science Basis. Contribution of Working Group I to the Fifth Assessment Report of the Intergovernmental Panel on Climate Change* [Stocker, T.F., Qin, D., Plattner, G.-K., Tignor, M., Allen, S.K., Boschung, J., Nauels, A., Xia, Y., Bex, V., & Midgley, P.M. (Eds.)]. Cambridge University Press, Cambridge, United Kingdom and New York, NY, USA.

Hayes, M. J. (2016). Comparison of Major Drought Indices: Introduction. *National Drought Mitigation Center.* Retrieved from http://drought.unl.edu/planning/monitoring/comparisonofindicesintro.aspx

Hegglin, E., & Huggel, C. (2008). An Integrated Assessment of Vulnerability to Glacial Hazards : A Case Study in the Cordillera Blanca, Peru. *Mountain Research and Development*, *28*(3/4), 299–309.

Heim, R. R. (2002). A review of Twentieth-Century drought indices used in the United States. *Bulletin of the American Meteorological Society*, *83*, 1149-1165.

Heinrich, P. (1992). Nonlinear Water Waves Generated by Submarine and Aerial Landslides. *Journal of Waterway, Port, Coastal, and Ocean Engineering, 118*, 249-266.

Heitner, K. L. (1969). A Mathematical Model for the Calculation of the Run-up of Tsunamis (PhD Thesis). California Institute of Technology. Earthquake Engineering Research Laboratory.

Heller, V., Hager, W. H., & Minor, H.-E. (2008). Scale effects in subaerial landslide generated impulse waves. *Experiments in Fluids*, *44*(5), 691-703.

Heller, V., Hager, W. H., & Minor, H.-E. (2009). Landslide generated impulse waves in reservoirs—Basics and computation. *VAW-Mitteilung,* Vol. 211, R. Boes, ed., Zurich: ETH Zurich.

Heller, V., & Hager, W. H. (2010). Impulse Product Parameter in Landslide Generated Impulse Waves. *Journal of Waterway, Port, Coastal, and Ocean Engineering, 136*, 145-155.

Heller, V., & Hager, W. H. (2011). Wave Types of Landslide Generated Impulse Waves. *Ocean Engineering, 38*, 630-640.

Heller, V. (2011). Scale effects in physical hydraulic engineering models. *Journal of Hydraulic Research*, *49*(3), 293-306.

Heller, V., Moalemi, M., Kinnear, R. D., et al. (2012). Geometrical Effects on Landslide-Generated Tsunamis. *Journal of Waterway Port Coastal and Ocean Engineering-ASCE*, *138*(4), 286-298.

Heller, V., & Spinneken, J. (2013). Improved landslide-tsunami prediction: Effects of block model parameters and slide model. *Journal of Geophysical Research-Oceans*, *118*(3), 1489-1507.

Heller, V., Bruggemann, M., Spinneken, J., & Rogers, B. (2016). Composite modelling of subaerial landslide–tsunamis in different water body geometries and novel insight into slide and wave kinematics. *Coastal Engineering*, *109*, 20-41.

Helsel, D. R., & Hirsch, R. M. (2002). Statistical Methods in Water Resources Techniques of Water Resources Investigations: Book 4, Hydrologic Analysis and Interpretation, Chapter A3. U.S. Geological Survey. Retrieved from https://pubs.usgs.gov/twri/twri4a3/pdf/twri4a3-new.pdf

Henry, A. J. (1906). *Climatology of the United States, Bulletin Q*. U.S. Weather Bureau Bull. 361, Washington, DC, 51–58.

Hibbard, S. & Peregrine, D.H. (1979). Surf and runup on a beach: a uniform bore. *J. Fluid Mech*., *95*, 323-345.

HiMAP - High Mountains Adaptation Partnership. (2014). Quillcay Plan de Acción Local Para la Adaptacion al Cambio Climatico Subcuenca de Quillcay, Mancomunidad Municipal WARAQ. Climate Change Resilient Development Project, United States Agency for International Development, Washington DC. Retrieved from http://pdf.usaid.gov/pdf_docs/PA00KNV6.pdf

Hirt, C., & Nichols, B. (1981). Volume of fluid (VOF) method for the dynamics of free boundaries. *Journal of Computational Physics, 39*(1), 201–225. doi:10.1016/0021-9991(81)90145-5

Hock, R. (1999). A distributed temperature index ice and snow melt model including potential direct solar radiation. *Journal of Glaciology*, *45*(149), 101-111.

Hock, R. (2003). Temperature index melt modelling in mountain areas. *Journal of Hydrology*, *282*,104–115.

Hock, R. (2005). Glacier melt: A review on processes and their modelling. *Progress in Physical Geography, 29*(3), 362-391.

Hock, R., Jansson, P., & Braun, L. N. (2005). Modelling the Response of Mountain Glacier Discharge to Climate Warming. In: Huber, U. M., Bugmann, H. K. M., & Reasoner, M. A. (Eds.). *Global Change and Mountain Regions (A State of Knowledge Overview)*, Springer, Dordrecht. p.243-252. Retrieved from http://www.gi.alaska.edu/~regine/Hock%26Jansson2005_MRIbook.pdf

Hofer, M., Moelg, T., Marzeion, B., et al. (2010). Empirical-statistical downscaling of reanalysis data to high-resolution air temperature and specific humidity above a glacier surface (Cordillera Blanca, Peru). *Journal of Geophysical Research-Atmospheres*, *115*(D12120).

Horizons - Horizons South America S.A.C. (2013). Informe Técnico del Proyecto, Consultoría Para El Levantamiento Fotogramétrico Detallado De La Sub Cuenca Del Río Quillcay Y La Ciudad De Huaraz Para El Proyecto, *Implementación de Medidas de Adaptación al Cambio Climático y Gestión de Riesgos en la Sub-cuenca Quillcay (IMACC-QUILLCAY) - BID-MINAM (PE-T 1168),* Ministerio Del Ambiente A Travel Del Fonam – Administrador De Los Recursos Del BID, Lima, Peru.

Hooke, R. L. (2005). *Principles of Glacier Mechanics, 2nd ed*. Cambridge: Cambridge University Press.

Huang, B., Yin, Y., Liu, G., et al. (2012). Analysis of waves generated by Gongjiafang landslide in Wu Gorge, three Gorges reservoir, on November 23, 2008. *Landslides*, *9*(3), 395-405.

Hubbard, B., Heald, A., Reynolds, J. M., Quincey, D., Richardson, S. D., Zapata, M. L., Santillan, N. P., & Hambrey, M. J. (2005). Impact of a rock avalanche on a moraine-dammed proglacial lake: Laguna Safuna Alta, Cordillera Blanca, Peru, *Earth Surf. Proc. Landf.*, *30*(10), 1251–1264.

Hubbard, B., & Glasser, N. (2005). *Field Techniques in Glaciology and Glacial Geomorphology*. West Sussex, England: John Wiley & Sons, Ltd.

Huffman, G. J., & Bolvin, D. T. (2012). TRMM and other data precipitation data set documentation. Retrieved from ftp://precip.gsfc.nasa.gov/pub/trmmdocs/3B42_3B43_doc.pdf

Huffman, G. J., Bolvin, D. T., Nelkin, E. J., Wolff, D. B., Adler, R. F., Gu, G., Hong, Y., Bowman, K. P., & Stocker, E. F. (2007). The TRMM Multisatellite Precipitation Analysis (TMPA): quasi-global, multiyear, combined-sensor precipitation estimates at fine scales. *J. Hydrometeorol.*, *8*, 38–55. doi:10.1175/JHM560.1

Huggel, C., Haeberli, W., Kääb, A., Hoelzle, M., Ayros, E., & Portocarrero, C. (2002). Assessment of Glacier Hazards and Glacier Runoff for Different Climate Scenarios Based on Remote Sensing Peruvian Andes. *Proceedings of EARSeL-*

LISSIG-Workshop Observing our Cryosphere from Space. Retrieved from http://las.physik.uni-oldenburg.de/eProceedings/vol02_1/02_1_huggel1.pdf

Huggel, C, Kaab, A ., Haeberli, W., et al. (2002). Remote sensing based assessment of hazards from glacier lake outbursts: a case study in the Swiss Alps. *Canadian Geotechnical Journal*, *39*(2), 316-330.

Huggel, C., Kaab, A ., Haeberli, W. (2003). Regional-scale GIS-models for assessment of hazards from glacier lake outbursts: Evaluation and application in the Swiss Alps. *Natural Hazards and Earth System Sciences*, *3*, 647-662.

Huggel, C., Haeberli, W., Kaäb, A., Bieri, D., & Richardson, S. (2004). An assessment procedure for glacial hazards in the Swiss Alps, *Canadian Geotech. J.*, *41*, 1068–1083.

Huggel, C., Salzmann, N., Allen, S., Caplan-Auerbach, J., Fischer, L., Haeberli, W., Larsen, C., Schneider, D., & Wessels, R. (2010). Recent and future warm extreme events and high-mountain slope stability. *Philosophical Transactions of the Royal Society A: Mathematical, Physical, and Engineering Sciences*, *368*, 2435–2459.

Huss, M., Farinotti, D., Bauder, A., & Funk, M. (2008). Modelling runoff from highly glacierized alpine drainage basins in a changing climate. *Hydrol. Process., 22*, 3888–3902.

Huss, M., & Farinotti, D. (2012). Distributed ice thickness and volume of all glaciers around the globe. *J. Geophys. Res., 117*. http://dx.doi.org/10.1029/2012JF002523 F04010.

Hutter, K., Wang, Y., & Chubarenko, I. P. (2011). *Physics of Lakes, Volume 1: Foundation of the Mathematical and Physical Background*. Heidelberg: Springer.

Hutter, K., Wang, Y., & Chubarenko, I. P. (2011). *Physics of Lakes, Volume 2: Lakes as Oscillators*. Heidelberg: Springer.

Imamura, F., Yalciner, A. C., & Ozyurt, G. (2006). *Tsunami modelling manual.* See http://www. tsunami.civil.tohoku.ac.jp/hokusai3/J/projects/manual-ver-3.1.pdf.

Imberger, J. (Ed.). (1998). *Coastal and Estuarine Studies: Physical Processes in Lakes and Oceans*. Washington D.C.: American Geophysical Union.

INDECI – Instituto Nacional de Defensa Civil. (2003). *Plan de Prevención ante Desastres: Usos del Suelo y Medidas de Mitigacion Ciudad de Huaraz*. Plate 33, Proyecto INDECI – PNUD PER/02/051 Ciudades Sostenibles, Lima. Retrieved from http://bvpad.indeci.gob.pe/doc/estudios_CS/Region_Ancash/ancash/huaraz.pdf

INDECI – Instituto Nacional de Defensa Civil. (2006). *Manual Básico para la Estimación del Riesgo*. Lima, Peru: DINAPRE- Dirección Nacional de Prevención, UEER- Unidad de Estudios y Evaluación de Riesgos.

INDECI – Instituto Nacional de Defensa Civil. (2011). *Informe de peligro Nº 003-12/05/2011/COEN-SINADECI/ 15:00 horas (Informe Nº 01): Peligro por aluvión en el departamento de Ancash*. Huaraz-Peru: COEN-SINADECI.

INDECI – Instituto Nacional de Defensa Civil. (2015). Laguna Palcacocha y su Impacto en los Distritos de Huaraz e Independencia, en Caso de Desborde y Probable Aluvión Departamento de Ancash. Dirección de Preparación-CEPIG. Lima, Peru.

IPCC – Intergovernental Panel on Climate Change. (2013): Annex I: Atlas of Global and Regional Climate Projections [van Oldenborgh, G.J., M. Collins, J. Arblaster, J.H. Christensen, J. Marotzke, S.B. Power, M. Rummukainen and T. Zhou (eds.)]. In: *Climate Change 2013: The Physical Science Basis. Contribution of Working Group I to the Fifth Assessment Report of the Intergovernmental Panel on Climate Change* [Stocker, T.F., Qin, D., Plattner, G.-K., Tignor, M., Allen, S.K., Boschung, J., Nauels, A., Xia, Y., Bex, V., & Midgley, P.M. (Eds.)]. Cambridge University Press, Cambridge, United Kingdom and New York, NY, USA.

Isfahani, A. H. G. & Brethour, J. M. (2009). On the Implementation of Two-equation Turbulence Models in *FLOW-3D*®. Flow Science, Inc.

Ives, J. (1986) Glacial Lake Outburst Floods and Risk Engineering in the Himalaya. *ICIMOD Occasional Paper No. 5*. Kathmandu, Nepal.

Jacobs, K., & Pulwarty, R. (2003). Water resource management: Science, planning and decision-making. *Water Resources Monograph Series*, *16*, 177-204.

Jeschke, M. L. (2009). Glacier Retreat in the Bolivian Andes as a Consequence of Global Climate Change Impacts on regional water supply according to the simulation of future runoff from Zongo glacier (MS Thesis). Diplomarbeit. Universität Potsdam.

Jol, H. M., & Bristow, C. S. (2003). GPR in sediments: advice on data collection, basic processing and interpretation, a good practice guide. *Geological Society, London, Special Publications*, *211*, 9-27.

Jomelli, V., et al. (2011). Irregular tropical glacier retreat over the Holocene epoch driven by progressive warming. *Nature*, *474*, 196-199.

Julian, P. R., & Fritts, H. C. (1968). On the possibility of quantitatively extending climatic records by means of dendroclimatological analysis. *Proc. First Statistical Meteorology Conf.,* Hartford, CT: Amer. Meteor. Soc., 76–82.

Juen, I. (2006*). Glacier mass balance and runoff in the tropical Cordillera Blanca, Perú* (doctoral dissertation). University of Innsbrook Tropical Glaciology Group, Institute of Geography.

Juen, I., Kaser, G., Georges, C. (2007). Modelling observed and future runoff from a glacierized tropical catchment (Cordillera Blanca, Perú). *Global and Planetary Change, 59*, 37–48.

Kafle, J., Pokhrel, P. R., Khattri, K. B., Kattel, P., Tuladhar, B. M., & Pudasaini, S. P. (2015). Landslide-generated tsunami and particle transport in mountain lakes and reservoirs. *Annals of Glaciology*, *57*(71), doi: 10.3189/2016AoG71A034, 2016.

Kamphuis, J.W., & Bowering, R.J. (1970). Impulse waves generated by landslides. *Proc. 12th Coastal Engineering Conf.,* ASCE, *1*, 575-588.

Karl, T.R., Nicholls, N., & Ghazi, A. (1999). CLIVAR/GCOS/WMO workshop on indices and indicators for climate extremes: Workshop summary. *Climatic Change, 42*, 3-7.

Kaser, G., Ames, A., & Zamora, M. (1990). Glacier fluctuations and climate in the Cordillera Blanca, Peru. *Annals of Glaciology, 14*, 136-140.

Kaser, G. (1995). Some notes on the behaviour of tropical glaciers. *Bull. Inst.fr. études andines, 24*(3), 671-681.

Kaser, G., & Georges, C. (1997). Changes of the equilibrium-line altitude in the tropical Cordillera Blanca, Peru, 1930-50, and their spatial variations. *Annals of Glaciology*, *24*, 344-349.

Kaser, G. (1999). A review of the modern fluctuations of tropical glaciers. *Global and Planetary Change*, **22**, 93-103.

Kaser, G., & Georges, C. (1999). On the mass balance of low latitude glaciers with particular consideration of the Peruvian Cordillera Blanca. *Geografiska Annaler Series A-Physical Geography*, *81A*(4), 643-651.

Kaser, G. (2001). Glacier-Climate Interaction at Low-Latitudes. *Journal of Glaciology, 47*(157), 195–204.

Kaser, G., & Osmaston, H. (2002). *Tropical Glaciers*. International Hydrology Series. Cambridge, UK: Cambridge University Press.

Kattleman, R. (2003). Glacial Lake Outburst Floods in the Nepal Himalaya: A Manageable Hazard? *Natural Hazards*, *28*, 145–154.

Kim, S. K., Liu, P. L-F., & Ligget, J. A. (1983). Boundary integral equation solutions for solitary wave generation propagation and run-up. *Coastal Engng,* 7(29S317).

Kim, B. M., & An, S. I. (2011). Understanding ENSO regime behavior upon an Increase in the warm-pool temperature using a simple ENSO model. *J. Clim., 24*, 1438–1450.

Kincer, J. B. (1919). The seasonal distribution of precipitation and its frequency and intensity in the United States. *Mon. Wea. Rev., 47*, 624–631.

Kirtman, B., Power, S.B., Adedoyin, J.A., Boer, G.J., Bojariu, R., Camilloni, I., Doblas-Reyes, F.J., Fiore, A.M., Kimoto, M., Meehl, G.A., Prather, M., Sarr, A., Schär, C., Sutton, R., van Oldenborgh, G.J., Vecchi, G., & Wang, H.J. (2013). Near-term Climate Change: Projections and Predictability. In: *Climate Change 2013: The*

Physical Science Basis. Contribution of Working Group I to the Fifth Assessment Report of the Intergovernmental Panel on Climate Change [Stocker, T.F., Qin, D., Plattner, G.-K., Tignor, M., Allen, S.K., Boschung, J., Nauels, A., Xia, Y., Bex, V., & Midgley, P.M. (Eds.)]. Cambridge University Press, Cambridge, United Kingdom and New York, NY, USA.

Kishi, T. & Saeki, H. (1966). The shoaling, breaking and runup of the solitary wave on impermeable rough slopes. In Proc. *ASCE, Tenth Conference on Coastal Engineering, Tokyo, Japan,* 322-348.

Klimes, J., Vilimek, V., & Omelka, M. (2009). Implications of geomorphological research for recent and prehistoric avalanches and related hazards at Huascaran, Peru. *Natural Hazards*, *50*, 193–209.

Klimes, J., Benesova, M., Vilimek, V., Bouska, P., Cochachin Rapre, A. (2013). The reconstruction of a glacial lake outburst flood using HEC-RAS and its significance for future hazard assessments: an example from Lake 513 in the Cordillera Blanca, Peru. *Natural Hazards*, DOI: 10.1007/s11069-013-0968-4

Klimes, J., Benesová, M., Vilímek, V., Bouska, P., Cochachin-Rapre, A. (2014). HEC-RAS and its significance for future hazard assessments: an example from Lake 513 in the Cordillera Blanca, Peru. *Natural Hazards*, *71*(3), 1617-1638.

Kowalik, Z. (2003). Basic relations between tsunamis calculation and their physics-II. *Science of Tsunami Hazards, 21.3*, 154-173.

Laenen, A., Scott, K. M., Costa, J. E., & Orzol, L. L. (1987). Hydrologic hazards along Squaw Creek from a hypothetical failure of the glacial moraine impounding Carver Lake near Sisters, Oregon. U.S. Geological Survey, Open-File Report 87-41.

Lavado-Casimiro, W. S., Labat, D., Guyot, J. L., Ronchail, J., & Ordonez, J. J. (2009). TRMM Rainfall Data Estimation over the Peruvian Amazon-Andes Basin and Its Assimilation into a Monthly Water Balance Model. New Approaches to Hydrological Prediction in Data-Sparse Regions. In *Proceedings of Symposium HS.2 at the Joint IAHS&IAH Convention*. Hyderabad, India. 245–252.

Lavado-Casimiro, W. S., & Espinoza, J. C. (2014). Impactos de El Niño y La Niña en las lluvias del Peru (1965–2007). *Revista Brasileira de Meteorologia*, *29*, 171–182, doi:10.1590/S0102- 77862014000200003

Lemieux, C. J., Gray, P. A., Douglas, A. G., et al. (2014). From science to policy: The making of a watershedscale climate change adaptation strategy. *Environmental Science & Policy*, *42*, 123-137.

LeVeque, R. J., George, D. L., & Berger, M. J. (2011). Tsunami modeling with adaptively refined finite volume methods. *Acta Numer., 20*, 211–289. DOI:10.1017/S0962492911000043

Lighthill, J. (1978). *Waves in Fluids*. Cambridge: Cambridge University Press.

Li, J. B., et al. (2011). Interdecadal modulation of El Nino amplitude during the past millennium. *Nature Clim. Change, 1*, 114–118.

Linsbauer, A., Paul, F., & Haeberli, W. (2012). Modeling glacier thickness distribution and bed topography over entire mountain ranges with GlabTop: Application of a fast and robust approach. *Journal of Geophysical Research-Earth Surface*, 117(F03007).

Linsbauer, A., Paul, F., Hoelzle, M., Frey, H., & Haeberli, W. (2009). The Swiss Alps without glaciers: A GIS-based modelling approach for reconstruction of glacier beds. *Proceedings of Geomorphometry*, edited by R. Purves et al., pp. 243–247, Univ. of Zurich, Zurich, Switzerland.

Linsbauer, A., Paul, F., Machguth, H., et al. (2013). Comparing three different methods to model scenarios of future glacier change in the Swiss Alps. *Annals of Glaciology, 54*(63), 241-253.

Liu, P. L.-F., et al. (1995). Runup of solitary waves on a circular island. *Journal of Fluid Mechanics, 302*, 259-285.

Liu, P. L. F., et al. (2005). Runup and rundown generated by three-dimensional sliding masses. *J. Fluid Mech., 536*, 107–44.

Lliboutry, L., Morales Arnao, B., Pautre, A., & Schneider, B. (1977a). Glaciological Problems Set by the Control of Dangerous Lakes in Cordillera Blanca, Peru: I. Historical Failures of Morainic Dams, Their Causes and Prevention. *Journal of Glaciology*, *18*(70), 239-254.

Lliboutry, L. (1977b). Glaciological Problems Set by the Control of Dangerous Lakes in Cordillera Blanca, Peru: II. Movement of a Covered Glacier Embedded Within a Rock Glacier. *Journal of Glaciology*, *18*(70), 239-254.

Luers, A. L., Lobella, D. B., Sklard, L. S., Addams, C. L., & Matson, P. A. (2003). A method for quantifying vulnerability, applied to the agricultural system of the Yaqui Valley, Mexico. *Global Environmental Change*, *13*, 255–267.

Mader, C. L., & Gittings, M. L. (2002). Modeling the 1958 Lituya Bay Mega Tsunami, II. *Science of Tsunami Hazards, 20*(5), 241-250.

Maeno, N., Naruse, R., & Nishimura, K. (1987). Physical characteristics of snow-avalanche debris Avalanche Formation, Movement and Effects. *Proceedings of the Davos Symposium, Sept. 1986, IAHS Pubi. no. 162*, 421-427.

Marcovitch, S. (1930). The measure of droughtiness. *Mon. Wea. Rev., 58*, 113.

Mark, B. G., McKenzie, J.M., & Gómez, J. (2005). Hydrochemical evaluation of changing glacier meltwater contribution to stream discharge: Callejon de Huaylas, Peru. *Hydrological Sciences Journal, 50*(6), 975–987.

Mark, B. G., & McKenzie, J. M. (2007). Tracing increasing tropical Andean glacier melt with stable isotopes in water. *Environ. Sci. Technol., 41*(20), 6955–6960.

Mark, B., & Seltzer, G. (2005). Evaluation of recent glacier recession in the Cordillera Blanca, Peru (AD 1962–1999): spatial distribution of mass loss and climatic forcing. *Quaternary Science Reviews, 24*, 2265-2280.

Mark, B. (2008). Tracing tropical Andean glaciers over space and time: Some lessons and transdisciplinary implications. *Global and Planetary Change, 60*, 101-114.

Mark, B. G., Bury, J., McKenzie, J. M., et al. (2010). Climate Change and Tropical Andean Glacier Recession: Evaluating Hydrologic Changes and Livelihood Vulnerability in the Cordillera Blanca, Peru. *Annals of the Association of American Geographers*, *100*(4), 794-805.

Marzeion, B., Cogley, J. G., Richter, K., & Parkes, D. (2014). Attribution of global glacier mass loss to anthropogenic and natural causes. *Science*, *345*(6199), DOI: 10.1126/science.1254702

Masson, D., & Frei, C. (2014). Spatial analysis of precipitation in a high-mountain region: exploring methods with multi-scale topographic predictors and circulation types. *Hydrol. Earth Syst. Sci.*, *18*, 4543–4563, doi: 10.5194/hess-18-4543-2014

Mathworks. (2011). *User's Guide* (r2011a). Retrieved from http://www.mathworks.com/help/matlab/ref/triscatteredinterp.html

Matthes, F. E. (1939). Report of Committee on Glaciers. *American Geophysical Union Transactions*, *20*, 518-523.

McKee, T.B, Doeskin, N.J., & Kieist, J. (1993). The Relationship of Drought Frequency and Duration to Time Scales. *Proc. 8th Conf. on Applied Climatology, January 17-22, 1993*. Boston, Masachusets: American Meteorological Society.

McKee, T. B., Doeskin, N. J., & Kieist, J. (1995). Drought Monitoring with Multiple Time Scales. *Proc. 9th Conf. on Aplied Climatology, January 15-20, 1995*. Boston, Masachusets: American Meteorological Society.

McQuigg, J. (1954). A simple index of drought conditions. *Weatherwise, 7*, 64–67.

McRoberts, D. B., Nielsen-Gammon, J. W. (2012). The Use of a High-Resolution Standardized Precipitation Index for Drought Monitoring and Assessment. *J. Appl. Meteor. Climatol.*, *51*, 68–83.

MEF – Ministry of Economy and Finances (2015). *Guía general para la identificación, formulación y evaluación social de proyectos de inversión pública, a nivel de perfil: Incorporando la gestión del riesgo en un contexto de cambio climático*. Sistema Nacional de Inversión Pública, Peru. Lima, Peru.

Mergili, M., & Schneider, J. F. (2011). Regional-scale analysis of lake outburst hazards in the southwestern Pamir, Tajikistan, based on remote sensing and GIS. *Nat. Hazards Earth Syst. Sci.*, *11*, 1447– 1462. doi: 10.5194/nhess-11-1447-2011

Mergili, M., Schneider, D., Worni, R., & Schneider, J. F. (2011). Glacial lake outburst floods (GLOFs): challenges in prediction and modelling. *Proceedings, 5th International Conference on Debris-Flow Hazard Mitigation: Mechanics, Prediction and Assessment*. Padua, Italy.

Miller, D.J. (1960). Giant Waves in Lituya Bay, Alaska. *Geological Survey Professional Paper 354-C.,* U.S. Government Printing Office, Washington D.C.

MINAM – Ministerio del Ambiente (2014). *Estrategia Nacional ante el Cambio Climático*. Ministerio del Ambiente, Peru.

Moelg, T., Cullen, N. J., & Kaser, G. (2009). Solar radiation, cloudiness and longwave radiation over low-latitude glaciers: implications for mass-balance modeling. *Journal of Glaciology*, *55*(190), 292-302.

Moelg, T., & Kaser, G. (2011). A new approach to resolving climate-cryosphere relations: Downscaling climate dynamics to glacier-scale mass and energy balance without statistical scale linking. *Journal of Geophysical Research-Atmospheres*, *116*(D16101).

Moeller, M., & Schneider, C. (2010). Calibration of glacier volume-area relations from surface extent fluctuations and application to future glacier change. *Journal of Glaciology*, *56*(195), 33-40.

Mohammed, F., McFall, B.C., & Fritz, H.M. (2011). Tsunami Generation by 3D Deformable Granular Landslides. *Solutions to Coastal Disasters,* 310-321.

Mohammed, F., & Fritz, H. M. (2012). Physical modeling of tsunamis generated by three-dimensional deformable granular landslides. *Journal of Geophysical Research-Oceans*, *117*(C11015).

Moorman, B. J., & Michel, F. A. (2000). Glacial hydrological system characterization using ground- penetrating radar. *Hydrological Processes*, *2667*, 2645-2667.

Monaghan, J.J., & Kos, A. (2000). Scott Russell's Wave Generator. *Physics of Fluids, 12*(3), 622-630.

Moser, R.D. (2009). Turbulence: Lecture Notes, ME381P3. Austin, TX: The University of Texas at Austin, Department of Mechanical Engineering.

Moss, R. H., Meehl, G. A., Lemos, M. C., et al. (2013). Hell and High Water: Practice-Relevant Adaptation Science. *Science*, *342*(6159), 696-698.

Mourre, L., Condom, T., Junquas, C., Lebel, T., Sicart, J. E., Figueroa, R., & Cochachin, A. (2016). Spatio-temporal assessment of WRF, TRMM and in situ precipitation

data in a tropical mountain environment (Cordillera Blanca, Peru). *Hydrol. Earth Syst. Sci.*, *20*, 125–141.

Müller, D., & Schurter, M. (1993). Impulse waves generated by an artificially induced rockfall in a swiss lake. *Proc. 25th IAHR Congress Tokyo*. IAHR, Madrid.

Muller, D.R. (1995). Auflaufen and Uberschwappen von Impulswellen an Talsperren: Zurich, VAW- ETH, Mitt. Nr. 137.

Murray, T., Stuart, G. W., Fry, M., et al. (2000). Englacial water distribution in a temperate glacier from surface and borehole radar velocity analysis. *Journal of Glaciology*, *46*(154), 389-398.

Murray, T., Booth, A., & Rippin, D. M. (2007). Water-content of glacier-ice: Limitations on estimates from velocity analysis of surface ground-penetrating radar surveys. *Journal of Environmental and Engineering Geophysics*, *12*(1), 87-99.

Najafi-Jilani, A., & Ataie-Ashtiani, B. (2012). Laboratory investigation of wave run-up caused by landslides in dam reservoirs. *Quarterly Journal of Engineering Geology and Hydrogeology*, *45*(1), 89-98.

Narama, C., Duishonakunov, M., Kääb, A., Daiyrov, M., & Abdrakhmatov, K. (2010). The 24 July 2008 Outburst Flood at the Western Zyndan Glacier Lake and Recent Regional Changes in Glacier Lakes of the Teskey Ala-Too Range, Tien Shan, Kyrgyzstan. *Natural Hazards and Earth System Sciences*, *10*, 647–659.

NASA LP DAAC. (2011). *ASTER Global Digital Elevation Model (GDEM). Version 2*. NASA EOSDIS Land Processes DAAC, USGS Earth Resources Observation and Science (EROS) Center, Sioux Falls, South Dakota (https://lpdaac.usgs.gov). Retrieved from http://dx.doi.org/10.5067/ASTER/AST14DEM.003. *ASTER GDEM is a product of NASA and METI*.

National Center for Atmospheric Research Staff (Eds). (2015). The Climate Data Guide: Overview: Climate Indices. Retrieved from https://climatedataguide.ucar.edu/climate-data/overview-climate-indices.

Navarro, F. J., Macheret, Y. Y., & Benjumea, B, (2005). Application of radar and seismic methods for the investigation of temperate glaciers. *Journal of Applied Geophysics*, *57*(3), 193-211.

Neal, A. (2004). Ground-penetrating radar and its use in sedimentology: principles, problems and progress. *Earth-Science Reviews*, *66*, 261–330.

Neidell, N. S., & Taner, M. T. (1971). Semblance and Other Coherency Measures for Multichannel Data. *Geophysics*, *36*(3), 482-497.

Novotny, J., & Klimes, J. (2014). Grain size distribution of soils within the Cordillera Blanca, Peru: an indicator of basic mechanical properties for slope stability evaluation. *J. Mount. Sci.*, *11*, 563–577.

Nussbaumer, S., Schaub, Y., Huggel, C., & Walz, A. (2014). Risk estimation for future glacier lake outburst floods based on local land-use changes. *Nat. Hazards Earth Syst. Sci*., *14*, 1611–1624.

Ochoa, A., Pineda, L., Crespo, P., & Willems, P. (2014). Evaluation of TRMM 3B42 precipitation estimates and WRF retrospective precipitation simulation over the Pacific–Andean region of Ecuador and Peru. *Hydrol. Earth Syst. Sci*., *18*, 3179–3193. doi: 10.5194/hess-18-3179-2014

Ohmura, A. (2001). Physical basis for the temperature-based melt-index method. *Journal of Applied Meteorology, 40*, 753-761.

OpenFOAM, (2016). *OpenFoam User Guide*. Retrieved from OpenCFD, Ltd., ESI Group. http://www.openfoam.com/documentation/user-guide/index.php

Osti, R., & Egashira, S. (2009). Hydrodynamic characteristics of the Tam Pokhari Glacial Lake outburst flood in the Mt. Everest region. *Nepal, Hydrol. Process*., *23*, 2943–2955.

Palmer, W. C. (1957). Drought-A normal part of climate. In *Weekly Weather and Crop Bulletin 44, No. la (January 10)*, 6-8.

Palmer, W.C. (1965). *Meteorological drought*. Research Paper No. 45, U.S. Department of Commerce Weather Bureau, Washington, D.C.

Palmer, W.C. (1968). Keeping track of crop moisture conditions, nationwide: The new Crop Moisture Index. *Weatherwise, 21*, 156–161.

Pannizo, A., Bellotti, G., & Girolamo, P. (2002). Application of Wavelet Transform Analysis to Landslide Generated Waves. *Coastal Engineering, 44*, 321-338.

Panizzo, A., & Girolamo, P. (2005). Forecasting Impulse Waves Generated by Subaerial Landslides. *Journal of Geophysical Research, 110*, 1-23.

Paterson, W. S. B. (2002). *The Physics of Glaciers* (3rd ed). Oxford: Butterworth Heinemann.

Paul, F., Maisch, M., Rothenbuehler, C., et al. (2007). Calculation and visualisation of future glacier extent in the Swiss Alps by means of hypsographic modeling. Global and Planetary Change, 55(4), 343-357.

Paul, F., & Linsbauer, A. (2012). Modeling of glacier bed topography from glacier outlines, central branch lines, and a DEM. *International Journal of Geographical Information Science*, *26*(7), 1173-1190.

Pedersen, G. & Gjevik, B. (1983). Run-up of solitary waves. *J. Fluid Mech.,* 135, 283-290.

Peduzzi, P., Herold, C., & Silverio, W. (2010). Assessing high altitude glacier thickness, volume and area changes using field, GIS and remote sensing techniques: the case of Nevado Coropuna (Peru). *The Cryosphere*, *4*, 313–323.

Pelinovsky, E. N., & Mazova, R. Kh. (1991). Exact analytical solutions of nonlinear problems of tsunami wave run-up on slopes with different profiles. *Natural Hazards,* 6.3, 227-249.

Peterson, T.C., et al. (2001). Report on the Activities of the Working Group on Climate Change Detection and Related Rapporteurs 1998-2001. WMO, Rep. WCDMP-47, WMO-TD 1071. Geneve, Switzerland.

Petrakov, D. A., Tutubalina, O. V., Aleinikov, A. A., Chernomorets, S. S., Evans, S. G., Kidyaeva, V. M., Krylenko, I. N., Norin, S. V., Shakhmina, M. S., Seynova, I. B. (2012). Monitoring of Bashkara Glacier lakes (Central Caucasus, Russia) and modelling of their potential outburst. *Natural Hazards*, *61*, 1293–1316.

Plewes, L. A., & Hubbard, B. (2001). A review of the use of radio-echo sounding in glaciology. *Progress in Physical Geography*, *25*(2), 203-236.

Pope, S. B. (2000). *Turbulent Flows*. Cambridge: Cambridge UP.

Portocarerro, C. (2014). *Reducing Risk from Dangerous Glacial Lakes in the Cordillera Blanca, Peru, Technical Report: The Glacial Lake Handbook*. B. Armstrong, et al. (Eds.), High Mountains Adaptation Program, United States Agency for International Development, Washington D.C.

Pouyaud, B., Zapata, M., Yerren, J., Gomez, J., Rosas, G., Suarez, W., & Ribstein, P. (2005). Avenir des ressources en eau glaciaire de la Cordillère Blanche/On the future of the water resources from glacier melting in the Cordillera Blanca, Peru. *Hydrological Sciences Journal*, *50*(6), 999–1022.

Proyecto Multinacional Andino: Geociencias para las Comunidades Andinas (2007). *Movimientos en Masa en la Región Andina: Una guía para la evaluación de amenazas*. Servicio Nacional de Geología y Minería, Publicación Geológica Multinacional, No. 4.

Qiu, L.-C. (2008). Two-dimensional SPH simulations of landslide-generated water waves. *Journal of Hydraulic Engineering-ASCE*, *134*(5), 668-671.

Quecedo, M., Pastor, M., & Herreros, M.I. (2004). Numerical Modelling of Impulse Wave Generated by Fast Landslides. *International Journal for Numerical Methods in Engineering, 59*, 1633-1656.

Quincey, D. J., Richardson, S. D., Luckman, A., Lucas, R. M., Reynolds, J. M., Hambrey, M. J., & Glasser, N. F. (2007). Early recognition of glacial lake hazards in the Himalaya using remote sensing datasets. Global and *Planetary Change*, *56*, 137-152. DOI:10.1016/j.gloplacha.2006.07.013

Rabatel, A., Bermejo, A., Loarte, E., et al. (2012). Can the snowline be used as an indicator of the equilibrium line and mass balance for glaciers in the outer tropics? *Journal of Glaciology*, *58*(212), 1027-1036.

Rabatel, A., et al. (2013). Current state of glaciers in the tropical Andes: a multi-century perspective on glacier evolution and climate change. *The Cryosphere*, *7*, 81-102.

Racoviteanu, A. (2007). GLIMS Glacier Database. Boulder, CO: National Snow and Ice Data Center/World Data Center for Glaciology. Digital Media.

Racoviteanu, A., Arnaud, Y., Williams, M., & Ordonez, J. (2008). Decadal changes in glacier parameters in the Cordillera Blanca, Peru, derived from remote sensing. *Journal of Glaciology, 54*(186), 499-510.

Radic, V., & Hock, R. (2010). Regional and global volumes of glaciers derived from statistical upscaling of glacier inventory data. *Journal of Geophysical Research-Earth Surface*, *115*(F01010), 10 pp.

Raetzo, H., Lateltin, O., Bollinger, D., & Tripet, J. (2002). Hazard assessment in Switzerland – Codes of Practice for mass movements. *Bulletin of Engineering Geology and the Environment*, *61*(3), 263–268.

Ramirez, E., Francou, B., Ribstein, P., et al. (2001). Small glaciers disappearing in the tropical Andes: a case-study in Bolivia: Glaciar Chacaltaya (16 degrees S). *Journal of Glaciology, 47*(157), 187-194.

Raper, S. C. B., & Braithwaite, R. J. (2009). Glacier volume response time and its links to climate and topography based on a conceptual model of glacier hypsometry. *Cryosphere*, *3*(2), 183–194.

Raup, B.H., Racoviteanu, A., Khalsa, S. J. S., Helm, C., Armstrong, R., & Arnaud, Y. (2007). The GLIMS Geospatial Glacier Database: a New Tool for Studying Glacier Change. *Global and Planetary Change*, *56*, 101-110. doi: 10.1016/j.gloplacha.2006.07.018

Reynolds, J. M. (1992). The identification and mitigation of glacier-related hazards: Examples from the Cordillera Blanca, Peru. In McCall, G. J. H., Laming, D. J. C., Scott, S. C. (Eds.) *Geohazards Natural and Man-made*. London, United Kingdom: Chapman and Hall, pp 143–157.

Reynolds, J.M., Dolecki, A., & Portocarrero, C. (1998). The construction of a drainage tunnel as part of glacial lake hazard mitigation at Hualcán, Cordillera Blanca, Peru. In Maund, J.G., Eddleston, M. (Eds.) *Geohazards in Engineering Geology*. Engineering Geology Special Publications, v. 15. London, United Kingdom: Geological Society, pp 25–34.

Reynolds, J. M. (2000). On the formation of supraglacial lakes on debris- covered glaciers, in: Debris-Covered Glaciers. *Proceedings of a workshop held at Seattle, Washington, USA*, September 2000, edited by: Nakawo, M., Raymond, C., and Fountain, A., 153– 161, IAHS Publication.

Reynolds, J. M. (2003). Development of glacial hazard and risk minimisation protocols in rural environments, Methods of glacial hazard assessment and management in the Cordillera Blanca, Peru. Reynolds Geo-Sciences Ltd., Flintshire (UK), 72 pp.

Reynolds, J.M. (2006). Role of geophysics in glacial hazard assessment. *First Break*, *24*, 60-66.

Reynolds, J. M. (2011), *An Introduction to Applied and Environmental Geophysics* (2nd ed.). Oxford, UK: Wiley-Blackwell.

Ribstein, P., Tiriau, E., Francou, B., et al. (1995). Tropical Climate and Glacier Hydrology - A Case-study in Bolivia. *Journal of Hydrology*, *165*(1-4), 221-234.

Richardson, S. D., & Reynolds, J. M. (2000). An Overview of Glacial Hazards in the Himalayas. *Quaternary International*, *65–66*, 31–47.

Risley, J., Walder, J., & Denlinger, R. (2006). Usoi Dam Wave Overtopping and Flood Routing in the Bartang and Panj Rivers, Tajikistan. U.S. Geological Survey Water-Resources Investigations Report 03-4004, 28 p.

Rivas, D., Cuellar, A., & McKinney, D. C. (2014). Quillcay Basin Water Resources Model. Center for Research in Water Resources. The University of Texas at Austin.

Rivas, D. S., Somos-Valenzuela, M. A., Hodges, B. R., & McKinney, D. C. (2015). Predicting outflow induced by moraine failure in glacial lakes: The Lake Palcacocha case from an uncertainty perspective. *Nat. Hazards Earth Syst. Sci.*, *15*, 1163-1179.

Rolstad, C., Whillans, I. M., Hagen, J. O., et al. (2000). Large-scale force budget of an outlet glacier: Jutulstraumen, Dronning Maud Land, East Antarctica. *Annals of Glaciology*, *30*, 35-41.

Romano, A., Bellotti, G., Briganti, R., & Franco, L. (2015). Uncertainties in the physical modelling of the wave overtopping over a rubble mound breakwater: The role of the seeding number and of the test duration. Coastal Engineering, 103, 15-21. DOI:10.1016/j.coastaleng.2015.05.005

Rosenzweig, C., Casassa, G., Karoly, D. J., Imeson, A., Liu, C., Menzel, A., Rawlins, S., Root, T. L., Seguin, B., & Tryjanowski, P. (2007). Assessment of observed changes and responses in natural and managed systems. In Parry, M. L., Canziani, O. F., Palutikof, J. P., van der Linden, P.J., Hanson, C.E. (Eds.). *Climate Change 2007: Impacts, Adaptation and Vulnerability. Contribution of Working Group II to the Fourth Assessment Report of the Intergovernmental Panel on Climate Change*. Cambridge University Press, Cambridge, pp 79–131.

Ross, E. A., et al. (1997). *National Engineering Handbook: Irrigation Guide*. National Resources Conservation Service. United States Department of Agriculture.

Rzadkiewicz, S.A., Mariotti, C., & Heinrich, P. (1997). Numerical Simulation of Submarine Landslides and their Hydraulic Effects. *Journal of Waterway, Port, Coastal, and Ocean Engineering, 123*, 149-157.

Saintenoy, A., Friedt, J. -M., Booth, A. D., et al. (2013). Deriving ice thickness, glacier volume and bedrock morphology of Austre Lovenbreen (Svalbard) using GPR. *Near Surface Geophysics*, *11*(2), 253-261.

Salm, B. (1993). Flow, flow transition and runout distances of flowing avalanches. *Annals of Glaciology*, *18*, 221-226.

Salzmann, N., Huggel, C., Rohrer, M., Silverio, W., Mark, B. G., Burns, P., & Portocarrero, C. (2013). Glacier changes and climate trends derived from multiple sources in the data scarce Cordillera Vilcanota region, southern Peruvian Andes. *The Cryosphere*, *7*, 103-118.

Sanabria, J., Calanca, P., Alarcón, C., & Canchari, G. (2014). Potential impacts of early twenty-first century changes in temperature and precipitation on rainfed annual crops in the Central Andes of Peru. *Reg. Environ. Change*, *14*, 1533–1548. doi: 10.1007/s10113-014-0595-y

Sass, O. (2007). Bedrock detection and talus thickness assessment in the European Alps using geophysical methods. *Journal of Applied Geophysics*, *62*(3), 254-269.

Schaub, Y., Huggel, C., & Cochachin, A. (2015). Ice-avalanche scenario elaboration and uncertainty propagation in numerical simulation of rock-/ice-avalanche-induced impact waves at Mount Hualcán and Lake 513, Peru. *Landslides*. DOI: 10.1007/s10346-015-0658-2

Scheel, M. L., Rohrer, M., Huggel, C., Santos Villar, D., Silvestre, E., & Huffman, G. J. (2011). Evaluation of TRMM Multi- satellite Precipitation Analysis (TMPA) performance in the Central Andes region and its dependency on spatial and temporal resolution. *Hydrol. Earth Syst. Sci.*, *15*, 2649–2663. doi: 10.5194/hess-15-2649-2011

Schneider, D., Bartelt, P., Caplan-Auerbach, J., Christen, M., Huggel, C., & McArdell, B. W. (2010). Insights into rock-ice avalanche dynamics by combined analysis of seismic recordings and a numerical avalanche model. *J. Geo. Res.*, *115*(F04026). doi: 10.1029/2010JF001734

Schneider, D., Huggel, C., Cochachin, A., Guillén, S., & García, J. (2014) Mapping hazards from glacier lake outburst floods based on modelling of process cascades at Lake 513, Carhuaz, Peru. *Adv. Geosci.*, *35*, 145–155.

Shafer, B.A. & Dezman, L.E. (1982). Development of a Surface Water Supply Index (SWSI) to assess the severity of drought conditions in snowpack runoff areas. In *Proceedings of the Western Snow Conference*, 164–175. Colorado State Univ., Fort Collins, CO.

Sharma, P. V. (1997). *Environmental Engineering and Geophysics*. Cambridge UP.

Sicart, J. E., Wagnon, P., & Ribstein, P. (2005). Atmospheric controls of the heat balance of Zongo Glacier (16°S, Bolivia). *Journal of Geophysical Research*, *110*(D12106).

Sicart, J.E., Ribstein, P., Francou, B., et al. (2007). Glacier mass balance of tropical Zongo glacier, Bolivia, comparing hydrological and glaciological methods. *Global and Planetary Change*, *59*(1-4), 27-36.

Sicart, J. E., Hock, R., & Six, D. (2008). Glacier melt, air temperature, and energy balance in different climates: The Bolivian Tropics, the French Alps, and northern Sweden. *Journal of Geophysical Research*, *113*(D24113).

Sicart, J. E., Hock, R., Ribstein, P., et al. (2010). Sky longwave radiation on tropical Andean glaciers: parameterization and sensitivity to atmospheric variables. *Journal of Glaciology*, *56*(199), 854-860.

Sicart, J. E., Hock, R., Ribstein, P., Litt, M., & Ramirez, E. (2011). Analysis of seasonal variations in mass balance and meltwater discharge of the tropical Zongo Glacier by application of a distributed energy balance model. *Journal of Geophysical Research*, *116*, 18 pp.

Silva, R., Valderrama, P., Pari, W., & Dueñas, S. (2010). Prospeccion Geofísica y Evaluación de Peligros Geológicos en los Depósitos Morrénicos de la Laguna Palcacocha, Cordillera Blanca – Ancash. *XV Congreso Peruano de Geología, Resúmenes Extendidos*. Sociedad Geológica del Perú, Pub. Esp. N° 9. Cusco, p. 1066-1070.

Slingerland, R. L., & Voight, B. (1979). Occurences, Properties and Predictive Models of Landslide-generated Impulse Waves. *Rockslides and Avalanches,* 2, 317-397, Ed. Voight, B. *Developments in Geotechnical Engineering,* 14B. Elsevier, Amsterdam.

Slingerland, R. L., & Voight, B. (1982). Evaluating hazard of landslide-induced water waves. *Journal of the Waterway, Port, Coastal and Ocean Division, Proceedings of the American Society of Civil Engineers*, *108*(WW4), 504-512.

Somos-Valenzuela, M. A. (2014). Vulnerability and Decision Risk Analysis in Glacier Lake Outburst Floods (GLOF). Case Studies: Quillcay Sub Basin in the Cordillera Blanca in Peru and Dudh Koshi Sub Basin in the Everest Region in Nepal (PhD Dissertation). The University of Texas at Austin, Austin, Texas.

Somos-Valenzuela, M. A., Chisolm, R. E., McKinney, D. C., & Rivas, D. A. (2014). Inundation Modeling of a Potential Glacial Lake Outburst Flood in Huaraz, Peru, Center for Research in Water Resources Online Report 14-01. Center for Research in Water Resources, The University of Texas at Austin.

Somos-Valenzuela, M. A., McKinney, D. C., Byers, A. C., Rounce, D. R., Portocarrero, C., & Lamsal, D. (2015). Assessing downstream flood impacts due to a potential GLOF from Imja Tsho in Nepal. *Hydrology and Earth System Sciences*, *19*(3), 1401–1412.

Somos-Valenzuela, M. A., Chisolm, R. E., Rivas, D. S., Portocarrero, C., & McKinney, D. C. (2016). Modeling a glacial lake outburst flood process chain: the case of Lake Palcacocha and Huaraz, Peru. *Hydrol. Earth Syst. Sci., 20*, 2519-2543. DOI:10.5194/hess-20-2519-2016, 2016.

St-Germain, P., Nistor, I., & Townsend, R. (2012). Numerical modeling of the impact with structures of tsunami bores propagating on dry and wet beds using the SPH method. *Int. J. Protect. Struct., 3*, 221–256. DOI:10.1260/2041-4196.3.2.221

Stoker, J. J. (1957). *Water Waves: The Mathematical Theory with Applications*. New York: Interscience Publishers.

Suarez, W., Chevallier, P., Pouyaud, B., et al. (2008). Modelling the water balance in the glacierized Paron Lake basin (White Cordillera, Peru). *Hydrological Sciences Journal -Journal des Sciences Hydrologiques*, *53*(1), 266-277.

Synolakis, C. E. (1987). The runup of solitary waves. *Journal of Fluid Mechanics*, *185*, 523-545.

Synolakis, C. E. (1990). Tsunami runup on steep slopes—How good linear theory really is. *Natural Hazards*, *4*, 221-234.

Synolakis, C. E., Bernard, E. N., Mofjeld, H. O., Titov, V. V., Kanoglu, U., & Gonzalez, F. I. (2008). Validation and verification of tsunami numerical models. *Pure Appl. Geophys., 165*, 2197–2228. DOI:10.1007/978-3-0346-0057-6_11

Tachikawa, T., Kaku, M., Iwasaki, A., Gesch, D., Oimoen5, Zheng Zhang, M., Danielson, J., Krieger, T., Curtis, B., Haase, J., Abrams, M., Crippen, R., & Carabajal, C. (2011). ASTER Global Digital Elevation Model Version 2 – Summary of Validation Results. NASA Land Processes Distributed Active Archive Center and the Joint Japan-US ASTER Science Team. ASTER GDEM Validation Team (Compiled by Dave Meyer). Retrieved from http://www.jspacesystems.or.jp/ersdac/GDEM/ver2Validation/Summary_GDEM2_validation_report_final.pdf

Tadepalli, S., & Synolakis, C. E. (1996). Model for the leading waves of tsunamis. *Physical Review Letters, 77*(10), 2141.

Tannehill, I. R. (1947). *Drought: Its Causes and Effects.* Princeton University Press.

Thornton, P. K., Ericksen, P. J., Herrero, M., et al. (2014). Climate variability and vulnerability to climate change: a review. *Global Change Biology*, *20*(11), 3313-3328.

Thornthwaite, C. W. (1948). An approach toward a rational classification of climate. *Geogr. Rev., 38*, 55–94.

Thornthwaite, C. W., & Mather, J. R. (1955). The water budget and its use in irrigation. In Stefferud, A. (Ed.). *Water—Yearbook of Agriculture 1955*. U.S. Dept. of Agriculture, 346–358.

Titov, V. V. & Gonzalez, F. I. (1997). Implementation and testing of the Method Of Splitting Tsunami (MOST) model. NOAA Technical Memorandum ERL PMEL-112 1927, NOAA, Seattle, WA, USA.

Titov, V. V., & Synolakis, C. E. (1998). Numerical modeling of tidal wave runup. *Journal of Waterway, Port, Coastal, and Ocean Engineering*, *124*(4), 157-171.

Trenberth, K. E. (1984). Signal versus noise in the Southern Oscillation. *Mon. Wea. Rev*., *112*, 326-332.

UGRH – Unidad de Glaciologia y Recursos Hidricos. (2009). Bathymetric survey of Lake Palcacocha. Autoridad Nacional de Agua (ANA) de Peru.

UGRH – Unidad de Glaciologia y Recursos Hidricos. (2010). *Area de Inventario de Glaciares y Lagunas*. Autoridad nacional del Agua, Direcccion de Conservacion y Planeamiento de Recursos Hidricos, Huaraz, Peru.

Urrutia, R. & Vuille, M. (2009). Climate change projections for the tropical Andes using a regional climate model: Temperature and precipitation simulations for the end of the 21st century. *Journal of Geophysical Research*, *14*(D02108). DOI:10.1029/2008JD011021

USAID – United States Agency for International Development. (2007). *Adapting to Climate Variability and Change: A Guidance Manual for Development Planning*. United States Agency for International Development.

USAID – United States Agency for International Development. (2012). *USAID Climate Change Adaptation Plan*. United States Agency for International Development.

USAID – United States Agency for International Development. (2014). *Climate-Resilient Development: A Framework for Understanding and Addressing Climate Change*. United States Agency for International Development.

Vance, T. R., van Ommen, T. D., Curran, M. A. J., Plummer, C. T., & Moy, A. D. (2012). A millennial proxy record of ENSO and eastern Australian rainfall from the Law Dome ice core, East Antarctica. *J. Clim., 26*, 710–725.

Valderrama, P., & Vilca, O. (2012). Dinamica e Implicancias del Aluvión de la Laguna 513, Cordillera Blanca, Ancash Perú. *Revista de la Asociación Geológica Argentina*, *69*(3), 400 – 406.

Valderrama, P., Pari, W., Silva, C., & Fídel, L. (2013). Evaluación Ingeniero – Geológico: Laguna de Palcacocha y su Influencia en la Ciudad de Huaraz

Cordillera Blanca. Informe Técnico No. A6631. *Instituto Geológico Minero y Metalúrgico (INGEMMET), Sector Energía y Minas*. Región Ancash.

Vaughan, D.G., Comiso, J.C., Allison, I., Carrasco, J., Kaser, G., Kwok, R., Mote, P., Murray, T., Paul, F., Ren, J., Rignot, E., Solomina, O., Steffen, K., & Zhang, T. (2013). Observations: Cryosphere. In: *Climate Change 2013: The Physical Science Basis. Contribution of Working Group I to the Fifth Assessment Report of the Intergovernmental Panel on Climate Change* [Stocker, T.F., Qin, D., Plattner, G.-K., Tignor, M., Allen, S.K., Boschung, J., Nauels, A., Xia, Y., Bex, V., & Midgley, P.M. (Eds.)]. Cambridge University Press, Cambridge, United Kingdom and New York, NY, USA.

Vergara Rodriguez, K. V. (2011).Variabilidad Climática, Percepción Ambiental y Estrategias de Adaptación de la Comunidad Campesina de Conchucos, Ancash (Licenciada Thesis). Pontifica Universidad Católica del Perú.

Vergara Rodriguez, K. V. (2015). *Línea de base y metodología para analizar riesgos, factores de vulnerabilidad y capacidades adaptativas locales*. UNESCO Project: Línea de base y metodología para analizar riesgos, factores de vulnerabilidad y capacidades adaptativas locales. The Mountain Institute, Inc.

Vilimek, V., Zapata, M. L., Klimes, J., Patzelt, Z., & Santillan, N. (2005). Influence of glacial retreat on natural hazards of the Palcacocha Lake area, Peru, *Landslides*, *2*, 107–115.

Voight, B. (Ed.). (1978). *Rockslides and Avalanches, 1: Natural Phenomena*. Developments in Geotechnical Engineering Vol. 14A, Amsterdam: Elsevier Scientific Publishing Company.

Vuille, M., & Bradley, R. S. (2000). Mean annual temperature trends and their vertical structure in the tropical Andes. *Geophysical Research Letters*, *27*(23), 3885-3888.

Vuille, M., Bradley, R.S., & Keimig, F. (2000). Interannual climate variability in the Central Andes and its relation to tropical Pacific and Atlantic forcing. *Journal of Geophysical Research- Atmospheres*, *105*(D10), 12447-12460.

Vuille M., Bradley, R.S., Werner, M., et al. (2003). 20th century climate change in the tropical Andes: Observations and model results. *Climatic Change*, *59*(1-2), 75-99.

Vuille M., Francou, B., Wagnon, P., Juen, I., Kaser, G., Mark, B., & Bradley, R. (2008). Climate change and tropical Andean glaciers: Past, present and future. *Earth-Science Reviews, 89*, 79-96.

Vuille, M., Kaser, G., & Juen, I. (2008). Glacier mass balance variability in the Cordillera Blanca, Peru and its relationship with climate and the large-scale circulation. *Global and Planetary Change, 62*, 14-28.

Wagnon, P., Ribstein, P., Kaser, G., & Berton, P. (1999). Energy balance and runoff seasonality of a Bolivian glacier. *Global Planeary Change*, *22*, 49–58.

Walder, J. S., & O'Connor, J. E. (1997). Methods for predicting peak discharge of floods caused by failure of natural and constructed earthen dams. *Water Resources Research*, *33*(10), 2337–2348.

Walder, J.S., & Watts, P. (2003). Tsunamis Generated by Subaerial Mass Flows. *Journal of Geophysical Research, 108*, 1-20.

Wang, W., Yao, T., Gao, Y., Yang, X., & Kattel, D. B. (2011). A first–order method to identify potentially dangerous glacial lakes in a region of the southeastern Tibetan Plateau. *Mountain Res. Develop.*, *31*, 122–130.

Wang, X., Liu, S., Guo, W., & Xu, J. (2008). Assessment and simulation of glacier lake outburst floods for Longbasaba and Pida lakes, China. *Mountain Res. Develop.*, 28, 310–317.

Wang, Y., Liu, P., & Chang, C. (2011). Solid Landslide Generated Waves. *Journal of Fluid Mechanics, 675*, 529-539.

Wang, W., Gao, Y., Anacona, P. I., Lei, Y., Xiang, Y., Zhang, G., Li, S., & Lu, A. (2015). Integrated hazard assessment of Cirenmaco glacial lake in Zhangzangbo valley, Central Himalayas. *Geomorphology*, DOI:10.1016/j.geomorph.2015.08.013

Wang, W., Chen, G., Zhang, H., Zhou, S., Liu, S., Wu, Y., & Fu-song Fan, F. (2016). Analysis of landslide-generated impulsive waves using a coupled DDA-SPH method. Engineering Analysis with Boundary Elements, 64, 267-277. DOI: 10.1016/j.enganabound.2015.12.014.

Watanabe, T., Ives, J., & Hammond, J. (1994). Rapid growth of a glacial lake in Khumbu Himal, Himalaya: Prospects for a catastrophic flood. *Mountain Research and Development*, *14*, 329–340.

Watanabe, T., Lamsal, D. & Ives, J. D. (2009). Evaluating the growth characteristics of a glacial lake and its degree of danger of outburst flooding: Imja Glacier, Khumbu Himal, Nepal. *Norsk Geografisk Tidsskrift/Norwegian Journal of Geography*, 63, 255-267. Oslo. ISSN 0029-1951.

Watts, P. (2000). Tsunami Features of Solid Block Underwater Landslides. *Journal of Waterway, Port, Coastal, and Ocean Engineering, 126*, 144-152.

Wegner, S. A. (2014). *Lo Que el Agua se Llevó: Consecuencias y Lecciones del Aluvión de Huaraz de 1941*. Technical Note 7 of the series "Technical Notes on Climate Change", Ministry of Environment, Lima, Peru.

West, L. J., Rippin, D. M., Murray, T., et al. (2007). Dielectric permittivity measurements on ice cores: Implications for interpretation of radar to yield glacial unfrozen water content. *Journal of Environmental and Engineering Geophysics*, *12*(1), 37-45.

Westoby, M. J., Glasser, N. F., Brasington, J., Hambrey, M. J., Quincey, D. J., & Reynolds, J. M. (2014a). Modelling outburst floods from moraine-dammed glacial lakes. *Earth Science Reviews.* doi: 10.1016/j.earscirev.2014.03.009

Westoby, M. J., Glasser, N. F., Hambrey, M. J., Brasington, J., Reynolds, J. M., & Hassan, M. A. A. M. (2014b). Reconstructing historic Glacial Lake Outburst Floods through numerical modelling and geomorphological assessment: Extreme events in the Himalaya. *Earth Surface Processes and Landforms*, *39*(12),1675-1692.

Westoby, M. J., Brasington, J., Glasser, N. F., Hambrey, M. J., Reynolds, J. M., Hassan, M. A. A. M., & Lowe, A. (2015). Numerical modelling of glacial lake outburst floods using physically based dam-breach models. *Earth Surf. Dynam.*, *3*, 171–199.

WGMS – World Glacier Monitoring Service (2012). Fluctuations of Glaciers 2005-2010 (Vol. X). Zemp, M., Frey, H., Gärtner-Roer, I., Nussbaumer, S.U., Hoelzle, M., Paul, F., & W. Haeberli (Eds.). ICSU (WDS) / IUGG (IACS) / UNEP / UNESCO / WMO, World Glacier Monitoring Service, Zurich, Switzerland. DOI: 10.5904/wgms-fog-2012-11.

Whipple, W., (1966). Regional drought frequency analysis. *Proc. ASCE*, *92*(IR2), 11-31.

Wiegel, R.L. (1955). Laboratory Studies of Gravity Waves Generated by the Movement of a Submarine Body. *Transactions of the American Geophysical Union, 36*(5), 759-774.

Wilcox, D. C. (1998). Turbulence Modeling for CFD, DCW Industries, Inc.

Wilhite, D. A., & Glantz, M. H. (1985). Understanding the drought phenomenon: The role of definitions. *Water International, 10*(3), 111–120.

Wilson, N. J., & Flowers, G. E. (2013). Environmental controls on the thermal structure of alpine glaciers. *The Cryosphere*, *7*, 167–182.

Winkler, M., Juen, I., Moelg, T., et al. (2009). Measured and modelled sublimation on the tropical Glaciar Artesonraju, Peru. *Cryosphere*, *3*(1), 21-30.

Wohl, E. E., Pulwarty, R. S., & Zhang, J. Y. (2000). Assessing climate impacts. *Proceedings of the National Academy of Sciences of the United States of America, 97*(21), 11141-11142.

Woodward, J., & Burke, M. J. (2007). Applications of Ground-Penetrating Radar to Glacial and Frozen Materials, *J. Environmental and Engineering Geophysics*, *12*(1), 69–85.

Worni, R., Stoffel, M., Huggel, C., Volz, C., Casteller, A., & Luckman, B. (2012). Analysis and dynamic modeling of a moraine failure and glacier lake outburst flood at Ventisquero Negro, Patagonian Andes (Argentina). *Journal of Hydrology*, *444–445*, 134–145.

Worni, R., Huggel, C., Clague, J. J., Schaub, Y., Stoffel, M. (2014). Coupling glacial lake impact, dam breach, and flood processes: A modeling perspective. *Geomorphology*, *224*, 161–176.

Xie, J., Nistor, I., & Murty, T. (2012). A corrected 3D SPH method for modeling breaking tsunami waves. *Nat. Hazards, 60*, 81–100. Special Issue: Tsunami Impacts on Coastlines. DOI:10.1007/ s11069-011-9954-x

Xie, S. P., Deser, C., Vecchi, G. A., Ma, J., Teng, H. Y., & Wittenberg, A. T. (2010). Global warming pattern formation: Sea surface temperature and rainfall. *J. Clim., 23*, 966–986.

Yakhot V. & Orszag, S. A. (1986). Renormalization group analysis of turbulence. I. Basic theory. *J. Sci. Comput*., *1*, 3-51.

Yde, J. C., Gillespie, M. K., Loland, R., et al. (2014). Volume measurements of Mittivakkat Gletscher, southeast Greenland. *Journal of Glaciology*, *60*(224), 1199-1207.

Yevjevich, V. (1967). An objective approach to definitions and investigations of continental hydrologic droughts. Hydrology Paper 23, Colorado State University, Fort Collins, CO.

Zamora, R., Ulloa, D., Garcia, G., Mella, R., Uribe, J., Wendt, J., Rivera, A., Gacitua, G., & Casassa, G. (2009). Airborne radar sounder for temperate ice: initial results from Patagonia. *J. Glaciol*., *55*(191), 507–512.

Zelt, Z. A. (1986). Tsunamis: The response of harbors with sloping boundaries to long wave excitation. *Rep.* KH-R-47. W. M. Keck Laboratory of Hydraulics and Water Resources, California Institute of Technology, Pasadena, CA. 318 pp.

Zelt, J. A. (1991). The run-up of nonbreaking and breaking solitary waves. *Coastal Engineering, 15*(3), 205-246.

Zhang, X., et al. (2005). Avoiding Inhomogeneity in Percentile-Based Indices of Temperature Extremes. *J. Climate*, *18*, 1641-1651. (Available as: JCLI3366.1.pdf)

Zhang, Q., Guan, Y., & Yang, H. (2008): ENSO amplitude change in observation and coupled models. *Adv. Atmos. Sci., 25*, 361–366.

Zweifel, A., Hager, W. H., and Minor, H. E. (2006). Plane Impulse Waves in Reservoirs. *Journal of Waterway, Port, Coastal, and Ocean Engineering, 132*, 358-368.

Zweifel, A., Zuccala, D., & Gatti, D. (2007). Comparison between Computed and Experimentally Generated Impulse Waves. *Journal of Hydraulic Engineering, 133*, 208-216.